2024-05-01

Analysis Of Additively Manufactured Inconel 718 Combustion Behavior In Promoted Oxygen Environments

Dominic George Dieguez
University of Texas at El Paso

ANALYSIS OF ADDITIVELY MANUFACTURED INCONEL 718 COMBUSTION BEHAVIOR IN PROMOTED OXYGEN ENVIRONMENTS

DOMINIC GEORGE DIEGUEZ

Doctoral Program in Material Science and Engineering

APPROVED:

Stephen W. Stafford, Ph.D., Chair

Darren M. Cone

David. A. Roberson, Ph.D.

Robert C. Roberts, Ph.D.

Stephen L. Crites, Jr., Ph.D.
Dean of the Graduate School

Dedication

To all the friends, family, and supporters who helped enable me to complete this – particularly my incredible mother and amazing wife.

ANALYSIS OF ADDITIVELY MANUFACTURED INCONEL 718 COMBUSTION BEHAVIOR IN PROMOTED OXYGEN ENVIRONMENTS

by

DOMINIC GEORGE DIEGUEZ, B.S.

DISSERTATION

Presented to the Faculty of the Graduate School of

The University of Texas at El Paso

in Partial Fulfillment

of the Requirements

for the Degree of

DOCTOR OF PHILOSOPHY

Department of Metallurgical, Materials and Biomedical Engineering

THE UNIVERSITY OF TEXAS AT EL PASO

May 2024

Acknowledgements

There are likely too many people that have helped me in my academic journey to fit on this page, but I'll attempt to thank as many as possible and hope that anyone not included here knows that any contribution they had (big or small) is greatly appreciated.

First and foremost, I need to acknowledge the tremendous influence that the faculty within the Metallurgical, Materials and Biomedical Engineering department have had on me, not only in their ability to teach me and grow my knowledge in this field but also for the advice and guidance that they provided over the years. I cannot thank you all enough, and I'd like to specifically highlight Dr. Bradley, Dr. Roberson, Dr. Varma, and Dr. Stafford for everything you've given me.

I've been very lucky to have had several incredible mentors over the course of this degree, but in particular I'd like to acknowledge Darren Cone for serving as my graduate advisor and making sure that I was always on track. Another person who deserves a great deal of recognition is Jonathan Tylka for not only guiding my path towards employment with NASA but also for providing the groundwork and technical expertise which made this research possible.

Logistically this work could not have been completed without the capabilities and experience of several folks at White Sands Test Facility, and I'd like to thank Karen Rodriguez, Susana Harper, Ilse Alcantara Reyes, Alfredo Juarez, and Staci Delfin. Additionally, NASA personnel including Sara Luna, Ron Lewis, Matthew Galeano, Mike Pedley, Alma Stephanie Tapia, and John Figert at Johnson Space Center's Materials and Processing Branch also provided support or guidance and are greatly appreciated for all that they have contributed.

Last but not least, I'd like to acknowledge my beautiful wife and pets for tolerating my absence during late nights and long weekends at the lab. I could not have accomplished this without you.

Abstract

Promoted combustion testing is a vital tool for engineers to establish the combustion and flammability characteristics of materials (metallic or otherwise) in oxygen enriched environments. Historically, much of the established data for metallic promoted combustion has been with regards to materials in their cast and wrought forms. However, with the emergence of additive manufacturing as a preferred method of fabrication, the need exists to evaluate how metals in that form behave. Recent testing has demonstrated that even if a metal or alloy is nominally the same with regards to chemistry, flammability between samples in the wrought form can differ significantly from those which were additively manufactured. This has provided a rationale to evaluate what underlying principles and conditions may be driving such a variability in flammability response. This work will serve as an analysis and characterization of one specific alloy (the nickel-based superalloy Inconel 718), a material popular for aerospace applications such as liquid fueled rocket components and turbine engines. Promoted combustion testing (per the ASTM G124 standard) was conducted on samples of both wrought and selective laser melted (SLM) fabrication, to provide comparison of flammability response between materials produced by each manufacturing method. Additionally, post-build treatments were applied to test samples to identify any effects on performance provided by hot isostatic pressing (HIP), oxygen-getting wrapping during HIP, stress relieving, and solutionizing/aging heat treatments. This project will utilize optical and scanning electron microscopy, energy dispersive spectroscopy, x-ray diffraction, and metallography to identify the differences between flammability behavior of additively manufactured and wrought Inconel 718. This information is key for engineers to understand the safety and oxygen compatibility of this material while in use by an industry which

will undoubtedly increase the adoption and use of additive manufacturing as a primary means for fabrication.

Table of Contents

List of Tables

List of Figures

List of Illustrations

Chapter 1: Introduction

Due to the inherently hostile conditions associated with space exploration, safety and risk are foundational concerns in the development process of any flight hardware or program. The extreme environments seen in service are sources of a variety of hazards, which engineers and scientists must account for to protect not only vehicles and hardware but also the lives of personnel tasked to operate such things. For these reasons, there are a multitude of tests and experiments to evaluate how safe an action or design may be.

One such hazard that must be designed for is oxygen compatibility. This refers to how compatible a material or product will be within an environment which contains some fraction of oxygen content. In simplest terms engineers need to know if a material can ignite in the presence of oxygen, how readily that ignition will occur if it does so, and how long such combustion will continue until extinguishment through some means can occur. It's sensible that fire is a concern for any engineered structure, however the risk is multiplied in the case of aerospace applications as these environments most often see elevated pressure, higher than breathing-air concentration of oxygen, or both. These factors are well documented for making combustion more probable and for making subsequent burning more severe.

When engineers are evaluating how compatible a material is with an oxygen environment, the cumulative process is known as an oxygen compatibility assessment (OCA). In the conductance of an OCA, engineers will likely reference promoted combustion data for the materials involved. A promoted combustion test (per ASTM standard G124) involves placing a 1/8" diameter rod of test material into a chamber which has controls for pressure and gas composition (ranging from pure oxygen to any percent mixture of diluent gas, such as nitrogen), and then igniting the bottom of the rod such that the flame will travel up the test sample until

extinguishment or full consumption. The data point yielded by this testing is a burn length, which then advises on how flammable the test material is at the conditions of the chamber (short burn length equates to less flammable, longer burn length equates to more flammable). This is important information to have as it allows one to have some degree of confidence in predicting if a material desired for an application will be flammable at the pressure and oxygen concentrations of its service environment.

Promoted combustion testing has been conducted broadly across the aerospace industry for many years, with NASA tracing internal test data back to at least the mid 1980's at its White Sands Test Facility in Las Cruces, NM. This has resulted in a large amount of data being generated over the decades for a variety of commonly used materials, such as the nickel-based superalloy Inconel 718. However, with few exceptions, these tests were almost exclusively conducted on sample rods which were cast and wrought. Until recently that posed no issue, but today's industry is rapidly evolving to adopt new ways to manufacture materials and components. While exciting, the breakneck speed at which these methods are developed means that a knowledge gap can form in what the life-cycle properties and ultimate performance of these newer materials will be in comparison to their more traditional counterparts. This lack of understanding can lead to premature assumptions that if a material or alloy has maintained its chemical constituency, additively manufacturing it should yield comparable results to casting and working it.

It has been found in recent testing that this is not always the case, and in particular oxygen compatibility can vary greatly between the methods as well as between materials which are subjected to post processing such as Hot Isostatic Pressing (HIP), applying oxygen-getting wraps during the HIP, and using solutionizing/aging heat treatments. It is not fully understood what the underlying causes are of this variability in flammability, which has provided a rationale for testing

and characterization to be done on materials representative of the various manufacturing configurations to better comprehend what drives performance. This is the premise behind this project, and if successful should be valuable in aiding engineers in their goal of safely using additively manufactured Inconel 718 in promoted oxygen environments.

It should be noted that this work will be with regards to specific parameters and conditions, namely that the material is Inconel 718 and that the environment is considered pure oxygen and in the range of 600 – 675 psia. Findings should not be assumed to directly correlate to other metals and alloy systems; however, attempts will be made to understand at a fundamental level how the manufacturing methods affect the structure of this material and what influence those structures will have on properties and performance. Similarities may exist to other materials, but experimental data should always be used for validation (in lieu of interpolating based off this work).

Chapter 2: Background and Literature Review

Background on ASTM G124 Test Method

The ASTM G124 test method refers to the "Standard Test Method for Determining the Combustion Behavior of Metallic Materials in Oxygen-Enriched Atmospheres" [1]. The method sees a metallic sample manufactured to a 6" length and 1/8" diameter and placed within a test chamber and fixed vertically by a sample holder. This test chamber is a controlled volume of gas which operators can manipulate to have specific values for pressure (psia) and oxygen concentration. In test scenarios where pure oxygen is not desired, fractions of diluent gas can be introduced to create a mixed gas environment (nitrogen is often used to emulate breathing air).

Gas inlet and outlet valves are utilized to control these parameters for the duration of a test. A power source then begins to provide current to an ignition wire (commonly a palladium-based product like Pyrofuze™), generating heat as electrical resistance builds up. This joule-heating eventually provides enough energy to ignite what's known as a promoter (NASA typically tends to use a small "puck" of magnesium). This promoter is attached to the bottom of the vertically fixed sample rod and is chosen such that when it ignites it releases a large amount of energy which is sufficient to ignite the sample material and begin the combustion process. A schematic of a typical chamber is shown below in fig. 1.

The sample is then allowed to burn in these conditions until extinguishment occurs or the material is entirely consumed by the combustion. Though several pieces of data can be gleaned from this testing, such as combustion velocity or the regression rate of the molten interface (RRMI), burn length is a particularly ubiquitous data point which is defined by the test. Burn length serves as a general analog to how flammable a material is, with longer lengths associated with being more flammable. A burn length of 3 cm or greater is considered a burn, and any less than

that no burns [4]. This binary response is used to establish flammability thresholds for a material within the specific conditions of pressure and oxygen concentration. These thresholds are then used to estimate the level of oxygen compatibility that material has with said environment, which informs engineers on the safety of their designs and how much margin exists with respect to pressure fluctuations or oxygen content.

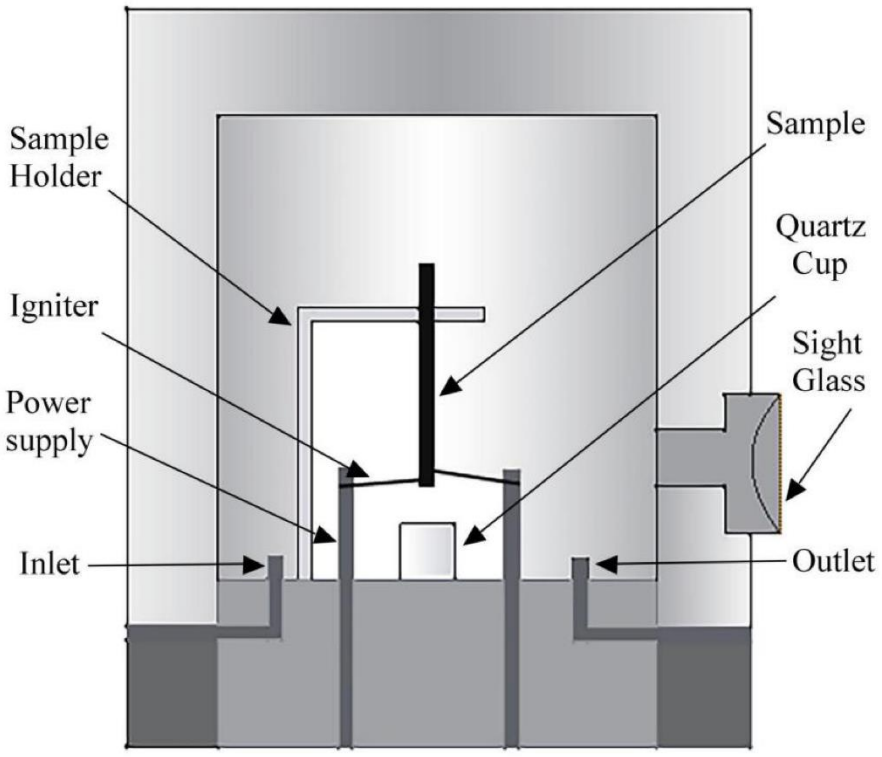

Fig. 1 – Schematic of a typical promoted combustion test chamber. Ref [1].

Generally speaking, samples which have undergone promoted combustion testing exhibit a burn tip comprised of three regions: the oxidized area, the melted/resolidified area, and the heat affected zone. The bulk material which has not been influenced by the heat of combustion is generally in the same state as it was prior to testing. A typical example of this is shown below in fig. 2, the burn tip of a combusted nickel-based alloy sample.

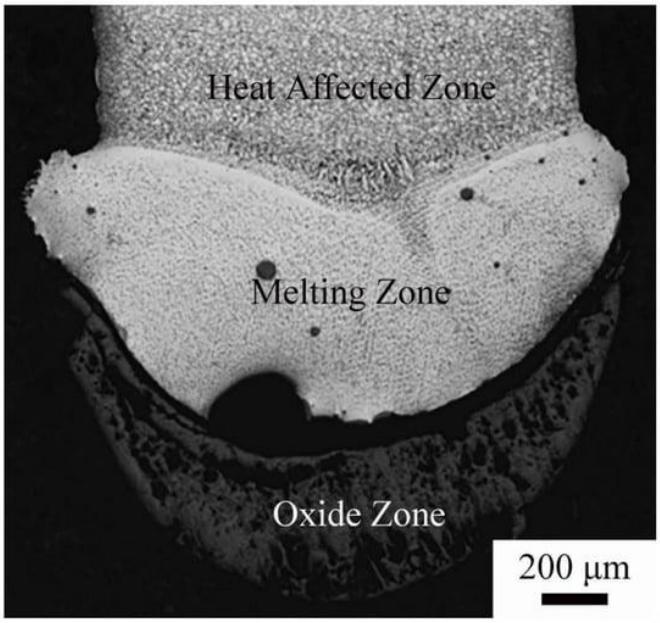

Fig. 2 – Micrograph displaying the different regions typically seen in the burn tip of a promoted combustion sample. Ref [3].

The Nickel-based Superalloy Inconel 718

Inconel 718 is a nickel-based precipitation-hardenable superalloy which has seen adoption for use in a wide variety of applications due to its high strength, corrosion resistance, and ability to resist creep in elevated temperatures [7]. Some applications that Inconel 718 has been selected for include liquid fueled rockets, cryogenic tanks, and several parts for use in turbine engines (both air and land based) in the form of casings, rings, or formed sheet metal. One strength of the alloy which has made it particularly desirable is the ease with which it can be fabricated into complex parts, as its resistance to post-weld cracking is considered superior to many other commonly used commercial alloys.

The chemical composition of Inconel 718 is shown in the table below. The primary constituents are nickel, chromium, and iron – though significant amounts of niobium and molybdenum are also present to enable precipitation hardening and improve weldability. Its microstructure is typically characterized by an austenitic matrix comprised of a solid saturated

solution of nickel and chromium. Precipitate phases γ' and γ" (coherent and semi coherent) can form, providing much of the improvement of mechanical strength after heat treatment. Less desirable structures (such as laves phases and δ phase) can also form and attempts are usually made to remove them via aging.

Table 1 – AMS Specification for chemical composition of Inconel 718. Ref [7].

Nickel (plus Cobalt)	50.00-55.00
Chromium	17.00-21.00
Iron	Balance*
Niobium (plus Tantalum)	4.75-5.50
Molybdenum	2.80-3.30
Titanium	0.65-1.15
Aluminum	0.20-0.80
Cobalt	1.00 max.
Carbon	0.08 max.
Manganese	0.35 max.
Silicon	0.35 max.
Phosphorus	0.015 max.
Sulfur	0.015 max.
Boron	0.006 max.
Copper	0.30 max.

Though exact parameters for heat treatments of Inconel 718 can vary based on desired application and service environment, there are usually three stages involved:

1. Homogenizing heat treatment: generally above 1000C for a short duration (1-3 hours) dependent on part thickness
2. Quench: rapid water cooling to room temperature
3. Aging: this is typically a two-step process to achieve significant formation of γ' and γ" precipitates while sacrificing minimal toughness
    a. First aging is between 720 – 760C for 8 hours
    b. Second aging is between 620 – 650C for 8 hours

Promoted Combustion of Selectively Laser Melted Inconel 718

In comparison to the standard microstructure of Inconel 718 (cast or wrought), additively manufactured material and particularly that which has been selectively laser melted tends to display a variety of differences because of the rapid solidification attributed to SLM [12]. Standard heat treatments have been found at times insufficient to dissolve the undesirable laves and micro-segregated phases which are necessary to release the most significant ageing constituents (namely niobium, titanium, and aluminum) into the matrix. This produces a microstructure which may have less than ideal constituents present during mechanical and oxygen compatibility testing. This is supported by the results found by D. Zhang et. Al [11], which showed that the high temperature gradient and relatively rapid solidification rate associated with SLM can limit the precipitation of strengthening phases (such as γ' and γ") and encourage the formation or retention of non-equilibrium phases which reduce mechanical strength.

Fig. 3 – Lowest burn pressure and highest no burn pressure associated with Inconel 718 per NASA testing at commercially pure oxygen content. Ref [6].

Material	Lowest Burn Pressure				Highest No-Burn Pressure				Rod Length (inches)
	MPa	psia	# of Tests	Burn Length (inches)	MPa	psia	# of Tests	Burn Length (inches)	
Inconel 718	2.8	400	13	0.2-1.4	2.1	300	20	0.2-0.6	12

The figure above displays the promoted combustion data which has so far been collected for traditionally manufactured (cast and wrought) Inconel 718. It shows that in an appx. 99% oxygen content atmosphere wrought Inconel 718 has a maximum no-burn pressure of about 300 psi and a minimum burn pressure of 400 psi. This has been supported by several tests (at least 13) at each condition.

Work which was done collaboratively between NASA White Sands Test Facility and Glenn Research Center appears to show that for selectively laser melted Inconel 718, niobium dendrites can appear in significant size and quantity within the transition zone between melt and heat affected zones in sample rods. This is shown below in fig. 4.

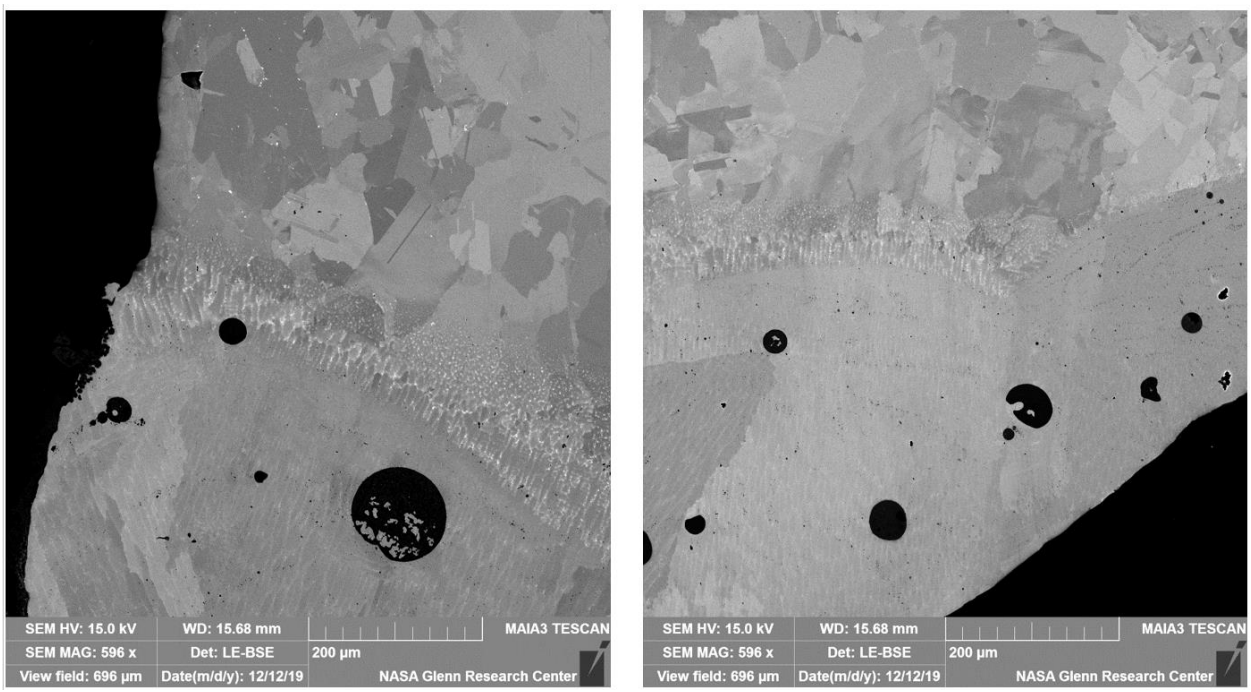

Fig. 4 – Micrographs of the burn interface observed in SLM Inconel 718 samples which had been hot-isostatic pressed + not wrapped + machined. Ref [16].

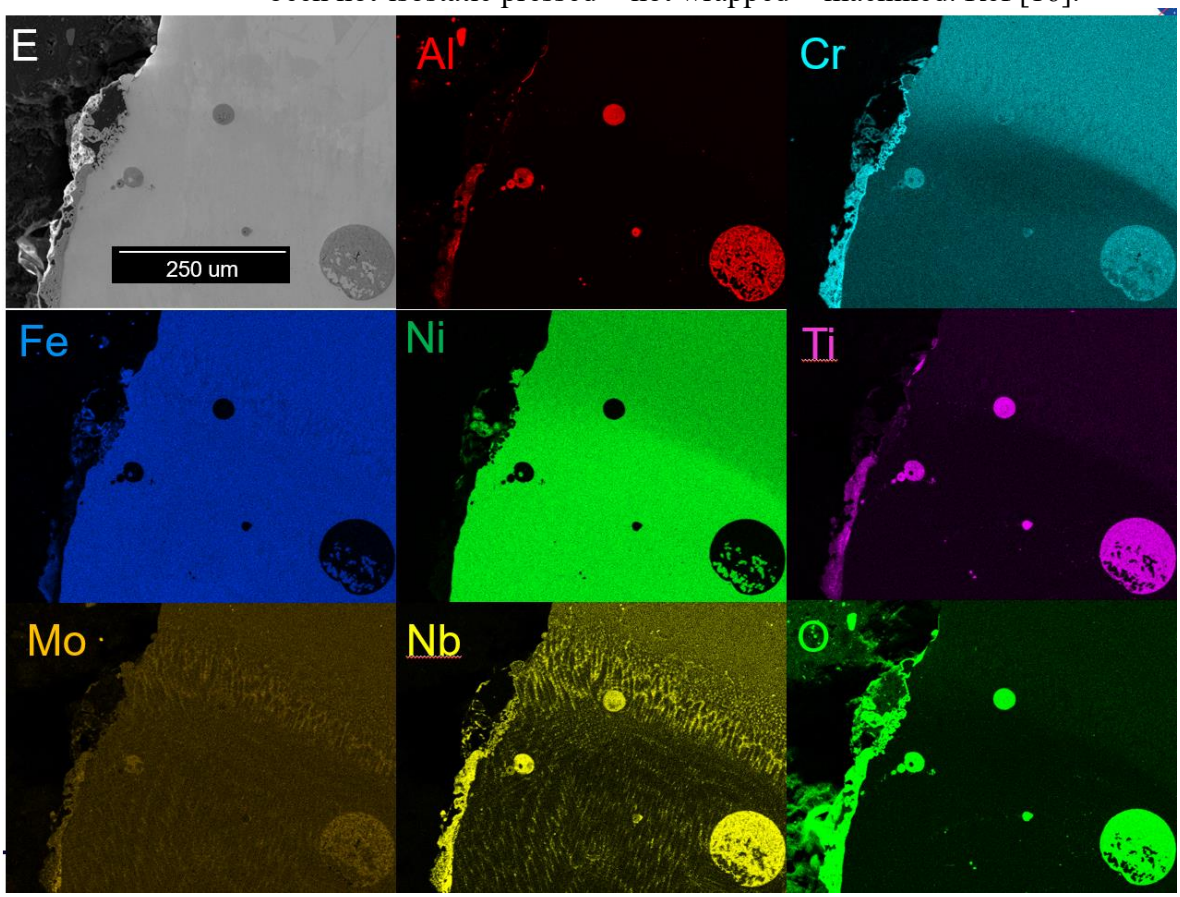

Fig. 5 – EDS Spectra generated from SLM HIP + not wrapped + machined samples which had been mounted and polished. Ref [16].

The micrographs above illustrate clearly a dendritic structure which appears to form in the transition region of these SLM Inconel 718 samples. Subsequent EDS mapping suggests that these structures are comprised of niobium, given their concentration and bright contrast overlap with the SEM images. Also notable are several elemental gradients which lead up to this burn interface – molybdenum and chromium appear to be more concentrated in the bulk (and conversely more depleted from the burn tip), while nickel seems to have a slightly higher concentration within the burn tip in comparison to the bulk material. This has led to strong speculation that the formation of niobium dendrites at the burn interface may play a significant role in how flammable Inconel 718 is, and as such the diffusion mechanism of niobium to this area (though not yet completely understood) is of great interest.

In addition, SLM samples which have been hot-isostatic pressed vs not seem to show a significant difference in microstructure even as combustion occurs [16]. This can be demonstrated clearly by electron-back scatter diffraction (EBSD) conducted on samples near their burn interface after testing [18]. Fig. 6 below shows how a sample which has only been subjected to post manufacturing heat treat shows recrystallization near the burn interface, whereas a sample which has an identical processing history (plus a hot-isostatic press) shows no comparable signatures of recrystallization in the same region.

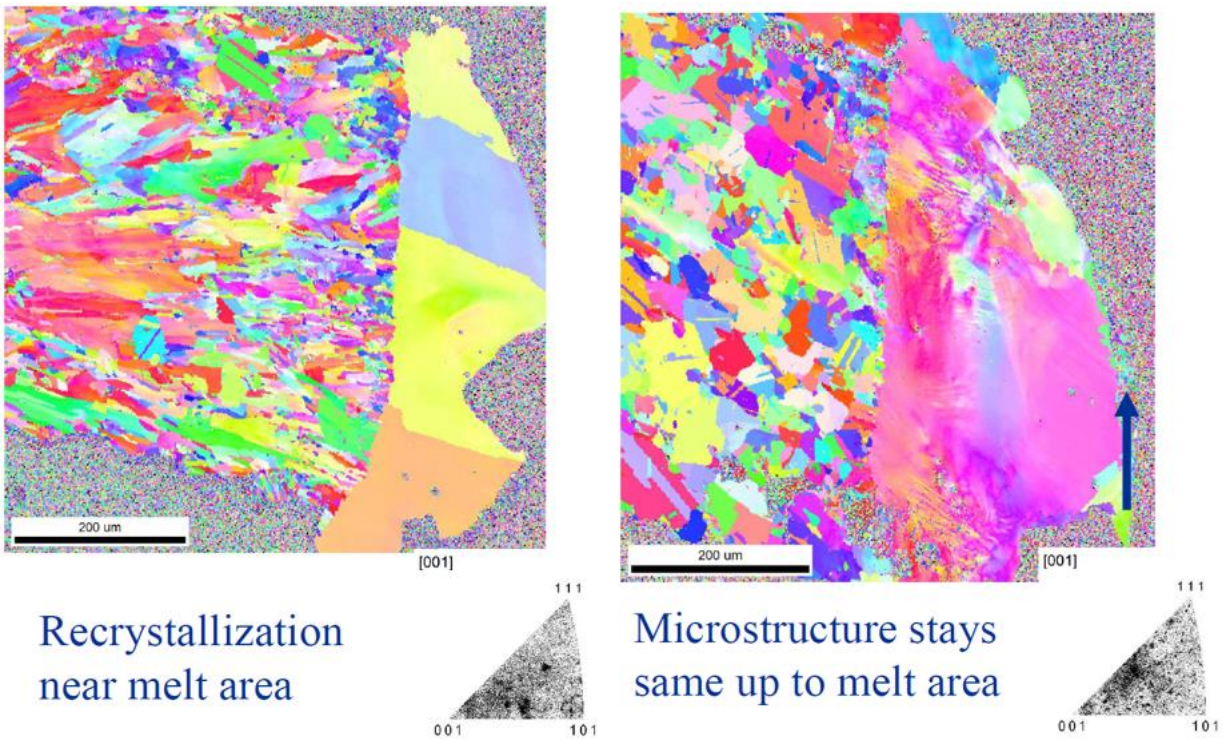

Fig. 6 – EBSD images showcasing how SLM non-hot isostatic pressed Inconel 718 behaves in comparison to the same material which has been hot isostatic pressed. Recrystallization is apparent local to the burn interface in the image to the left (non-HIP), while the image to the right (HIP) shows little to no recrystallization. Ref [18].

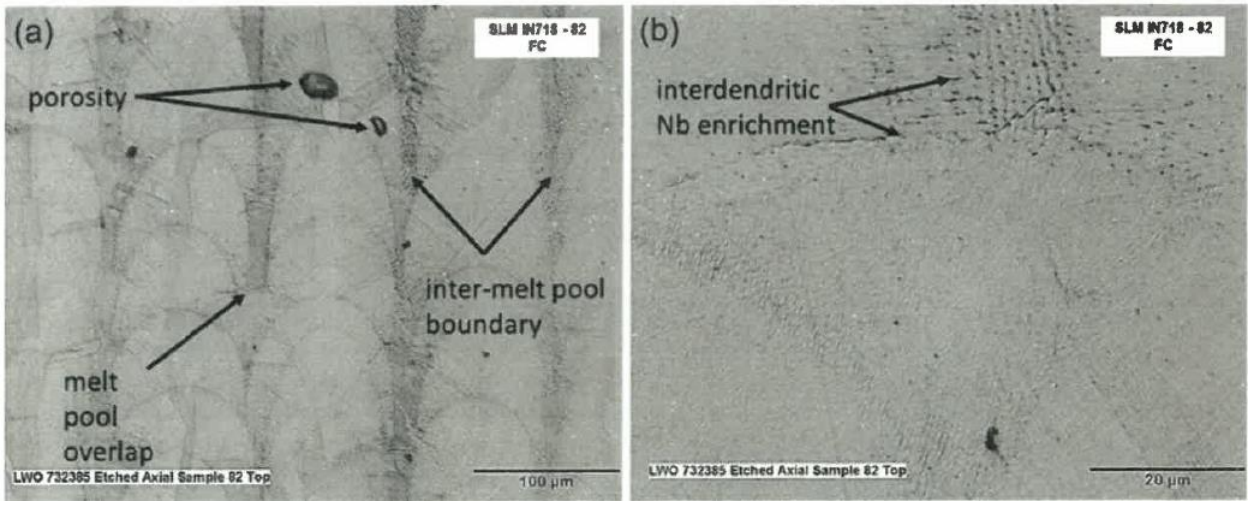

Fig. 7 – As printed and promoted combustion tested SLM Inconel 718 showing inter-melt pool boundaries which contain niobium enrichment Ref [17].

The micrographs shown above display how samples which have been combustion tested while in the as-printed condition can retain a columnar dendritic grain structure as a result of the rastering pattern used during the printing process [17]. The darker regions appear to suggest a lack

of vector scan overlap, and upon further magnification display microsegregation of niobium to the dendrite boundaries. Transmission electron microscopy (TEM) will be required to confirm the morphology and composition of these structures to differentiate between MC carbides, δ-phase, or γ" precipitates.

One of the recent pre-eminent authorities on the promoted combustion behavior of Inconel 718 (additive or wrought) is Jonathan Tylka, who has conducted work over the last several years to identify what variables may potentially be driving the flammability responses of additively manufactured Inconel 718. A fairly robust examination of the factors which may have significance in this performance was presented in 2019 as a joint experiment between NASA's White Sands Test Facility, Marshall Spaceflight Center, Glenn Research Center, and the NASA Engineering and Safety Center [18]. Three main takeaways from this work were:

A. When wrapped during HIP, machining did not seem to influence burn lengths for the samples significantly. When not wrapped during HIP however, machined samples appeared less flammable and non-machined samples seemed more flammable.
B. For a set of samples which were all HIP + wrapped + heat treated but not machined, three variables were found statistically to drive approximately 80% of the flammability response observed (titanium nitride volume fraction, carbon percentage, and molybdenum percentage).
C. The dendritic niobium features that could be seen in some sample burn interfaces appeared to coincide with carbon content, leading to a hypothesis that perhaps the structures were residual NbC carbides which were able to remain bonded together in the region.

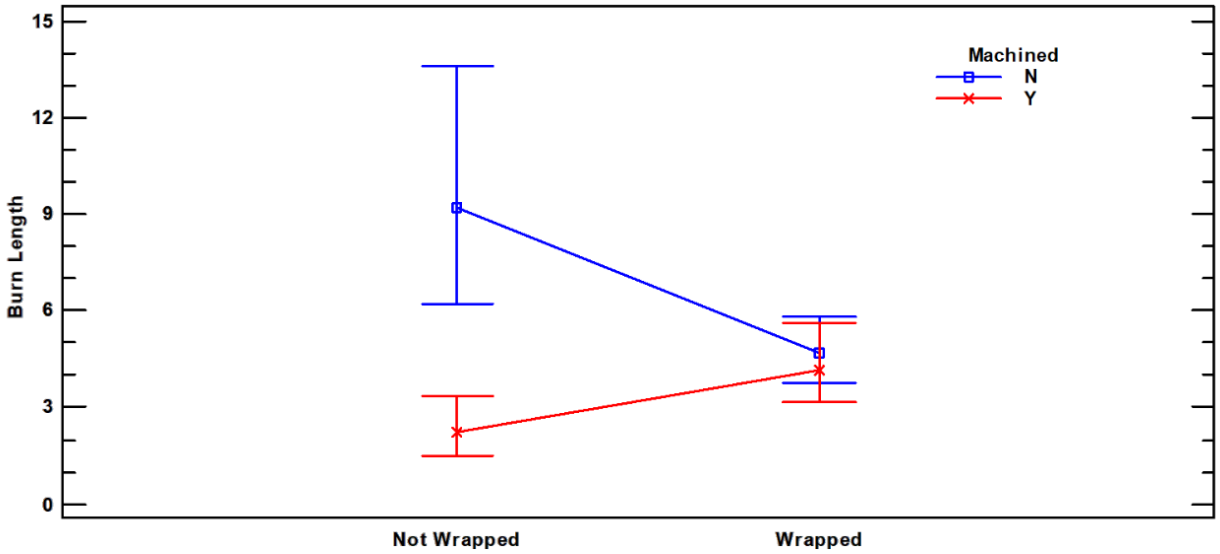

Fig. 8 – Graph of Wrapped vs Not Wrapped Sample Burn Lengths, with Discrete Representations of Samples being Machined or Not-Machined within those subsets. Ref [18].

As mentioned above, analysis done by Tylka appears to show that for samples which received wrapping during HIP burn length is fairly comparable between those which were machined and not-machined. However, for the samples which did not receive wrapping during HIP, machined samples seem to display lower flammability than those that were not-machined.

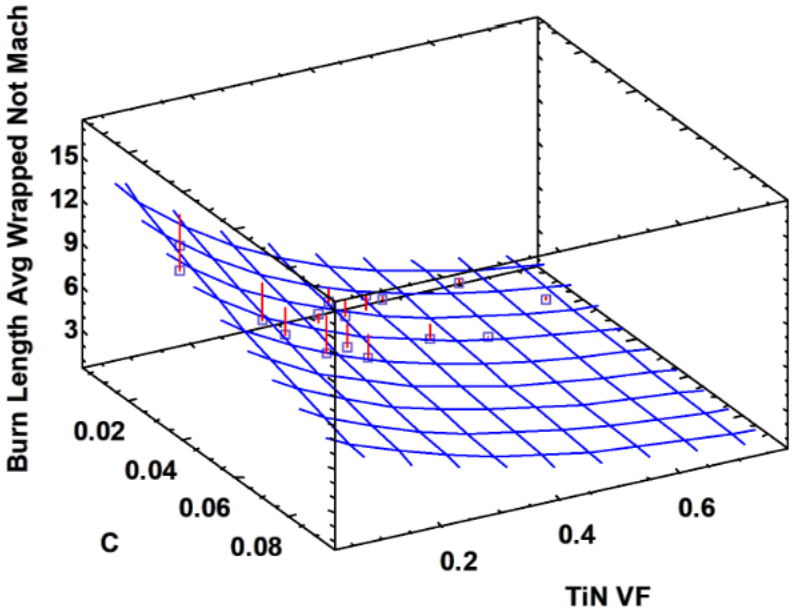

Fig. 9 – Model Displaying Burn Length as a function of both TiN Volume Fraction and Carbon Content. Ref [18]

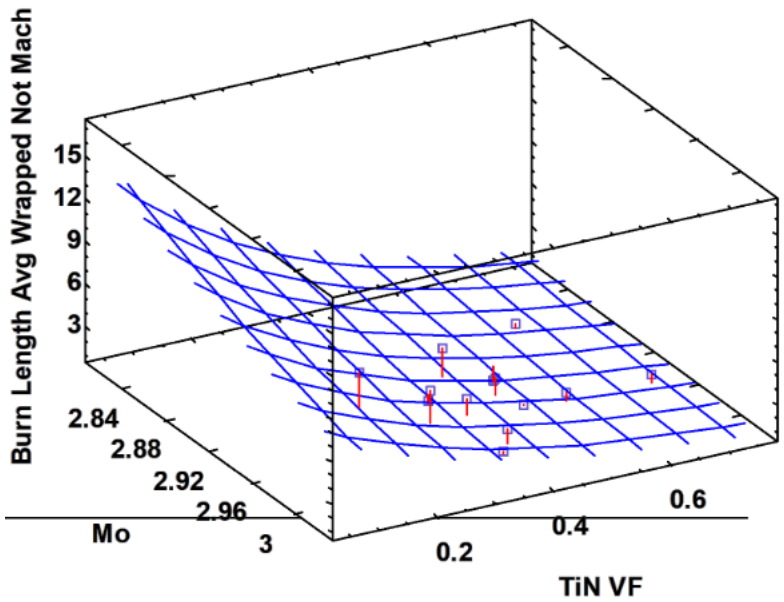

Fig. 10 – Model Displaying Burn Length as a function of both TiN Volume Fraction and Molybdenum Content. Ref [18].

The models shown in the above two figures show that within this study conducted by Tylka, samples which were wrapped during HIP but not machined show a strong flammability response to volume fraction of titanium nitrides as well as carbon and molybdenum content. As molybdenum and carbon content increase flammability appears to decrease, leading to a hypothesis that carbide formation (with either niobium or molybdenum) may be decreasing the free availability of such flammable constituents and thus lowering propensity to burn. With regards to titanium nitrides, as their volume fraction increases it would seem that flammability decreases – once more lending to the thought that perhaps formation of such structures may inhibit the amount or mobility of flammable constituents.

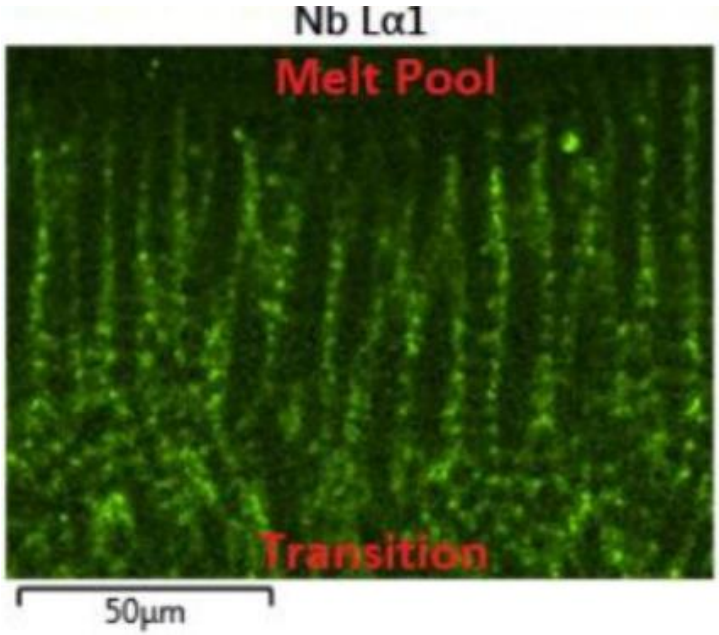

Fig. 11 – Niobium Dendrites in a Sample Burn Interface. Ref [18].

Due to observed overlap of niobium dendritic structures with carbon within some samples burn interfaces, it was also discussed within this work that they may be the result of NbC carbides which were able to maintain integrity through the burn interface and then degrade once in the liquid melt pool.

Though this dissertation may be unable to fully support or deny these observations (due to sample size restrictions or limitations on quantitative chemical analysis methods), it will be a goal of the author to address them within the conclusions of the document.

Chapter 3: Previous Testing

Previous Testing Procedure

A primary rationale for the testing which became the basis of this dissertation was a 2019 senior capstone research project that the author contributed towards as part of a team of undergraduates. The sections below will outline what samples were received for this previous experiment, as well as details for the executed test plan and the individual instruments/methods used for characterizing the materials.

Sample Descriptions

15 sample rods of additively manufactured Inconel 718 were supplied by NASA White Sands Test Facility, of which 14 had been subjected to NASA-STD-6001B Test 17/ASTM G124 promoted combustion testing (1 of the samples was an exemplar which had not been combusted). Table 2 (below) outlines the samples received, their identifiers, their processing history, and burn lengths. Note that sample S18 has a listed burn length of zero, this being due to it being the sample which was not combusted.

Table 2 – Outline of Previous Testing Sample Manufacturing, Post-Processing, and Burn Lengths.

		Post-Processing History				
Sample ID	Manufactured Form	HIP	Wrapped	Heat Treated	Machined	Burn Length (cm)
85	SLM	Y	Y	Y	N	6.6
S18	SLM	Y	N	Y	N	0
S12	SLM	Y	N	Y	N	2.6
W11	Wrought	N	N	Y	N	6.7
G2-52	SLM	Y	N	Y	N	8.6
G2-94	SLM	Y	N	Y	Y	1.3
G2-78	SLM	Y	Y	Y	N	5.7
G2-80	SLM	Y	Y	Y	Y	3.6
WH-2	Wrought	N	N	Y	N	7.2
WH-12	Wrought	Y	N	Y	N	7
WH-6	Wrought	Y	Y	Y	N	8.8
B1-55	SLM	Y	Y	Y	N	5.3
C1-107	SLM	Y	Y	Y	N	3.6
G3-95	SLM	Y	Y	Y	N	5.9
H1-53	SLM	Y	Y	Y	N	5.4

They were photographed and dimensions were verified, and a test plan was devised which would allow for several forms of characterization to identify what if any observable deviations existed between the rods. The test plan consisted of five analysis techniques, listed below:

1. X-Ray Fluorescence (XRF)
2. Scanning Electron Microscopy (SEM)
3. X-Ray Diffraction (XRD)
4. Metallography and Optical Microscopy
5. Microhardness Testing

X-Ray Fluorescence

Conducted with the use of an Olympus DELTA handheld XRF gun, to verify basic chemical composition data for the test rods. A section length of each rod was selected which

existed some distance away from the burn tip (so to be as representative as possible of the pre-test composition) and was lightly ground with metallographic polishing paper (400 grit) to remove surface contaminants, dirt, and residual oxides. Three readings were then made of the area and the aggregate was documented as the chemistry of that test rod. The values were all then tabulated and compared against the established chemical composition for Inconel 718 to identify any significant variances or deviations from the specification.

Scanning Electron Microscopy/Energy Dispersive Spectroscopy

All SEM analysis was completed with the use of a Hitachi SU-3500 variable pressure microscope. Test rods were analyzed non-destructively to identify surface features and morphology of the burn tips. Energy dispersive spectroscopy (EDS) was also conducted on select areas to verify chemical composition found with XRF, as well as to analyze any easily distinguishable surface features. A particular emphasis was placed on evaluating levels of porosity and particulate-sintering in the AM test materials.

X-Ray Diffraction

A Bruker D8 Discover was used to conduct x-ray diffraction on the test samples. All test samples were sectioned and mounted within metallographic epoxy resin mounts, and the scans were run within the heat affected region to identify which phases were present. For all data included within this work, the scan time was 25 minutes per sample.

Metallography and Optical Microscopy

All the sample rods were sectioned using an abrasive cut off wheel and water-based lubricant, generating inch long sections which were measured from the burn tip towards the bulk. This length was chosen to fit within the constraints of the available mounting molds and is believed to have been able to contain the regions of greatest importance (burn tip, heat affected zone, and

beginning of bulk). An additional inch was sectioned past this length, for a total of 2 inches rod sectioned, to provide an additional daughter sample of bulk material to polish and analyze. It should be noted that for two of the test rods (G252 and WH6), their short length only provided for one sample to be mounted and so only contain a parent rod with no daughter rod.

Sectioned samples were then mounted using Koldmount fast-curing epoxy resin. This mixture was chosen as it does not require heat to cure, minimizing any ability to alter the microstructure of the heat affected and recrystallized zones of the rods. Each metallographic mount contained two sections of the sample rod – the first which contained the burn tip (denoted as the "parent") and the second which contained additional bulk material for comparison (denoted as the "daughter").

Each sample was then polished with metallographic silicon-carbide grit papers in the order of 240, 400, 600, and 800 grit. This was followed by a fine polish with felt pads and a 1-micron alumina suspension as the abrasive. Early on, an issue arose in that streaks were present in most samples after the 600-grit polishing step. The morphology and orientation of the marks resembled "comet tails", which are indicative of particle fall-out which can occur when preparing selectively laser melted samples. To negate this, an additional step of ultrasonically cleaning the samples for 2 minutes in isopropyl alcohol between polishing stages was introduced and significantly reduced the occurrence of the markings. Finished samples were then etched for 12-15 seconds with Kalling's Reagent No 2 (100 mL ethanol + 100mL hydrochloric acid + 5 grams cupric chloride), and lastly rinsed with deionized water and dried within a fume hood.

Optical microscopy was then conducted on all samples with the use of a Zeiss Observer D.1m inverted light microscope. Images were taken of the samples from 6 distinct regions: 1.) Burn Tip (*BT – taken from the burned tip of the parent sample*), 2.) Parent Bulk (PB – *taken from the midsection of the parent sample which was non heat affected*), 3.) Parent End (*PE – taken from the end opposite the burn tip of the parent sample*), 4.) Daughter End 1 (*DE1 – taken from the end of the daughter sample which is the mated surface to the non-burned end of the parent sample*), 5.) Daughter Bulk (*DB – taken from the midsection of the daughter sample*), and 6.) Daughter End

2 (*DE2 – taken from the end of the daughter sample opposite DE1*). An image representing these regions graphically is shown below (Fig. 12):

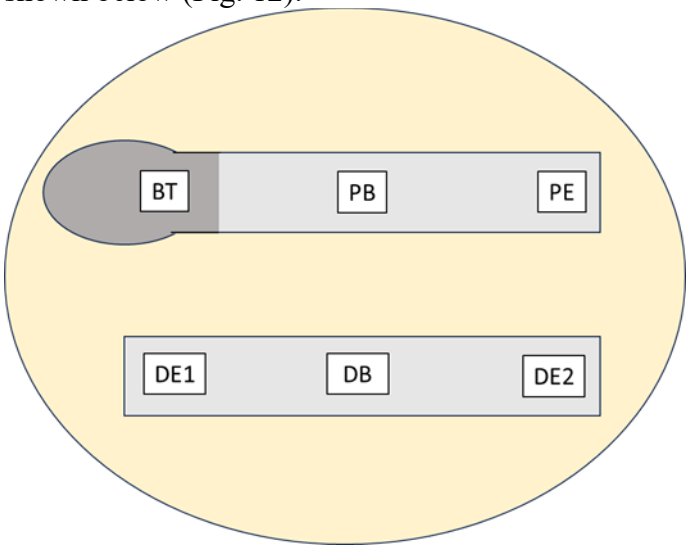

Fig. 12 – Graphical Representation of the Parent and Daughter Samples of Each Rod within the mount

Microhardness

All microhardness testing was completed with the use of a Duramin A300 tester. The methodology developed to analyze the rods placed a particular emphasis on the parent sample, as those hardness values would likely be the most significant since they measured what hardness gradient may exist as one travels from the burn tip though the heat affected and recrystallized regions to the bulk. The daughter rods were also tested across their length to provide a good aggregate of bulk microhardness, giving a solid basis of comparison to the values found closer to the burn tip. In total, seven hardness readings were taken from each parent rod, and three were taken from each daughter rod. As mentioned previously, two samples (G252 and WH6) only yielded parent rods and so only had the first seven readings included in this data.

The initial five tests were run just outside of the burned region, where the transition to bulk started to occur. These are denoted as the "OTZ – Outside Transition Zone" readings and were taken approximately 1 mm apart from each other in a straight line running axially along the center of the polished rod. The next reading was taken in bulk of the parent rod (noted as "PB – Parent

Bulk") and was followed by a reading done at the very end of the parent rod opposite the burn tip (noted as "PE – Parent End"). For the samples which yielded daughter rods, three additional readings were taken at both ends of the rod and the center midpoint. The edge which mated to the parent rod was "DE1 – Daughter Edge 1", the opposite end was "DE2 – Daughter Edge 2", and the final reading in the midpoint was "DB – Daughter Bulk". A graphical representation of the areas tested is shown below in Fig. 13:

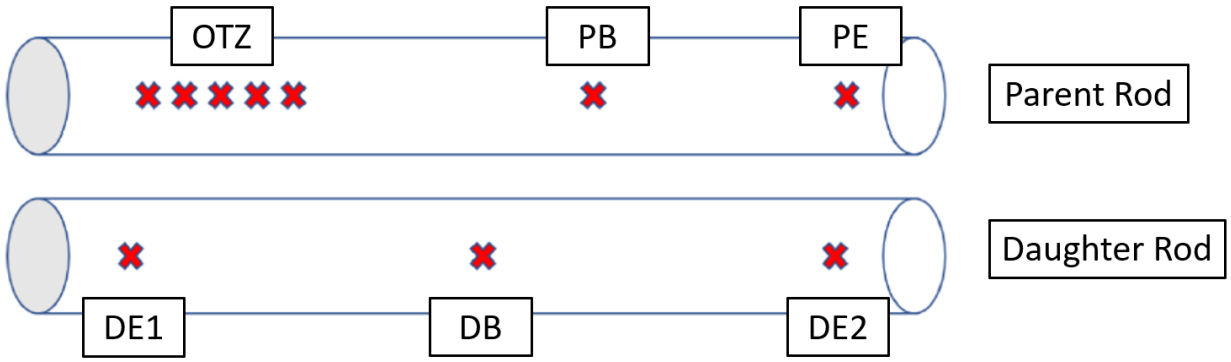

Fig. 13 – Graphical representation of the microhardness testing locations across the parent and daughter rods

Previous Testing Results

The subsections below will describe the results yielded from this initial round of testing and analysis and will be followed by a Key Takeaways section which provides the rationale for the testing which became the basis of this dissertation.

X-Ray Fluorescence

Table 3 below displays the aggregated XRF data which was collected for all sample rods. Though each rod was successfully identified as Inconel 718, significant variances existed for individual element compositions between samples and in some cases were out of the established specifications for the alloy. Most notable was the observation of large amounts of aluminum in several of the samples (C1-107, G2-52, S18, and sample 85). The specification for aluminum

content in Inconel 718 maxes out at 0.8%, yet every rod registered a number above that and in the case of the aforementioned samples the values were as high as 13.21%.

There are a few ideas for how these values could be so high, but it is postulated that the instrument itself likely needed calibration and could have been inflated due to the background during the scans (an aluminum table). Though efforts were made to ensure that the sample material was in as complete coverage as possible of the gun window, signal noise from the background is the most likely explanation. One other interesting observation is that three out of the four samples with very high aluminum content also registered detectable amounts of manganese, whose content was observed as zero in the other rods. Cobalt was only detectable in two of the rods (WH-12 and WH-2), both of which were wrought.

With regards to major alloying constituents, chromium and iron were within specification and were also fairly consistent across the samples. Nickel content however was less predictable, and generally speaking was on the lower end of the established range for the alloy. The specification calls for 50-55% nickel in Inconel 718, but for 11 out of 15 rods the observed content was below 50 (with a minimum value seen of 42.82%). There is some explanation for the rods with very low nickel content, as they were the same rods previously mentioned that had very high aluminum content (artificially reducing the true nickel content as the software for the XRF gun will always sum up the detected elements to 100%).

Overall, the XRF data generated is to be treated as a qualitative estimation to track trends of certain elemental constituents in the sample rods. Due to the significant amount of error included in the calibration of the instrument, the data cannot be considered a quantitative representation of the true chemical composition of the rods.

Table 3 – Table displaying the XRF results for each sample rod

Elements	G3 - 95	H1 - 53	C1 - 107	WH - 12	WH - 6	B1 - 55	W11	G2 - 52
Ni	48.37 +/- 0.21	47.39 +/- 0.20	44.97 +/- 0.20	49.42 +/- 0.20	47.82 +/- 0.21	47.64 +/- 0.19	50.44 +/- 0.20	43.61 +/- 0.20
Cr	18.69 +/- 0.17	17.38 +/- 0.16	16.81 +/- 0.16	18.35 +/- 0.16	18.14 +/- 0.17	18.45 +/- 0.16	18.18 +/- 0.16	17.76 +/- 0.16
Fe	17.66 +/- 0.16	19.52 +/- 0.15	16.90 +/- 0.14	17.10 +/- 0.14	16.80 +/- 0.15	18.42 +/- 0.15	17.17 +/- 0.14	16.42 +/- 0.14
Nb	4.64 +/- 0.04	4.46 +/- 0.04	4.31 +/- 0.03	4.67 +/- 0.04	4.49 +/- 0.04	4.66 +/- 0.04	4.60 +/- 0.04	4.32 +/- 0.03
Al	3.85 +/- 0.15	5.52 +/- 0.15	10.12 +/- 0.18	4.10 +/- 0.14	5.29 +/- 0.17	4.62 +/- 0.14	3.78 +/- 0.14	10.29 +/- 0.18
Mo	2.75 +/- 0.03	2.70 +/- 0.03	2.49 +/- 0.02	2.79 +/- 0.03	2.62 +/- 0.03	2.80 +/- 0.03	2.76 +/- 0.03	2.57 +/- 0.02
Ti	1.81 +/- 0.10	1.18 +/- 0.08	2.22 +/- 0.10	1.56 +/- 0.09	2.45 +/- 0.12	2.10 +/- 0.10	1.08 +/- 0.08	3.80 +/- 0.13
S	1.79 +/- 0.04	1.14 +/- 0.03	1.59 +/- 0.03	1.19 +/- 0.03	1.82 +/- 0.04	0.95 +/- 0.03	1.48 +/- 0.04	0.79 +/- 0.03
Si	0.46 +/- 0.03	0.72 +/- 0.03	0.34 +/- 0.03	0.51 +/- 0.03	0.56 +/- 0.04	0.36 +/- 0.03	0.50 +/- 0.03	0.44 +/- 0.03
Mn	0	0	0.24 +/- 0.06	0	0	0	0	0
Co	0	0	0	0.31 +/- 0.06	0	0	0	0
Total	100	100	100	100	100	100	100	100

Elements	S18	S12	G2 - 78	WH - 2	G2 - 80	85	G2 - 94	Specifications
Ni	43.57 +/- 0.22	47.19 +/- 0.21	48.38 +/- 0.19	50.52 +/- 0.19	51.76 +/- 0.19	42.82 +/- 0.20	51.98 +/- 0.19	50.00- 55.00
Cr	17.63 +/- 0.18	18.34 +/- 0.17	18.78 +/- 0.16	18.53 +/- 0.16	19.14 +/- 0.16	16.98 +/- 0.16	19.06 +/- 0.16	17.00- 21.00
Fe	17.14 +/- 0.16	17.69 +/-0.16	17.78 +/- 0.15	17.29 +/- 0.14	18.19 +/- 0.15	16.50 +/- 0.14	18.16 +/- 0.15	Balance*
Nb	4.05 +/- 0.04	4.42 +/- 0.04	4.68 +/- 0.04	4.68 +/- 0.04	5.09 +/- 0.04	4.00 +/- 0.03	5.02 +/- 0.04	4.75- 5.50
Al	9.04 +/- 0.20	6.97 +/- 0.18	4.29 +/- 0.14	2.90 +/- 0.13	ND	13.21 +/- 0.20	ND	0.20- 0.80
Mo	2.45 +/- 0.03	2.66 +/- 0.03	2.78 +/- 0.03	2.78 +/- 0.03	3.14 +/- 0.03	1.56 +/- 0.09	3.08 +/- 0.03	2.80- 3.30
Ti	3.79 +/- 0.14	1.29 +/- 0.09	1.76 +/- 0.09	1.12 +/- 0.08	1.23 +/- 0.08	2.34 +/- 0.11	1.16 +/- 0.08	0.65- 1.15
S	1.35 +/- 0.04	0.97 +/- 0.04	1.16 +/- 0.03	0	1.03 +/- 0.03	1.04 +/- 0.03	1.19 +/- 0.03	0.015 max
Si	0.78 +/- 0.04	0.46 +/- 0.03	0.40 +/- 0.03	0.58 +/- 0.03	0.41 +/- 0.03	0.58 +/- 0.03	0.35 +/- 0.03	0.35 max
Mn	0.21 +/- 0.07	0	0	0	0	0.17 +/- 0.06	0	0.35 max
Co	0	0	0	0.42 +/- 0.06	0	0	0	1.00 max
Total	100	100	100	100	100	100	100	100

Scanning Electron Microscopy/Energy Dispersive Spectroscopy

As mentioned previously, scanning electron microscopy was done during the stages of non-destructive testing – before samples had been sectioned, mounted, and polished. Thus, the imaging that was conducted was done exclusively on the outer surface of the rods and primarily with the focus of identifying unique features, the level of porosity present, and how well sintered the surface particulate was with relation to wrapping, hot isostatic-pressing (HIP), and machining as post processing techniques. Below, several surface characterizations will be shown of various configurations of manufacturing and processing. It should be noted that one variable not listed or considered is heat treating, as it was a constant applied to all samples analyzed.

Six samples will be presented here, with four of them being from the "G2" material group (G2-52, G2-78, G2-80, and G2-94). These samples were isolated specifically as they demonstrated

the full range of post-processing combinations possible for SLM rods in this study. Additionally, sample 85 was included as it showcased significant EDS data and sample WH-2 was included to provide a representative wrought surface finish to compare with the SLM samples.

Sample G2-80: SLM HIP + Wrapped + Machined

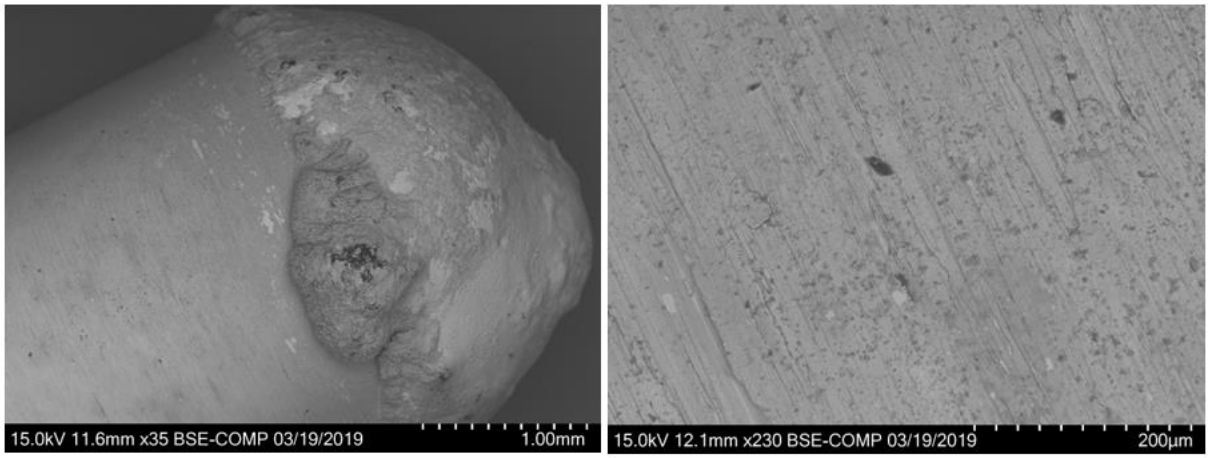

Fig. 14: (Left) Burn tip 35x, (Right) Bulk surface 230x of Sample G2-80

Sample G280 is representative of SLM test material which had been hot isostatic pressed with wrapping, and also received post-machining. The burn tip shows a characteristic oxidized area and signature cloudy transition region. Slight elemental contrast can be seen within the tip due to the back-scattered electron mode selected for imaging. When looking at the bulk surface, strong directionality can be seen in the form of machining marks in a circumferential orientation about the rod.

Sample 85: SLM HIP + Wrapped + Not Machined

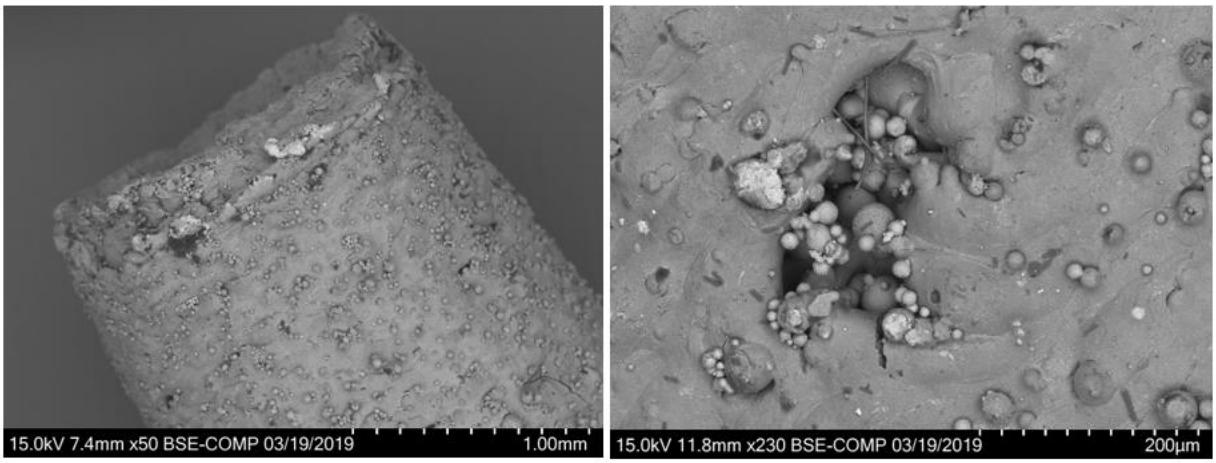

Fig. 15: (Left) Burn tip 50x, (Right) Bulk Surface 230x of Sample 85

Sample 85 is representative of SLM test material which had been hot isostatic pressed with wrapping but did not receive machining. The "oxide ball" typically seen on the end of sample burn tips has fallen off (this is not incredibly uncommon, as the oxidized area is generally very brittle), so the end of the rod is essentially showing the transition to bulk region. Noticeable in the bulk of the sample is a high level of un-sintered particulate across the surface (which was seen across the entire length of the rod).

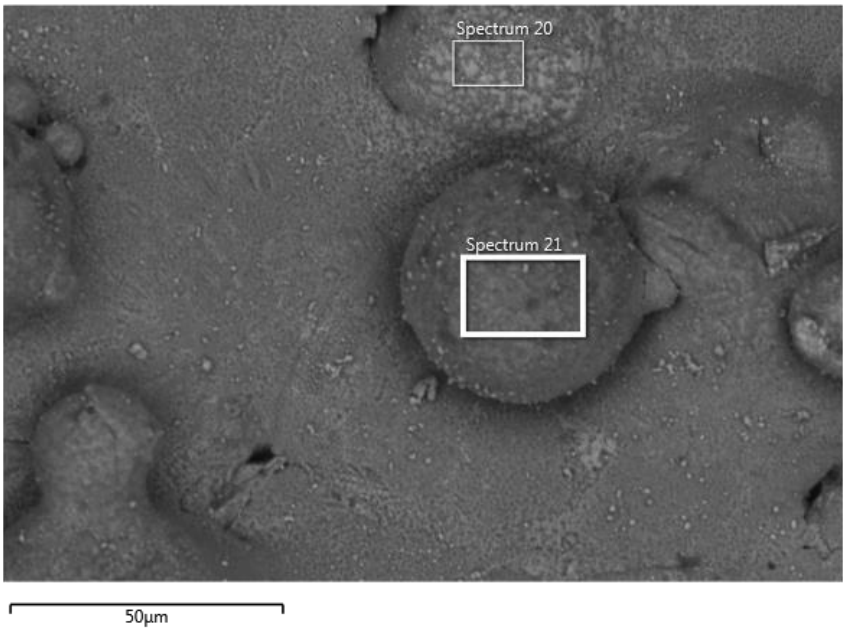

Fig. 16 – Micrograph of Sample 85 displaying two un-sintered particles on the rod surface which were analyzed with Energy Dispersive Spectroscopy (EDS)

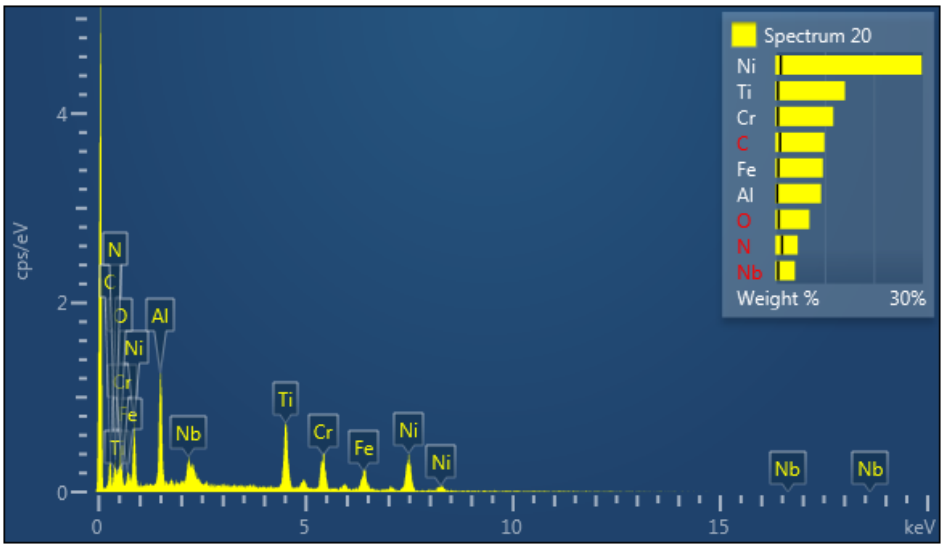

Fig. 17 – EDS Spectra generated from lighter contrast surface particulate from Sample 85

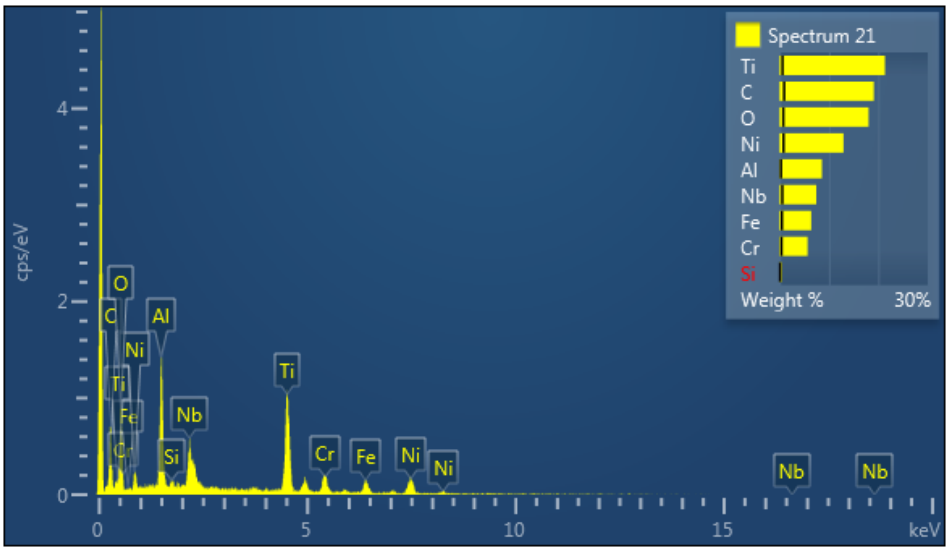

Fig. 18 – EDS Spectra generated from darker contrast surface particulate from Sample 85

The above images display a micrograph of two surface particles (one lighter, one darker) as well as energy dispersive spectroscopy (EDS) spectra's which were generated from them to show differences in chemistry. What can be seen is that the lighter particles appear to have higher concentrations of nickel and chromium, while the darker have more titanium, carbon, and oxygen. This is representative of several different particles which were analyzed across the sample. Interestingly, aluminum content was again higher than expected in these regions.

Sample G2-94: SLM HIP + Not Wrapped + Machined

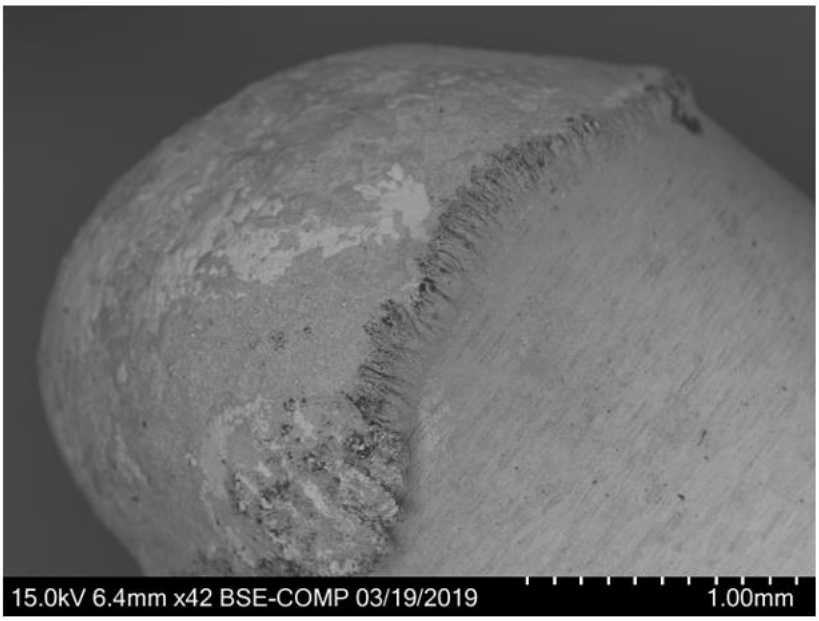

Fig. 19 – Burn Tip 42x of Sample G2-94

Sample G2-94 is representative of SLM test material which was hot-isostatic pressed without wrapping and then subsequently machined. Similar to other samples, the oxidized region can be observed and displays elemental contrast along its' surface. The cloudy transition zone structure is also present, and the residual circumferential markings from the machining process can also be seen.

Sample G2-52: SLM HIP + Not Wrapped + Not Machined

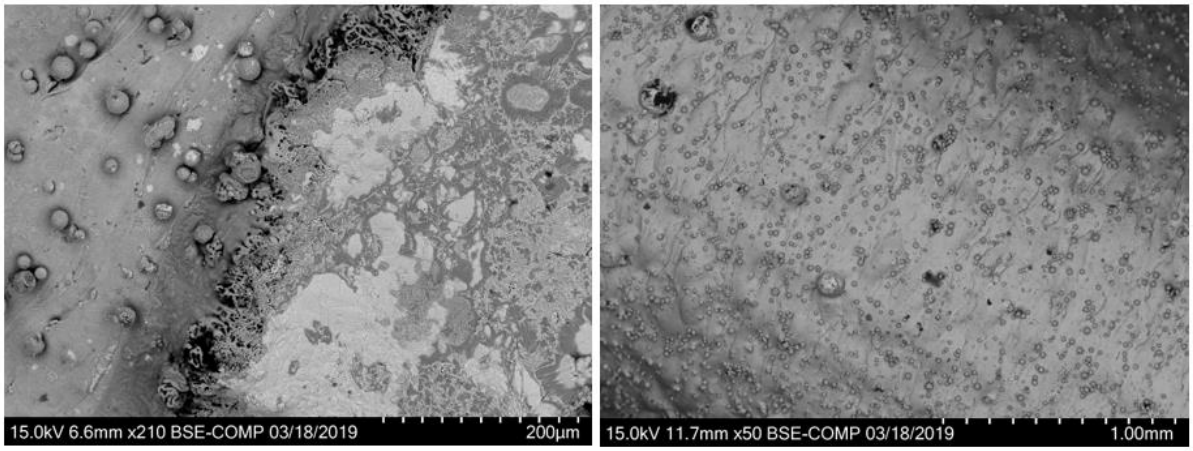

Fig. 20 – (Left) Burn Tip transition to bulk 210x, (Right) Bulk Surface 50x of Sample G2-52

Sample G2-52 is representative of SLM test material which was hot-isostatic pressed without wrapping or post-machining. The left image above demonstrates the morphology of the transition from burn tip to bulk material on the sample. The topography and elemental contrast are indicative of the complexity of the molten mixture at extinguishment during testing. The image to the right above shows representative bulk surface material of the sample. As expected, the lack of machining has left significant un-sintered particulate across the rod – however one notable observation is that there appear to be two categories of particle, one which is relatively small and one which sees some particles as large as 100 microns in diameter.

Fig. 21 – Micrograph of Sample G2-52 showing two un-sintered particles which were analyzed with EDS

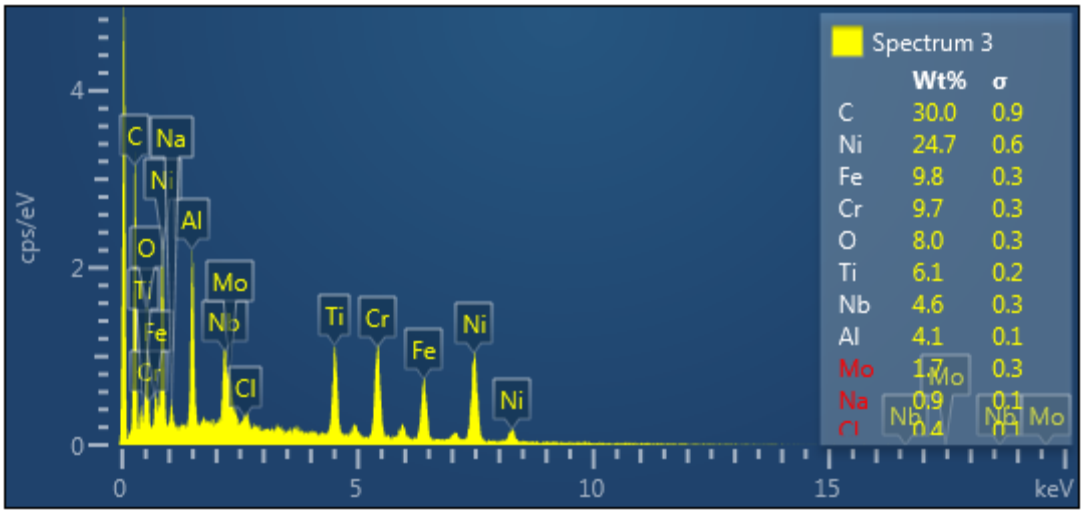

Fig. 22 – EDS Spectra generated from the larger un-sintered particle on Sample G2-52

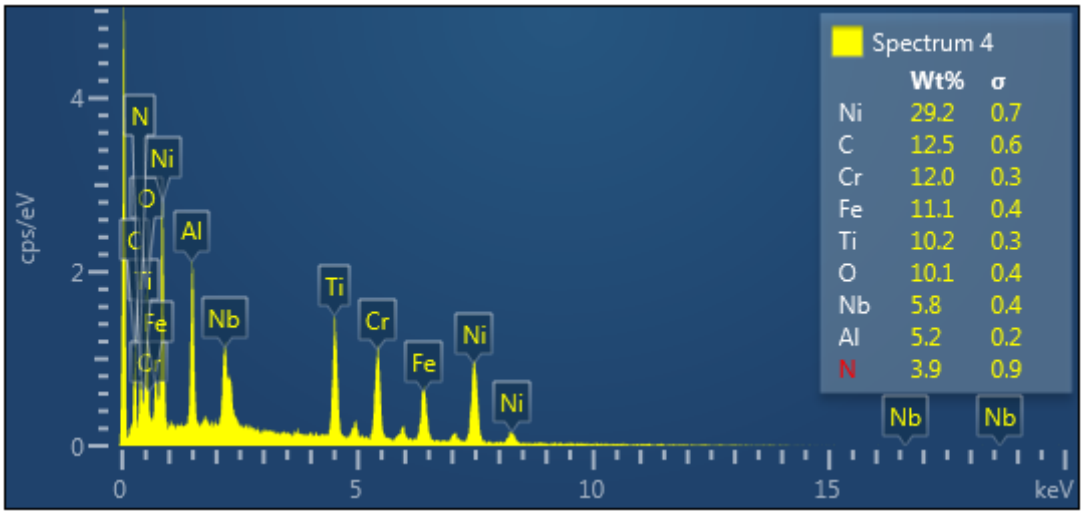

Fig. 23 – EDS Spectra generated from the smaller un-sintered particle on Sample G2-52

The above images show a surface region of sample G2-52 which was imaged and scanned with EDS to demonstrate what chemical differences may exist between the two sizes of particle which remained un-sintered on the surface. The spectra seem to show that the larger particles have higher concentrations of carbon – which is not surprising given that the black coloration on the particles surface is typical of carbon seen in other samples as well as the SEM stage itself. The smaller particles show less carbon and more of the major alloying constituents like nickel, chromium, and iron. It can't be stated with certainty whether the particles truly have different

chemistries or if the larger profile of the larger particles just made it easier for carbon deposition and isn't a result of testing or manufacturing.

Sample G2-78: SLM HIP + Wrapped + Not Machined

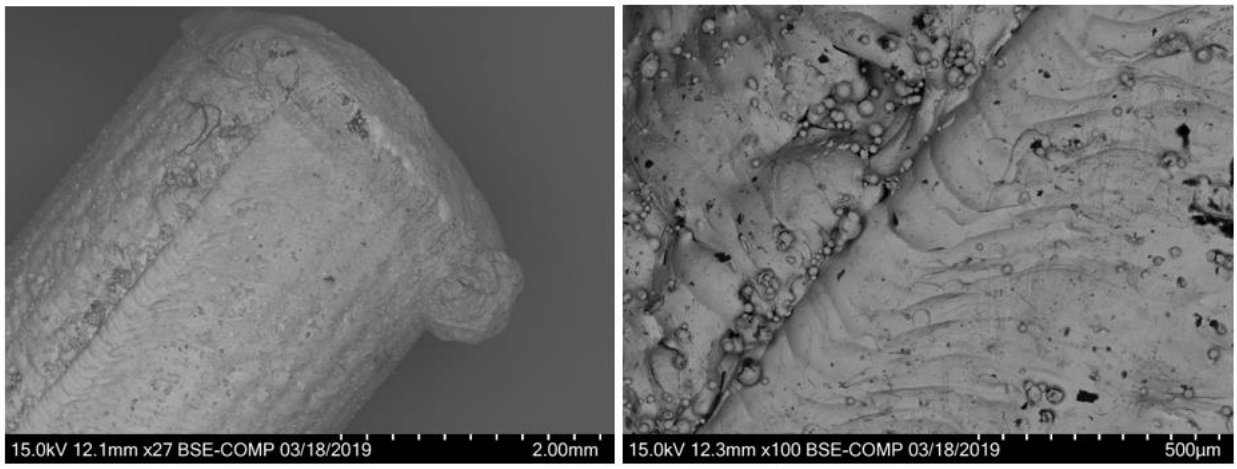

Fig. 24 – (Left) Burn Tip 27x, (Right) Bulk Surface 100x of Sample G2-78

Sample G2-78 is representative of SLM test material which was hot-isostatic pressed with a wrapping and received no post-machining. The burn tip is stout and shorter than other samples, indicating that oxidized material may have broken or fallen off the rod at some point. Un-sintered particles can again be seen across the surface of the sample, but most noticeable with this rod is how prevalent the melt raster line is from the manufacturing process. The build direction is easily discernible and was more obvious than what was seen in other samples.

Sample WH-2: Wrought + Not HIP + Not Wrapped + Not Machined

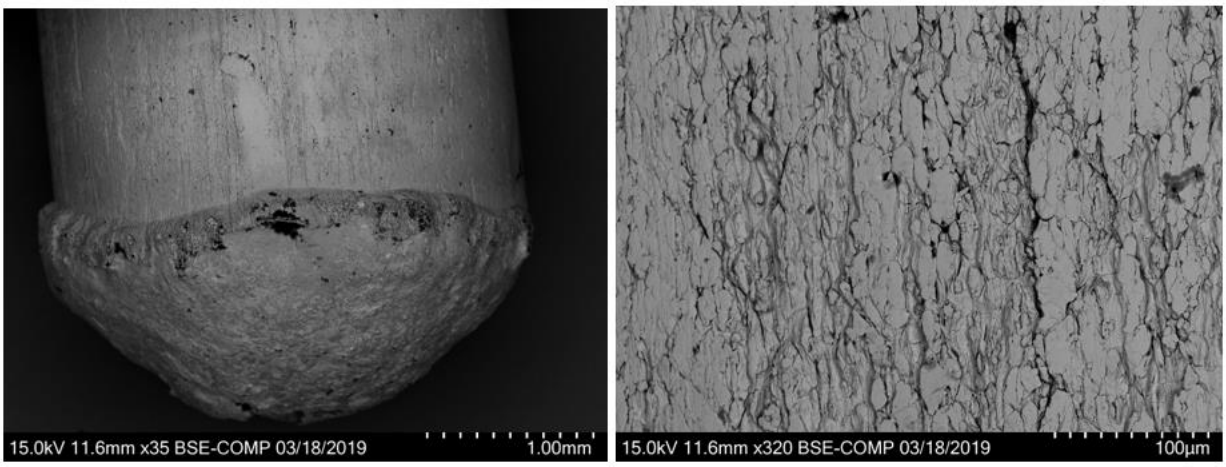

Fig. 25 – (Left) Burn Tip 35x, (Right) Bulk Surface 320x of Sample WH-2

Sample WH-2 is representative of wrought test material which received no hot-isostatic pressing, wrapping, or machining post processing. The burn tip size and geometry are not significantly different from what has been seen in the SLM samples, though it could be noted that the elemental contrast seen in those samples burn tip surfaces are not as distinct here. The major difference can be seen in the surface structure of the bulk, which now shows highly directional cold-working signatures in lieu of the particulate based structures of the SLM samples.

X-Ray Diffraction

As mentioned above, x-ray diffraction was conducted on all samples after they had been mounted and polished to provide a flat surface. This is more ideal for accuracy and reducing signal loss in comparison to the rounded cylindrical surface of the rods as they were received. 25-minute scans were conducted over the range of 30˚ - 100˚. Phases typical of Inconel 718 were observed, with a predominant γ-matrix of nickel-chromium solid solution along with spectra peaks for simple nickel, δ-phase (Ni_3Nb), γ’ precipitates (Ni_3Al), and γ” precipitates (Ni_3Nb).

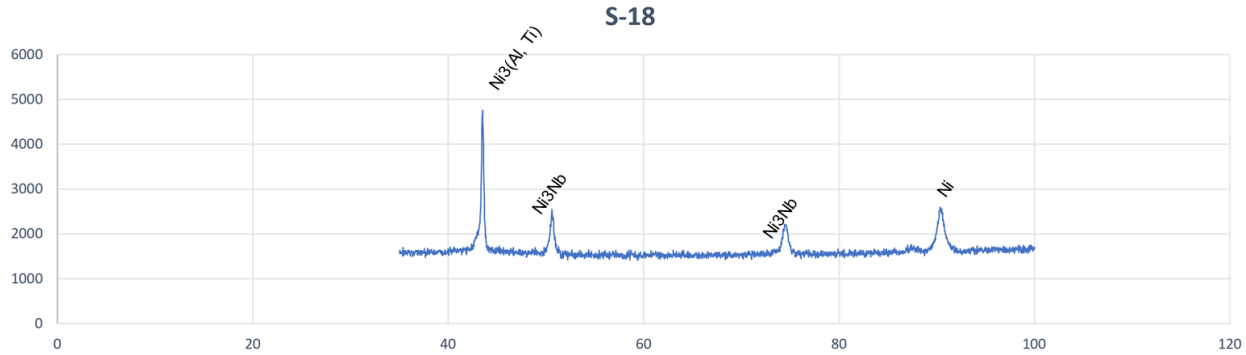

Fig. 26 – XRD Spectra generated by Sample S-18

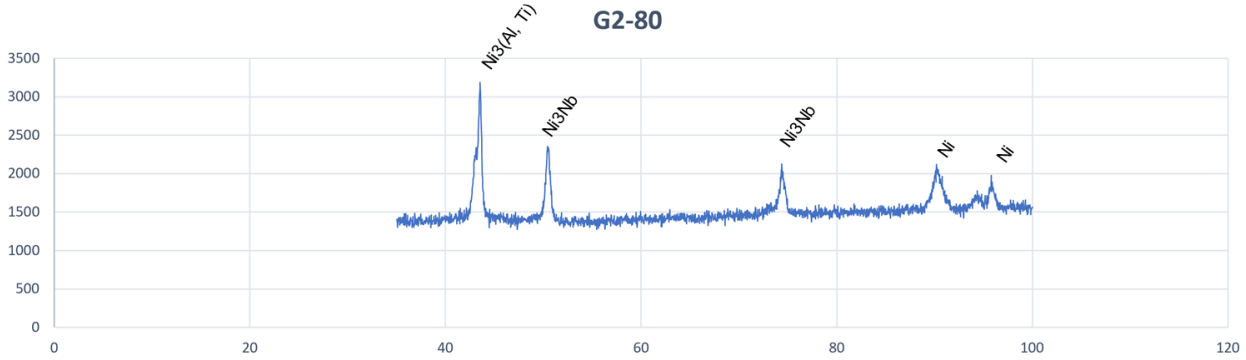

Fig. 27 – XRD Spectra generated by Sample G2-80

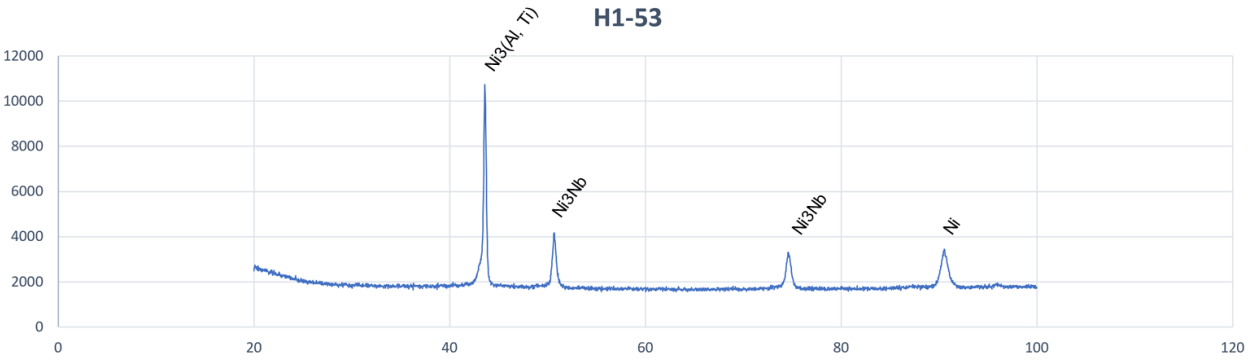

Fig. 28 – XRD Spectra generated by Sample H1-53

Fig.'s above are representative of the typical spectra generated from the SLM test rods. Though signal intensity (in counts per second) did vary between the rods, generally speaking the contact angles could all be matched indicating identical phases present across the samples. Near approximately 45˚ (2θ) one can observe the Ni_3Al γ' precipitate phase, the secondary peak closer to 50˚ (2θ) is the Ni_3Nb γ" precipitates, the δ-phase Ni_3Nb is then seen at approximately 75˚ (2θ), and lastly the peak for simple nickel can be found around 90˚ (2θ).

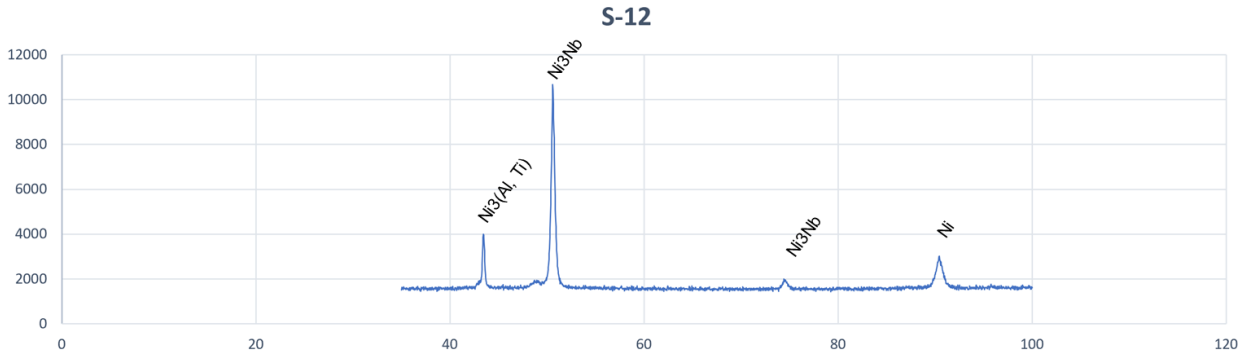

Fig. 29 – XRD Spectra generated by Sample S12

Interestingly, one sample (S12) whose spectra is seen above shows a reversal in peak intensity – the primary peak is the Ni_3Nb γ" precipitate instead of the Ni_3Al γ' precipitate. This sample had a processing history of SLM hot isostatic-pressing without wrapping or machining, which is a configuration shared with sample G2-52 (though that spectra did not reflect what was seen here for S12). Notably, this sample S12 had a significantly shorter burn length (2.6 cm) than sample G2-52 (8.6 cm).

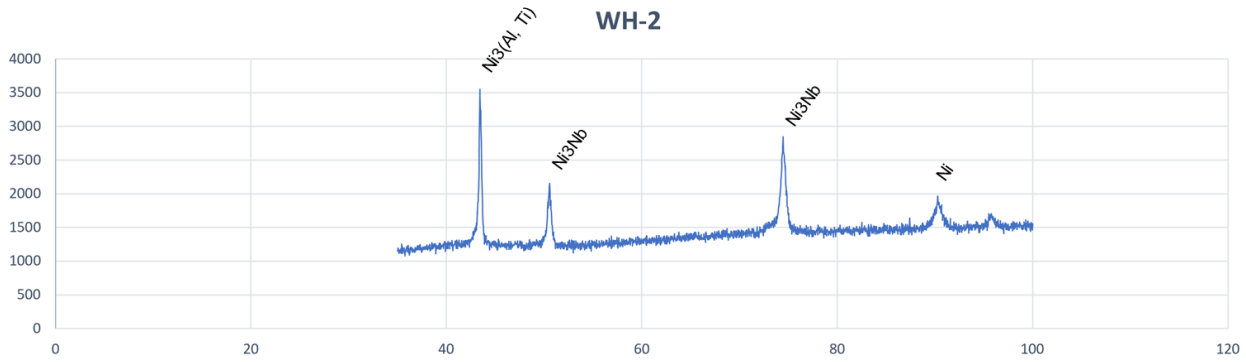

Fig. 30 – XRD Spectra generated by Sample WH-2

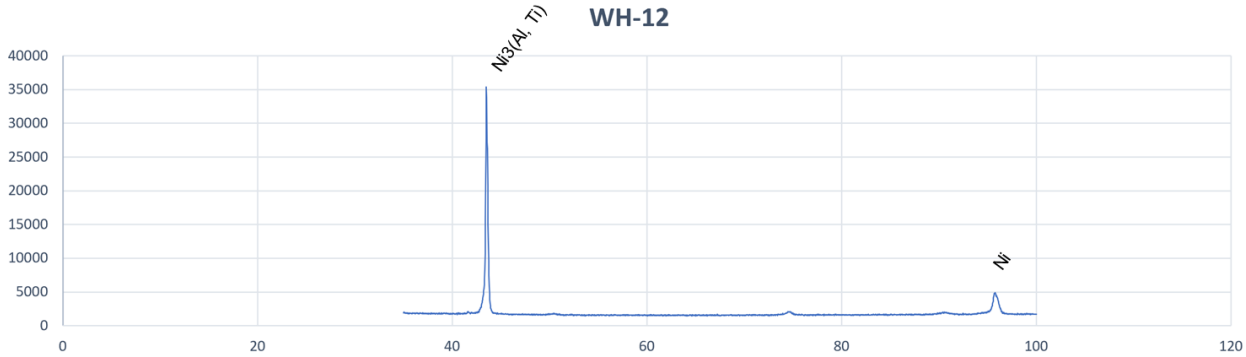

Fig. 31 – XRD Spectra generated by Sample WH-12

With regards to wrought test material, the figures above (26 and 27) show what diffraction spectra could be generated. Sample WH-2 appears to show similar scope and geometry to the other SLM samples, with primary Ni_3Al phase followed by subsequent peaks for Ni_3Nb precipitates and δ-phase. However, the other wrought samples are more accurately described by what is seen for sample WH-12, with the same primary Ni_3Al phase present but a relative lack of detection of any of the Ni_3Nb structures (phase or precipitate).

Metallography and Optical Microscopy

Samples were polished (to a one-micron finish) and subsequently etched with Kalling's No 2 Reagent to reveal their microstructures. The micrographs below are indicative of some of the features which were observed, including what was seen in burn tips (like gas porosity and woven-like texturing) as well as within the bulk (such as twins, acicular precipitate structures, and generally equiaxed grains).

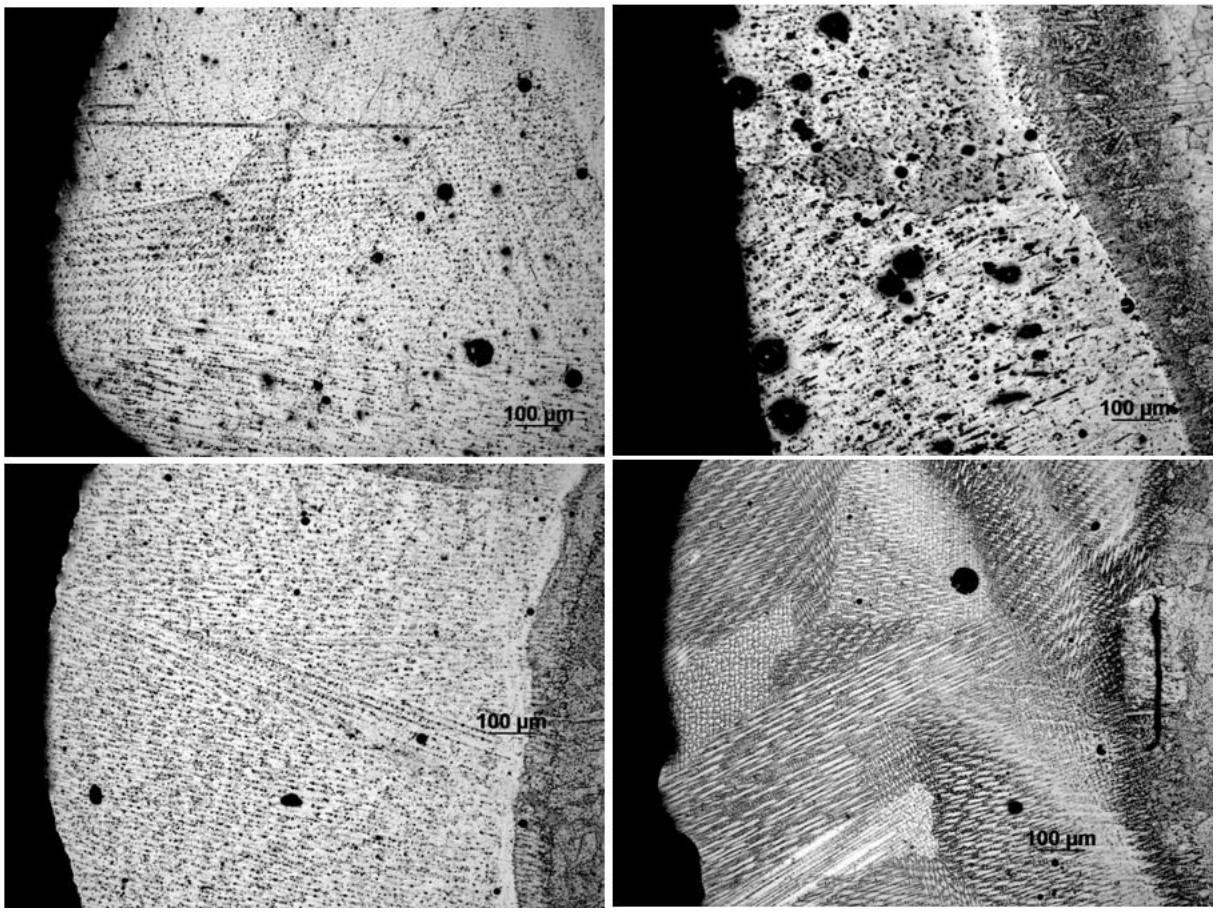

Fig. 32 – Burn tip micrographs for the G2 series samples (top left G2-52, top right G2-78, bottom left G2-80, bottom right G2-94). All images taken at 100x

Pictured above are burn tip micrographs for the four G2 series samples. Most immediately noticeable is the presence of a woven-like texture in several of the burn tips, being highly directional but in various orientations (this is most striking in sample G2-94). All the images also show entrapped gas porosity, though to varying degrees. Of note is the burn interface and transition zone of sample G2-78, which is not only larger than what was seen in other samples but also less uniform in thickness.

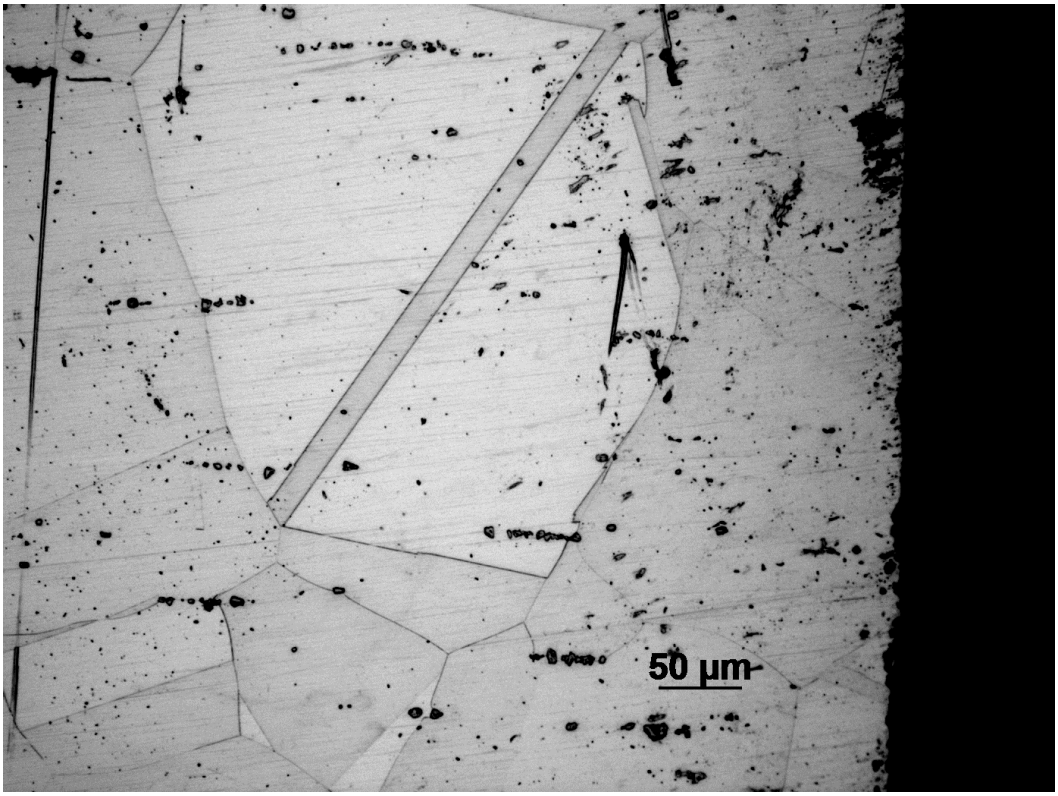

Fig. 33 – Micrograph of Daughter End 2 from Sample WH-12, 200x

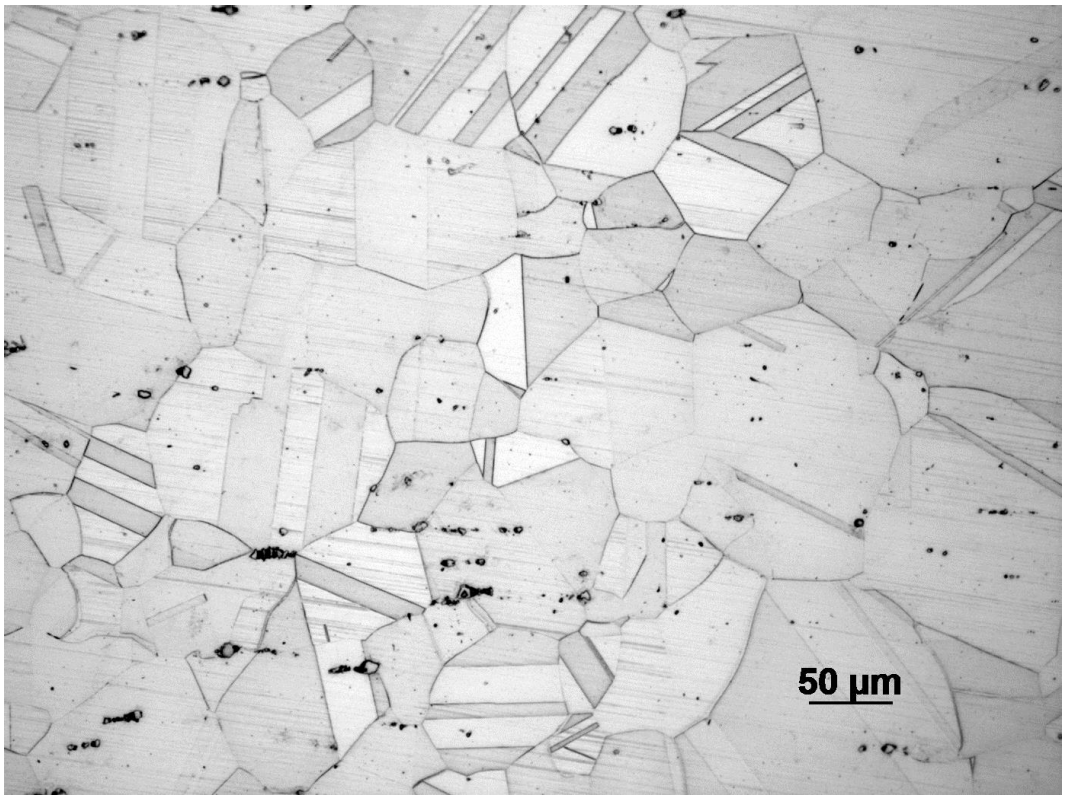

Fig. 34 – Micrograph of Daughter Bulk from Sample WH-2, 200x

Optical imaging of wrought test samples (above) showed that throughout the rods, twinning could be observed in the microstructure. These likely formed after the homogenizing heat treatment post manufacturing, which is used to dissolve residual laves phases and undesirable carbides into the matrix. It has been seen after this process that recrystallization can occur which leads to grain growth as well as the formation of bands of annealing twins.

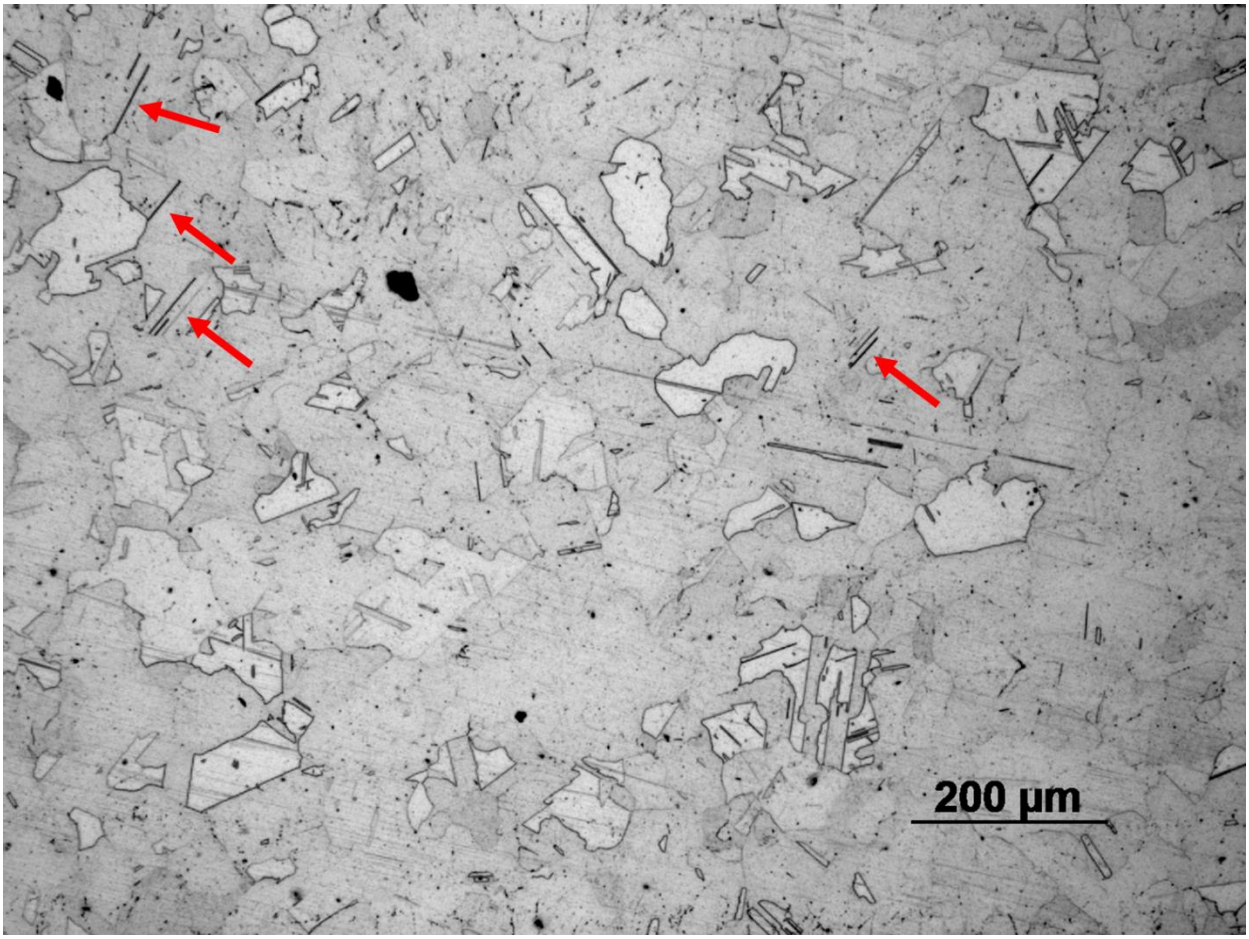

Fig. 35 – Micrograph of the Parent Bulk of Sample G2-94, 100x

The bulk microstructure of sample G2-94 (above) displays what was typical of the SLM samples in this study, with a binary phase matrix of generally equiaxed grains and broadly dispersed acicular structures which are believed to be precipitates which resulted from the post-manufacturing heat treatments.

Microhardness

Tabulated below are the hardness readings taken from each sample, all values are in Rockwell C (converted from Vickers, which is the standard during actual indention with the Duramin tester used). The first column shows an average value, representative of the aggregate of all five readings taken just outside the transition zone for each rod. Note once more that samples

G2-52 and WH-6 were both too short to yield a daughter sample and so only have readings from the parent.

Table 4 – Microhardness data collected from all samples in this study, including values from each individual region of the rod as well as overall averages.

Sample:	Avg. HRC (OTZ):	HRC (PB):	HRC (PE):	HRC (DBE1):	HRC (DBB):	HRC (DBE2):	Overall Average
S18	47.54	46.6	49.1	48.1	47.9	52.1	48.56
S12	48.22	47.4	47.4	54.6	47.4	54.9	49.98667
85	50.5	49.6	46.1	40.4	38.5	48.4	45.58333
C1-107	49.92	52.9	52.7	47.1	52.9	50.1	50.93667
B1-55	47.28	43	46.6	46.8	46.1	39	44.79667
H1-53	50.52	51.1	50.4	50.1	52.7	53.2	51.33667
G294	52.58	51.1	50.7	46.6	51.1	51.4	50.58
G278	52.16	51.8	53.4	53.4	51.1	54.1	52.66
G395	54.48	57.2	57	53.2	52.9	53.2	54.66333
G252	50.46	47.4	49.9	N/A	N/A	N/A	49.25333
G280	50.02	50.7	52.1	52.7	47	47.9	50.07
WH12	50.1	47.1	39.4	44.2	45.6	50.9	46.22
WH6	48.46	46.6	42.5	N/A	N/A	N/A	45.85333
WH2	50.1	51.6	54.1	45.1	48.1	47.4	49.4
W11	52.12	49.1	47.6	53.7	52.4	51.6	51.08667

Key Takeaways

The primary takeaway from this work conducted in 2019 was that more testing would be needed to positively identify correlations between manufacturing/post-processing and flammability. Several pieces of data support the hypothesis that minute differences in the chemistry or structure of the sample rods may influence performance, as some rods which saw identical processing (for example, S12 and G2-52) had drastically different burn lengths. These two rods also demonstrated via XRD that even though they had the same processing history, the resultant microstructure can consist of different phases and/or concentrations of phases which

could have an effect on flammability – higher peak intensity of the Ni_3Nb γ" precipitate instead of the Ni_3Al γ' precipitate seems to show a reduction in burn length.

Additionally, metallography displayed variability in the volume and orientation of the burn interfaces between samples as well as unique features in the burn tips which currently are not predictable (such as the Widmanstätten-like weaving seen in sample G2-94). From a chemistry standpoint, the data included in this testing is inconclusive and provides a rationale for more quantitative analytical methods (such as Inductively Coupled Plasma Optical Emission Spectroscopy) to study the minute differences in elemental composition between batch lots and between samples of the same batch lot after post-processing. It has been hypothesized that machining may be removing material which has been preferentially concentrated with certain constituents as a result of diffusion induced by the hot isostatic pressing process.

Chapter 4: Experimental Procedure

Sample Descriptions

This dissertation will be attempting to analyze two sets of samples of Inconel 718 promoted combustion rods. The first (denoted from this point on as "Sample Set 1") is a set of 16 rods which will be subjected to a full metallurgical analysis with the goal of characterizing microstructure, chemical constituency and diffusion, and variability of phases from the bulk through the burn interface region. The second (denoted from this point on as "Sample Set 2") is a set of 6 rods which were sectioned and polished such that a transverse cross section directly representative of the burn interface could be analyzed via transmission electron microscopy and atomic-level energy dispersive spectroscopy. Details regarding these sample sets are included below:

Table 5 – Sample Set 1: Full Metallurgical Analysis Sample Descriptions

Powder Batch Lot	WSTF Test No:	SLM/Wrought	HIP 'ed	Wrapped	Heat Treated	Machined	Burn Length (cm)
A1	8044	SLM	Y	Y	Y	N	3.7
	8174	SLM	Y	N	Y	Y	3.1
	8065	SLM	N	N	N	Y	1.7
D1	8082	SLM	Y	Y	Y	N	7.9
	8158	SLM	Y	Y	Y	Y	2.6
	8184	SLM	N	N	N	Y	5.5
C1	8490	SLM	Y	N	Y	N	2.7
	8525	SLM	Y	N	Y	Y	4.8
	8541	SLM	Y	Y	Y	N	2.3
	8544	SLM	Y	Y	Y	Y	1.5
Unmarked	7676	Wrought	N	N	N	N	3.7
G2	8488	SLM	Y	N	Y	N	13.4
	8522	SLM	Y	Y	Y	N	3.1
	8531	SLM	Y	Y	Y	Y	7.2
Unmarked	7670	SLM	N	N	Y	N	2
	7679	Wrought	N	N	N	N	1.9

Table 6 – Sample Set 1 Powder History

Powder Batch Lot	WSTF Test No:	SLM/Wrought	Virgin or recycled	Lot Size	Powder Cut Max-Min micron	Median Powder Cut Range Micron	Vacuum Melt Production Atomize Type	Gas
A1	8044	SLM	V	Small	30	30	Gas	Ar
A1	8065	SLM	V	Small	30	30	Gas	Ar
A1	8174	SLM	V	Small	30	30	Gas	Ar
C1	8490	SLM	V	Small	30	30	Gas	N
C1	8525	SLM	V	Small	30	30	Gas	N
C1	8541	SLM	V	Small	30	30	Gas	N
C1	8544	SLM	V	Small	30	30	Gas	N
D1	8082	SLM	V	Small	29	30.5	Gas	Ar
D1	8158	SLM	V	Small	29	30.5	Gas	Ar
D1	8184	SLM	V	Small	29	30.5	Gas	Ar
G2	8488	SLM	V	Small	34	28	Gas	Ar
G2	8522	SLM	V	Small	34	28	Gas	Ar
G2	8531	SLM	V	Small	34	28	Gas	Ar

The samples shown above in Table 5 were selected due to the fact that they represent the various combinations of processing histories possible within the samples provided by White Sands Test Facility as well as minimize the number of powder batch lots involved (thus decreasing the likelihood of variability between batch lots from skewing analysis or interpretation). These samples were subjected to a full metallurgical analysis, comprised of the following tests and methods:

1. As-Received Photography
2. Burn Tip Stereomicroscopy
3. Metallographic Preparation and Optical Microscopy
4. Scanning Electron Microscopy (both in the as-received state and following metallography)
5. Energy Dispersive Spectroscopy (both in the as-received state and following metallography)

6. X-Ray Fluorescence
7. X-Ray Diffraction

The sections below will describe in greater detail the particular methodologies used for each of the above analysis techniques.

Table 7 – Sample Set 2: TEM Analysis Sample Descriptions

Powder Batch Lot	WSTF Test No:	HIP 'ed	Wrapped	Heat Treated	Machined	Burn Length (cm)
A2	8064	Y	Y	Y	N	1.9
	8159	Y	Y	Y	N	8
G2	8068	Y	N	Y	N	6.3
	8152	Y	N	Y	Y	5
	8046	Y	Y	Y	N	3.2
	8473	Y	Y	Y	Y	4.9

Table 8 – Sample Set 2 Powder History

Powder Batch Lot	WSTF Test No:	SLM/Wrought	Virgin or recycled	Lot Size	Powder Cut Max-Min micron	Median Powder Cut Range Micron	Vacuum Melt Production Atomize Type	Gas
A2	8064	SLM	V	Small	35	27.5	Gas	Ar
A2	8159	SLM	V	Small	35	27.5	Gas	Ar
G2	8046	SLM	V	Small	34	28	Gas	Ar
G2	8068	SLM	V	Small	34	28	Gas	Ar
G2	8152	SLM	V	Small	34	28	Gas	Ar
G2	8473	SLM	V	Small	34	28	Gas	Ar

The samples from Sample Set 2 were selected on the basis of powder batch lot and burn length variability. Samples 8068, 8152, 8046 and 8473 are all from the G2 batch lot and also represent the 4 sequences (HIP + Not Wrapped + Not Machined, HIP + Not Wrapped + Machined, HIP + Wrapped + Not Machined, and HIP + Wrapped + Machined) of processing histories available for analysis. Samples 8064 and 8159 were chosen because they are from the same batch lot and have identical processing history but have significantly different burn lengths. Sample Set

2 rods were precision sectioned and then polished before being sent to the Texas Materials Institute at the University of Texas at Austin for Focused-Ion Beam (FIB) preparation. Once electron transparent lamellae were produced, TEM imaging and EDS was conducted at their facility. Greater detail on this process and methodology will also be included in the sections below.

SAMPLE SET 1 PROCEDURES

As mentioned above, the rods included in Sample Set 1 were subjected to a full metallurgical investigation including various methods of microscopy, metallographic preparation, chemical analysis, and spectroscopy. The procedure for each method as well as descriptions of utilized equipment and instrumentation are provided below in the order in which each step was conducted on the samples.

As-Received Photography

Upon reception, the 16 sample rods were photographed with a 12 mega-pixel dual lens camera in order to document their length and color. For ideal contrast the rods were imaged on blue paper and white balancing was conducted on the camera to achieve as close to true-color representation as possible. A dimensional reference (in centimeters) is shown along the bottom of each image and the sample number is included at the top left. A representative of these images is shown below for sample 8065.

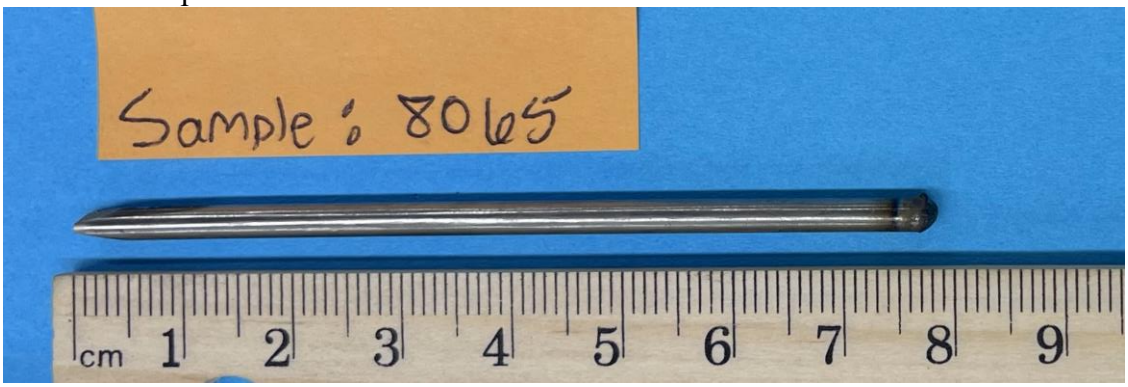

Fig. 36 – Example of As-Received Photography

Burn Tip Stereomicroscopy

Once each sample rod had been photographed using a traditional camera, greater emphasis was placed on obtaining higher resolution images of the burn tips as they exhibited significant variability between samples. For this purpose, an Olympus SZX10 stereomicroscope with an SC50 digital camera attachment was used to photograph the approximate last 6 millimeters of each rod at 18.75x magnification (showing the burn tip, burn interface, heat affected zone, and bulk material). A representative of this imaging is shown below for sample 8084.

Fig. 37 – Example of Burn Tip Stereomicroscopy

As-Received Scanning Electron Microscopy

Following as received photography and stereomicroscopy, the sample rods were sectioned such that 1 full inch of material (including the burn tip end) was produced. This size was selected for several reasons:

a.) 1 inch from the burnt end contained all of the regions of main interest (burn tip, burn interface, heat affected zone, and bulk),

b.) 1 inch (or 2.54 cm) is the ideal length of a specimen for use in the TERAPRESS mounting instrument for metallographic preparation

c.) 1 inch was also an ideal length for the readily available sample holders for scanning electron microscopy and energy dispersive spectroscopy

For sectioning, a Pace Technologies® Mega-T400 Abrasive Cutting Saw was used with a Maxcut MAX-C400 16" abrasive blade for hard non-ferrous materials installed. It should be noted that only 14 rods were sectioned, as 2 rods (8082 and 8488) were already shorter than 1 inch as a result of their combustion testing. An illustration demonstrating the sectioning is shown below:

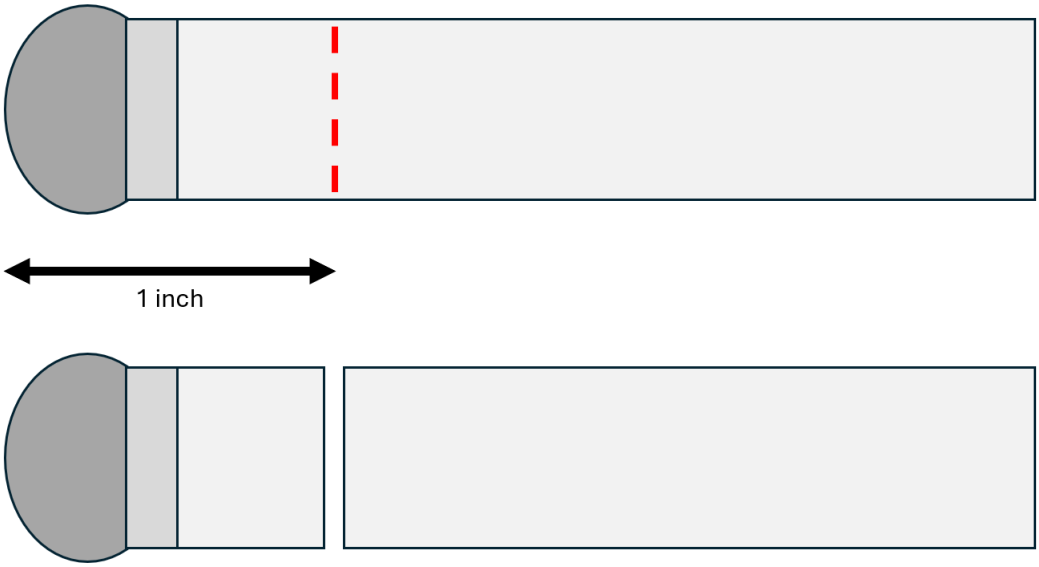

Fig. 38 – Graphical Representation of Sample Set 1 Sectioning

Once the samples were sectioned, they were mounted with carbon tape onto 25.4 mm aluminum SEM sample holders and then inserted into a Hitachi SU-3500 variable pressure scanning electron microscope. An example of a pre-observation reference image of several samples on a stage is shown below:

Fig. 39 – Sample Rods Mounted on an SEM Stage

The scanning electron microscope was used in the high-vacuum mode at an accelerating voltage of 10.0 kV and spot intensity setting of 60. Imaging primarily used the secondary electron (SE) detector and settings. Because the rods at this point were in the as-received state (so only outer surfaces were available to observe) the primary regions of interest were the bulk, burn tip, and burn interface. The standard procedure for imaging the samples is listed below, along with a graphical representation of where the images were taken from for each rod.

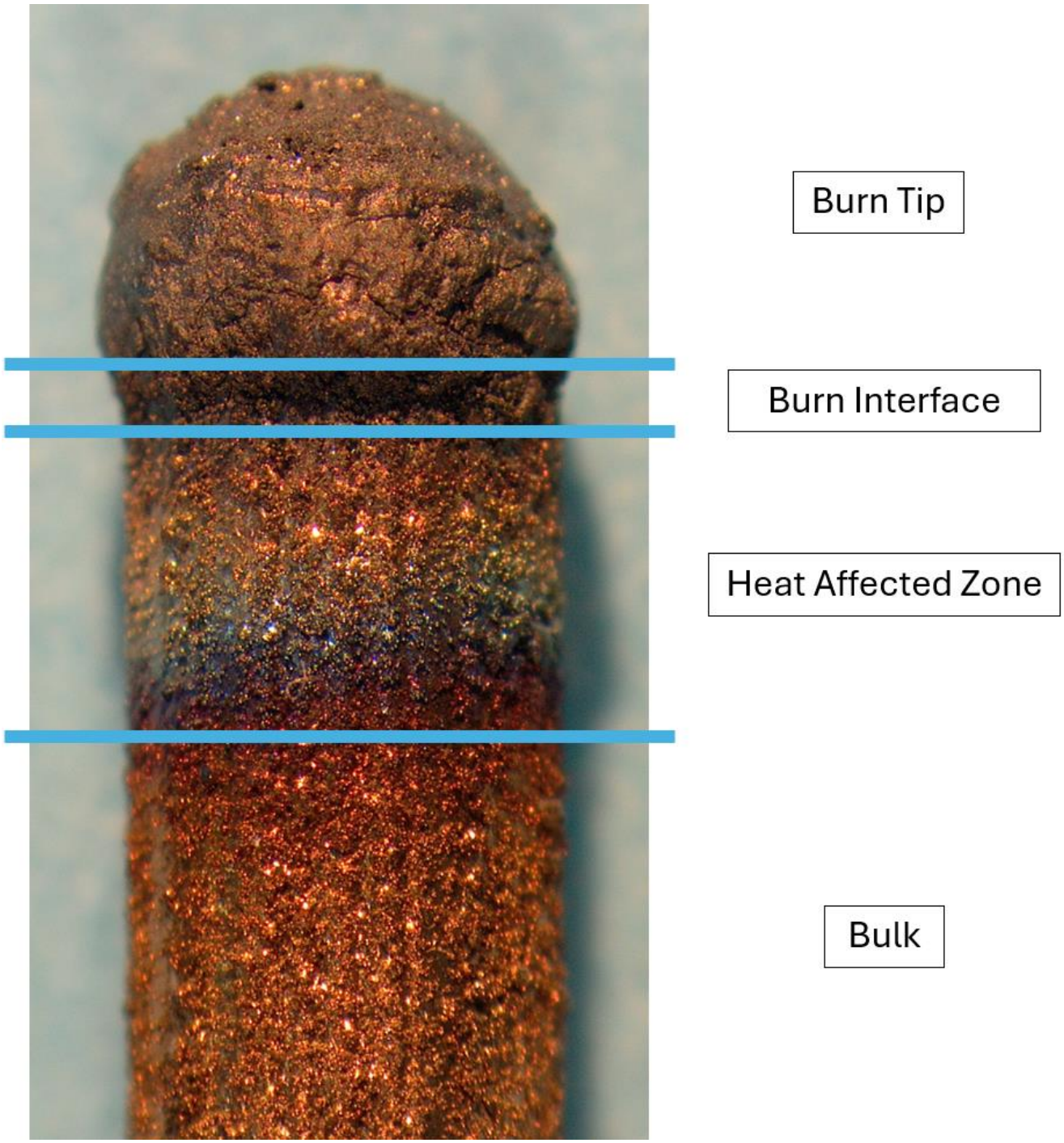

Fig. 40 – Representation of the Main Areas of Interest for Each Sample Rod

The standard imaging schedule for each rod in Sample Set 1 is listed below. It should be noted that these specifications were used as a baseline for every sample and that in instances where additional features were observed, deviations exist for higher magnification imaging.

Table 9 – As Received SEM Imaging Schedule

As-Received SEM Imaging	
Region:	Magnification:
Burn Tip	35x
Burn Interface	100x
	250x
	1000x
Bulk	50x
	250x
	500x

As-Received Energy Dispersive Spectroscopy

As samples were already inserted in the electron microscope for imaging, energy dispersive spectroscopy was done simultaneously for the same regions of interest. The peripheral used was an Oxford X-Max^{50} silicon drift detector and beam settings included an elevated accelerating voltage of 20.0 kV and an increased spot intensity of 80 in order to achieve the necessary output count rates (cps) for elemental mapping in the Aztec EDS software. For each of the regions listed below, an elemental map and tabulated spectra were generated. It should be noted that the spectra for burn tips also included high values for aluminum and carbon from the sample stage and tape.

Table 10 – As Received EDS Mapping Schedule

As-Received EDS Maps	
Region:	Magnification:
Burn Tip	35x
Burn Interface	100x
Bulk	250x

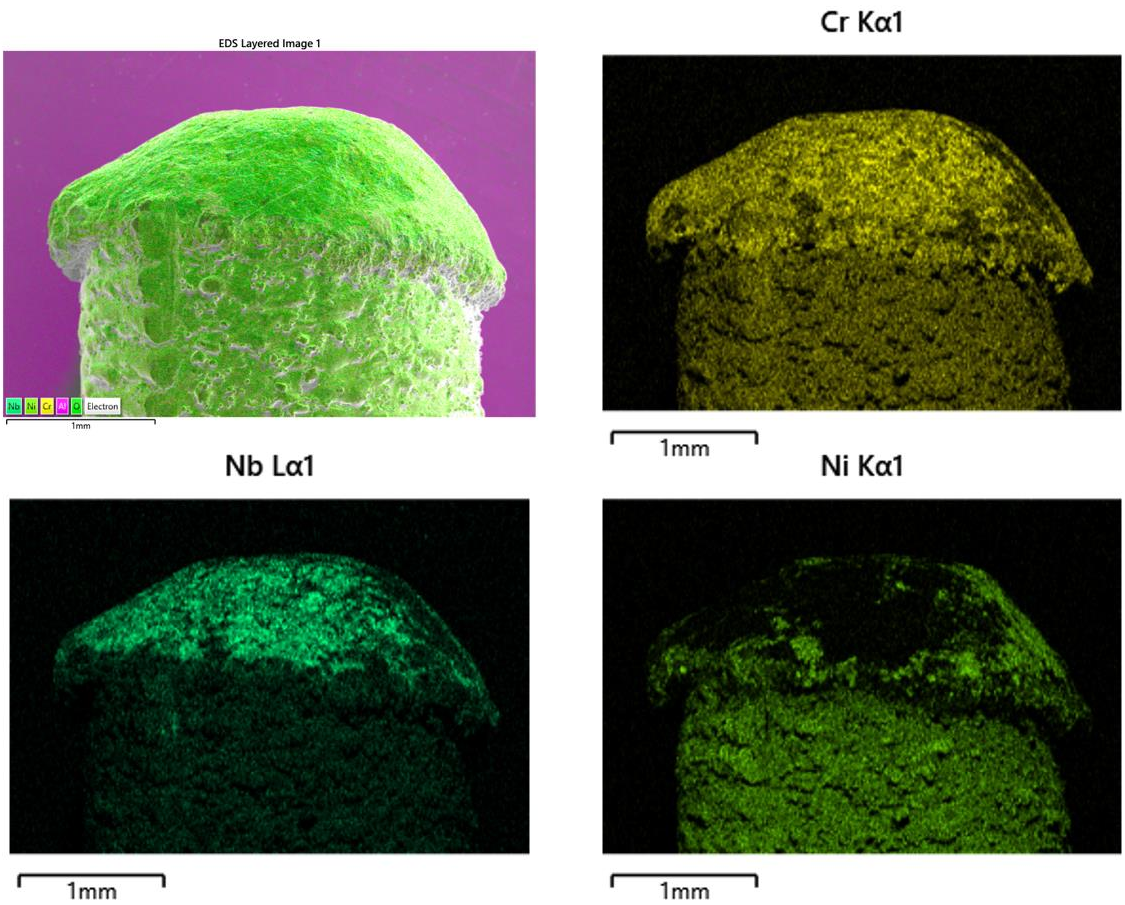

Fig. 41 – Representation of As-Received Burn Tip EDS Mapping

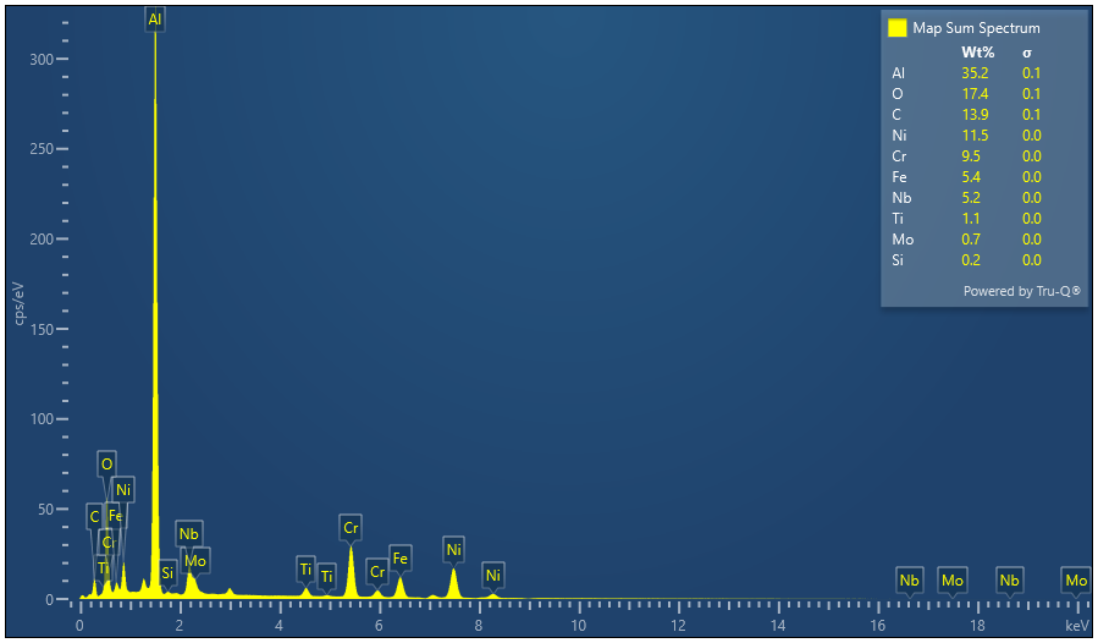

Fig. 42 – Representation of Spectra Generated from As-Received Burn Tip EDS

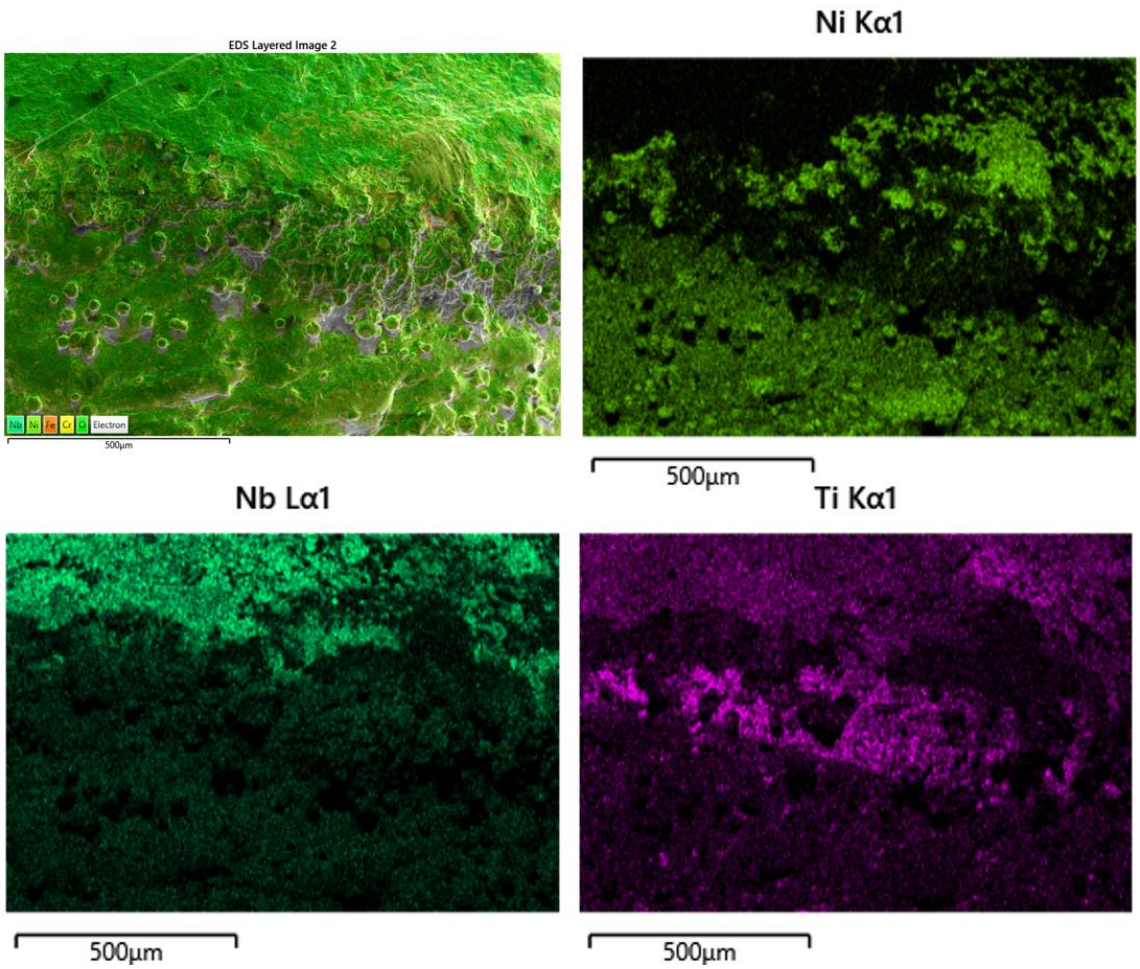

Fig. 43 – Representation of As Received Burn Interface EDS Mapping

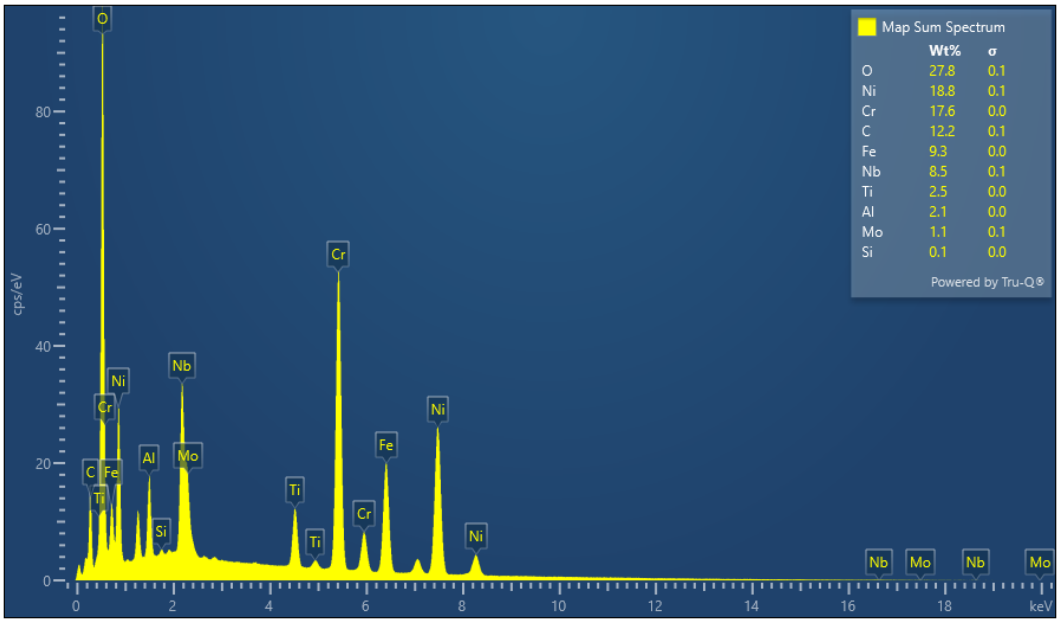

Fig. 44 – Representation of Spectra Generated from As Received Burn Interface EDS

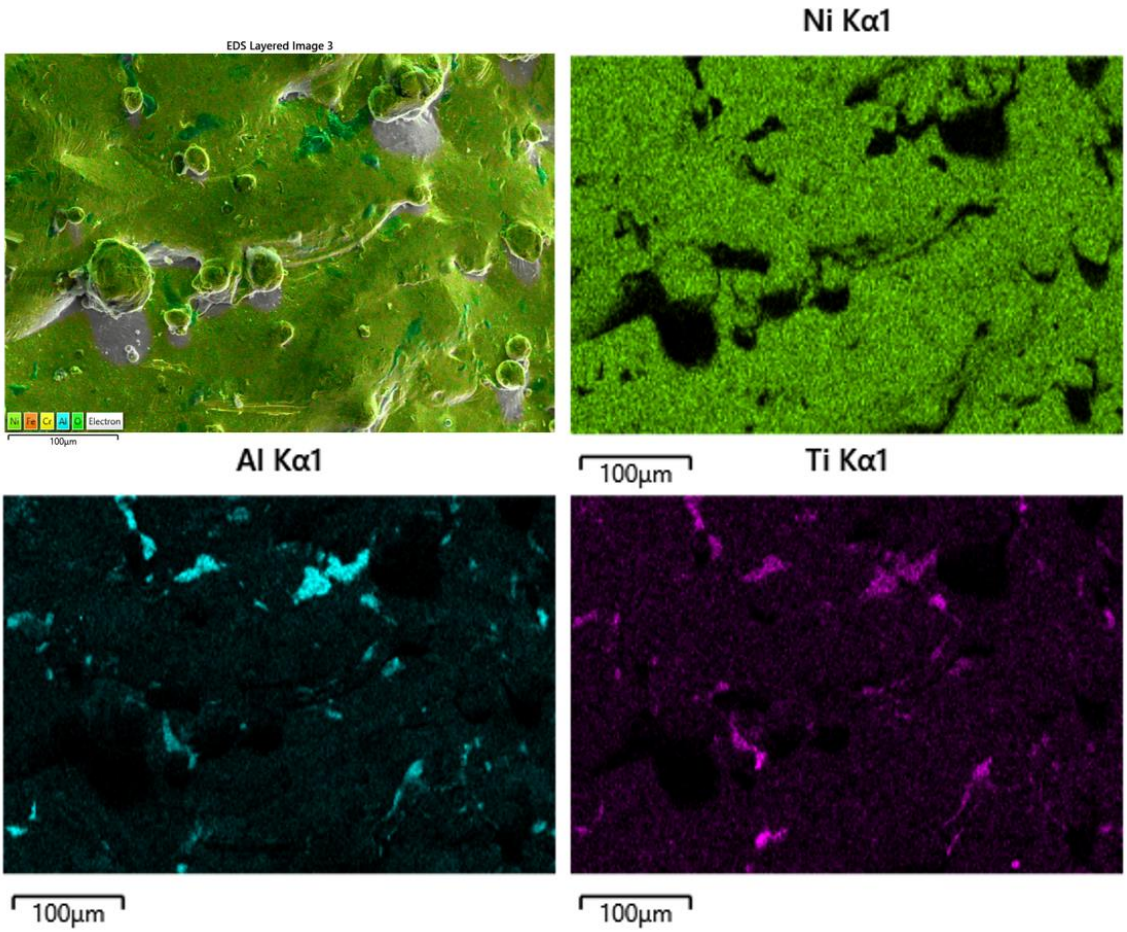

Fig. 45 – Representation of As Received Bulk EDS Mapping

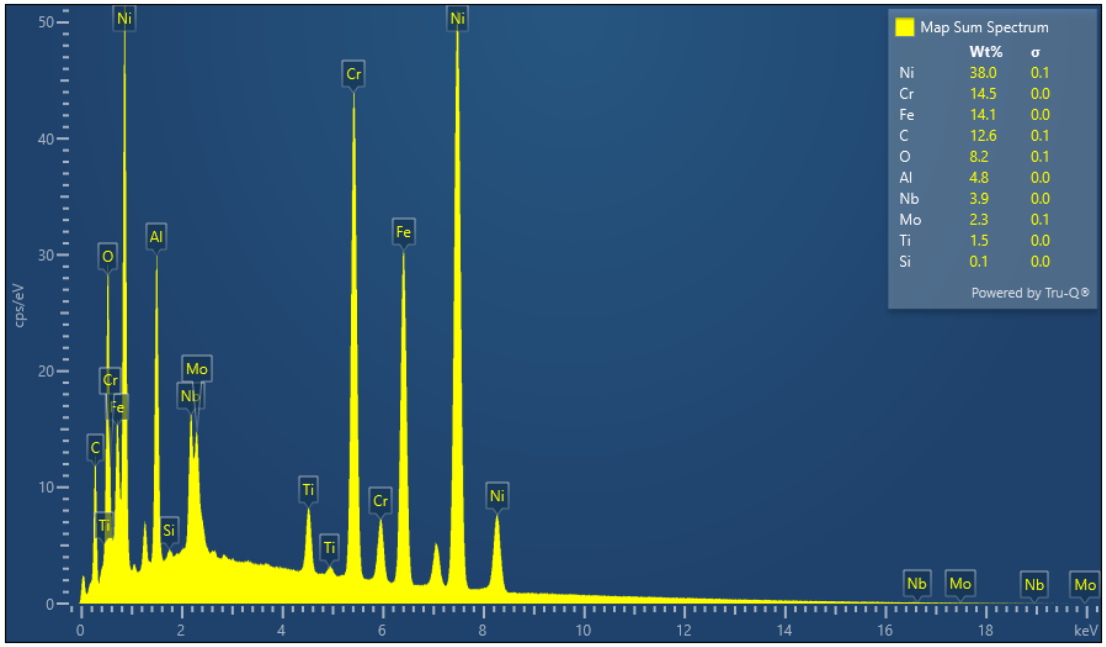

Fig. 46 – Representation of Spectra Generated from As Received Bulk EDS

X-Ray Fluorescence

In order to complement the chemical analysis already being conducted via EDS for each rod, X-Ray Fluorescence was also utilized to survey the surface chemical constituency of the bulk of each rod whose dimensions allowed (three samples – 8082, 8184, and 8488 – were too small to be analyzed with XRF and returned "Proximity Error" messages when attempted). For the 13 samples which could be analyzed, three readings were taken from the bulk material leftover after sectioning using an Olympus DELTA XRF handheld gun and then aggregated to determine the established chemistry for each sample.

In attempting to minimize the likelihood of background interference with the readings for this method, samples were taped up-right to the counter of the UTEP metallurgy lab and scanned vertically. An image displaying this setup is shown below.

Fig. 47 – XRF Analysis Sample Setup

Metallography

Once all samples had been sectioned to ideal size, they were mounted in the axial orientation within a Pace Technologies® TERAPRESS TP-7500 compression mounting press. The mount mixture for all samples consisted of a main binder of red phenolic premium compression mounting resin and a polished-surface layer of copper conductive mount (in order to facilitate subsequent SEM/EDS analysis in the high vacuum condition). The curing schedule within the Pace software included a heating time of 8 minutes at 210˚C and 30 psi followed by water cooling to ambient temperature over 13 minutes. Once completed, the backs of each mount were engraved with the sample number to ensure traceability. A graphical representation of the samples post-mounting is shown below.

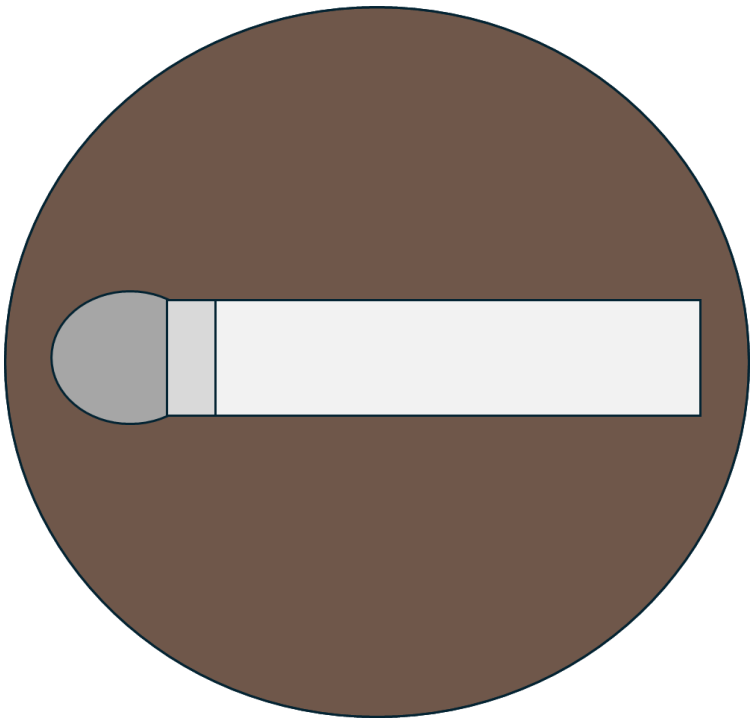

Fig. 48 – Graphical Representation of Samples Post-Mounting

The metallographic grinding process consisted of polishing at 240, 320, and 600 grit on silicon-carbide paper. The polishing wheel utilized was a Pace Technologies® NANO-1000T manual polisher at 200 rpm with a light stream of water as lubricant. Coarser grit papers (i.e. 80

or 120) were foregone due to the relatively shallow depth of the sample rods. Samples were considered to have completed grinding once a flat plane was established at 600 grit with a width of approximately 0.3175 cm (the full diameter of the sample rods, and as such representative of a true middle cross section). Fine polishing was then conducted on each rod over four steps:

1.) 6-micron diamond suspension on a Nylon pad,
2.) 3-micron diamond suspension on a Nylon pad,
3.) 1-micron diamond suspension on a Nylon pad,
4.) 1-micron diamond suspension on a Felt pad

The rationale for using Nylon pads for the first three fine polishing steps was to obtain superior edge-retention as the outer edges of each rod were considered significant for subsequent SEM and EDS analysis. This was then followed by the final step of polishing on the softer felt pad to remove any residual scratches from the previous metallographic steps.

Etching was then conducted on the polished samples using Fry's reagent (100 ml HCl - 75ml distilled water – 65 ml denatured alcohol – 12.5 grams $CuCl_2$) for an average dwell time of 2-5 seconds. Samples were then rinsed with ethanol and dried within a fume hood to reduce watermarks prior to optical imaging.

Optical Microscopy

Once polishing and etching of each sample was completed, rods were optically imaged using an Olympus GX-53 Inverted Metallurgical Microscope equipped with an SC-50 digital camera. All samples were imaged within 24 hours of etching to minimize the influence of surface oxidation on final pictures. The areas of interest reflect what was shown previously in fig. 36, and the standard imaging schedule (including magnifications) is shown below.

Table 11 – Optical Microscopy Imaging Schedule

Optical Imaging	
Region:	Magnification:
Burn Tip	50x
	100x
	200x
Burn Interface	200x
	500x
Heat Affected Zone (HAZ)	50x
	100x
	200x
	500x
Bulk	50x
	100x
	200x
	500x

Polished Scanning Electron Microscopy

Following metallography and optical imaging, samples were again observed with scanning electron microscopy in order to characterize the cross section of material unavailable during the previous step of as-received electron microscopy. The instrument and imaging conditions largely stayed the same as before, a Hitachi SU-3500 variable pressure scanning electron microscope was used with typical values of 10 kV for accelerating voltage and 60.0 for spot intensity. The detector used for imaging did change however, as this round of analysis used back-scattered electron images as opposed to the secondary electron images seen previously. The reasoning for this shift was to provide better elemental/phase contrast as opposed to the topography highlighted in the as-received microscopy.

As the polished interiors for each sample were now visible, several new areas of interest were identified for this imaging schedule. Attention was still paid towards the burn tip, burn interface, and bulk – though certain features within these regions were now more closely observed.

Within the burn tip, images were taken of the general microstructure but also of spherical oxides which were fairly consistent between the samples. In instances where these oxides appeared significantly different in size or composition, multiple oxide types were noted and imaged. Similarly, oxidation seen along the outer perimeter of the burn tip was imaged and is considered to be representative of non-homogenously layered oxides which exist on the surface of the liquid melt pool at extinguishment. For the purposes of this work, these oxides will be denoted as "solidified melt pool surface oxides". Also within the burn tips of several samples were semi-structured crevices adjacent to the burn interface which were also imaged.

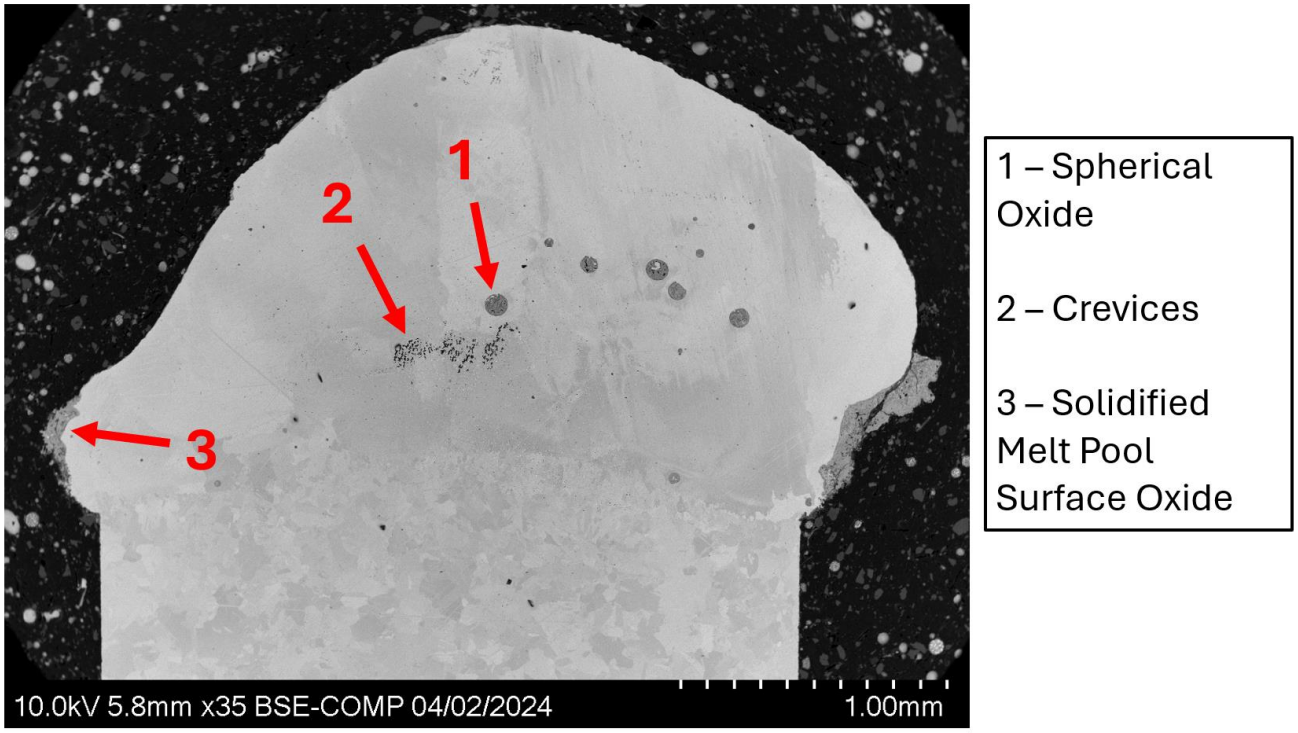

Fig. 49 – Micrograph of a sample burn tip displaying typical areas of interest

During this microscopy, it was also observed that the burn interfaces for these samples displayed distinctive regions when adjoining the melt pool as opposed to adjoining the sample

bulk. For this reason, it was decided that imaging for this region should consist of not only the bulk of the interface but also the areas where the interface structure met and blended into both the melt pool and bulk. Within this document these areas will be denoted as “burn interface melt-side” and “burn interface bulk-side”. The figure below depicts the areas that these images were taken from with relation to the other regions of the rod.

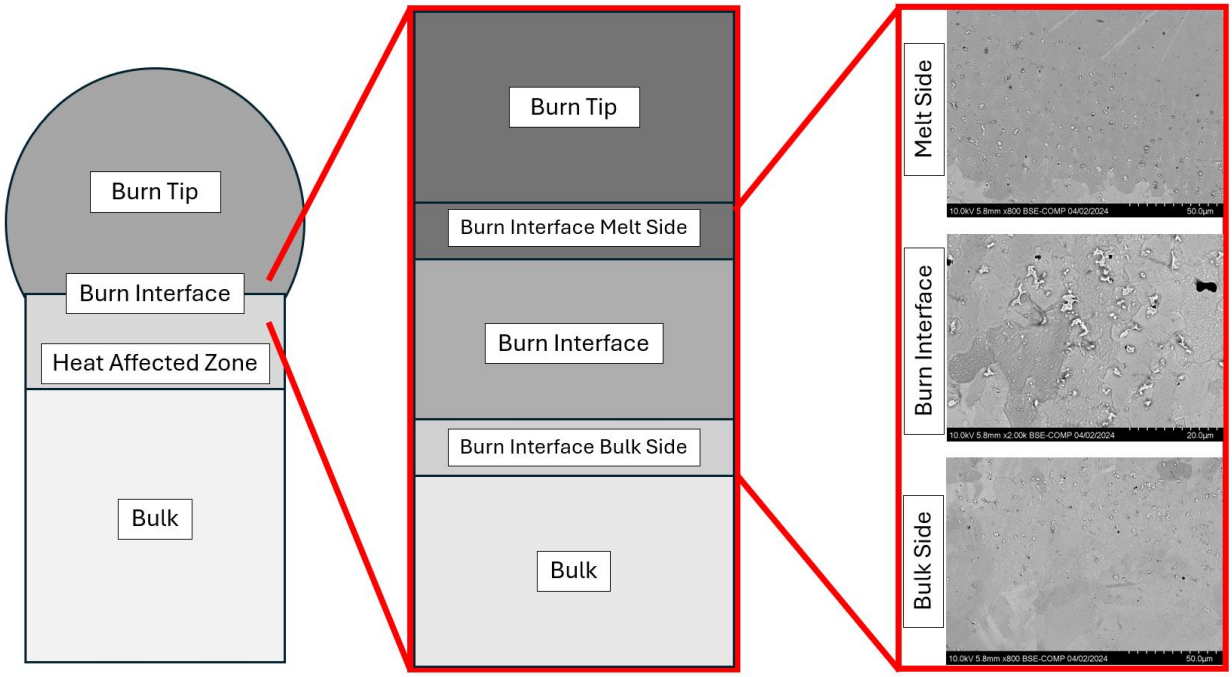

Fig. 50 – Graphic depicting the burn interface regions imaged during mounted SEM

The bulk of each rod was also imaged at several magnifications, as well as the outer surface of the rods in those bulk regions. For some samples which displayed strong indications of the additive manufacturing process (such as individual melt pools and rastering), higher magnification images were also obtained. A full imaging schedule is shown below.

Table 12 – Polished Scanning Electron Microscopy Imaging Schedule

Polished Scanning Electron Microscopy	
Region:	Magnification:
Burn Tip	35x
	150x
	1000x
	3000x
Burn Tip Spherical Oxides	Varies
Solidified Melt Pool Surface Oxide	600x
	2000x
Burn Tip Crevices	1000x
	3000x
	7000x
Burn Interface (Melt Side)	800x
Burn Interface (Bulk Side)	800x
Burn Interface	2000x
Bulk	150x
	500x
	2000x
Bulk Outer Surface	300x
	1000x

Polished Energy Dispersive Spectroscopy

Chemical analysis via energy dispersive spectroscopy was conducted on the polished rods to establish elemental composition and distribution. The microscope and EDS detector used are the same as listed above, and once more the accelerating voltage was 20 kV and spot intensity was 80. Similar to previous analyses, the regions of interest for this analysis included the burn tip (and oxides contained within), the burn interface, and the bulk.

For the burn tip, EDS maps were generated from a macro-view to see how elements were diffusing from the bulk into the melt pool. Point scans were also taken from the center of the burn tip and heat affected zones to semi-quantify the differences in chemistry on either side of the interface. Mapping was then conducted on the spherical oxides present in the burn tip, which was followed by point scans of the various different phases present in the oxide to see what the prevailing constituents were. Examples of these analyses are shown below.

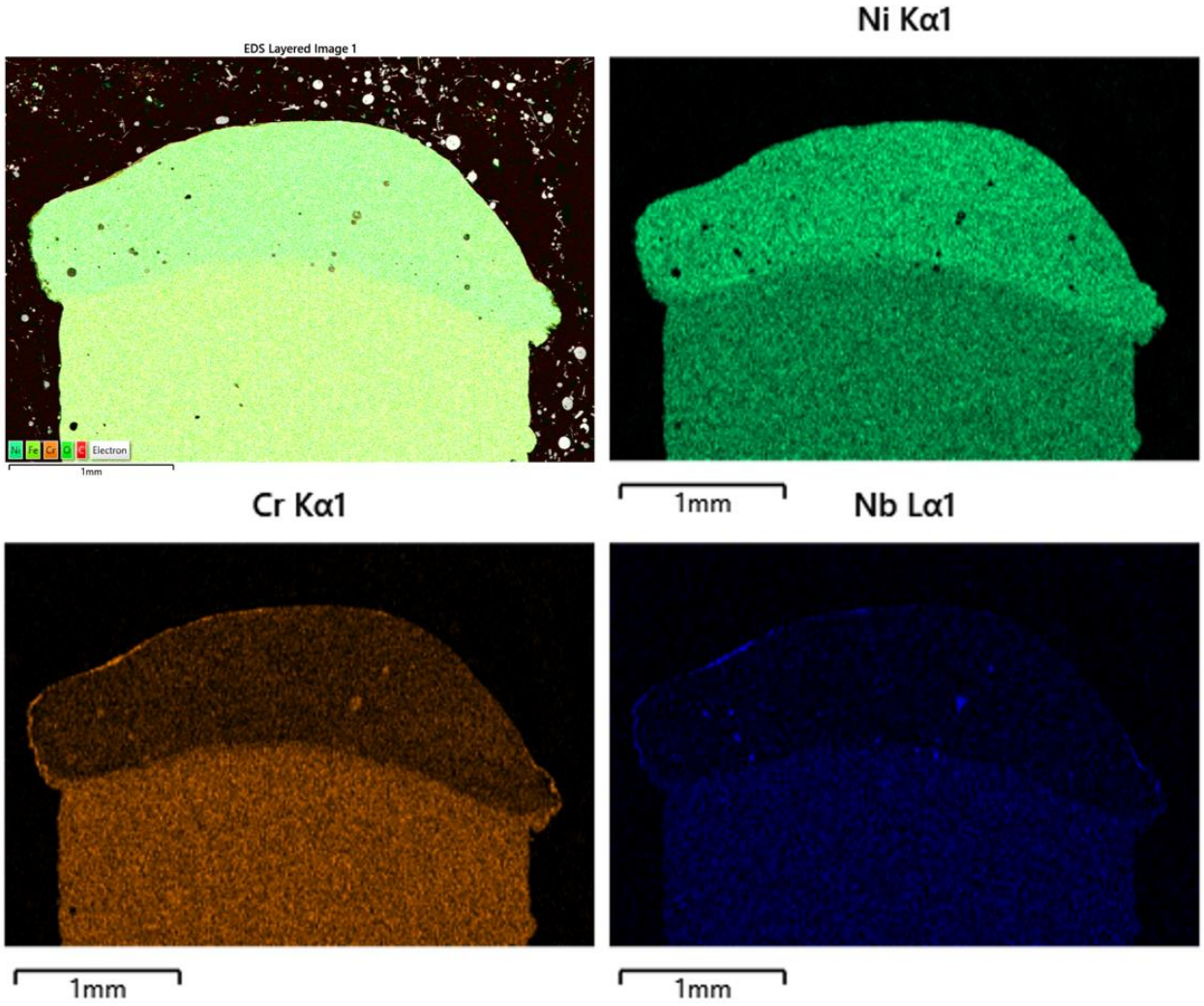

Fig. 51 – Representation of Polished Burn Tip EDS Mapping

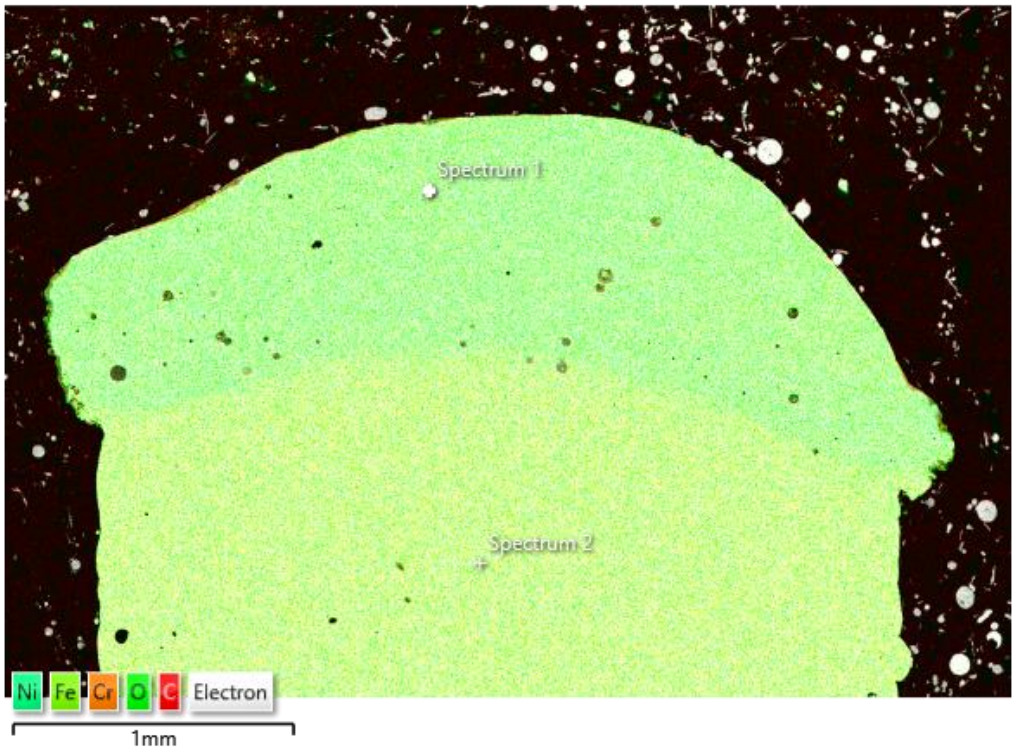

Fig. 52 – Representation of Polished EDS Point Scan Locations for Burn Tips

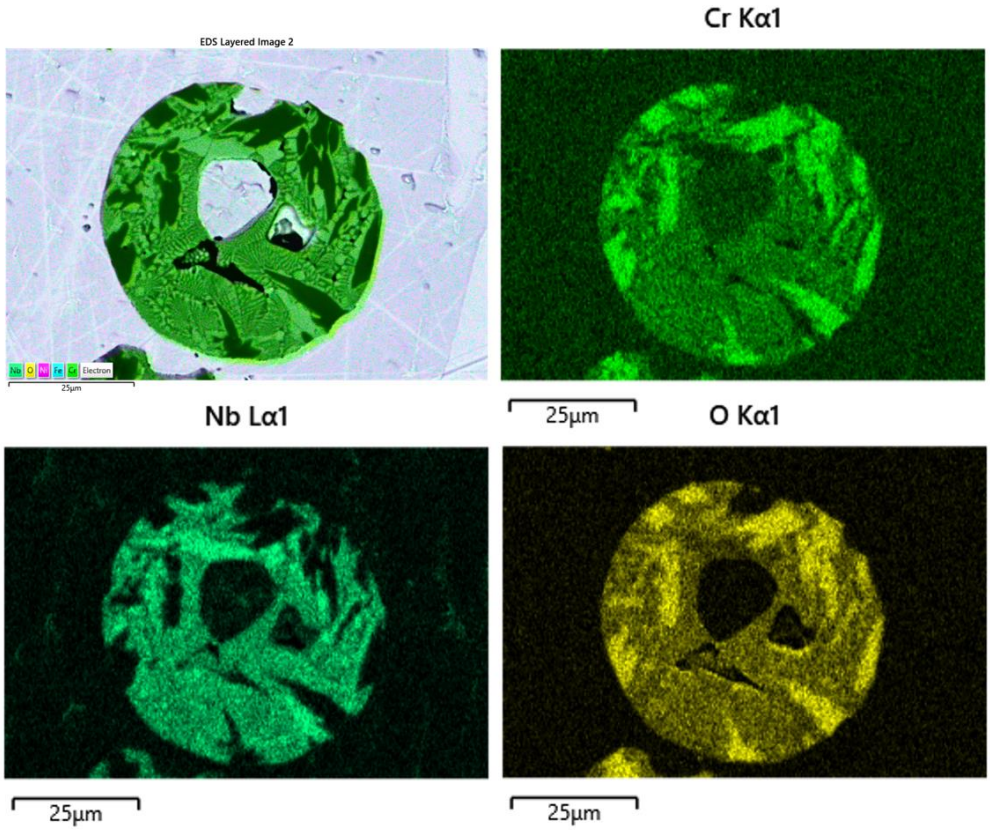

Fig. 53 – Representation of Polished Spherical Oxide EDS Mapping

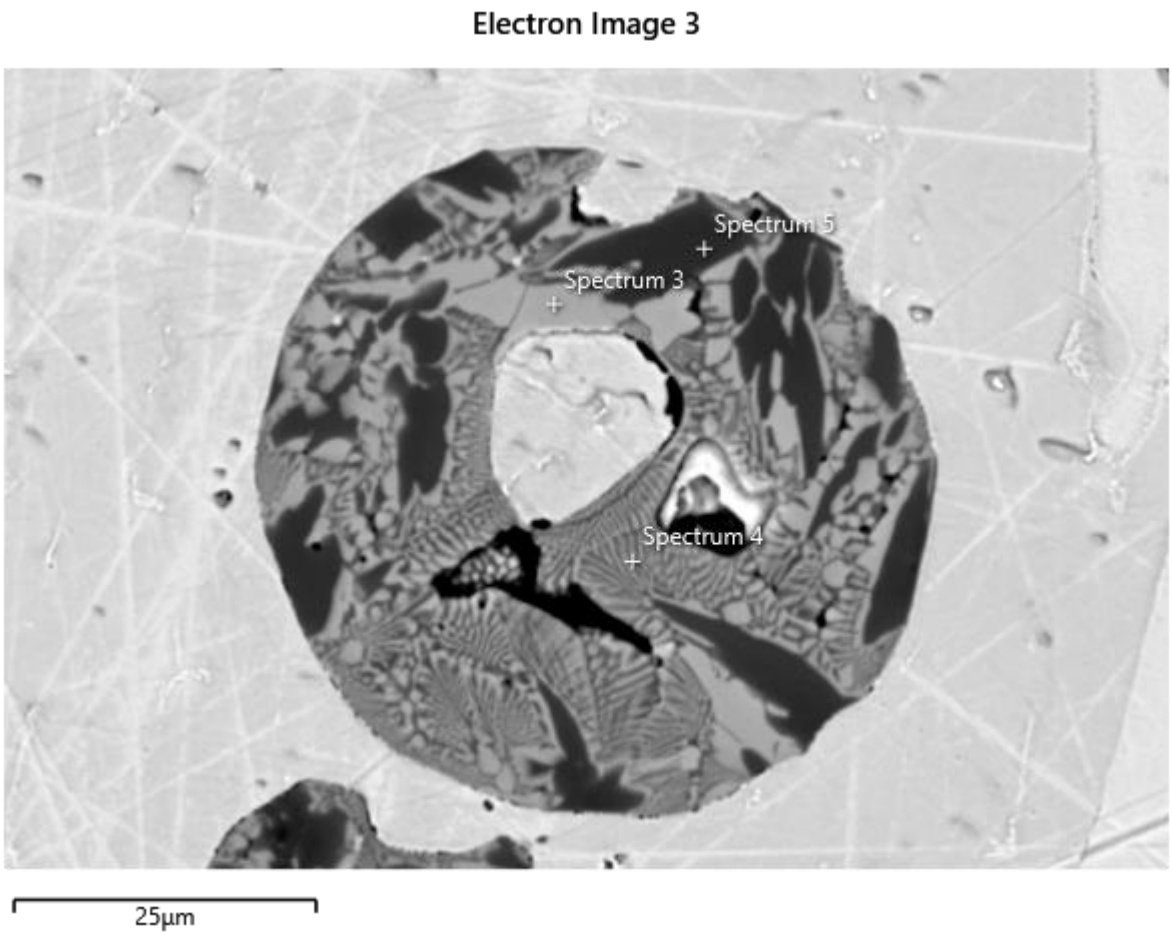

Fig. 54 – Representation of Polished EDS Point Scan Locations for Spherical Oxides

After the burn tip areas of interest were examined, the burn interface was analyzed at a higher magnification to better observe what microchemical diffusion or segregation was occurring. The interface was EDS mapped and point scans were taken on either end (burn tip side and bulk side) to compare chemistries. A line-scan was also generated starting from the bulk and traveling through the interface and into the burn tip region. This was included to observe how the intensity of the signal detected for each element varied as one travels from bulk to burn, and was documented both as a stacked overlay of all signals as well as individual spectra for each element. Examples of these analyses are shown below.

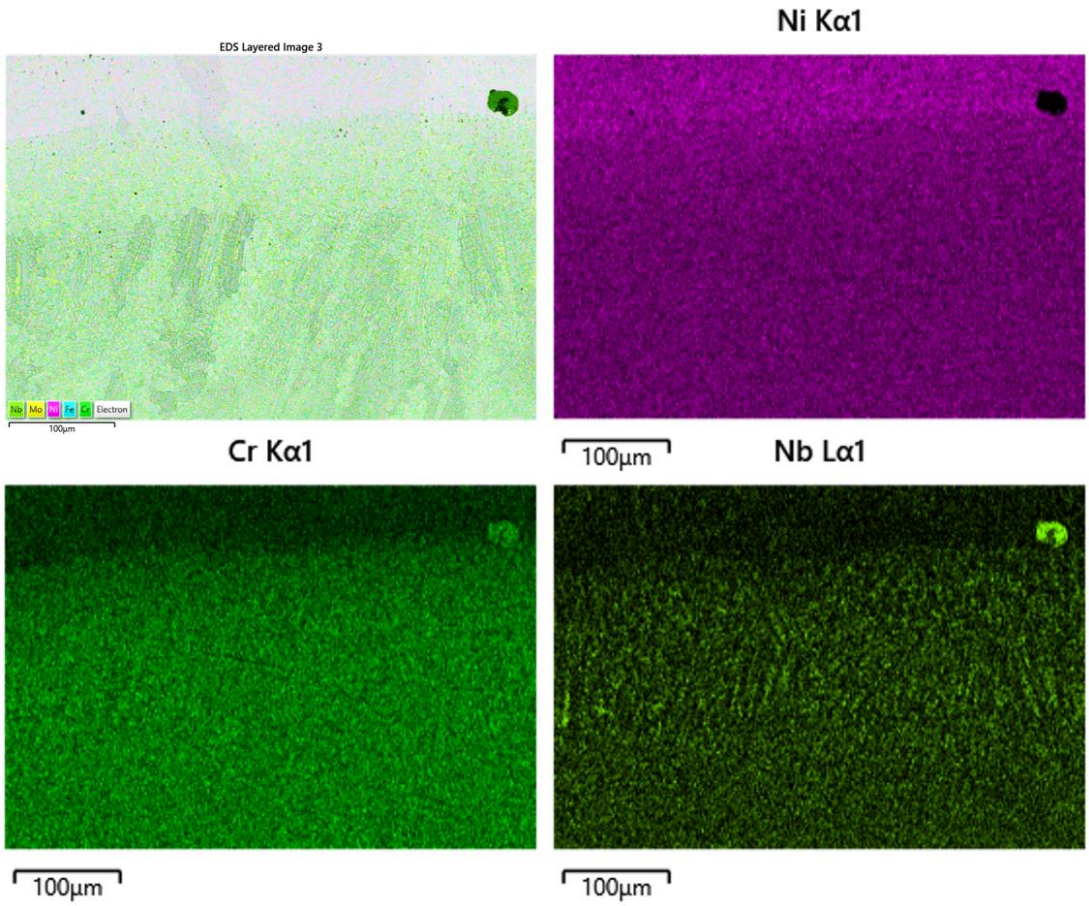

Fig. 55 – Representation of Polished Burn Transition EDS Mapping

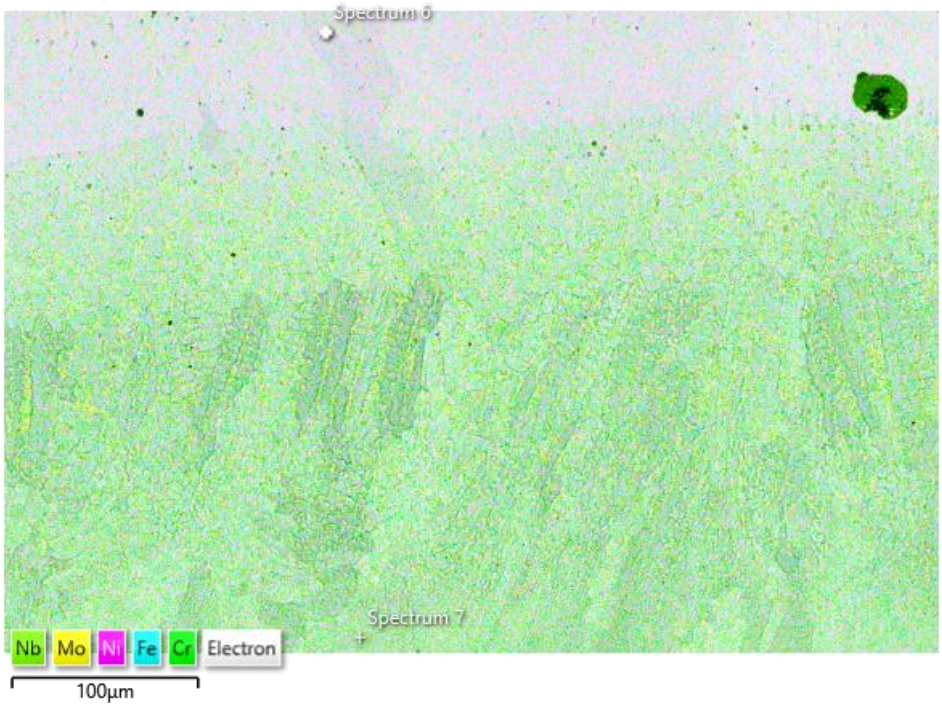

Fig. 56 – Representation of Polished EDS Point Scan Locations for Burn Interfaces

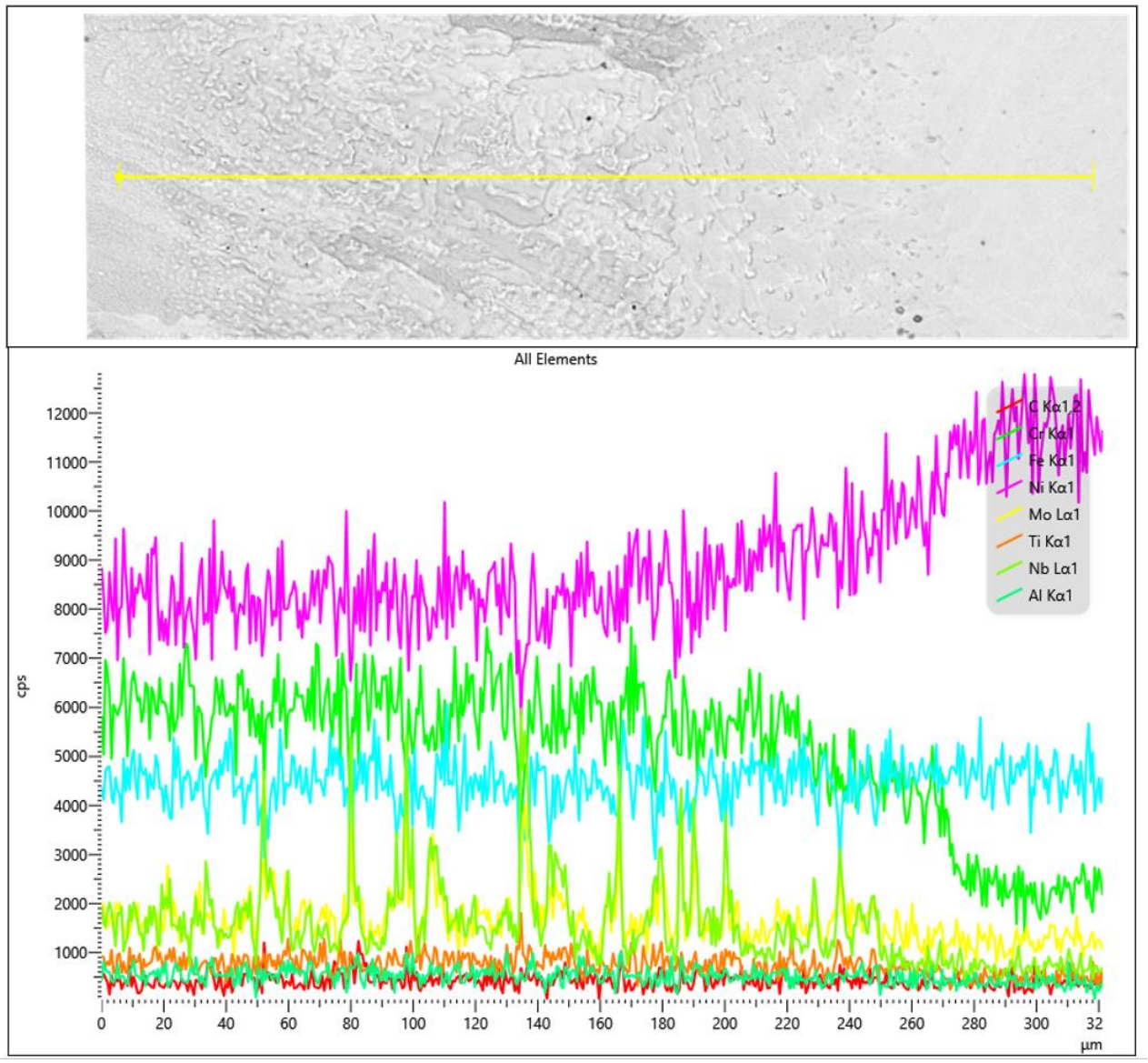

Fig. 57 - Representation of an EDS Line-Scan (Stacked) through a Polished Burn Interface

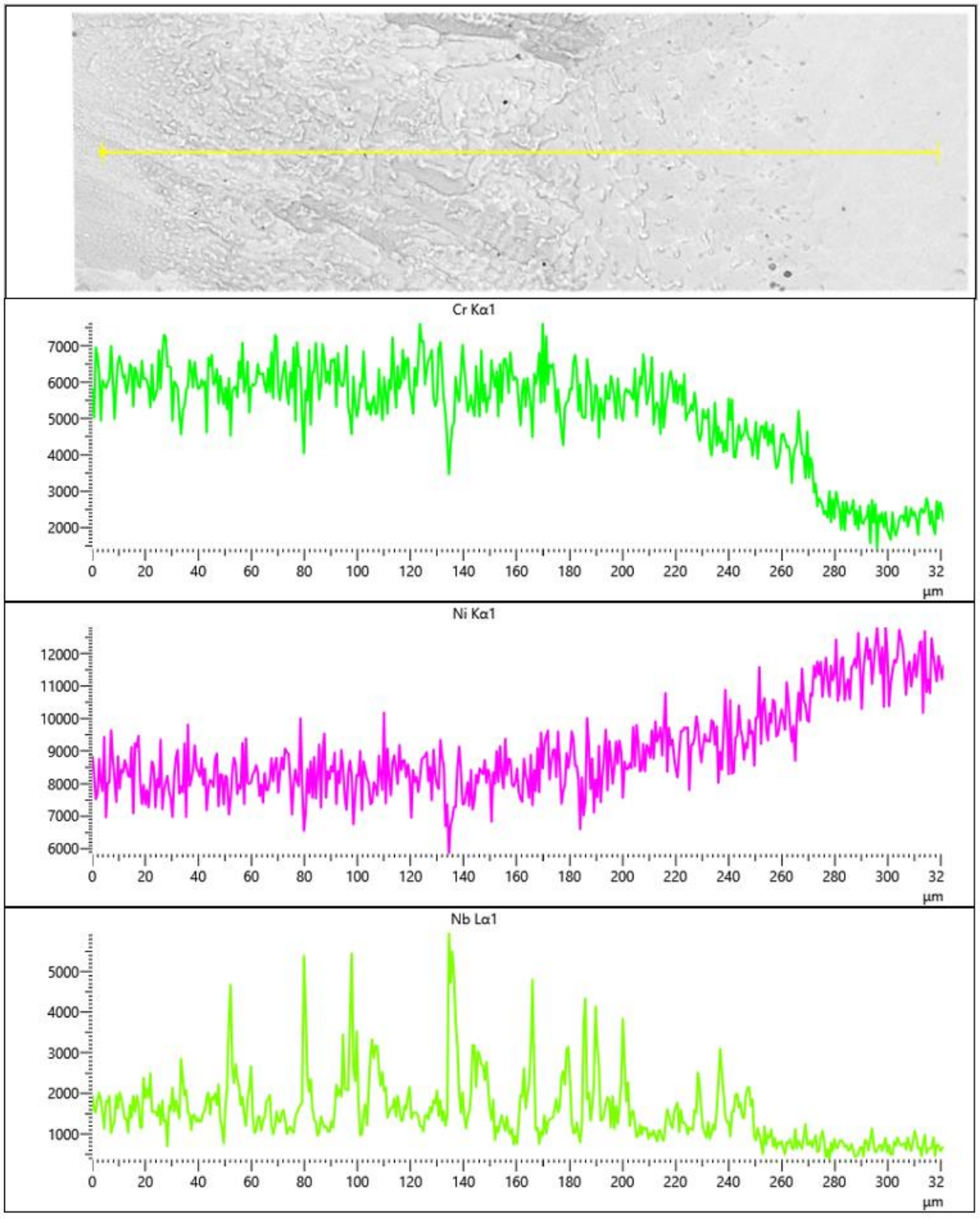

Fig. 58 – Representation of an EDS Line-Scan (Tiled) through a Polished Burn Interface

After analysis was completed on the burn interface, the bulk of each rod was subsequently EDS mapped and point scanned. The area selected for these scans was at least 1 cm away from the burn interface (in the case of very short samples) but typically even further (4 – 5 cm away) for a majority of the rods to ensure it was unaffected base material. The point analysis used in this step is what provided the data for the bulk-chemistry analysis which will be shown later in the results section. In addition, the outer surface of the rod was also EDS mapped and point scanned to see if there were any significant elemental gradients local to the surface. Examples of each of these analyses are shown below.

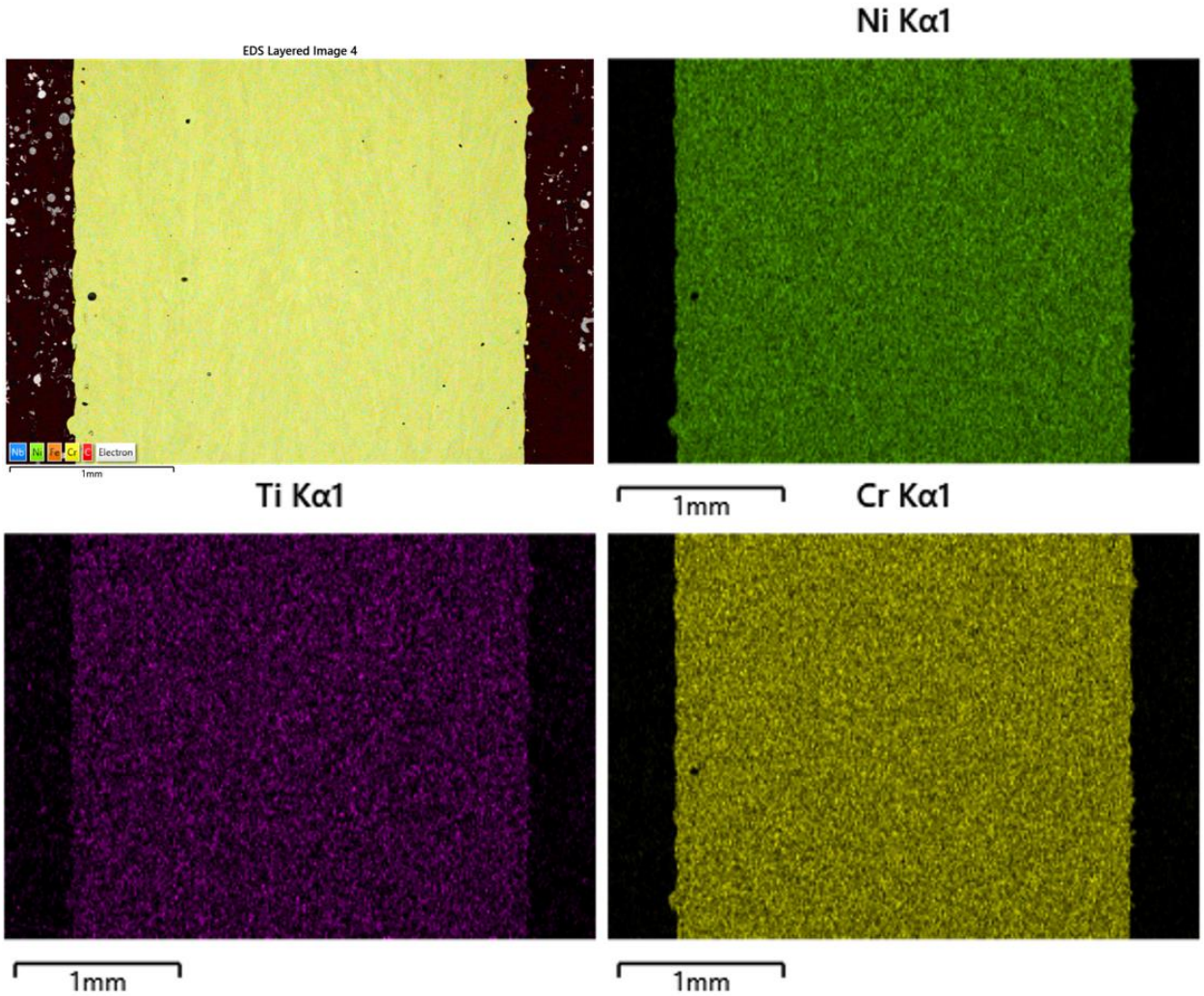

Fig. 59 – Representation of Polished Bulk EDS Mapping

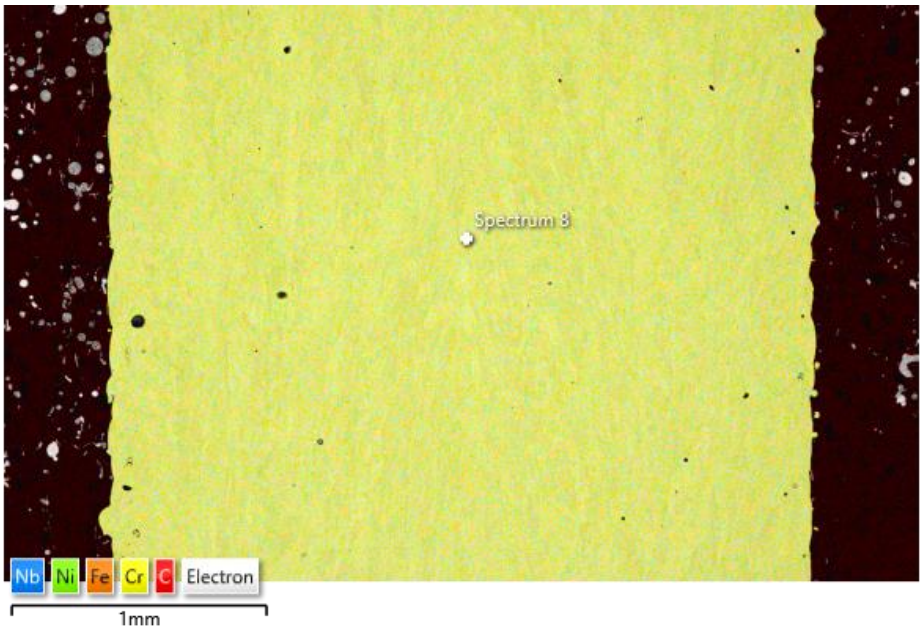

Fig. 60 – Representation of Polished EDS Point Scan Location in Sample Bulk Regions

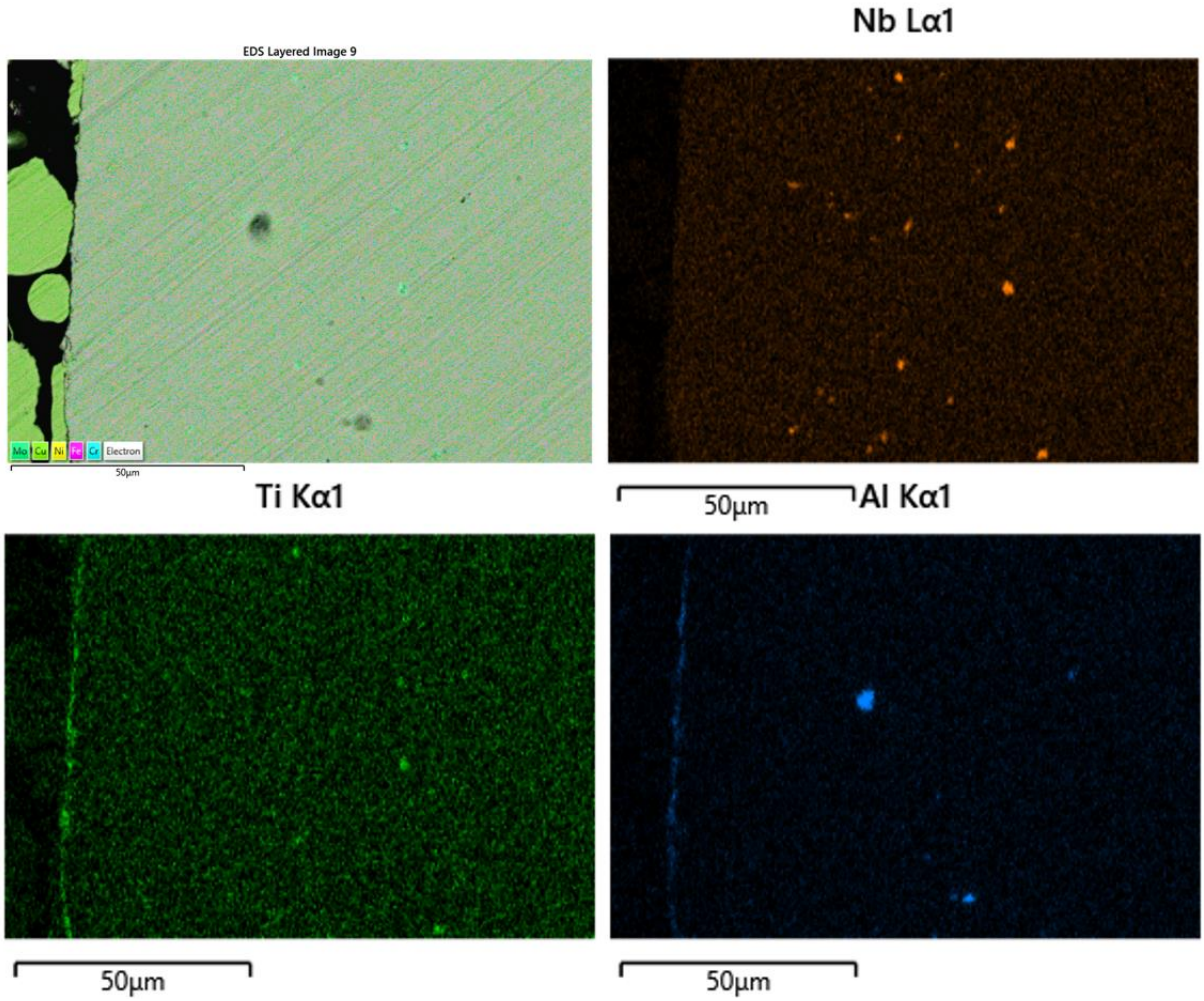

Fig. 61 – Representation of Polished Outer Surface EDS Mapping

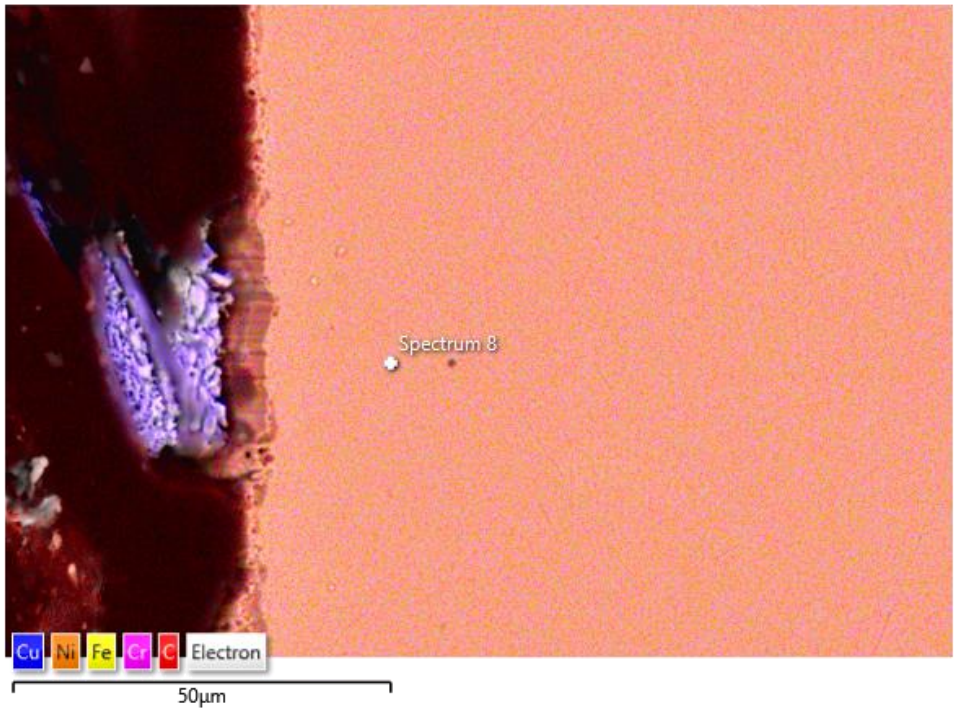

Fig. 62 – Representation of Polished EDS Point Scan Location for Outer Surface Regions

Table 13 – Polished Energy Dispersive Spectroscopy Analysis Schedule

Polished Energy Dispersive Spectroscopy		
Region:	Analysis Method	Magnification:
Burn Tip	Map	35x
	Point Scan	35x
Burn Tip Spherical Oxides	Map	Varies
	Point Scan	Varies
Burn Interface	Map	250x
	Point Scan	250x
	Line Scan (Stacked)	250x
	Line Scan (Tiled)	250x
Bulk	Map	35x
	Point Scan	35x
Bulk Outer Surface	Map	1000x
	Point Scan	1000x

X-Ray Diffraction

Following all microscopy and energy dispersive spectroscopy, x-ray diffraction (XRD) was conducted on all of the rods in their bulk and heat affected regions. This was to confirm the differences in surface structure/phases between the two areas for each sample. The instrument used was a Bruker D8 Discover diffractometer with the following parameters:

1. Scan speed: 0.3 seconds
2. Step size: 0.02 degrees
3. Slit size: 0.6 mm
4. Columnator: 1 mm
5. Range: 20 – 100 degrees

The approximate duration for each scan was 21 minutes, and again was conducted twice (both in the bulk of each rod as well as the heat affected zone). An illustration of these locations is shown below.

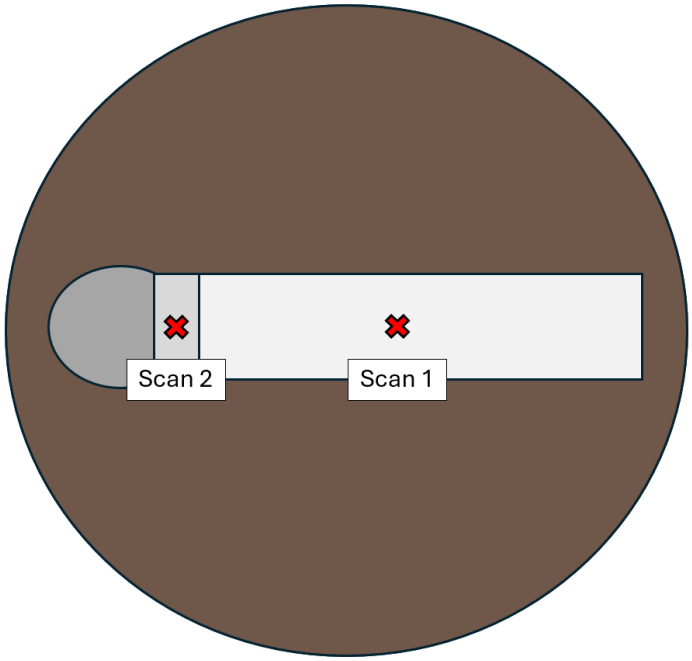

Fig. 63 – Graphical Representation of XRD Scan Locations on Sample Set 1 Rods

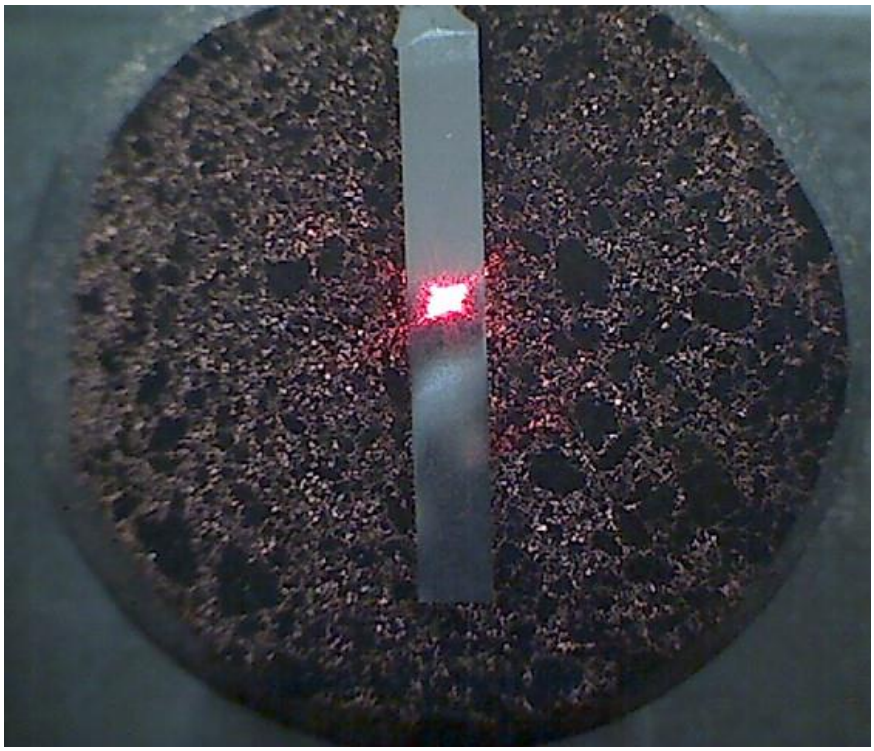

Fig. 64 – Representation of Bulk XRD Scan Location

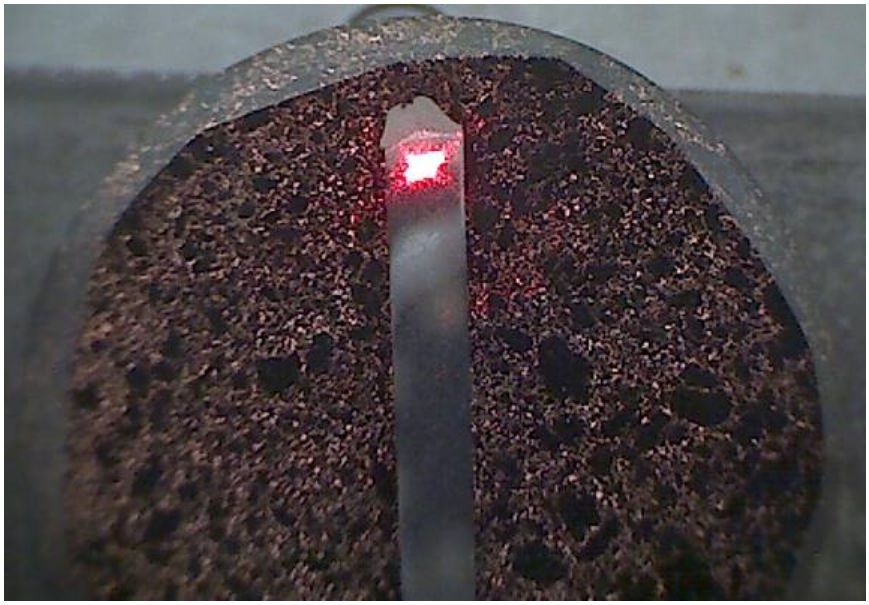

Fig. 65 – Representation of Heat Affected Zone XRD Scan Location

SAMPLE SET 2 PROCEDURES

The rods observed in Sample Set 2 were selected for transmission electron microscopy and atomic-level energy dispersive spectroscopy. In order to prepare adequate lamella at the University of Texas at Austin's Texas Materials Institute, these samples needed to be sectioned and polished to enable focused ion-beam preparation and subsequent analysis. The following sections will describe in greater detail the procedure used to prepare these samples as well as the steps taken at the Texas Materials Institute to image and characterize them from an elemental standpoint.

Rod Sectioning and Polishing

The first step in preparing the sample set 2 rods for TEM was to precision section the desired area from the bulk sample rod such that the cut surface intersected the burn interface cross section. This was to provide a fairly smooth surface (approximately 600 grit polish) which the TEM lamellae could be harvested from. The saw used was a Pace Technologies® PICO-175 precision cutter with a hard non-ferrous cutting blade equipped.

After sectioning, the burn tips were polished at a low speed on 240 grit paper so that the bottom surface (opposite the precision sectioned surface) was flat and could be easily adhered to a carbon taped SEM stage as this was necessary for subsequent focused ion-beam preparation. An illustration demonstrating this process is shown below.

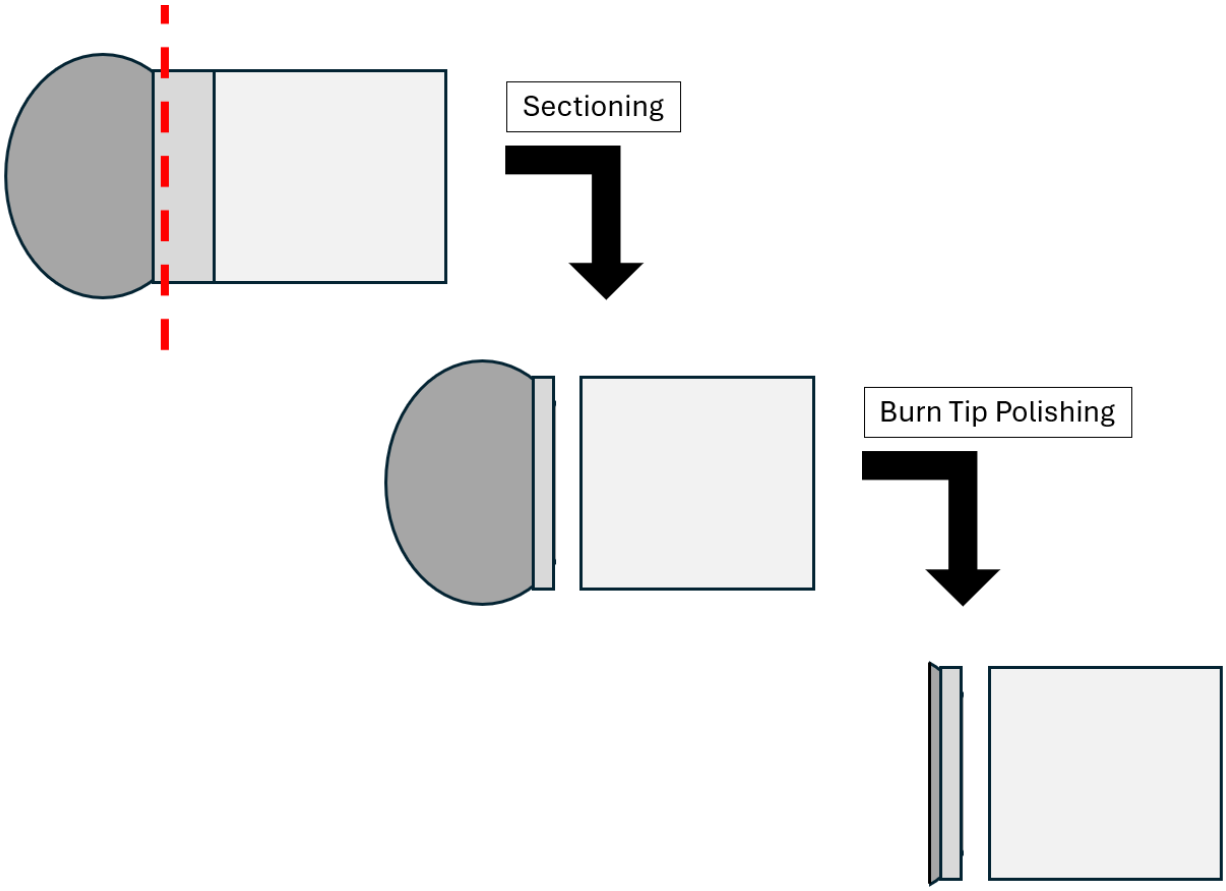

Fig. 66 – Graphical Representation of Sample Set 2 Rod Sectioning and Polishing

Focused Ion Beam Preparation

Once samples were adequately polished, they were shipped to the University of Texas at Austin's Texas Materials Institute (TMI) so that electron transparent lamellae could be produced from the precision sectioned surface of the samples (as this cross section is representative of the burn interface). The instrument used was a Fisher Scientific® Scios 2HiVac Dual Beam FIB/SEM, which would mill out a rectangular lamella from the polished surface, then being micro-welded to a probe would be lifted out of the surface and subsequently ion-milled before deposition onto a TEM grid. The approximate dimensions of these lamellae were 8 µm length x 7 µm width x 2 µm thickness (this thickness then being reduced to electron transparent dimensions via ion milling). This process is demonstrated below through images captured during fabrication.

Fig. 67 – Image showing Precision Sectioned side (left) and Polished Burn Tip side (right) of a Sample Set 2 Rod

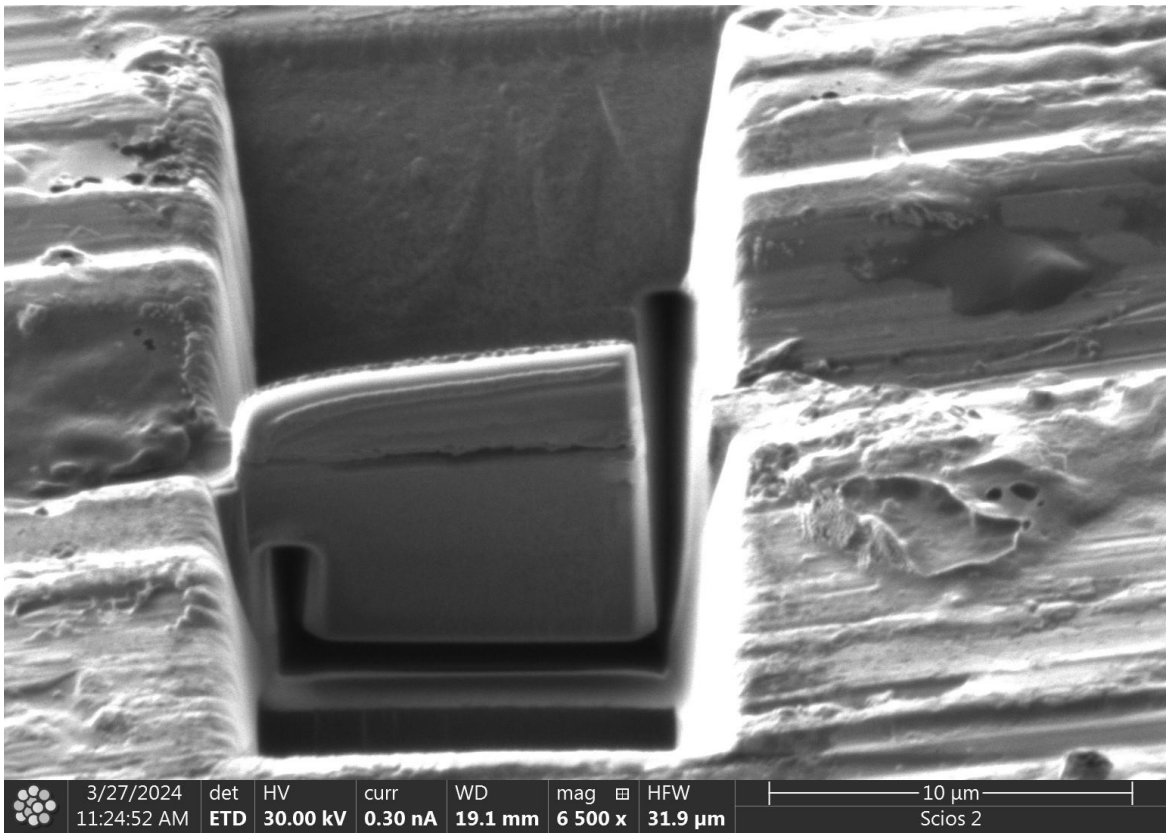

Fig. 68 – Micrograph Displaying Surface a Lamella was Milled from

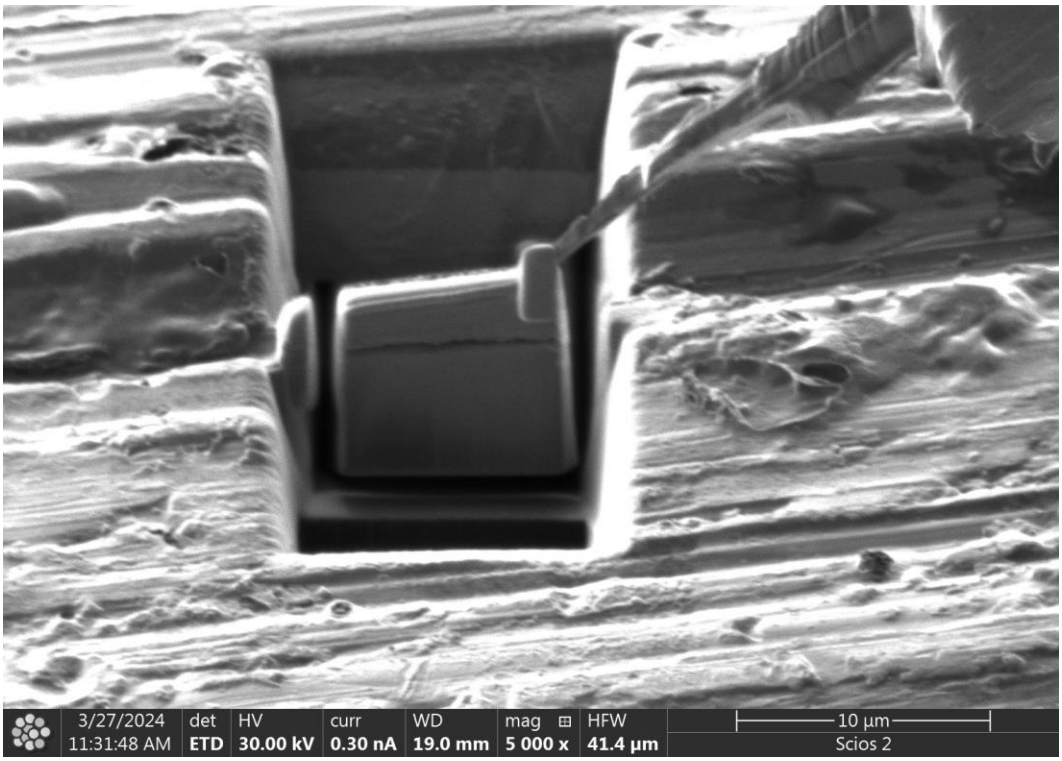

Fig. 69 – Micrograph Displaying a Lamella Micro-welded to a Probe for Lift-out

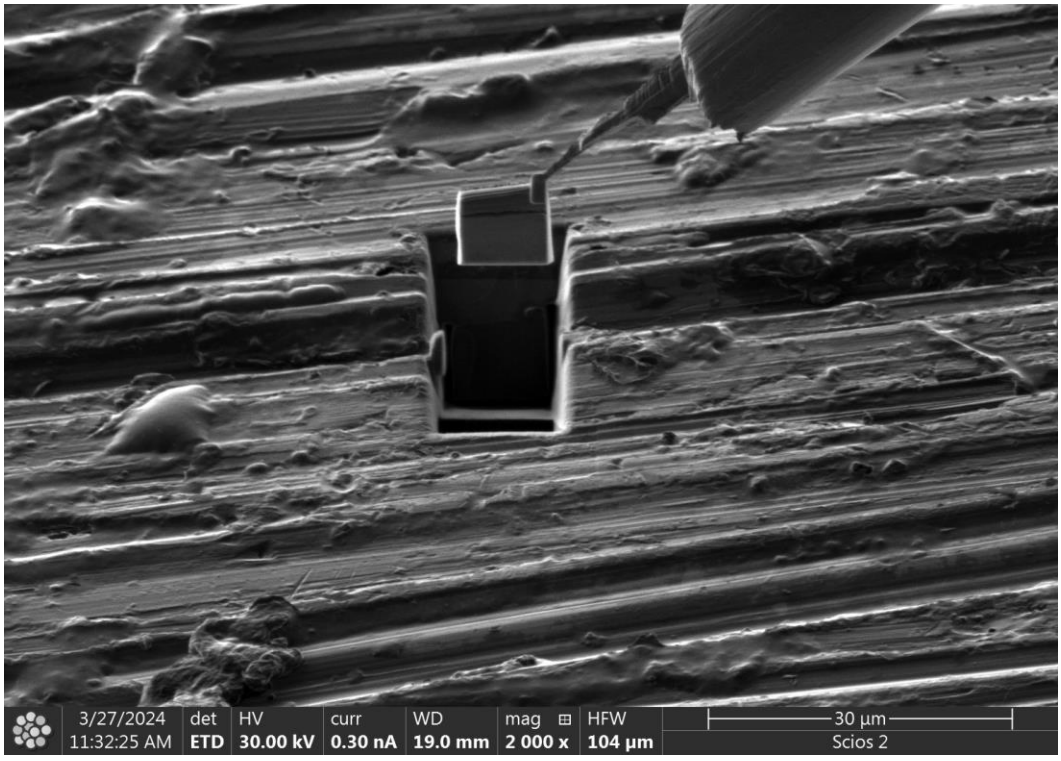

Fig. 70 – Micrograph Displaying a Lamella being Lifted-out from the Polished Surface

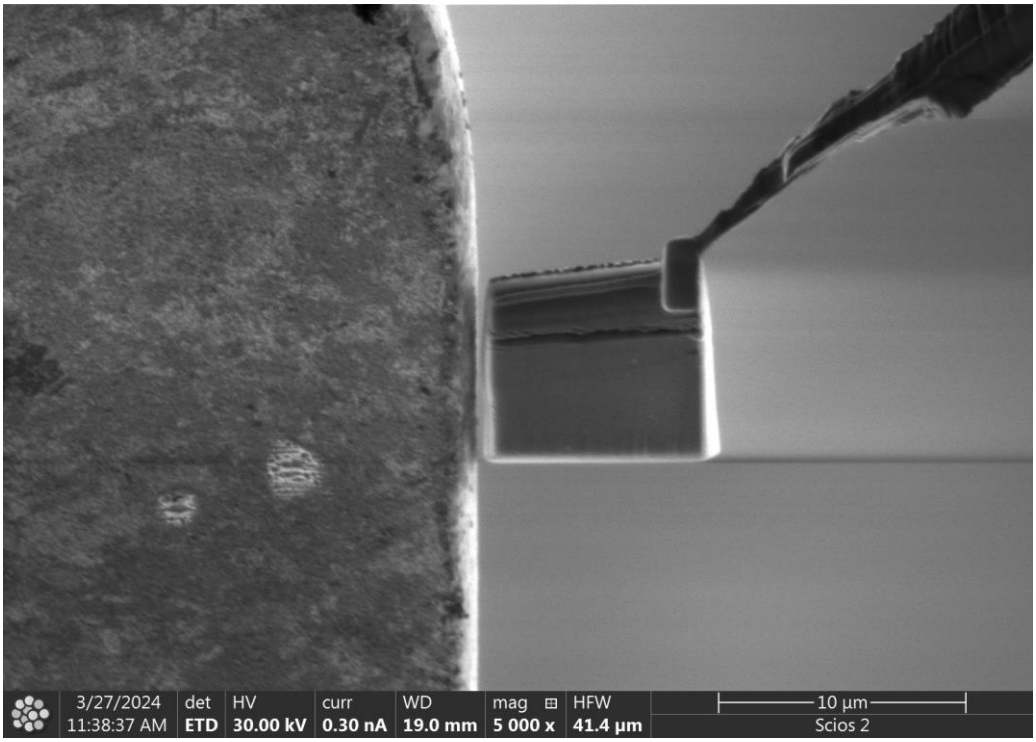

Fig. 71 – Micrograph Displaying a Lamella being attached to a TEM Grid

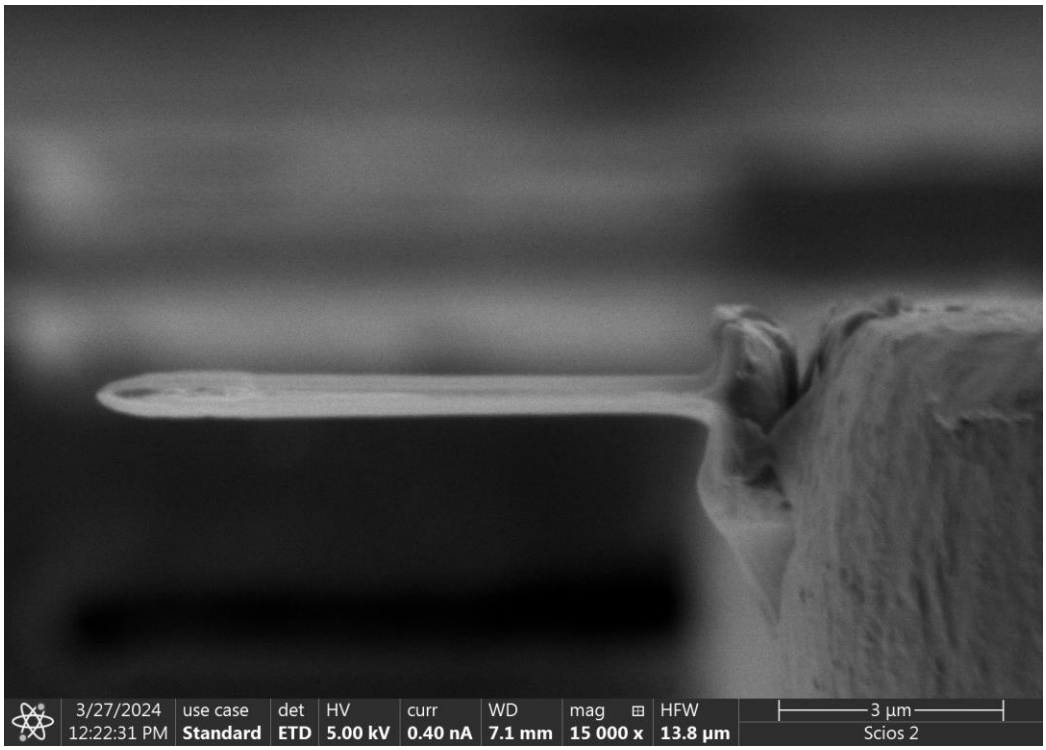

Fig. 72 – Micrograph Displaying the Electron Transparent Lamella Mounted to the TEM Grid

Transmission Electron Microscopy Imaging

Once grids were prepared for imaging, they were inserted into a JEOL NEOARM Low kV STEM Corrected microscope. Pictures were obtained with a Gatan OneView CMOS camera and in two detector modes to capture contrast in both the annular dark field (ADF) and annular bright field (ABF) conditions. Due to the inherently chaotic nature of the region (being an interface of burnt and resolidified metal with heat affected/recrystallized material) there was not a specific imaging schedule in place, but pictures were generally taken in the range of 600,000x to 12,000,000x magnification. The software used to view and process the images was Gatan's DigitalMicrograph platform. Efforts were made to produce images which provided a general characterization of the lamella as well as any notable features. Representative examples of images taken in the three conditions (OneView, ADF, and ABF) are shown below.

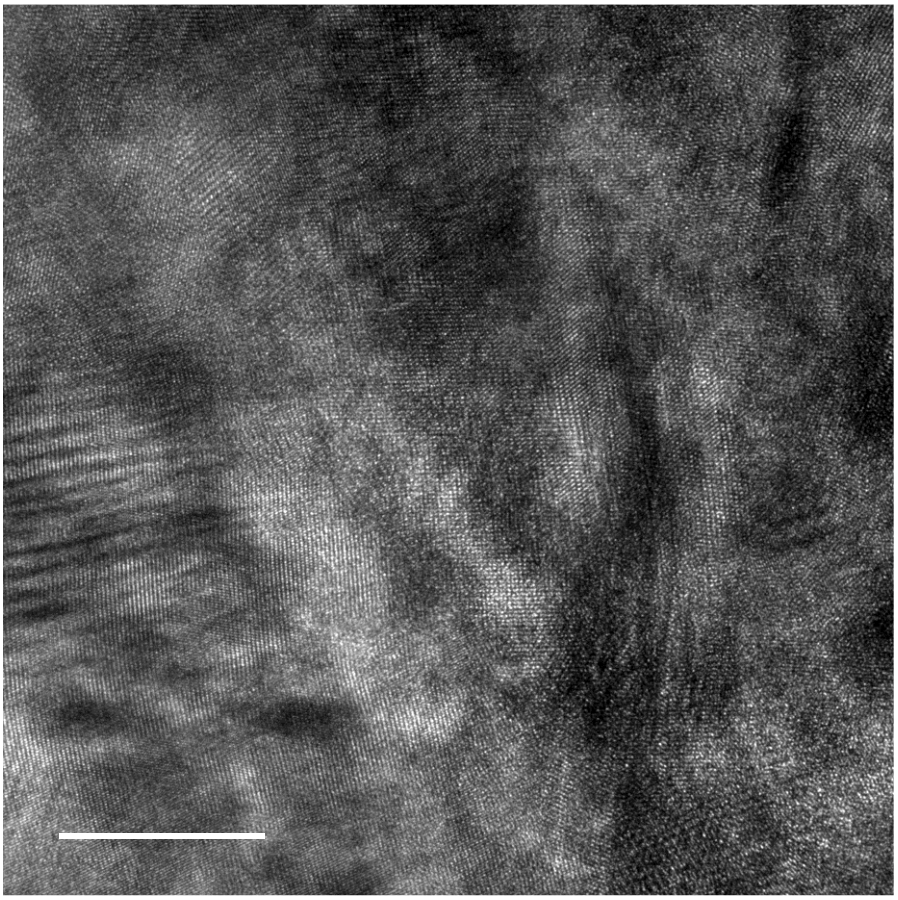

Fig. 73 – TEM Micrograph of Sample 8046 (OneView Camera) at 1,000,000x

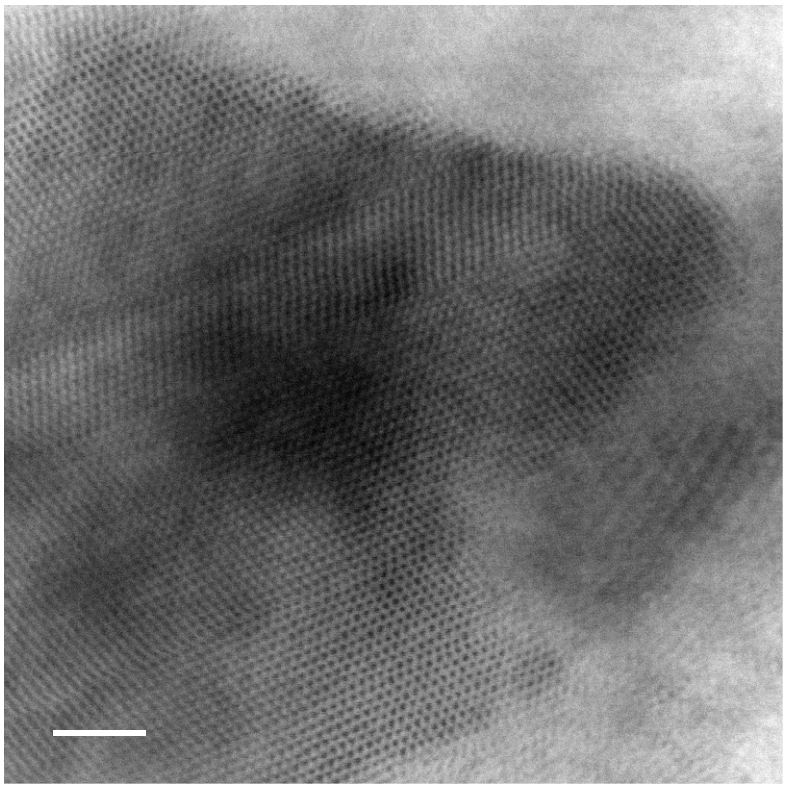

Fig. 74 – TEM Micrograph of Sample 8046 (ABF mode) at 12,000,000x

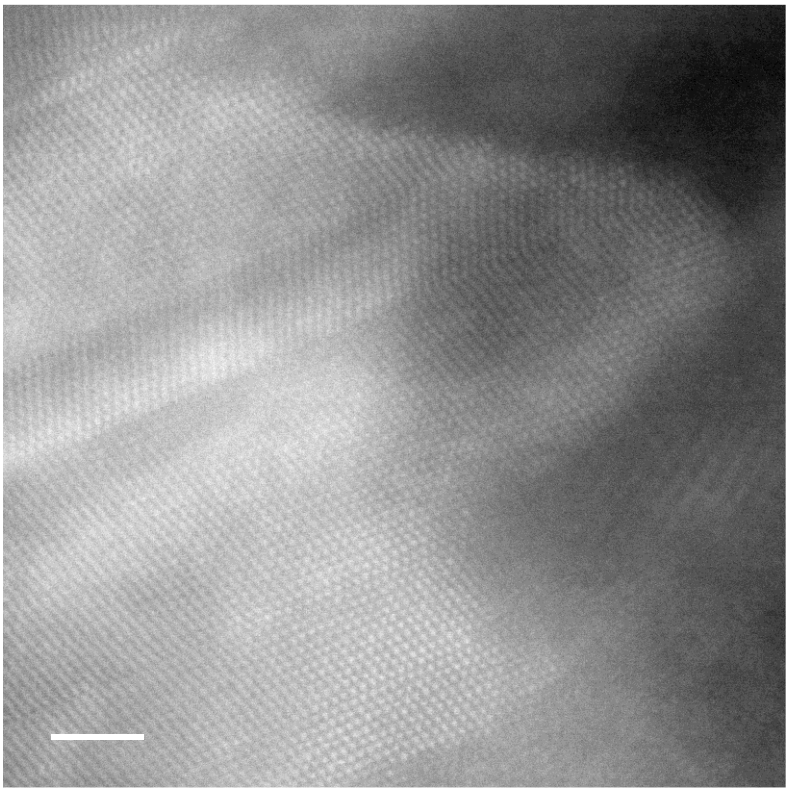

Fig. 75 – TEM Micrograph of Sample 8046 (ADF mode) at 12,000,000x

Transmission Electron Microscopy EDS

Energy dispersive spectroscopy was conducted on the TEM lamella following imaging, with the analysis also completed within the aforementioned JEOL NEOARM microscope using JEOL's proprietary large angle silicon drift EDS detector. Similar to imaging, there was not a particular schedule for analysis established between samples outside of attempting to provide a general chemical evaluation of the bulk of the lamella with more detailed observations of notable features. Data was then processed within Fischer Scientific's® Pathfinder X-Ray Microanalysis suite in order to generate spectra and elemental maps. A few representative examples are included below.

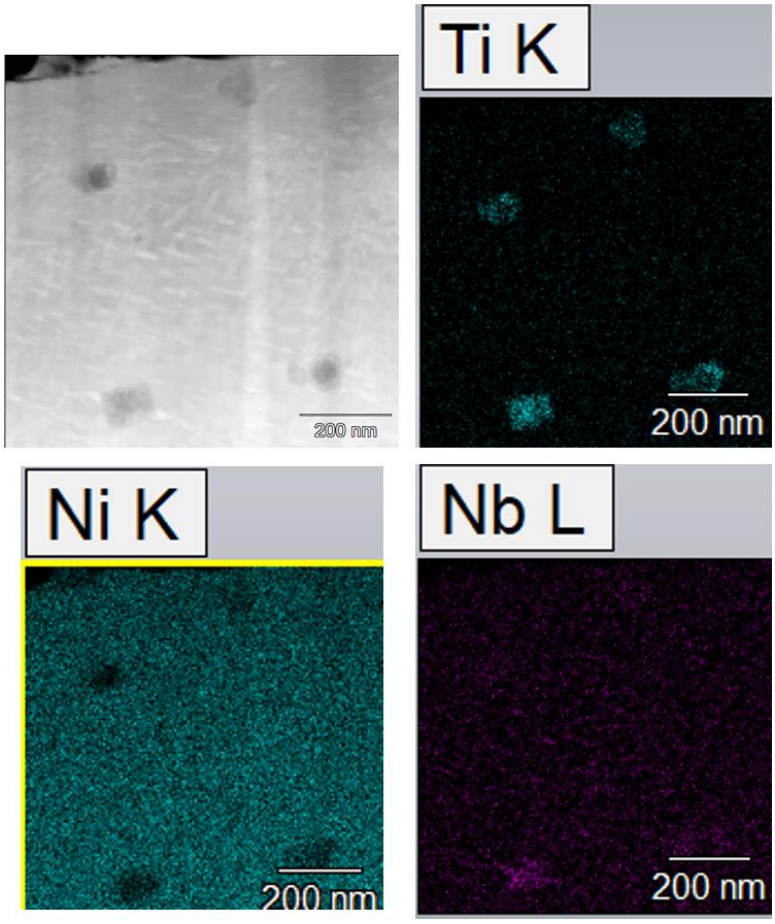

Fig. 76 – Example of TEM EDS Maps of Sample 8046

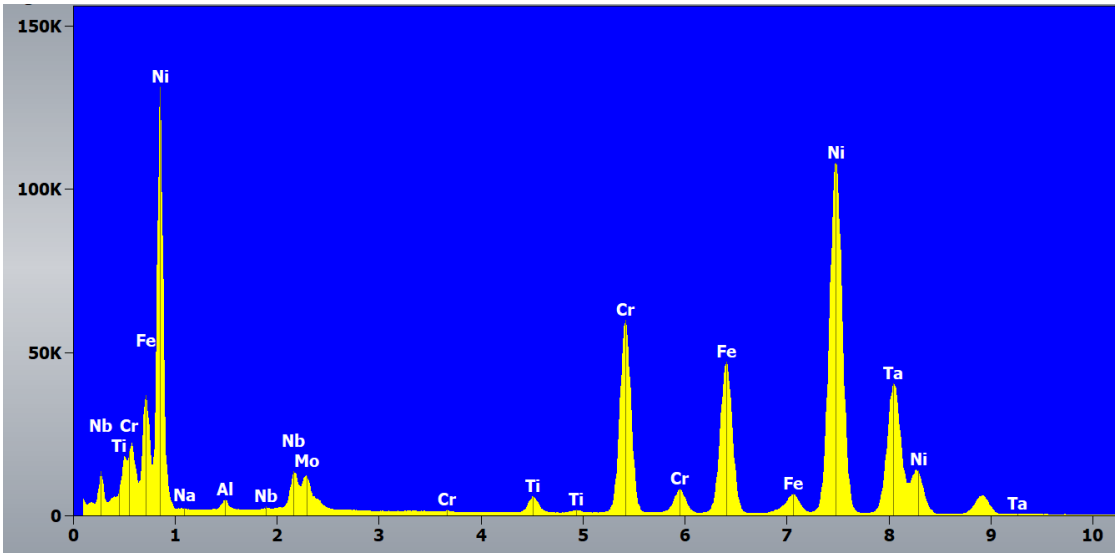

Fig. 77 – Example of TEM EDS Spectra Generated of Sample 8046

Table 14 – Example of Tabularized EDS Data for Sample 8046

	Weight %	Atom %
Ni K	47.80	46.05
Cr K	17.45	18.98
Fe K	16.37	16.58
Ta L	9.66	3.02
Al K	5.98	12.54
Ti K	2.05	2.42
Nb K	0.47	0.28
Mo K	0.22	0.13
Na K	0.00	0.00

Chapter 5: Test Results

Sample Set 1 Results

As Received Photography

Fig. 78 – As Received Photography of Samples 7670, 7676, 7679, and 8044

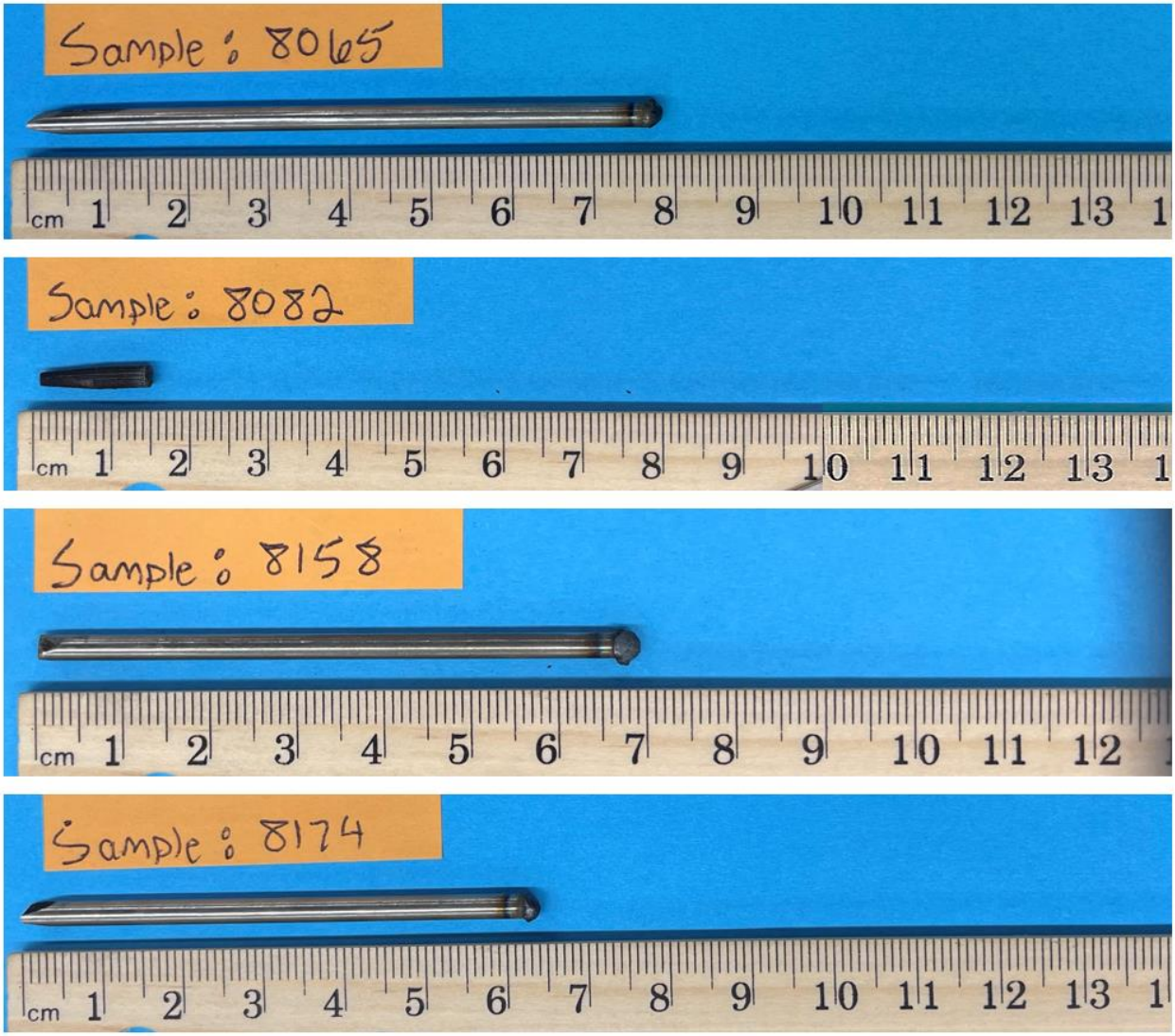

Fig. 79 – As Received Photography of Samples 8065, 8082, 8158, and 8174

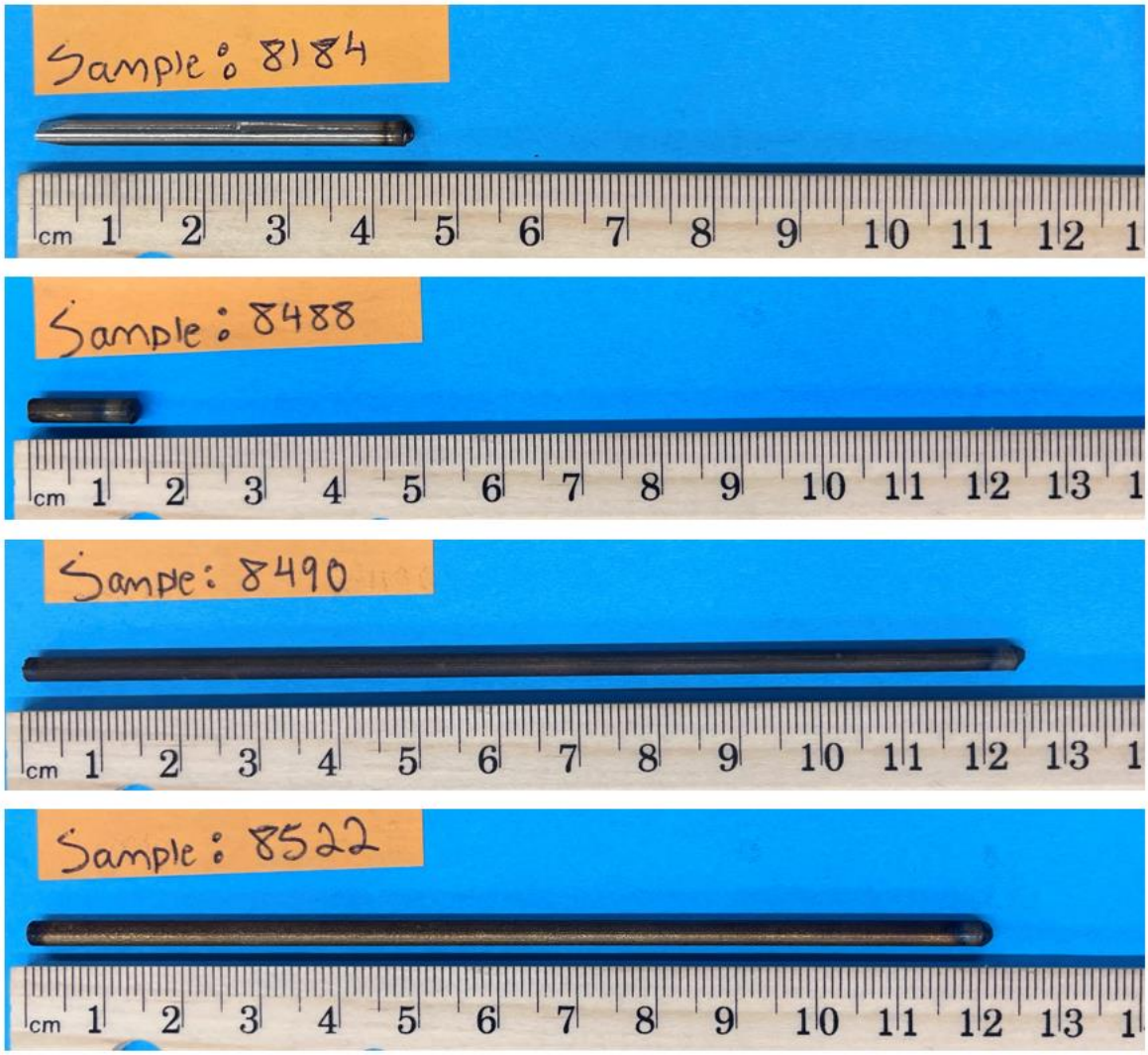

Fig. 80 – As Received Photography of Samples 8184, 8488, 8490, and 8522

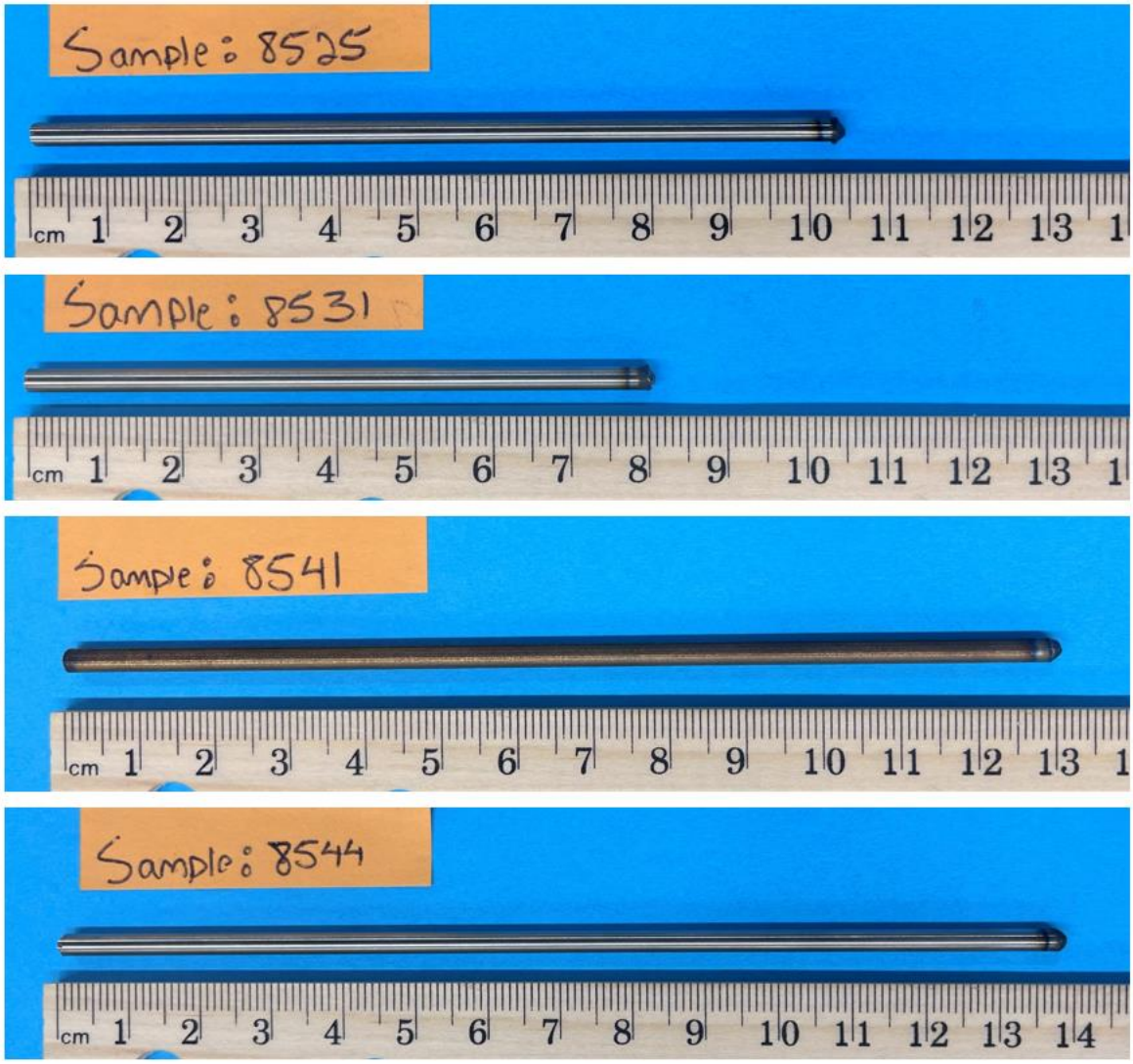

Fig. 81 – As Received Photography of Samples 8525, 8531, 8541, and 8544

Burn Tip Stereomicroscopy

Pictured below are the stereomicroscope images taken from each sample burn tip at 18.75 magnification. Several features are immediately of note, namely that the burn tip morphology and size can differ significantly but generally follows the trend of a "mushrooming" burn tip head and protruding lip of material indicative of the burn interface. Much more clearly observable now is also the variation in surface topography as samples which received machining are smoother and those which didn't are rougher. Directional printing patterns are also visible in certain samples, demonstrating variability in print parameters used during their SLM fabrication.

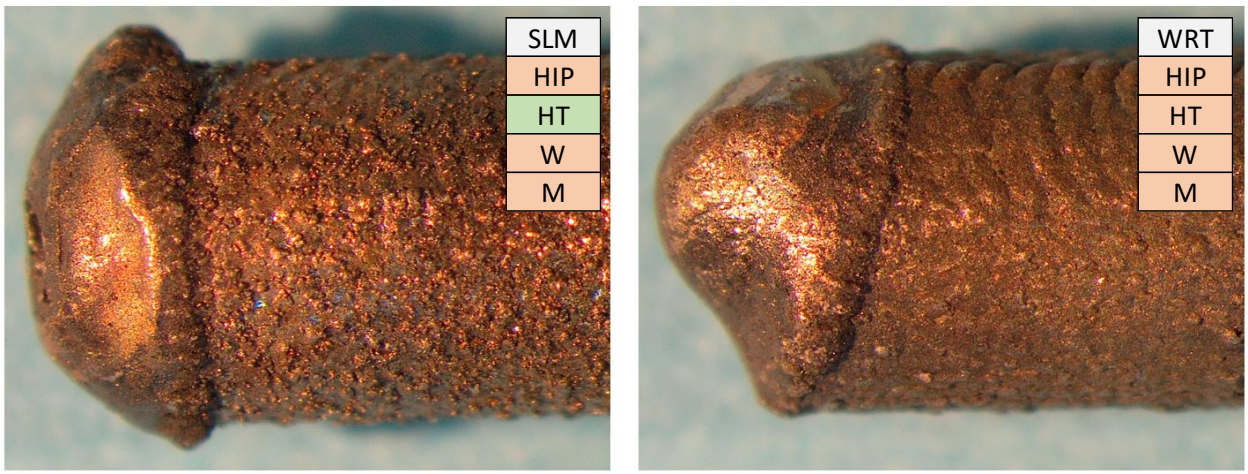

Fig. 82 – Burn Tip Stereomicroscopy of Samples 7670 and 7676

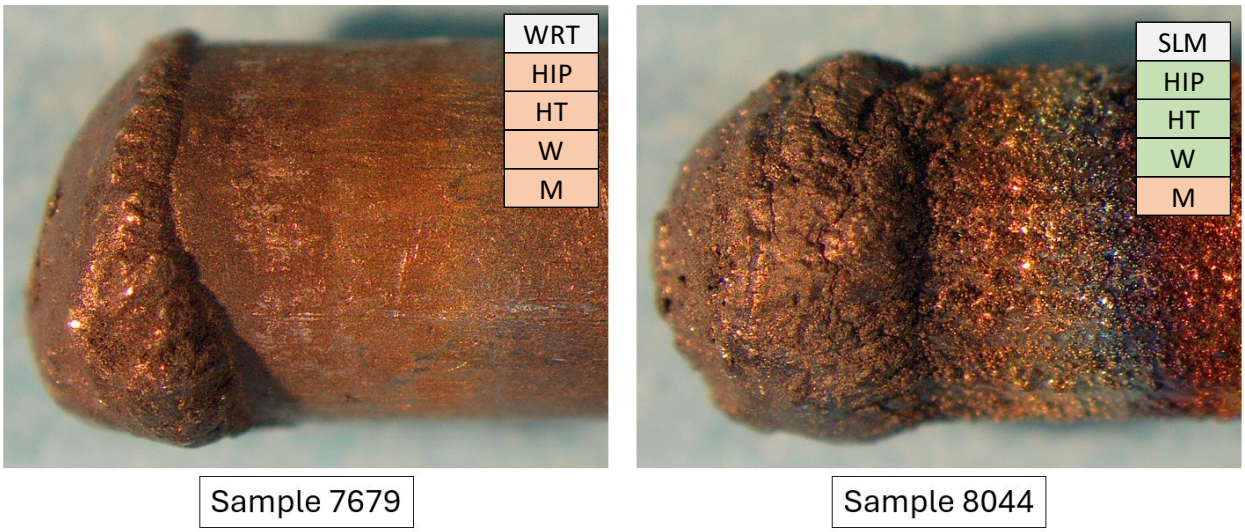

Fig. 83 – Burn Tip Stereomicroscopy of Samples 7679 and 8044

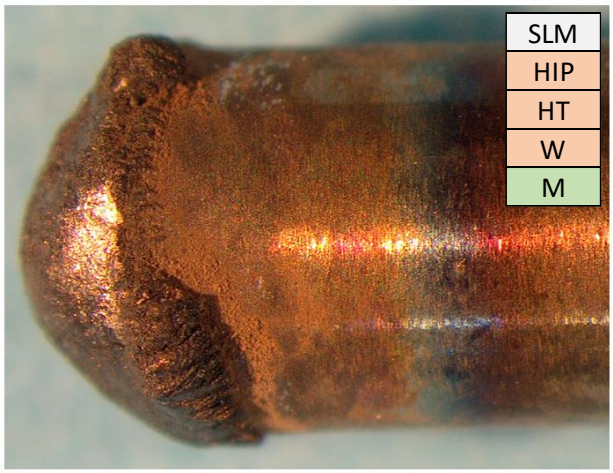

Sample 8065

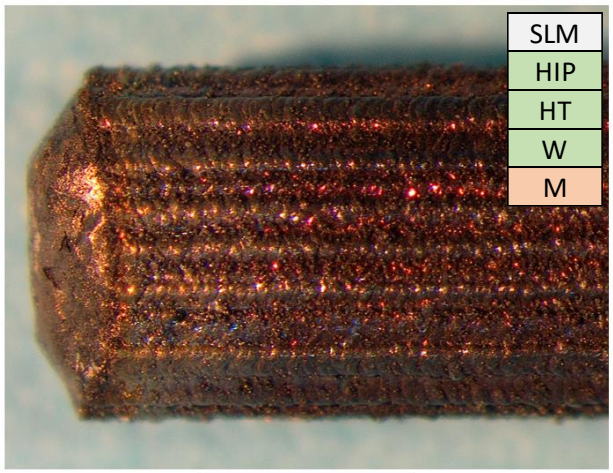

Sample 8082

Fig. 84 – Burn Tip Stereomicroscopy of Samples 8065 and 8082

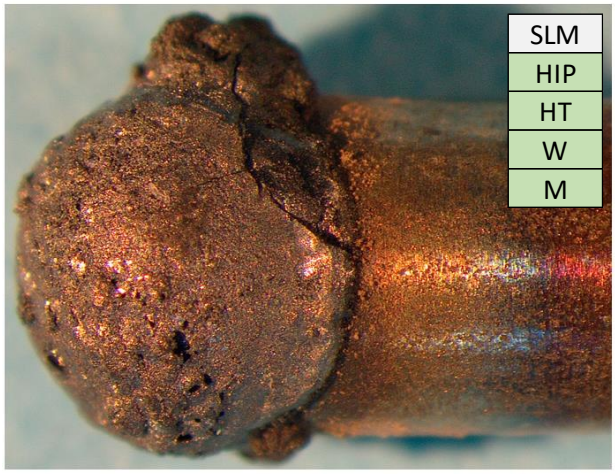

Sample 8158

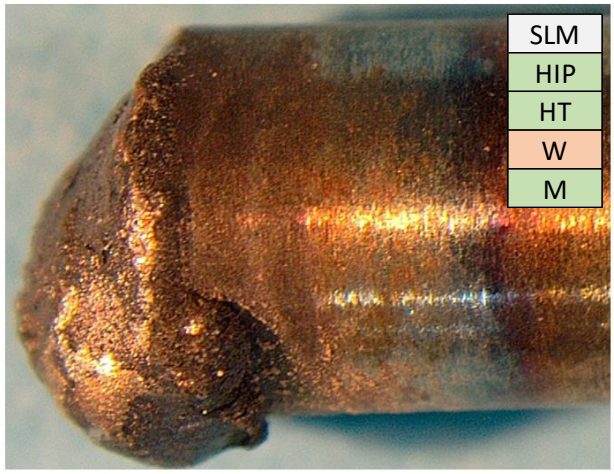

Sample 8174

Fig. 85 – Burn Tip Stereomicroscopy of Samples 8158 and 8174

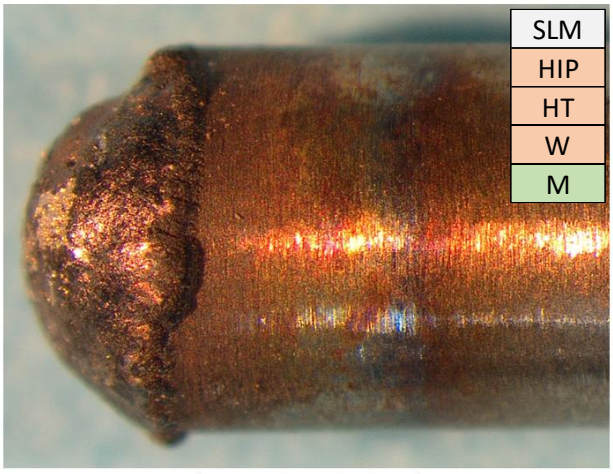

Sample 8184

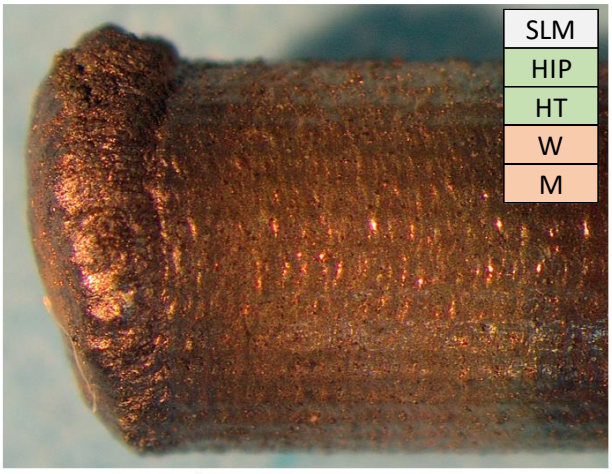

Sample 8488

Fig. 86 – Burn Tip Stereomicroscopy of Samples 8184 and 8488

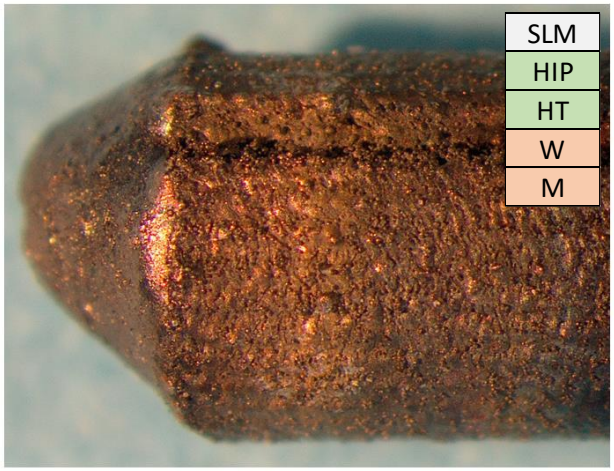

Sample 8490

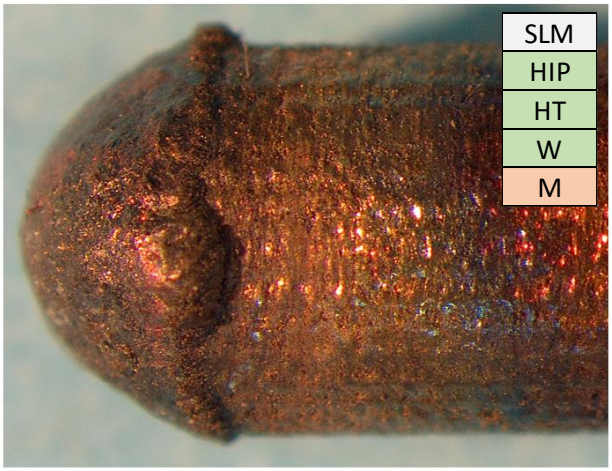

Sample 8522

Fig. 87 – Burn Tip Stereomicroscopy of Samples 8490 and 8522

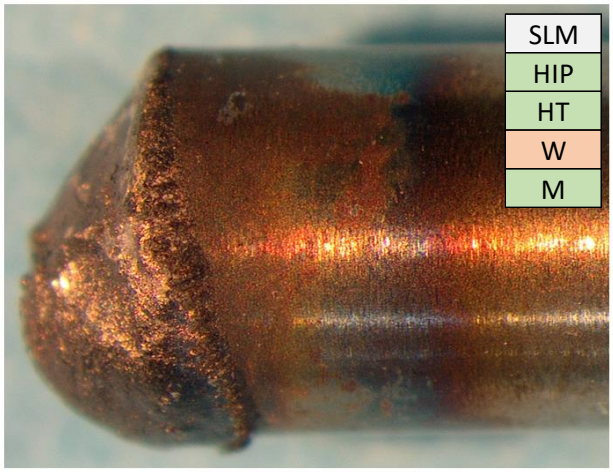

Sample 8525

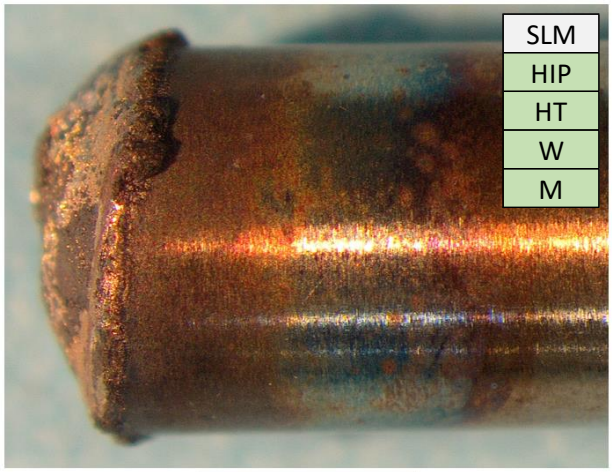

Sample 8531

Fig. 88 – Burn Tip Stereomicroscopy of Samples 8525 and 8531

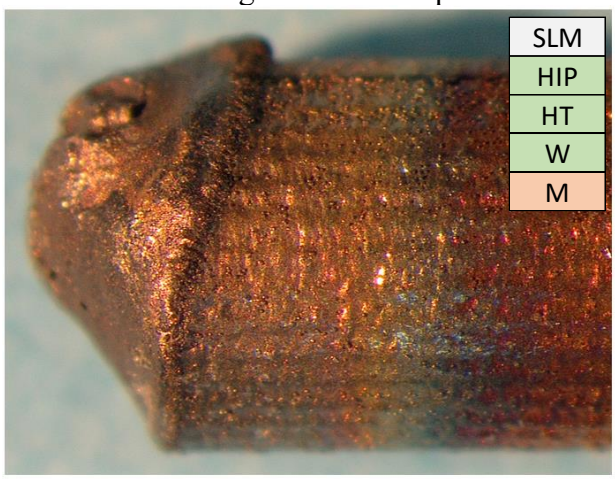

Sample 8541

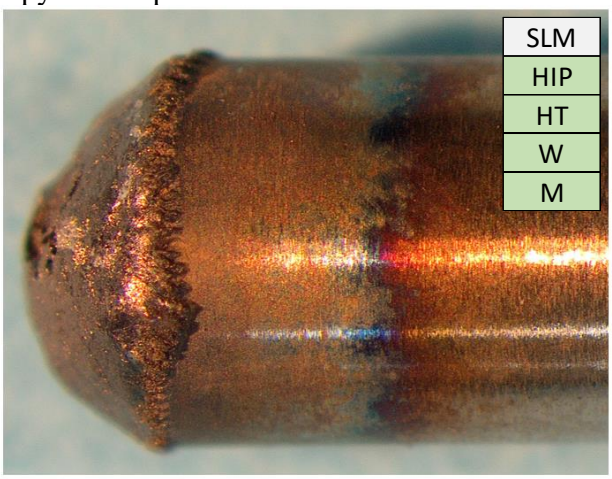

Sample 8544

Fig. 89 – Burn Tip Stereomicroscopy of Samples 8541 and 8544

As-Received Scanning Electron Microscopy

As mentioned above in the procedure section, attention was focused on three regions of interest during as-received SEM analysis – the burn tip, burn interface, and bulk. With regards to sample burn tips, images were collected at 35x and as such largely display the same characteristics seen during stereomicroscopy. The primary purpose of these obtaining these micrographs was for documentation and additional points of reference for the chemical mapping described below, for this reason they won't be referenced heavily here but several examples are included to demonstrate some of the variabilities observed during this step of analysis.

Perhaps the most easily observable difference between the sample burn tips is their shape and size, which can differ drastically. For some samples (like 8082) the burn tip is relatively flat and shallow, in contrast to others (such as 8158) which have large bulbous burn tips that likely contain a considerable volume of residual oxide from testing.

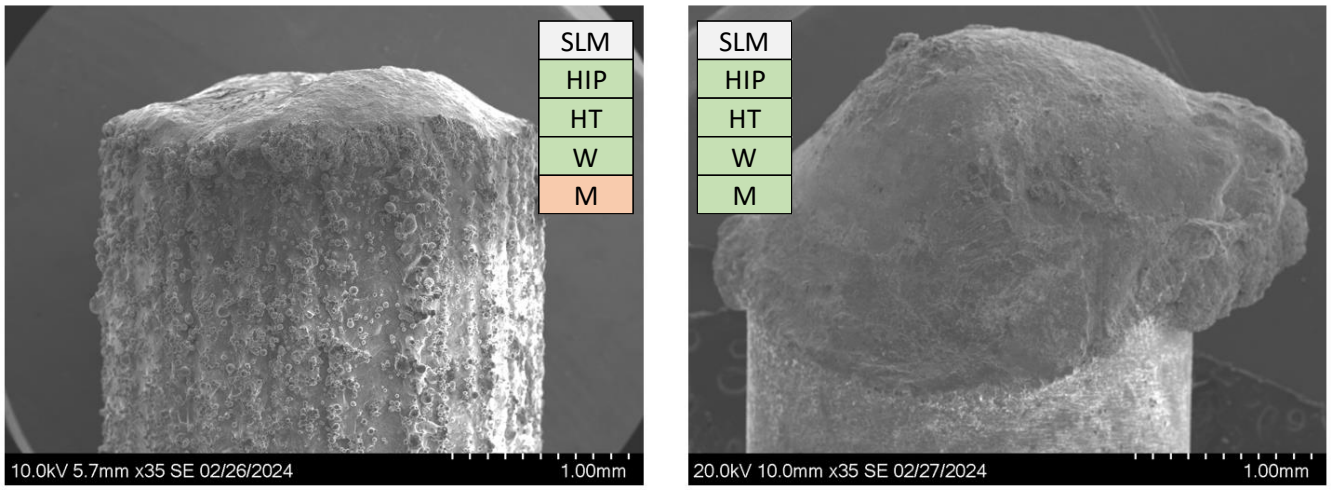

Fig. 90 – As Received Burn Tip SEM Micrographs of Samples 8082 and 8158 (35x)

Additionally, the burn interface itself is not always homogenous in terms of how straight or flat it is relative to the rod. Though most of the samples display burn interfaces which are basically perpendicular to the rod orientation, a few (such as 7676, 7679, 8525, and 8541) show interfaces that are much more significantly slanted or leaning. In the case of samples such as these, the burn interface was able to travel up the rods in a non-equilibrium fashion.

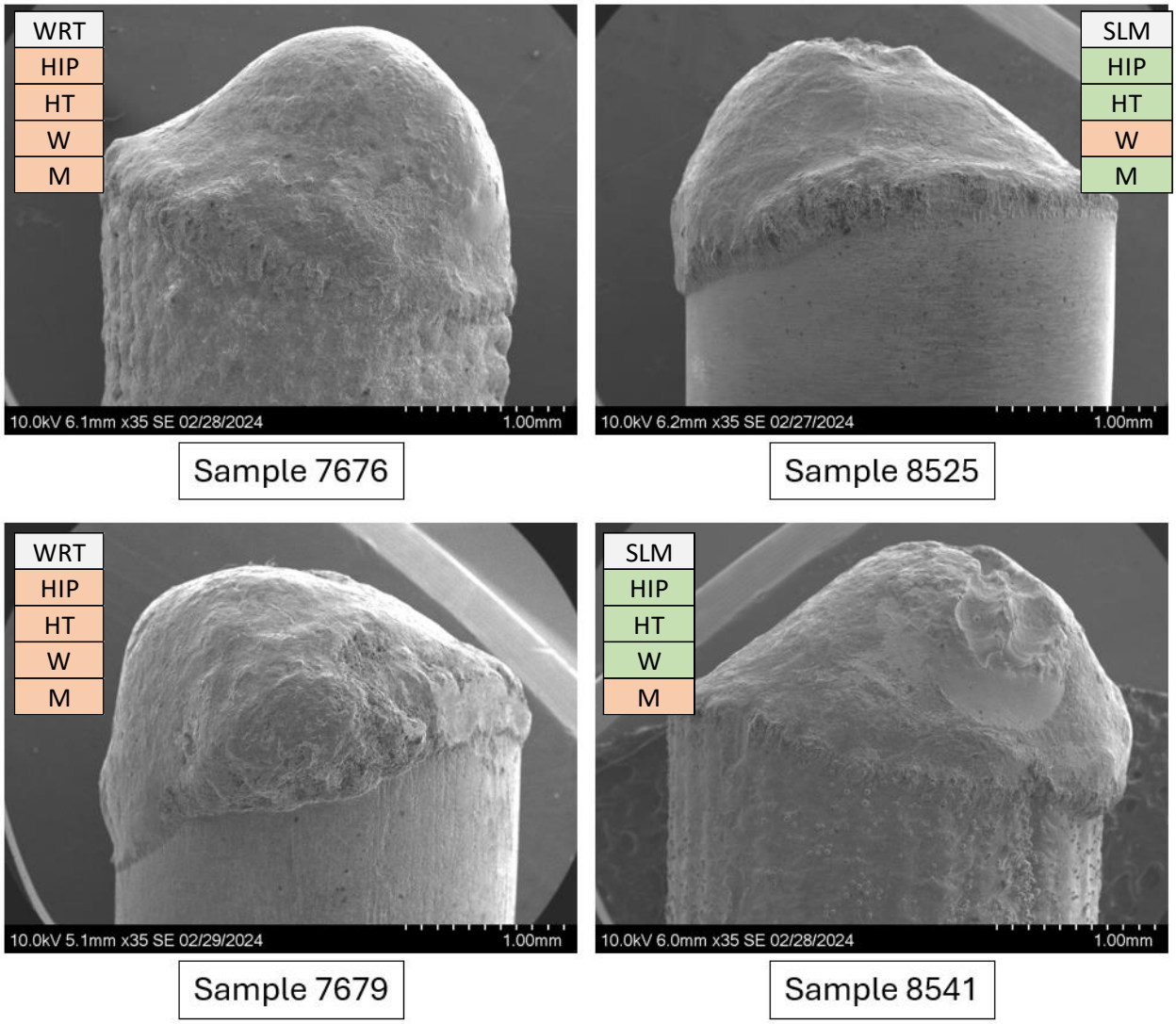

Fig. 91 – As Received Burn Tip SEM Micrographs of Samples 7676, 8525, 7679, and 8541 (35x)

The bulks of each sample rod were also imaged, and tended to demonstrate surface finishes which align with post-processing (i.e. smooth for those which were machined, rougher for those without, varying concentrations of unsintered particulate, compacted features following hot isostatic pressing, etc.). Generally speaking, the surfaces could be characterized within two primary groups – those that were smooth or obviously machined, and those which had particles and printing seams visible.

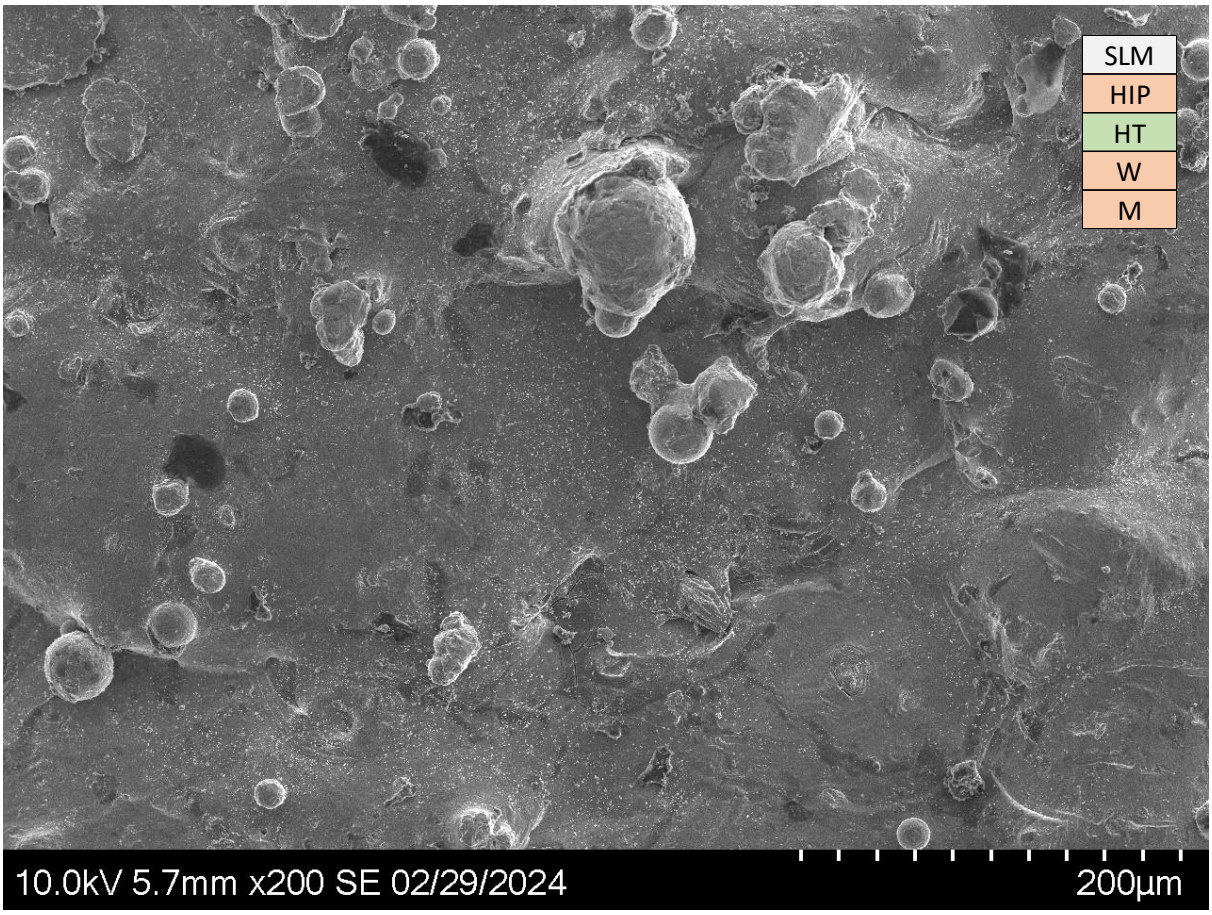

Fig. 92 – As Received Bulk SEM Micrograph of Sample 7670 (200x)

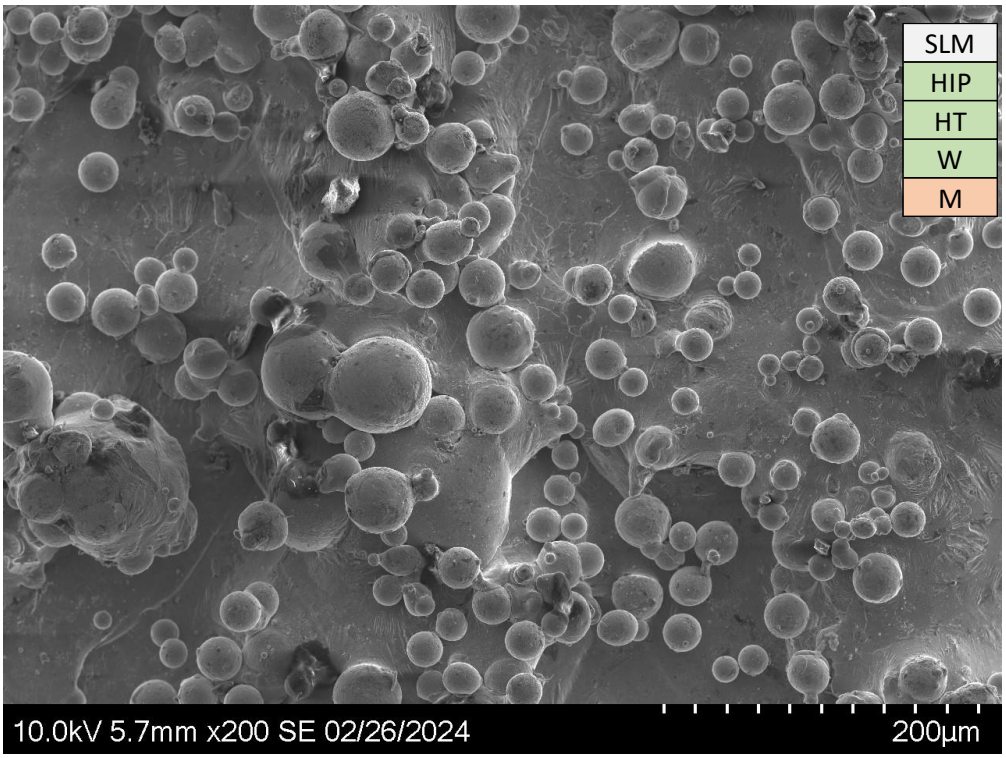

Fig. 93 – As Received Bulk SEM Micrograph of Sample 8044 (200x)

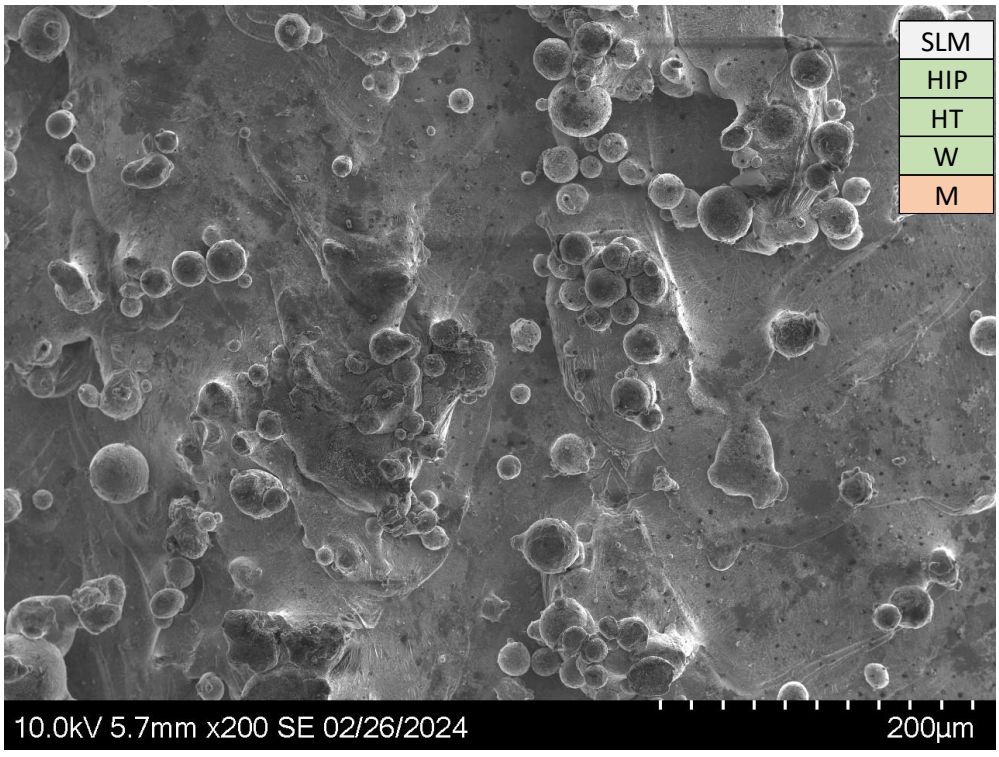

Fig. 94 – As Received Bulk SEM Micrograph of Sample 8082 (200x)

Particle size and distribution was dependent on the sample, but for those which had less particulate on the surface (7670) it was observed that small fleck-like pieces of material could be found between them which was not really seen on samples more heavily concentrated with particulate.

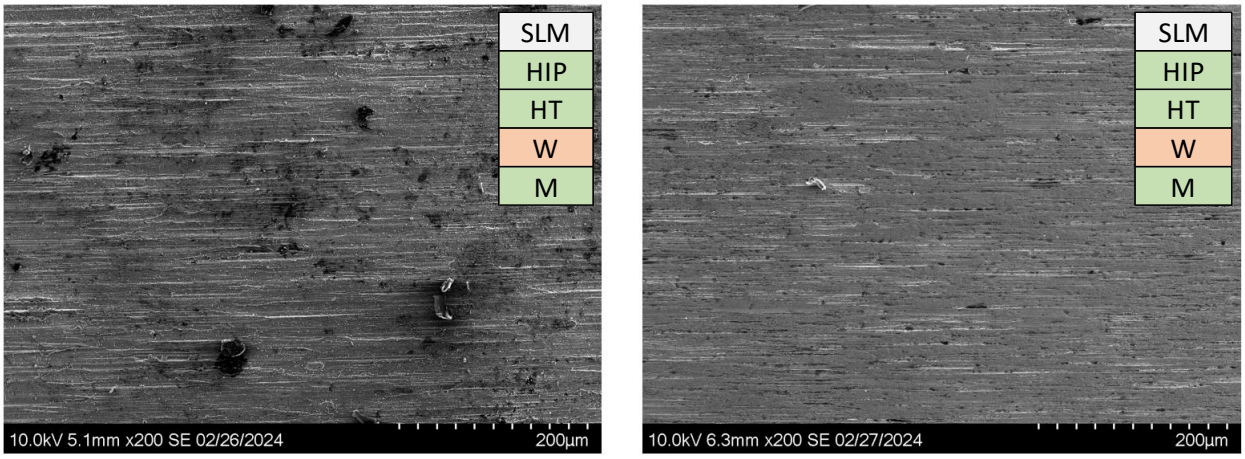

Sample 8174 Sample 8525

Fig. 95 – As Received Bulk SEM of Samples 8174 and 8525 (200x)

Samples which received machining had clear indications of circumferential directionality as a result. Though some also included regions of carbon contamination, as a whole these samples tended to display comparable surface features.

The region of interest which proved most notable was the burn interface, as these images demonstrated a wide range of characteristics that were not entirely anticipated based on previous studies and work. The burn interface typically shows a cloudy overhang of re-solidified material that protrudes over the heat affected zone of the rod. Macroscopic images (taken at 100x) show this trend for several samples from this sample set below.

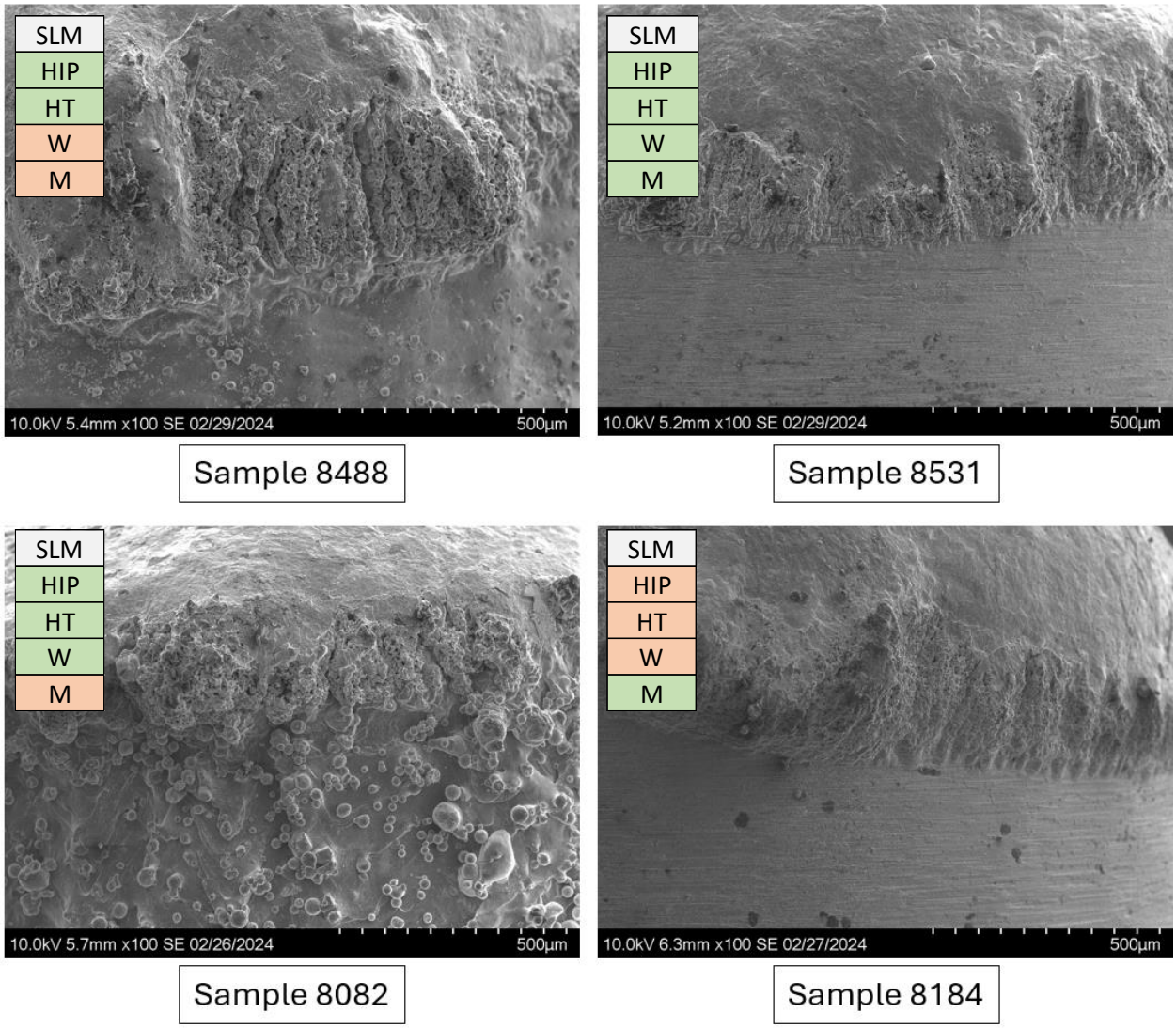

Fig. 96 – As Received Burn Interface SEM Micrographs of Samples 8488, 8531, 8082, and 8184 (100x)

Upon further inspection, it was observed that for many of the samples in this study there were smaller granular features which were only visible at higher magnifications within these interfaces. In particular, when increasing the magnification of the clouded regions of the interface there were structures which displayed fine rocky agglomerations of material on their surfaces, as shown below.

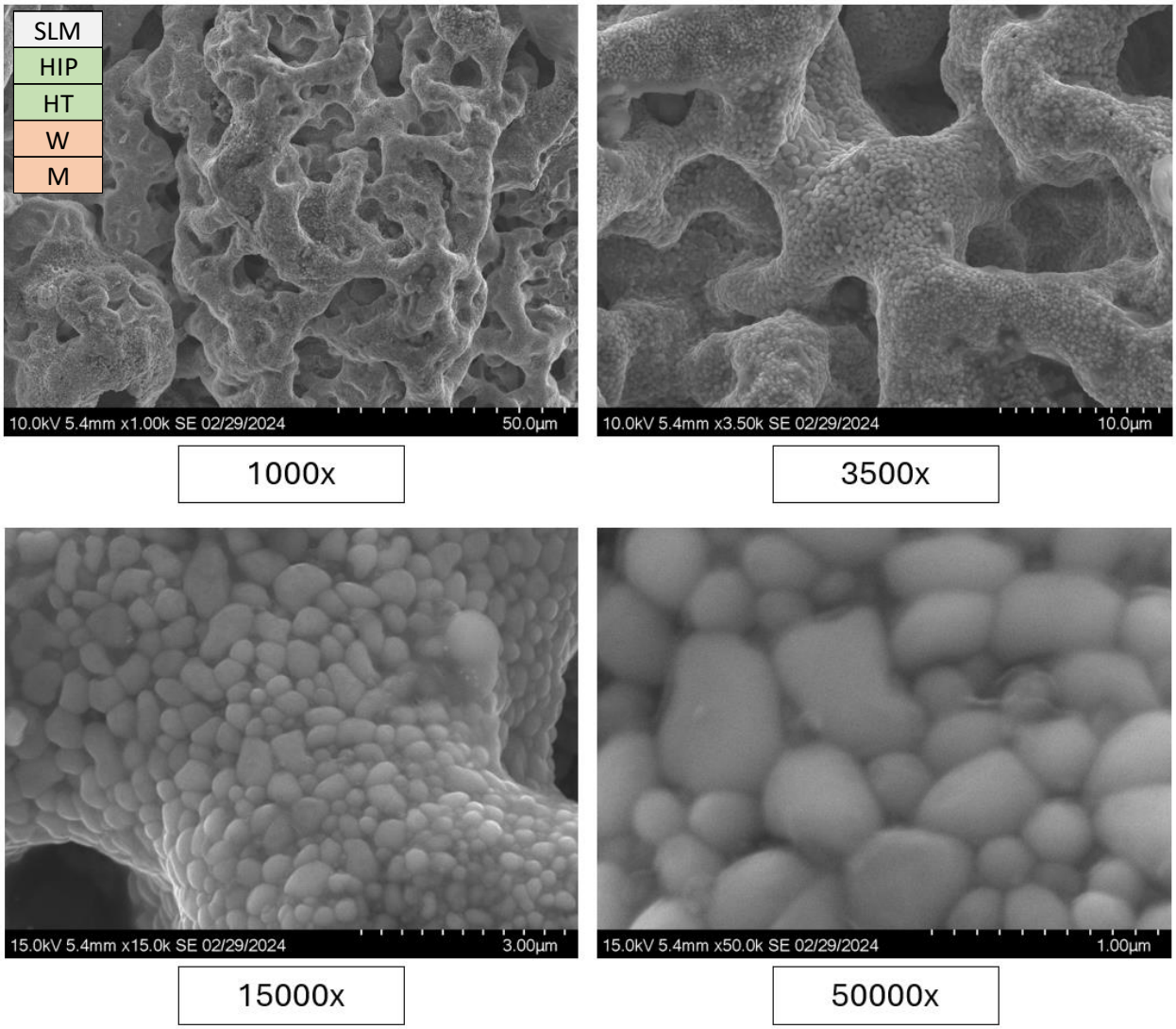

Fig. 97 – Sample 8488 Burn Interface SEM Imaging (1000x, 3500x, 15000x, and 50000x)

The network of surface material seen within the burn interface of Sample 8488 (above) was generally spherical and very fine, measuring approximately between 0.2 – 0.5 µm in diameter per nodule. Though this trend of rounded features appears to follow for most other samples, there were instances (such as seen in sample 7679) where they were much more angular and sharp as seen below.

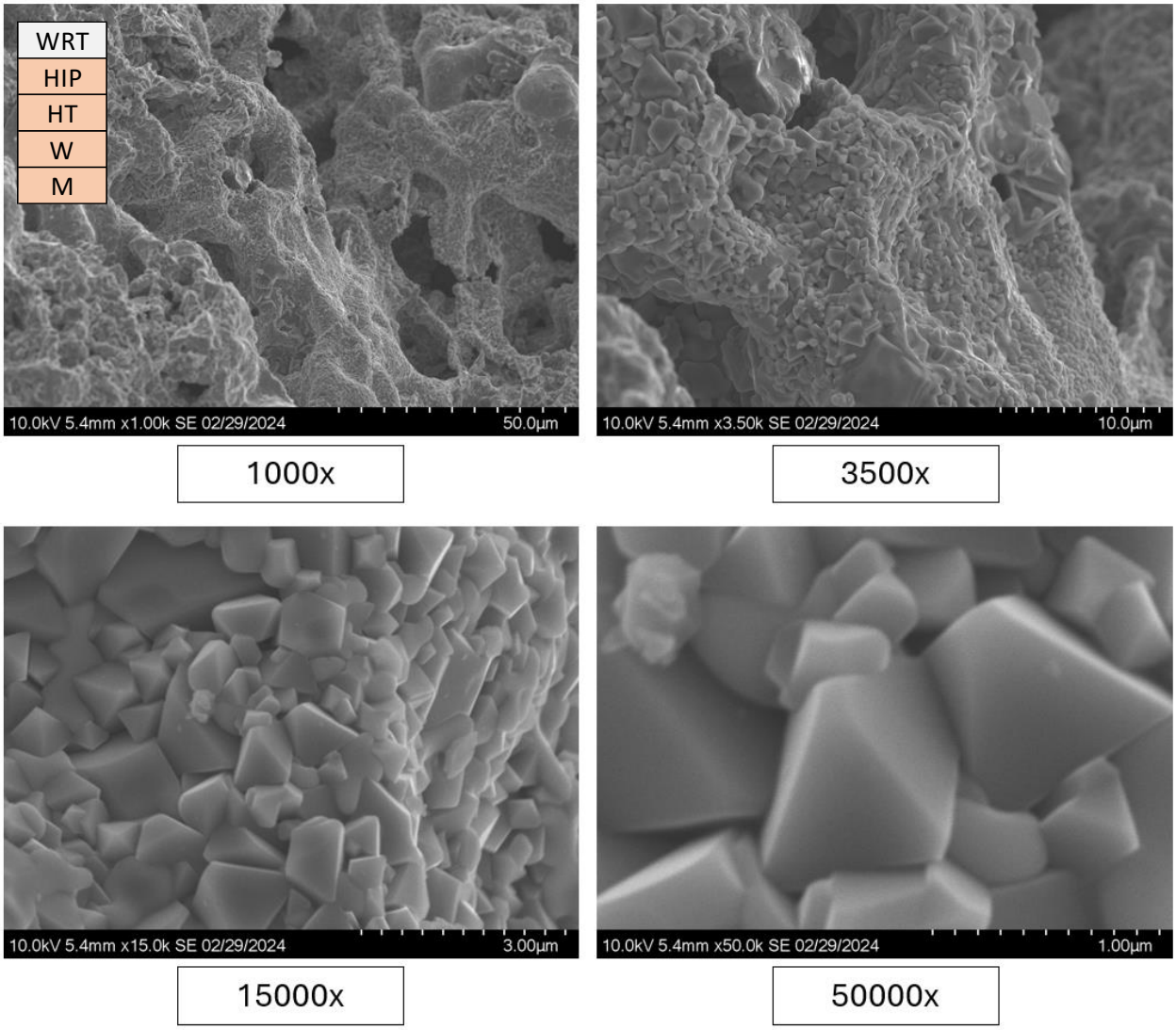

Fig. 98 – Sample 7679 Burn Interface SEM Imaging (1000x, 3500x, 15000x, 50000x)

As-Received Energy Dispersive Spectroscopy

Comparable to SEM imaging, as received EDS focused on the burn tip, burn interface, and bulk regions for scans and mapping. The burn tips typically demonstrate a concentration of chromium, niobium, and oxygen – coupled with depletion of nickel and iron. Data shown below in the polished EDS section will display that the interior of the burn tip sees the reverse of this trend with regards to metallics, showing that the elements chromium and niobium "float" to the surface of the liquid melt pool as opposed to staying concentrated in the liquid like nickel and iron. These higher concentrations of chromium and niobium then appear to solidify after flame extinguishment as a thin layer around the volume of the burn tip, explaining their observed intensities for the samples shown below. Nickel and iron then solidify preferentially in the interior of the burn tip as opposed to on the outer surface, as demonstrated by their depletion relative to the surrounding rod material seen below.

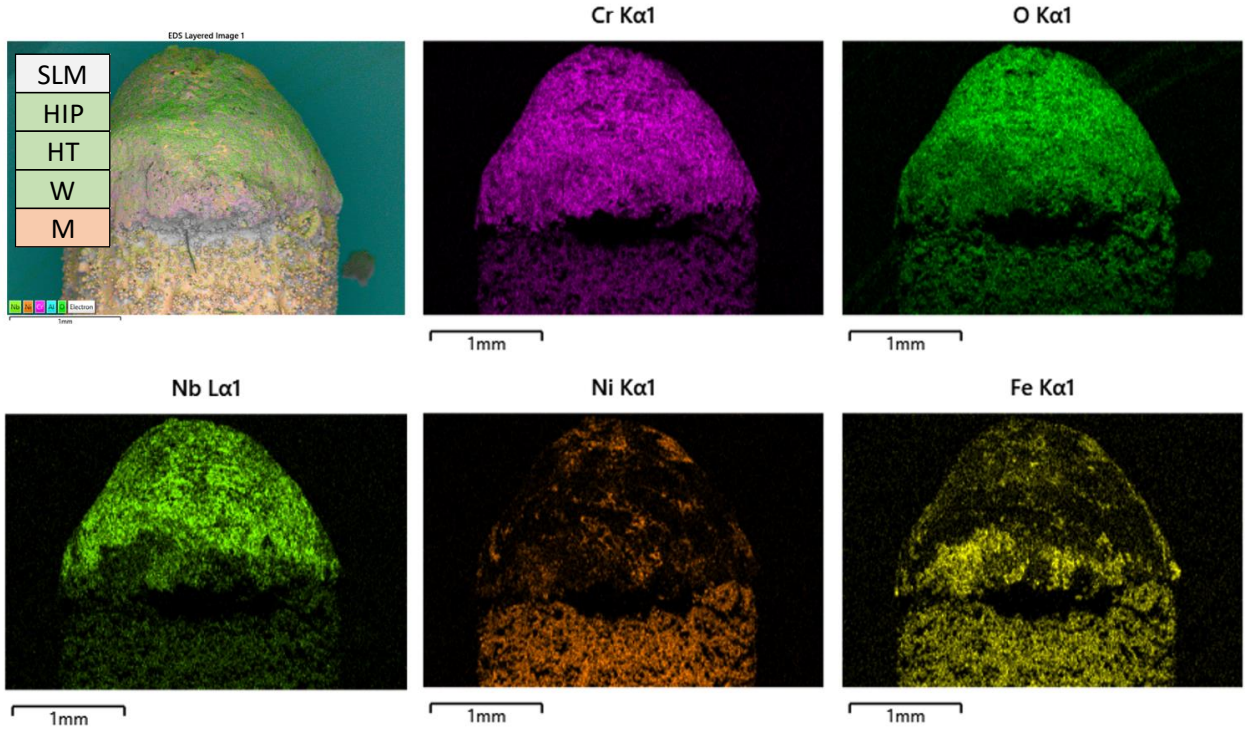

Fig. 99 – As Received Burn Tip EDS Maps of Sample 8044 (35x)

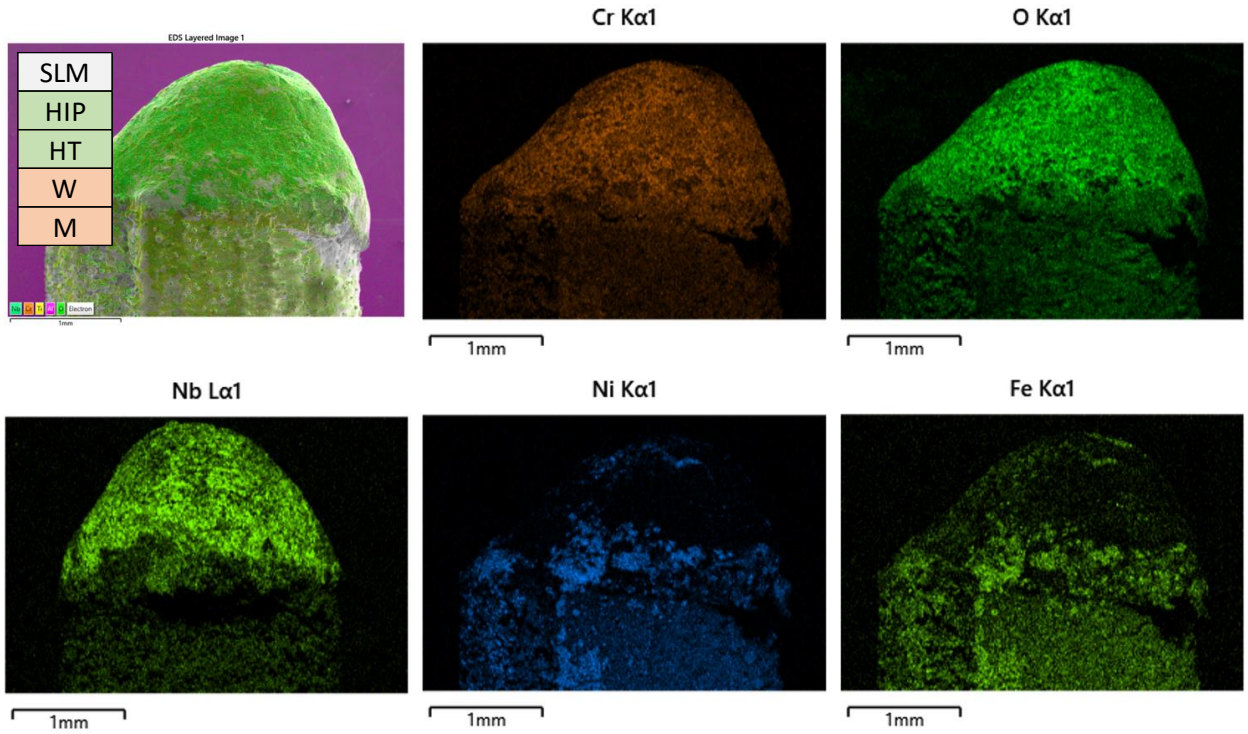

Fig. 100 – As Received Burn Tip EDS Maps of Sample 8490 (35x)

EDS mapping of the burn interfaces (conducted at a higher magnification of 100x) reinforce what was seen during burn tip analysis, as constituents like chromium and niobium increased in concentration while others like nickel and iron decrease as one travels across the burn interface and onto the burn tip surface. However, it could be seen now that thin layers of titanium (and to a lesser extent iron) exist right at the interface with the titanium condensing where the surface of the rod begins to blend into the interface and the iron concentrating at the start of the burn tip overlap.

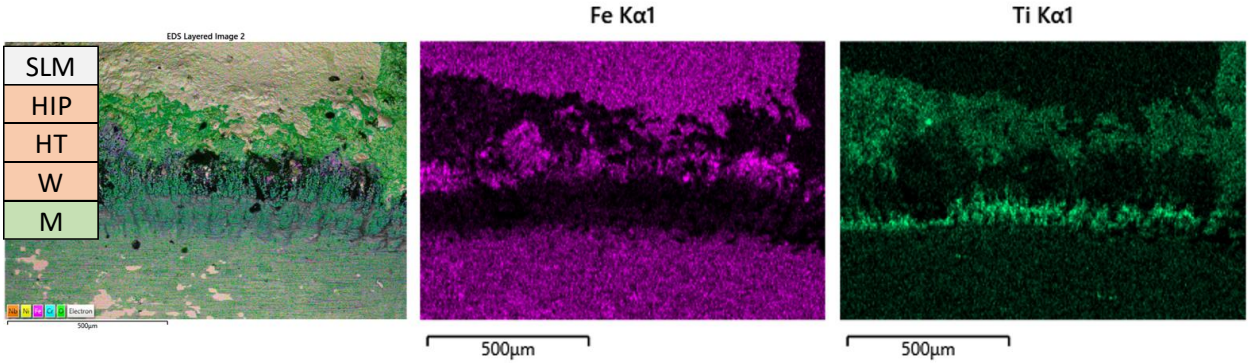

Fig. 101 – As Received Burn Interface EDS Maps of Sample 8065 (100x)

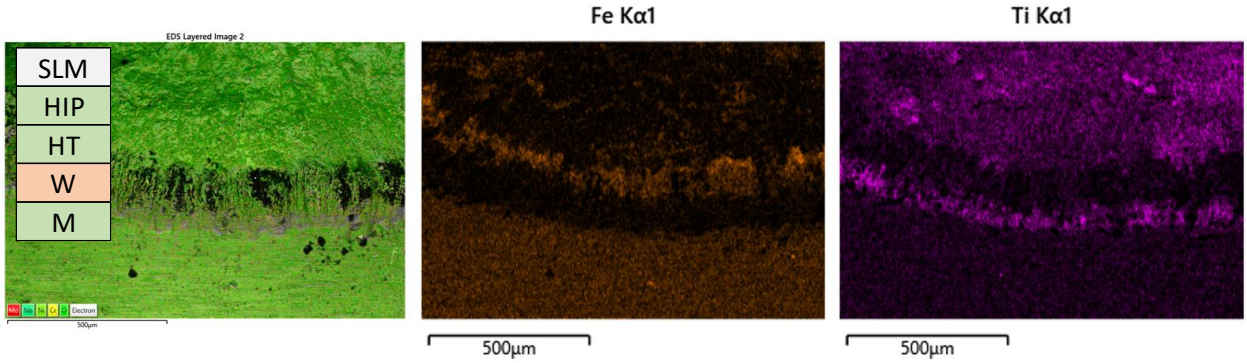

Fig. 102 - As Received Burn Interface EDS Maps of Sample 8174 (100x)

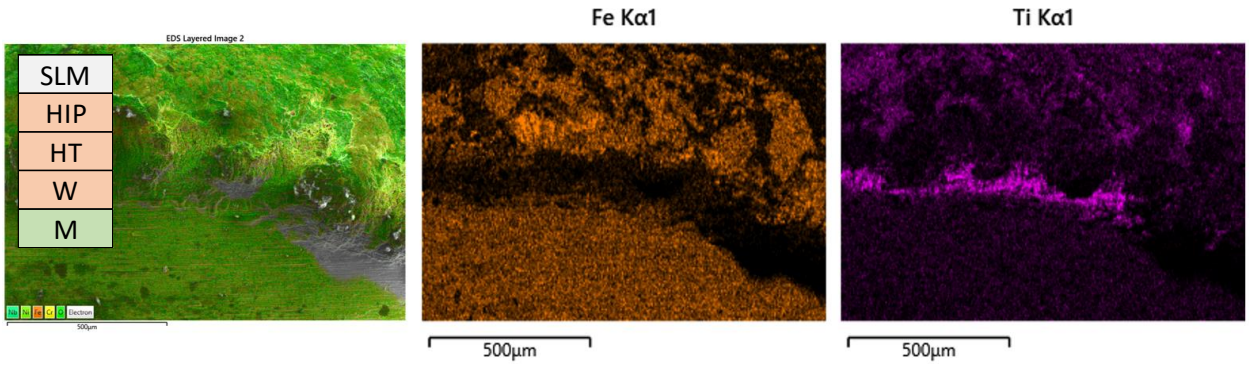

Fig. 103 – As Received Burn Interface EDS Maps of Sample 8184 (100x)

For as received bulk surface EDS analysis, samples typically fell into two categories which either saw elemental homogeneity in the case of machined rods or overlapped concentrations of aluminum, titanium, and oxygen (particularly for samples that exhibited unsintered particulate on their surfaces). Representatives of both types are shown below (8174 which was machined and homogenous) as well as those which displayed variability (7670, 8044, and 8082).

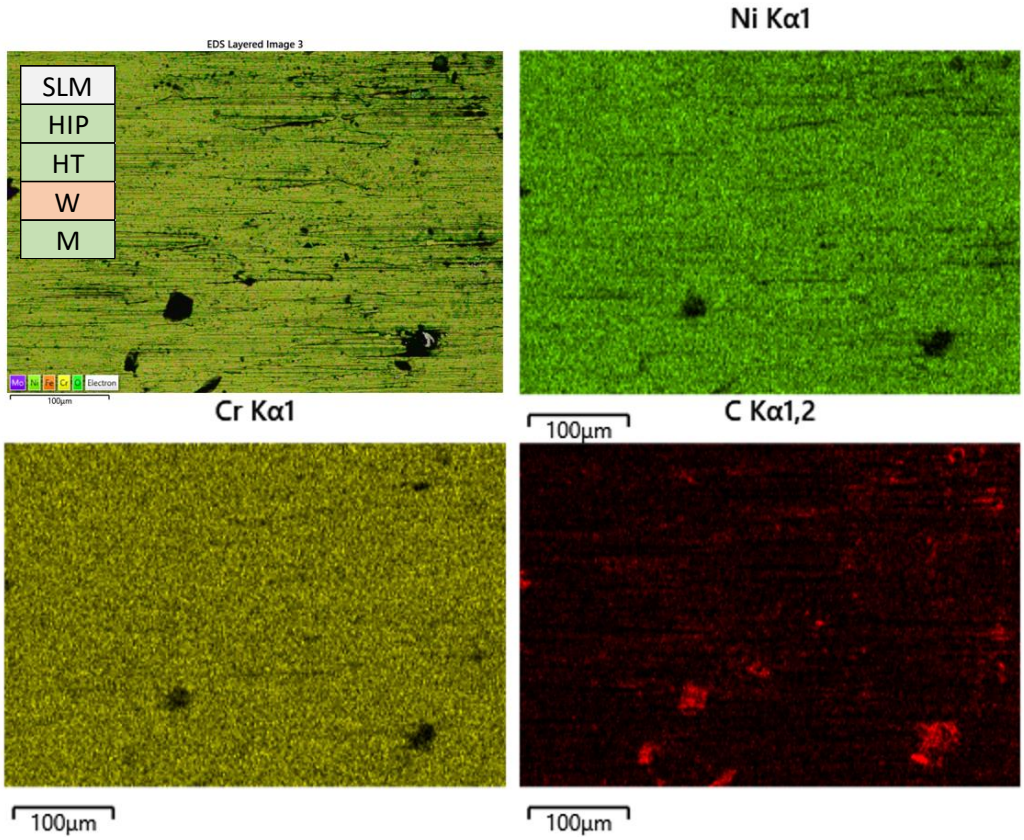

Fig. 104 – As Received Bulk EDS Maps of Sample 8174 (250x)

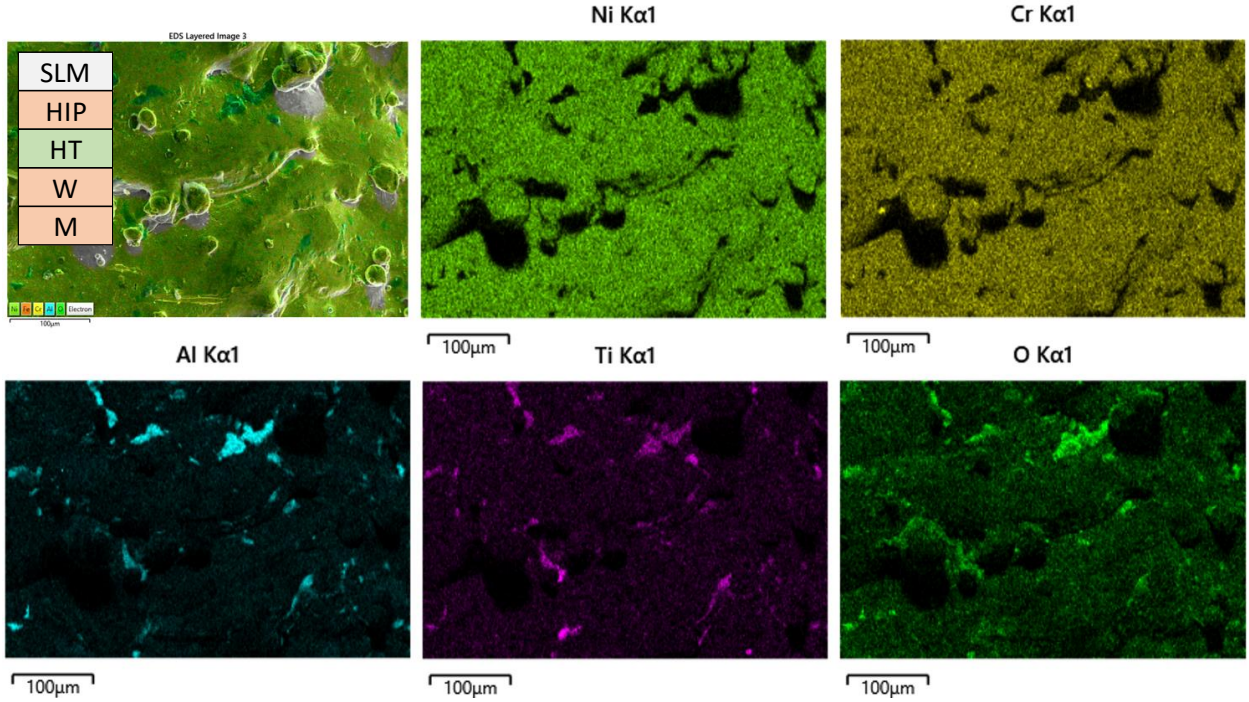

Fig. 105 – As Received Bulk EDS Maps of Sample 7670 (250x)

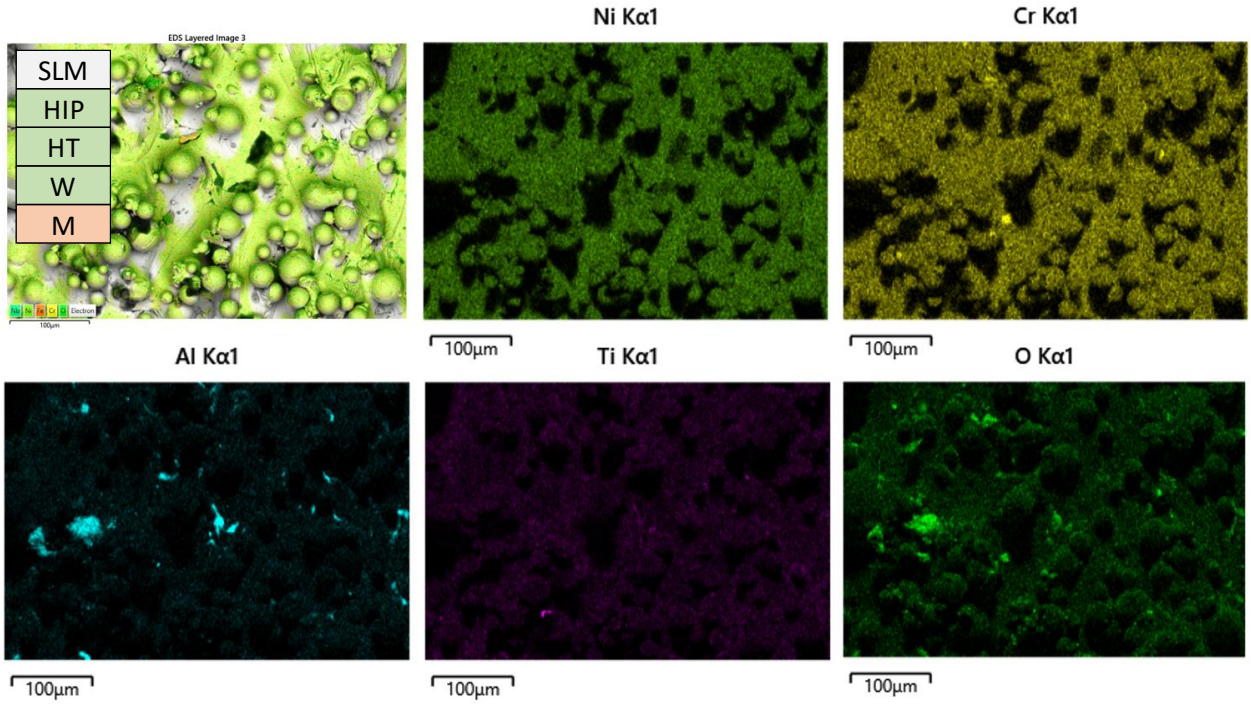

Fig. 106 – As Received Bulk EDS Maps of Sample 8044 (250x)

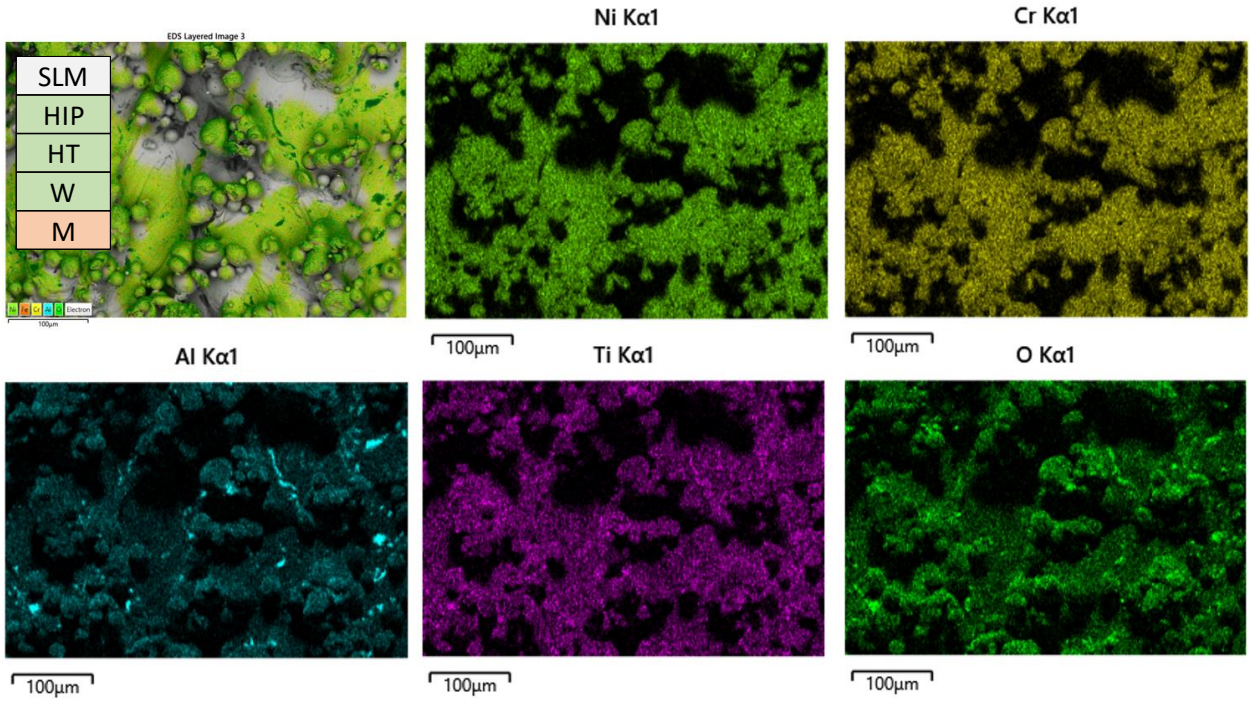

Fig. 107 – As Received Bulk EDS Maps of Sample 8082 (250x)

X-Ray Fluorescence

Table 15 – Compiled XRF Chemical Data for Sample Set 1

XRF Chemistry												
Batch Lot	Sample Number	Nickel	Chromium	Iron	Niobium	Molybdenum	Titanium	Aluminum	Carbon	Manganese	Silicon	Sulfur
A1	8044	49.90	19.09	18.08	5.05	2.90	1.60	ND	-	ND	2.58	0.81
A1	8065	51.69	18.68	18.31	5.11	2.93	1.07	ND	-	0.06	0.52	1.25
A1	8174	50.86	18.76	18.14	4.98	2.93	1.12	ND	-	ND	1.22	1.98
C1	8490	**46.13**	**16.98**	**17.25**	**4.30**	**2.53**	**1.47**	**6.44**	**-**	**-**	**2.81**	**2.1**
C1	8525	51.36	18.14	18.37	4.70	2.85	1.03	ND	ND	0.19	0.97	2.38
C1	8541	47.17	17.23	17.46	4.30	2.58	1.67	5.04	-	0.16	1.70	2.69
C1	8544	51.73	18.02	18.43	4.83	2.91	1.05	ND	-	0.19	0.75	1.89
D1	8082	-	-	-	-	-	-	-	-	-	-	-
D1	8158	50.02	18.86	18.90	4.87	3.00	1.06	ND	-	0.14	0.72	1.44
D1	8184	-	-	-	-	-	-	-	-	-	-	-
G2	8488	-	-	-	-	-	-	-	-	-	-	-
G2	8522	44.74	18.12	16.50	4.15	2.53	1.51	4.36	-	-	5.45	2.63
G2	8531	49.79	19.02	17.61	4.71	2.82	1.14	ND	-	ND	1.69	3.23
N/A	7670	42.32	17.41	16.37	3.73	2.23	1.11	5.44	-	-	9.30	2.08
N/A	7676	48.53	17.48	16.99	4.00	2.43	3.21	9.46	-	0.17	1.47	0.99
N/A	7679	50.41	18.03	17.24	4.58	2.70	1.12	2.52	-	ND	1.07	1.85
N/A	Standard	50.00 - 55.00	17.00 - 21.00	Balance	4.75 - 5.50	2.80 - 3.30	0.65 - 1.15	0.20 - 0.80	0.08	0.35	0.35	0.0015

The table above displays the chemical data yielded for sample set 1 rods via x-ray fluorescence. Values which are highlighted in yellow represent those which deviated significantly from the established chemistry of Inconel 718 per AMS standard 5596B. ND was used to indicate when an element was Not Detected but still listed in the results of the XRF software, dashes indicate elements which were entirely absent from results.

Notably there are inflated values for aluminum, silicon, and sulfur – driving a lower-than-expected observed percentage of the primary constituent nickel. Though there are a number of factors which may influence the accuracy and validity of XRF data, it is believed that the small size of the samples was most significant in introducing error into readings as they were unable to fully cover the window of the XRF gun (thus allowing for background signal from the surroundings to potentially skew the results). This is also why three samples (8082, 8184, and 8488) were unable to be analyzed with this test method and have no data listed above.

Due to the difficulties experienced with using XRF to establish chemistry (as well as the fact that the method itself is meant as a surface analysis tool and may not be indicative of the true bulk chemistry of the rods), the data was supplemented with EDS point scans conducted on the interior cross sections of the rods following metallography. That data is shown below.

Table 16 – Compiled EDS Chemical Data for Sample Set 1

EDS Chemistry											
nnn Sample Batch	Sample Number	Nickel	Chromium	Iron	Niobium	Molybdenum	Titanium	Aluminum	Carbon	Manganese	Silicon
A1	8174	48.60	17.90	17.20	4.90	3.00	0.90	0.40	7.20	-	-
A1	8044	48.50	17.80	16.90	5.00	3.00	0.80	0.40	7.50	-	-
A1	8065	52.00	19.30	18.40	5.90	3.00	1.00	0.50	-	-	-
C1	8490	49.40	17.30	17.50	4.60	2.70	0.60	0.50	7.40	-	-
C1	8525	49.20	16.90	17.10	4.70	2.70	1.00	0.40	7.50	0.30	-
C1	8544	48.90	17.20	17.30	4.90	2.70	1.20	0.50	-	-	-
C1	8541	49.00	16.90	17.40	4.90	2.80	0.70	0.50	7.80	-	-
D1	8082	49.20	18.40	18.10	4.70	-	1.30	0.50	7.60	-	-
D1	8184	47.00	18.00	17.50	5.10	2.90	0.90	0.50	7.90	-	-
D1	8158	51.10	19.60	19.10	5.30	3.30	1.00	0.60	-	-	-
G2	8531	48.50	18.40	17.20	4.70	2.80	0.90	0.50	7.00	-	-
G2	8522	48.00	17.80	17.00	4.80	3.30	1.00	0.50	7.60	-	-
G2	8488	48.30	18.10	17.10	5.00	2.50	0.90	0.40	7.50	-	-
N/A	7679	48.10	17.40	16.20	4.20	2.40	0.90	0.50	7.70	-	0.20
N/A	7676	48.10	17.50	17.00	5.10	2.80	1.10	0.50	7.90	-	-
N/A	7670	48.30	17.90	17.00	5.20	2.90	0.90	0.50	7.30	-	-
N/A	Standard	50.00 - 55.00	17.00 - 21.00	Balance	4.75 - 5.50	2.80 - 3.30	0.65 - 1.15	0.20 - 0.80	0.08	0.35	0.35

The elemental analysis conducted with interior surface EDS point scans was much more consistent, however also included carbon content which is significantly higher than what the standard allows (in excess of 7.0% when the max allowable is 0.08%). It's not known what the exact cause of this higher carbon signal is, though it may have been contamination during the metallographic process or stray signal being detected from the carbon-based adhesives used on the SEM stage.

In either case, the data appears to show relative consistency between the samples and (excluding carbon) falls into specification for Inconel 718. It's difficult to say with any certainty however if any genuine chemical disparities exist as neither XRF nor EDS are truly quantitative elemental analysis techniques. Had time and resources been available, optical emission spectroscopy (and more specifically inductively coupled plasma optical emission spectroscopy) would have been the preferred methods for establishing chemistry, as those techniques would have confirmed with greater accuracy the constituencies of trace and tramp elements.

Optical Microscopy

Following metallography and chemical etching, all 16 sample rods were optically imaged to observe their microstructure. Four main regions of interest were identified, being the burn tip, burn interface, heat affected zone, and bulk portions of the rod. The burn tips were imaged at 50, 100, and 200x magnifications to show both a macroscopic view as well as finer microstructural details and texturing of the area.

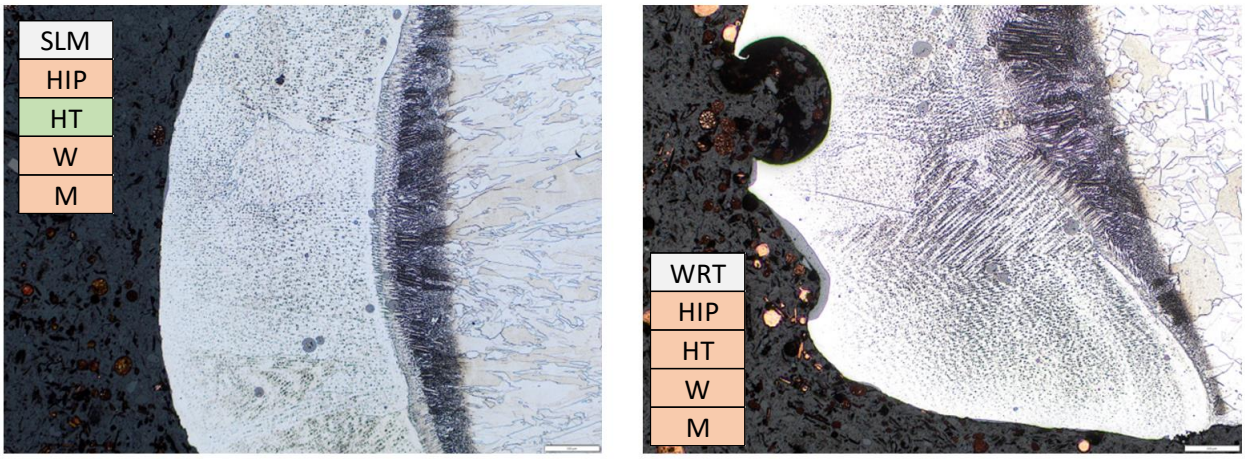

Fig. 108 – Polished Burn Tip Micrographs for Samples 7670 and 7676 (50x)

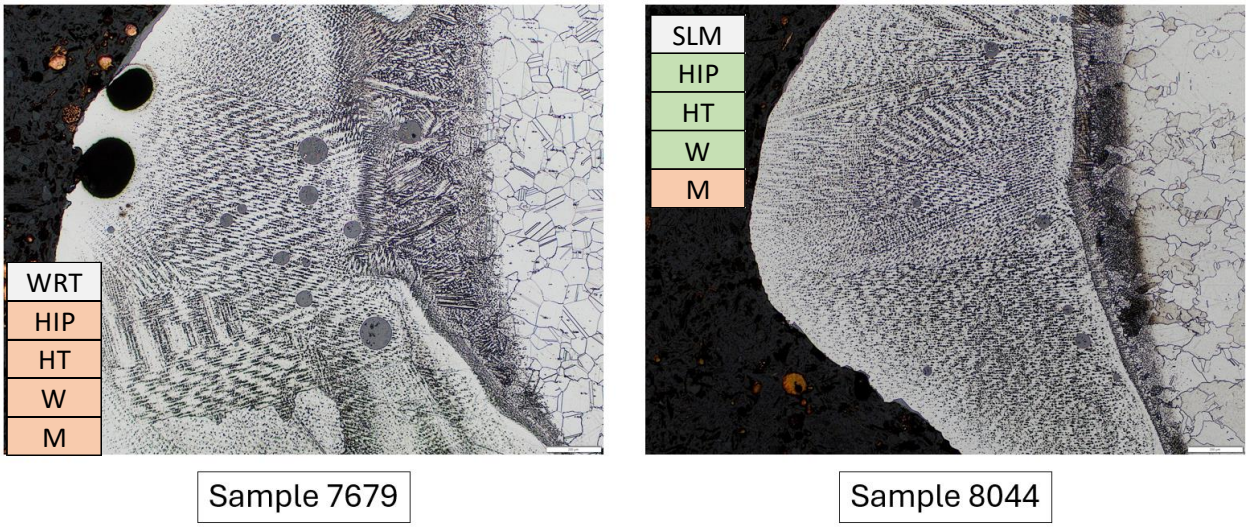

Fig. 109 – Polished Burn Tip Micrographs for Samples 7679 and 8044 (50x)

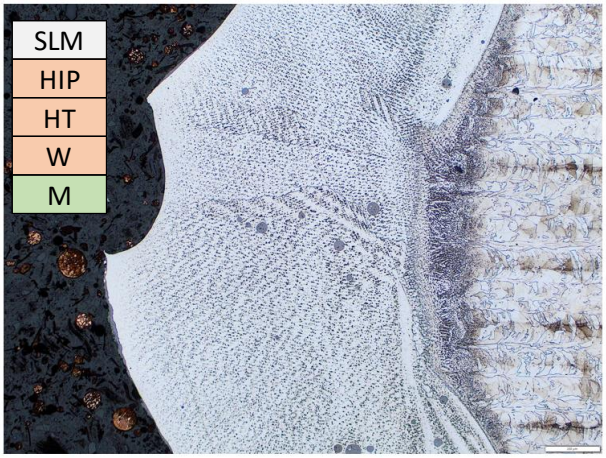

Sample 8065

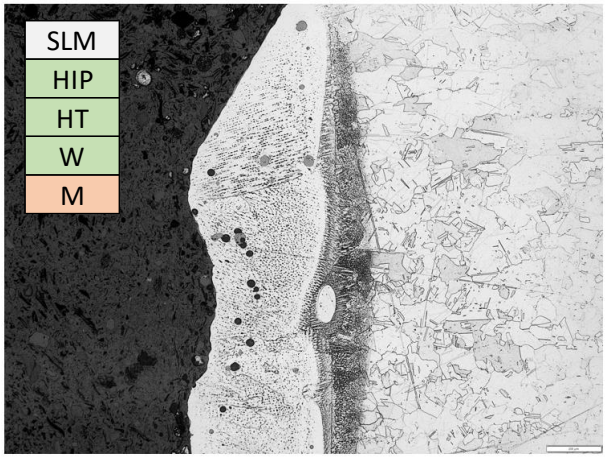

Sample 8082

Fig. 110 – Polished Burn Tip Micrographs for Samples 8065 and 8082 (50x)

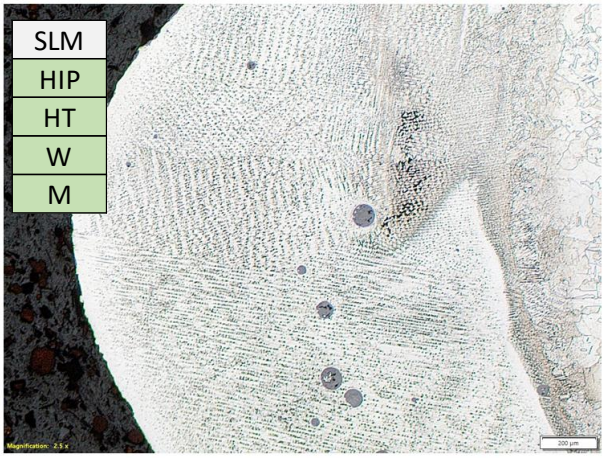

Sample 8158

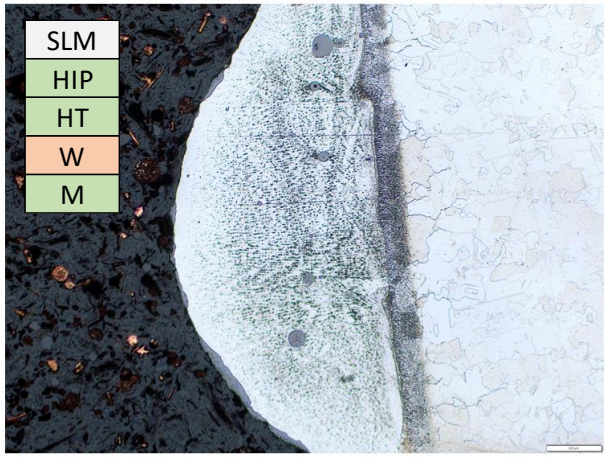

Sample 8174

Fig. 111 – Polished Burn Tip Micrographs for Samples 8158 and 8174 (50x)

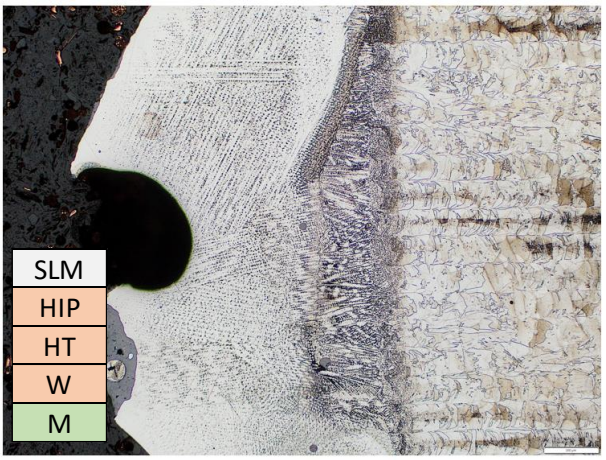

Sample 8184

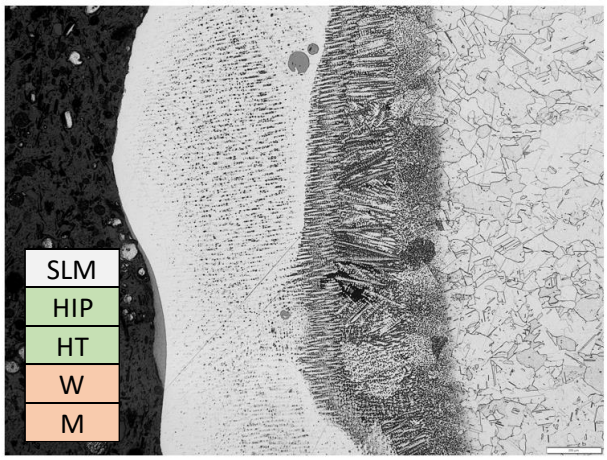

Sample 8488

Fig. 112 – Polished Burn Tip Micrographs for Samples 8184 and 8488 (50x)

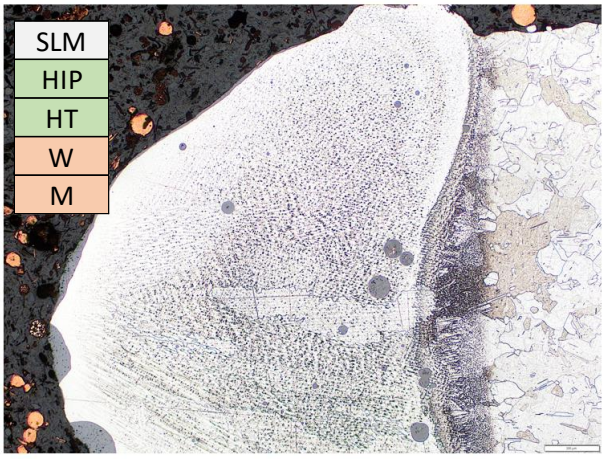

Sample 8490

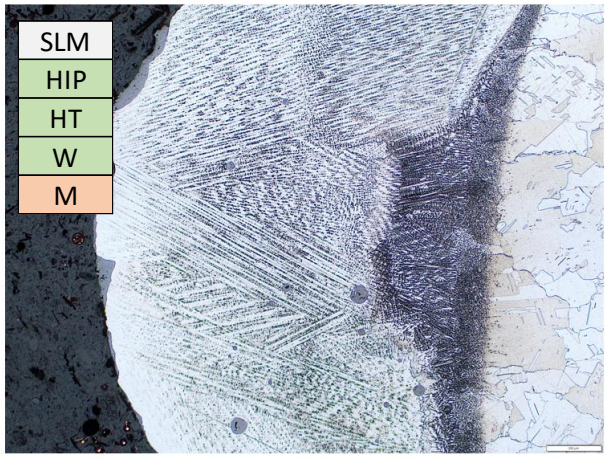

Sample 8522

Fig. 113 – Polished Burn Tip Micrographs for Samples 8490 and 8522 (50x)

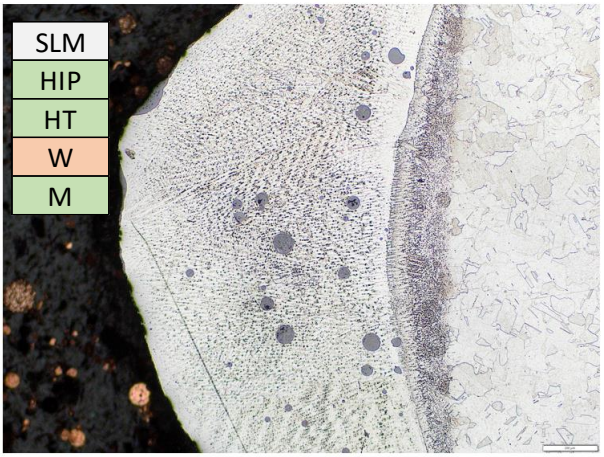

Sample 8525

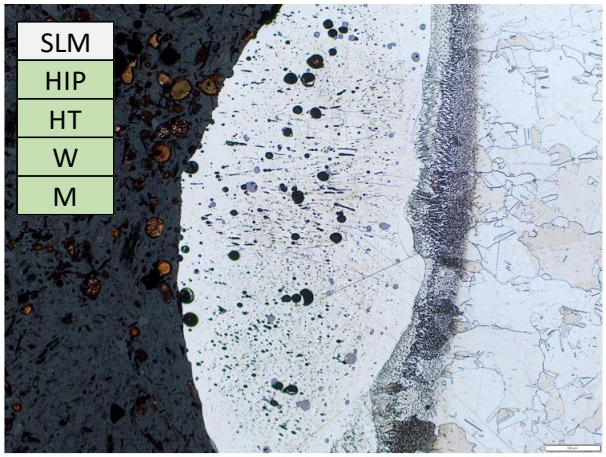

Sample 8531

Fig. 114 – Polished Burn Tip Micrographs for Samples 8525 and 8531 (50x)

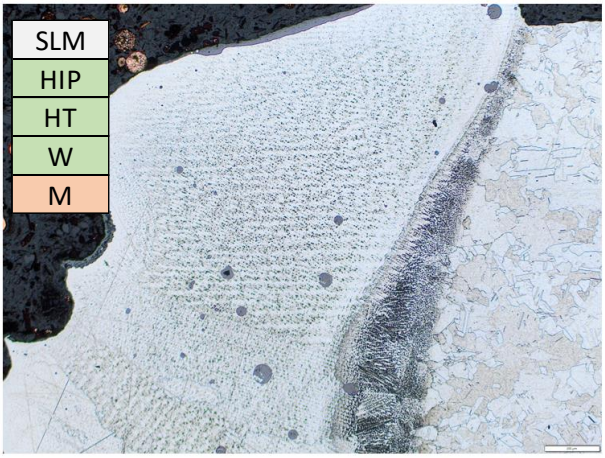

Sample 8541

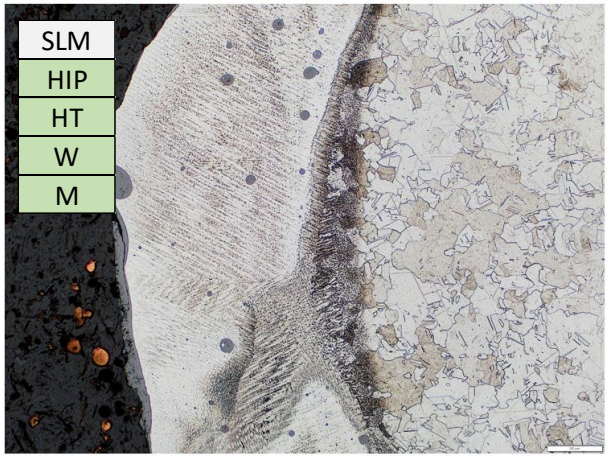

Sample 8544

Fig. 115 – Polished Burn Tip Micrographs for Samples 8541 and 8544 (50x)

At first glance, one clear observation of the burn tip micrographs may be that they tend to exhibit discrete regions of highly directional acicular structures which can exist in various orientations. This lack of homogeneity in directionality may suggest variable solidification conditions at flame extinguishment following combustion testing. Some samples are particularly notable for these features and even resemble Widmanstatten-like patterns (such as samples 7676, 7679, and 8522).

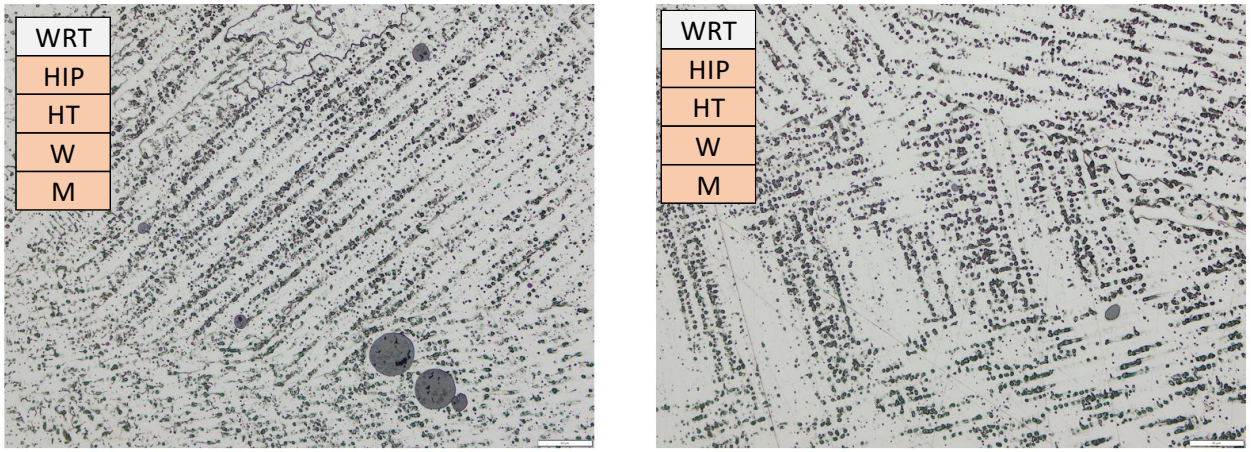

Fig. 116 – Polished Burn Tip Micrographs of Samples 7676 and 7679 (200x)

Moving from the burn tip to the burn interfaces, the microstructures are significantly darker (thus were preferentially affected by the chemical etching) and show dendritic features which are present throughout the region but tended to concentrate in the centers. Of note is the variability in burn interface geometry and size, for some samples the interface is relatively perpendicular to the rod (such as samples 8174 and 8525) whereas others see the line slanted and more wedge-shaped (samples 7676 and 7679). In terms of size, the interfaces could be quite short (approximately 100 μm for sample 8174) or much longer (over 350 μm for sample 8488). It would appear that for samples with greater burn lengths the burn interfaces were also larger, and vice versa.

Additionally, a majority of the rods showed convex interfaces (where they form a “c-shape” with relation to the rod) but two did not and were instead concave relative to the rod. This would lead to the belief that in the case of those samples (8082 and 8531), material was consumed

by combustion at a faster rate in the center of the rods than the material at the outer surface. Interestingly, those two rods also had the second and third longest burn lengths (respectively) from the entire sample set.

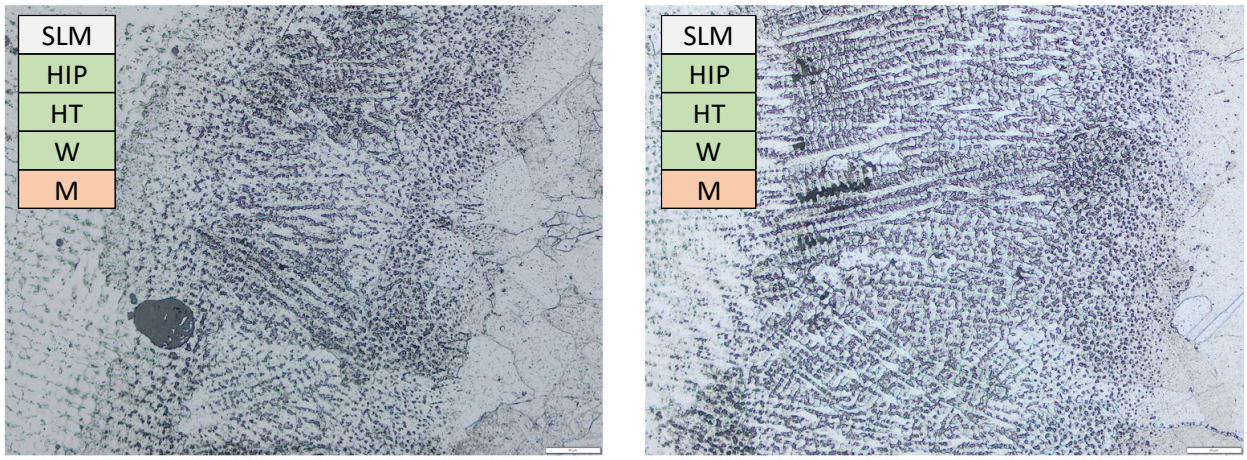

Fig. 117 – Polished Burn Interface Micrographs of Samples 8541 and 8522 (200x)

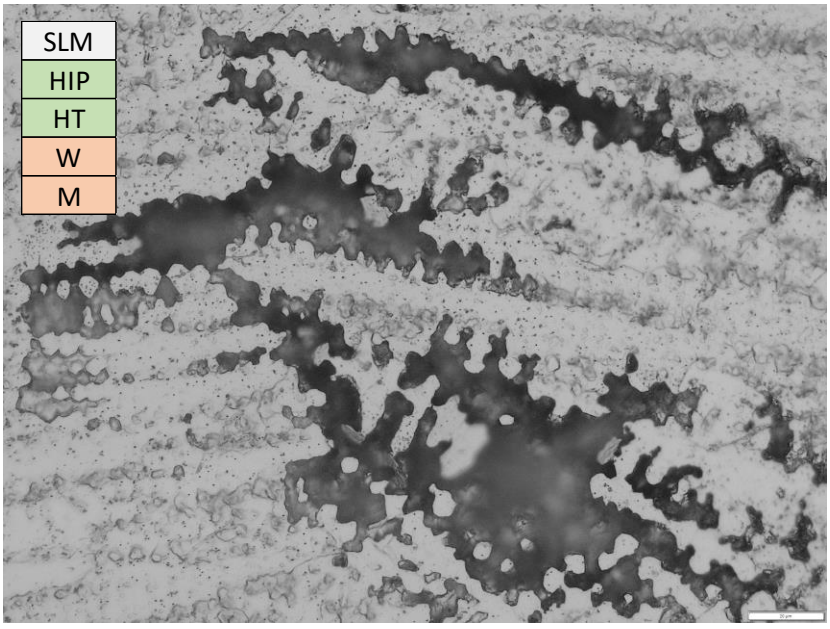

Fig. 118 – Polished Burn Interface Micrograph of Sample 8488 (500x)

The figure above shows that within these burn interfaces, some samples also displayed significant crevices which overlapped with the dendritic structures previously observed. Though the length and width of these features varied, the majority were fairly shallow. The exception to this rule would be those seen in sample 8488 above which had enough depth to be completely out of focus with the plane at the polished surface of the rod.

In comparing the heat affected zone to the bulk of the rods, it's generally observed that grains have recrystallized and grown in contrast to the standard austenitic microstructure seen in the bulk. In the case of both regions, the microstructure can be characterized as a binary phase matrix comprised of equiaxed grains. Some samples display acicular precipitates (a residual from the post-processing heat treatment) as well as annealing twins. As grain recrystallization can promote the formation of these twins, their concentration is typically higher in the heat affected zone in comparison to the bulk.

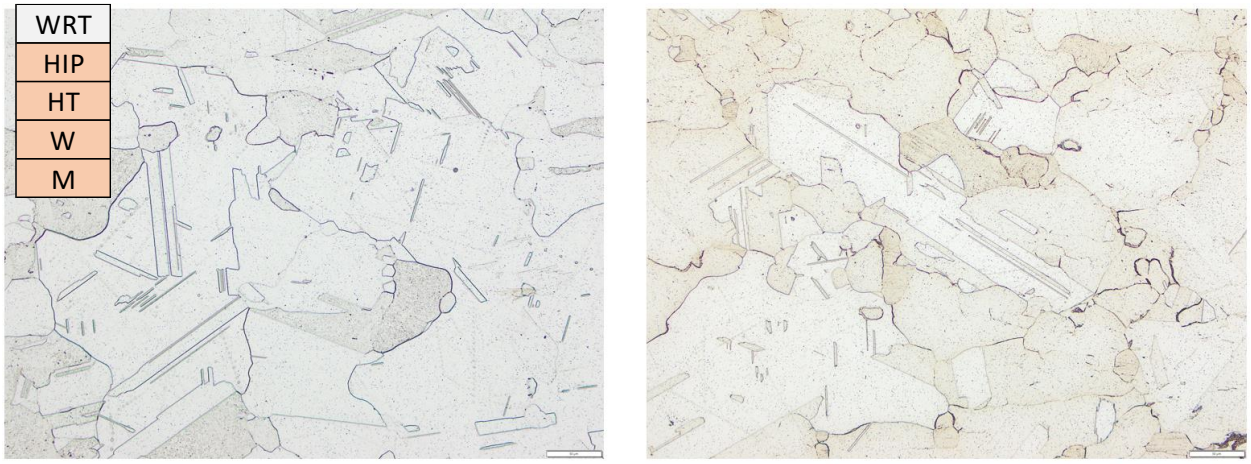

Fig. 119 – Polished Heat Affected Zone and Bulk Micrographs for Sample 7676 (200x)

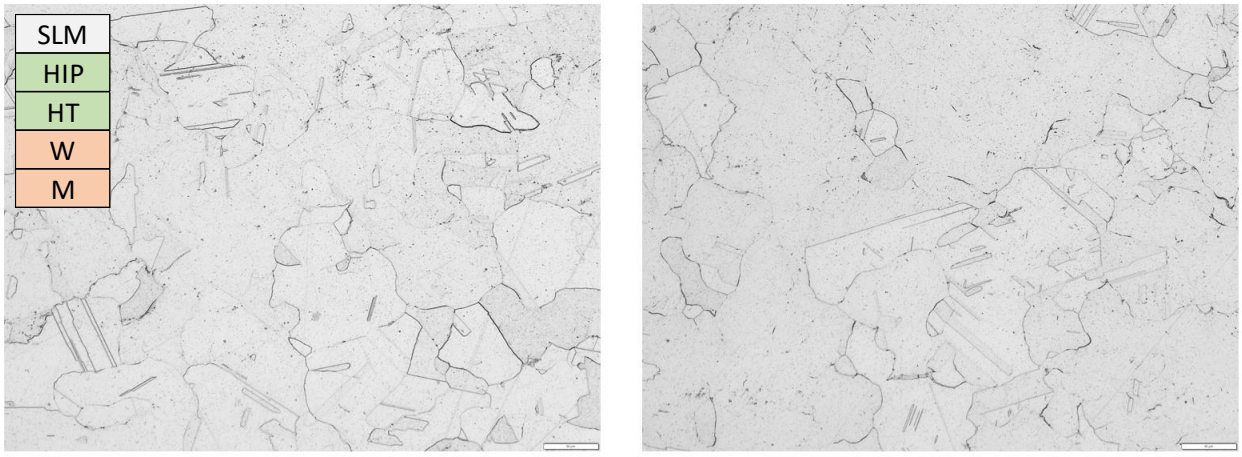

Fig. 120 – Polished Heat Affected Zone and Bulk Micrographs for Sample 8488 (200x)

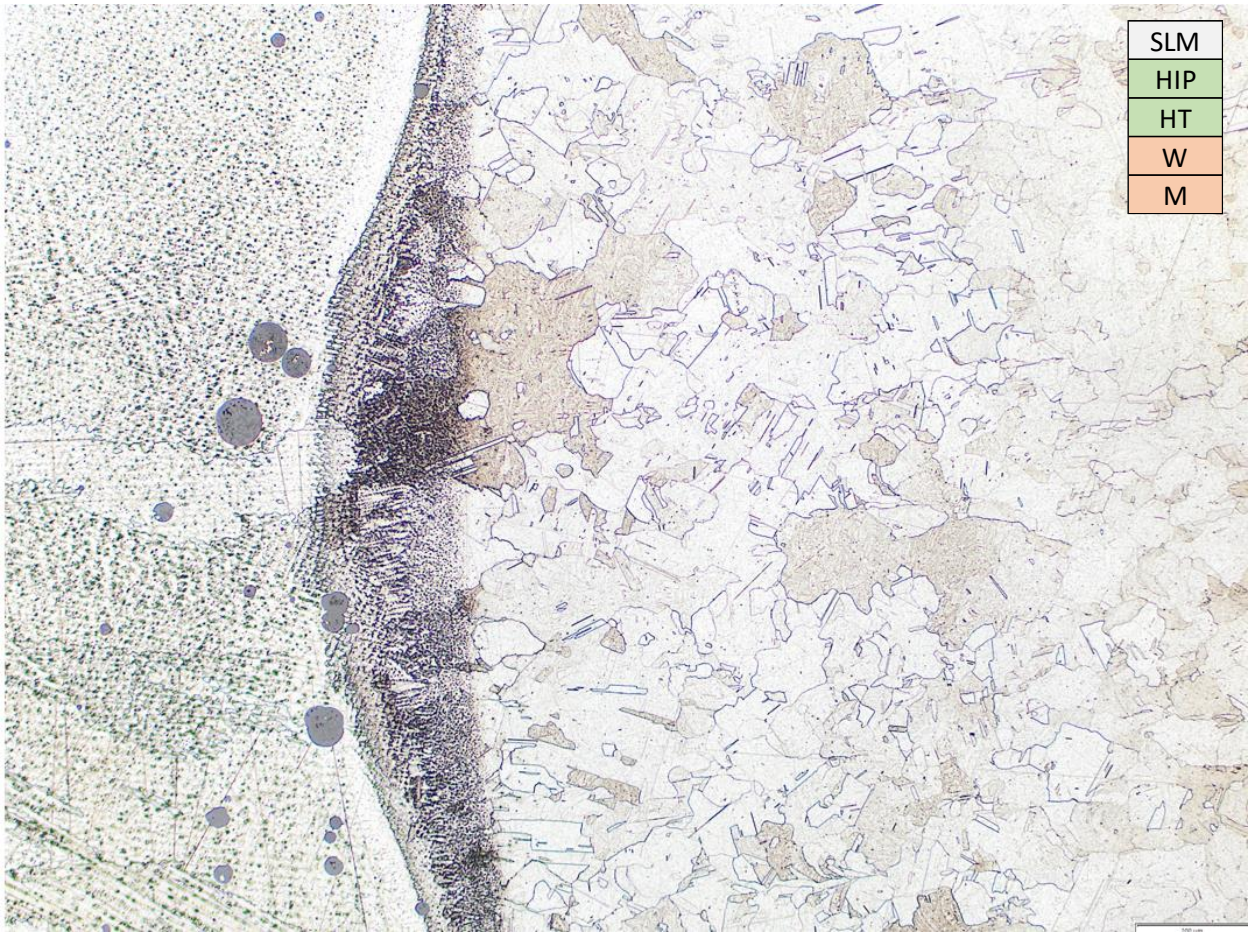

Fig. 121 – Polished Heat Affected Zone Micrograph of Sample 8490 (50x)

Micrographs comparing the heat affected zone and bulk regions are included above for samples which were characteristic of the sample set (7676 and 8488). Additionally, a lower magnification micrograph of the heat affected zone on sample 8490 is shown to demonstrate how the microstructure varies and changes as one travels away from the burn interface from a macroscopic view.

The exceptions to the above descriptions would be samples 8065 and 8184 (both of which were in the "green state", i.e. as printed). In the case of these two samples, the printing pattern of the rods could be seen even visibly with the naked eye before imaging on the optical microscope. The microstructure seen for these rods was completely different from the others, and displayed rows of highly directional print melt pools from the SLM processing. The rastering that can be seen shows that where there was a lack of scan overlap, a boundary layer of material with a dendritic or woven-like texturing can be found (as supported by its darker contrast, this material preferentially etched compared to the surrounding areas).

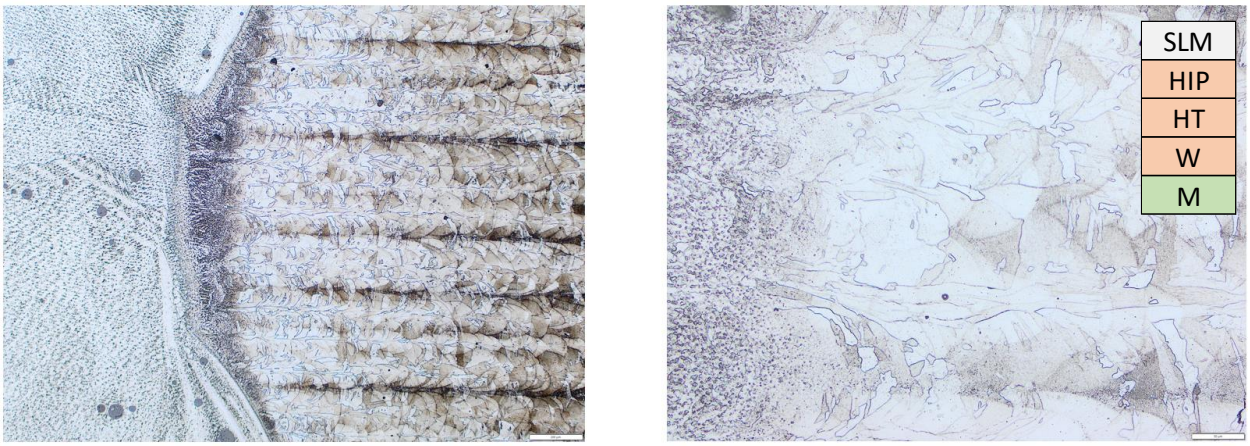

Sample 8065 HAZ 50x

Sample 8065 HAZ 200x

Fig. 122 – Polished Heat Affected Zone Micrographs of Sample 8065 (50x and 200x)

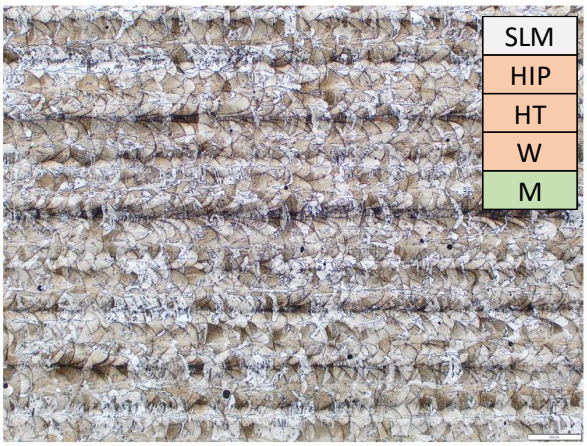

Sample 8065 Bulk 50x

Sample 8065 Bulk 200x

Fig. 123 – Polished Bulk Micrographs of Sample 8065 (50x and 200x)

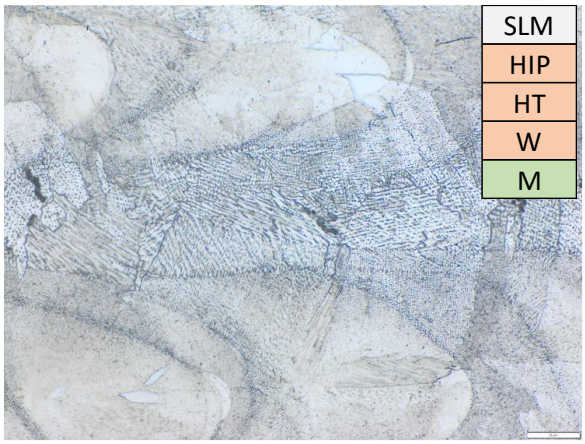

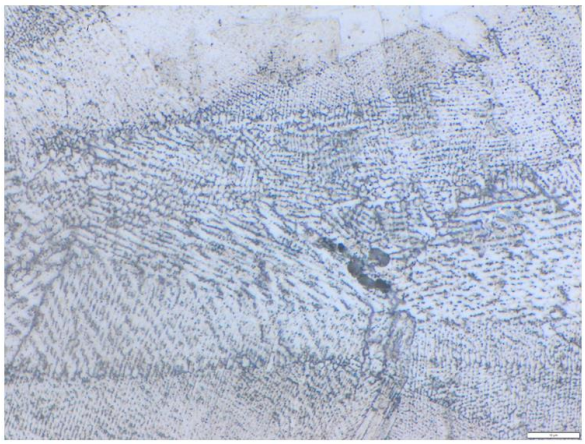

Sample 8065 Scan Boundary 500x

Sample 8065 Scan Boundary 1000x

Fig. 124 – Polished Bulk Scan Boundary Micrographs of Sample 8065 (500x and 1000x)

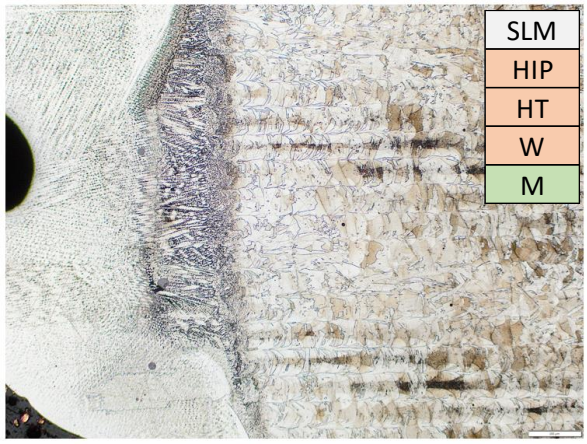

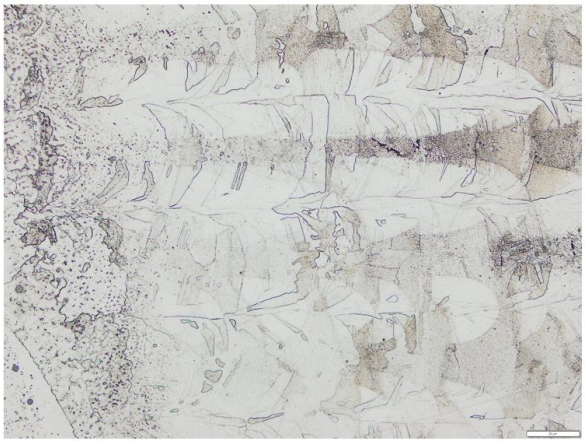

Sample 8184 HAZ 50x

Sample 8184 HAZ 200x

Fig. 125 – Polished Heat Affected Zone Micrographs of Sample 8184 (50x and 200x)

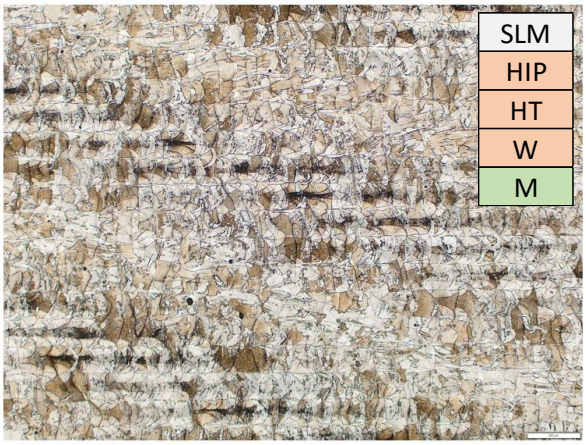

Sample 8184 Bulk 50x

Sample 8184 Bulk 200x

Fig. 126 – Polished Bulk Micrographs of Sample 8184 (50x and 200x)

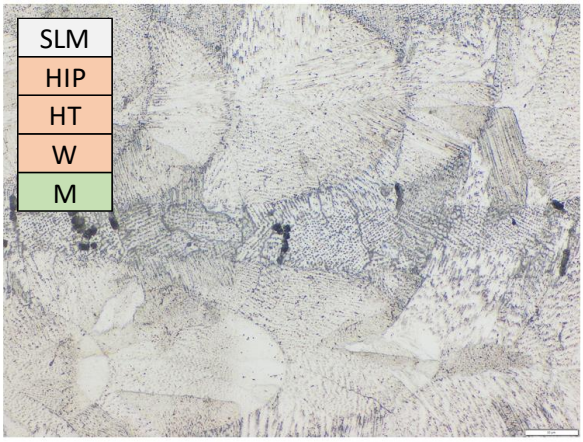

Sample 8184 Scan Boundary 500x

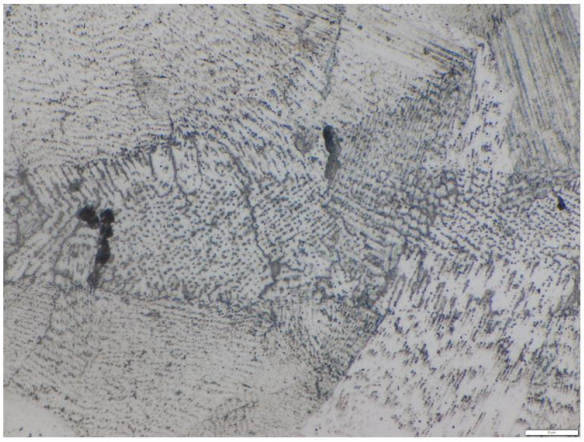

Sample 8184 Scan Boundary 1000x

Fig. 127 – Polished Bulk Scan Boundary Micrographs of Sample 8184 (500x and 1000x)

Polished Scanning Electron Microscopy

Following optical microscopy, the polished samples were inserted into the Hitachi Su-3500 SEM for imaging and energy dispersive spectroscopy. As mentioned above in the procedure section, the imaging schedule for polished samples followed several magnifications of the sample burn tips, the spherical oxides within the burn tips, the solidified melt pool surface oxides, the dendritic crevices in the burn interface (if they were present), the burn interface (both interior as

well as around the direct interface to bulk and melt sides), the bulk, and the outer surface of the bulk regions.

Similar to what was seen in optical microscopy, the sample burn tips tended to display regions of varying solidification directionality. With higher magnification it became clear that these regions also demonstrated differences in hardness, as the polishing process was not visible on darker areas but scratches could be seen in lighter ones (as seen below for sample 8174).

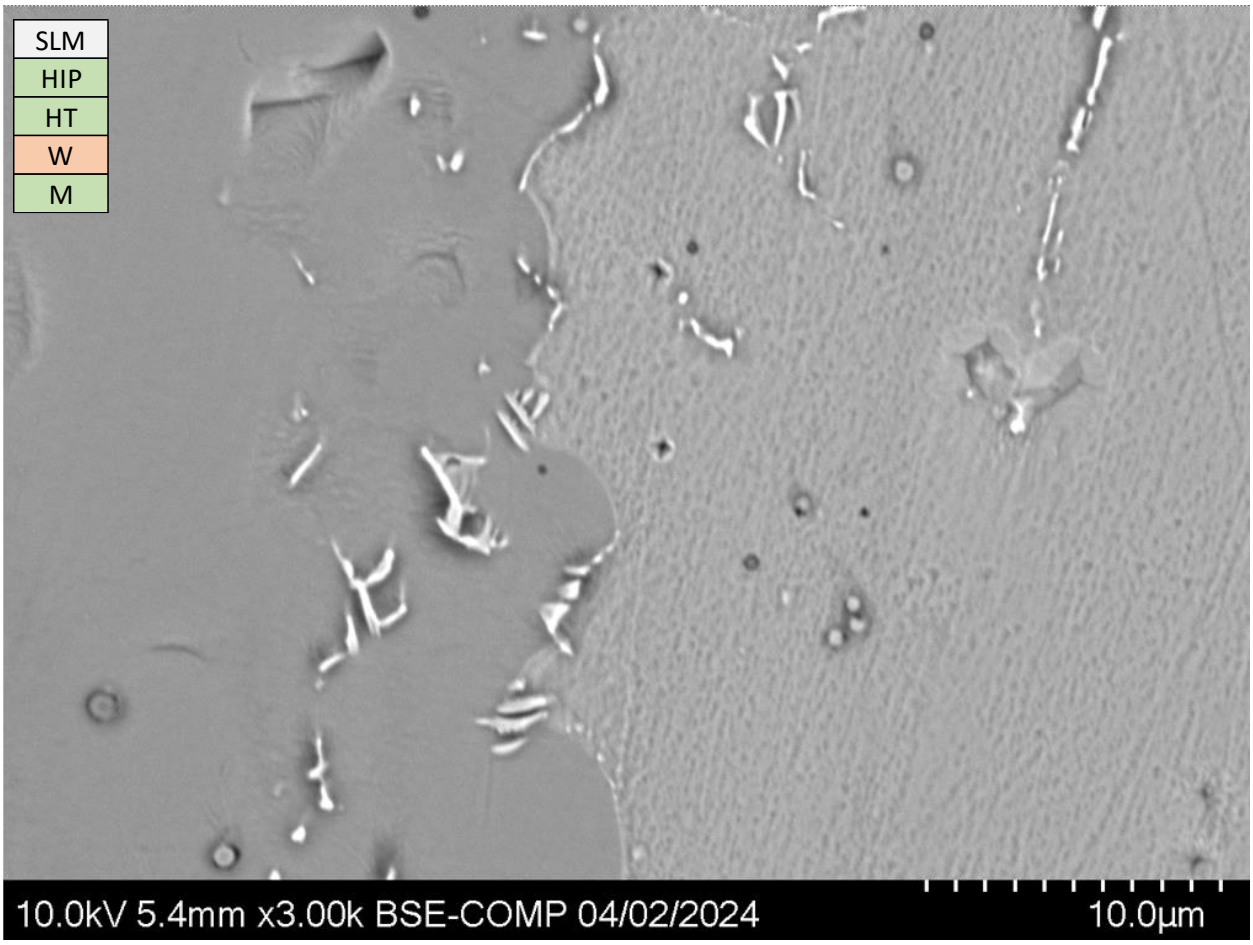

Fig. 128 – Polished Burn Tip SEM Micrograph of Sample 8174 (3000x)

What was most clearly obvious after polished SEM imaging was that virtually all of the samples exhibit very fine stringed structures throughout the burn tip which were later confirmed through EDS to be primarily composed of niobium. Representative examples of these structures are shown below next to macroscopic views of their burn tips.

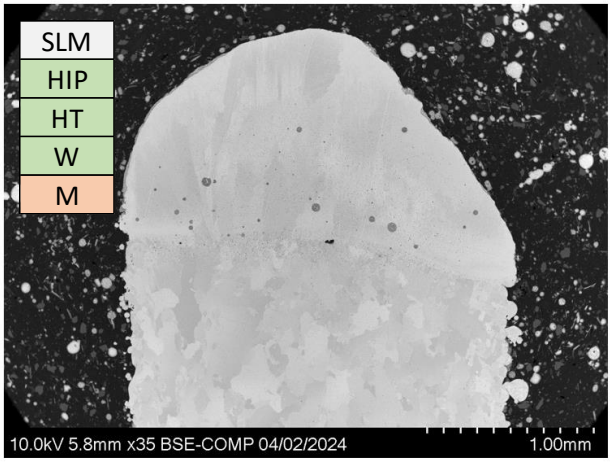

Sample 8044 Burn Tip 35x

Sample 8044 Burn Tip 3000x

Fig. 129 – Polished Burn Tip SEM Micrographs of Sample 8044 (35x and 3000x)

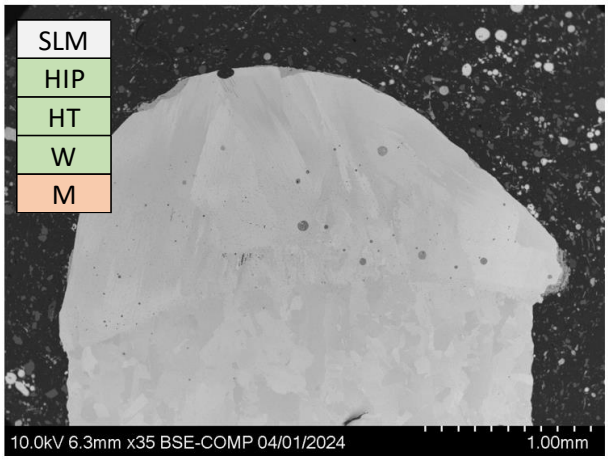

Sample 8522 Burn Tip 35x

Sample 8522 Burn Tip 3000x

Fig. 130 – Polished Burn Tip SEM Micrographs of Sample 8522 (35x and 3000x)

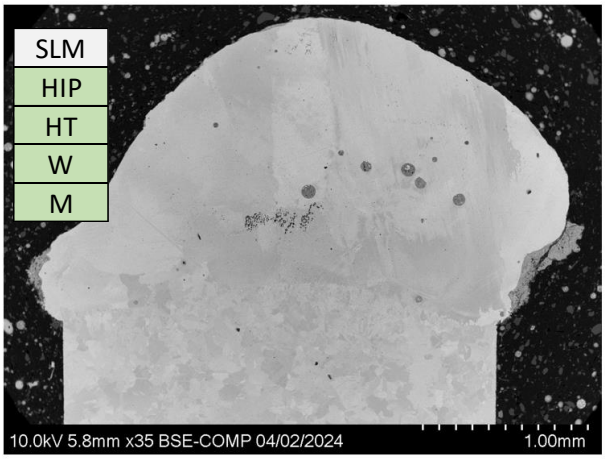

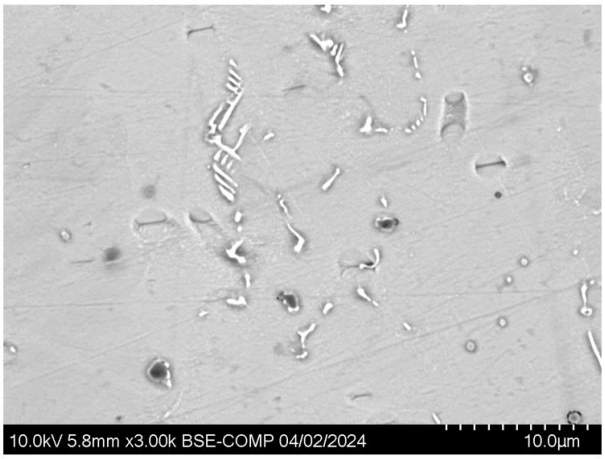

Sample 8158 Burn Tip 35x

Sample 8158 Burn Tip 3000x

Fig. 131 – Polished Burn Tip SEM Micrographs of Sample 8158 (35x and 3000x)

Within the burn tip region, spherical oxides were present and subsequently imaged. These oxides did vary in size, but generally existed in the range of 40 – 100 µm in diameter. They typically contained a light and dark phase, and through EDS these phases were found to be higher in niobium and titanium (for lighter regions) and aluminum and oxygen (for darker regions). These oxides show large plates of the Al-O rich regions surrounded by a matrix of the lighter Nb-Ti oxide material, with what can be described as lamella of the Al-O rich oxide propagating within. Some characteristic examples are included below.

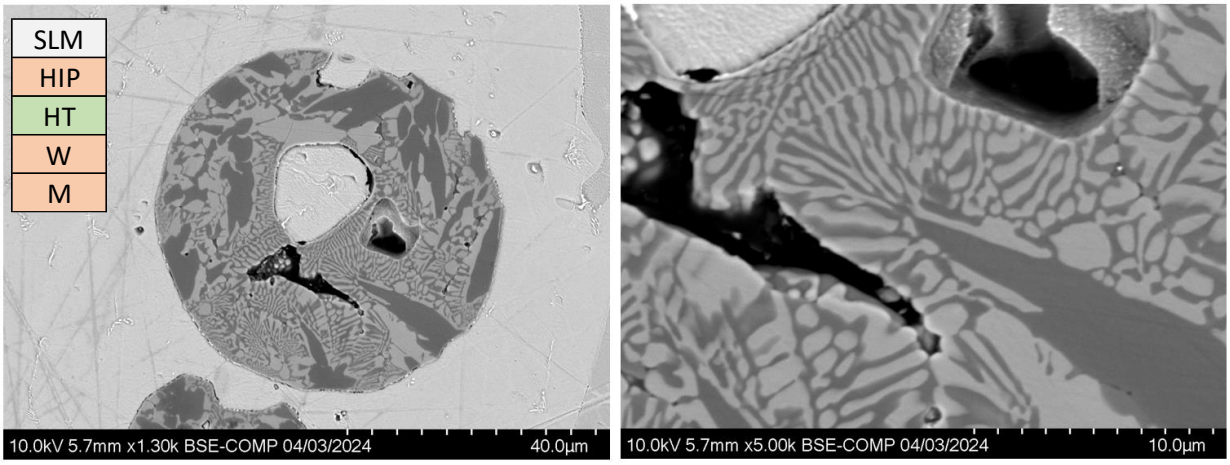

Sample 7670 Burn Tip Oxide 1300x Sample 7670 Burn Tip Oxide 5000x

Fig. 132 – Polished Burn Tip Oxide SEM Micrographs of Sample 7670 (1300x and 5000x)

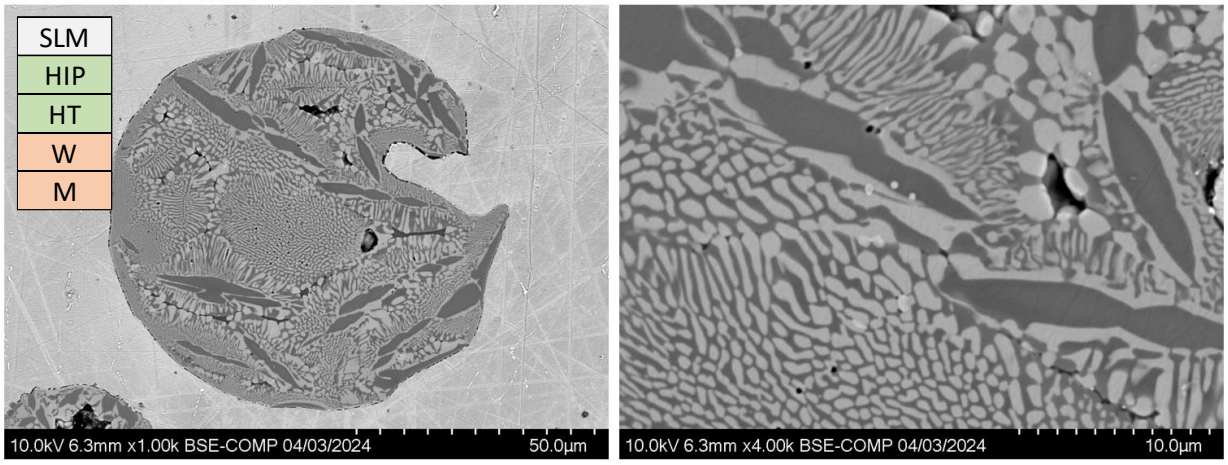

Sample 8488 Burn Tip Oxide 1000x Sample 8488 Burn Tip Oxide 4000x

Fig. 133 – Polished Burn Tip Oxide SEM Micrographs of Sample 8488 (1000x and 4000x)

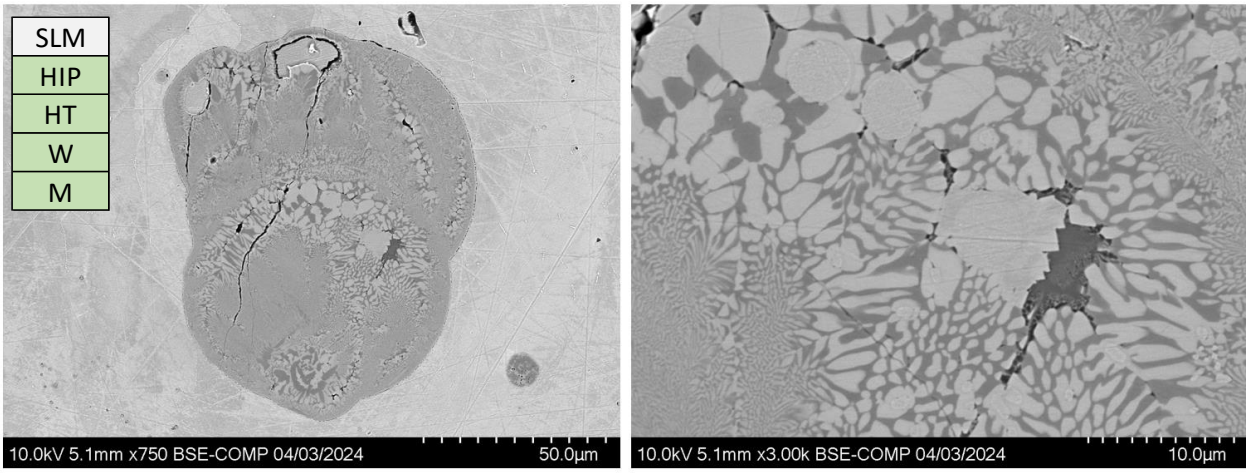

Sample 8531 Burn Tip Oxide 750x Sample 8531 Burn Tip Oxide 3000x

Fig. 134 – Polished Burn Tip Oxide SEM Micrographs of Sample 8531 (750x and 3000x)

There were a few exceptions to the standard seen throughout sample set 1 for the spherical burn tip oxides, two rods exhibited oxides that were porous in their centers or appeared to collapse in on themselves. Sample 8174 had several oxides within its' burn tip whose centers were porous, and sample 8531 showed an oxide that appeared to collapse in on itself – leaving behind a "pinecone like" inner structure. Demonstrative micrographs of such features are shown below.

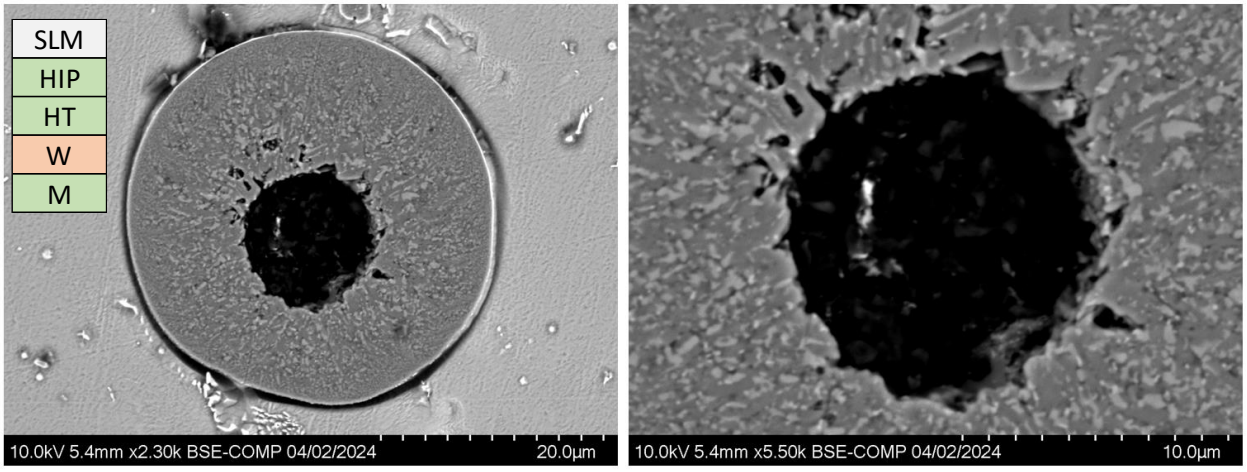

Sample 8174 Burn Tip Oxide 2300x Sample 8174 Burn Tip Oxide 5500x

Fig. 135 – Polished Burn Tip Oxide SEM Micrographs of Sample 8174 (2300x and 5500x)

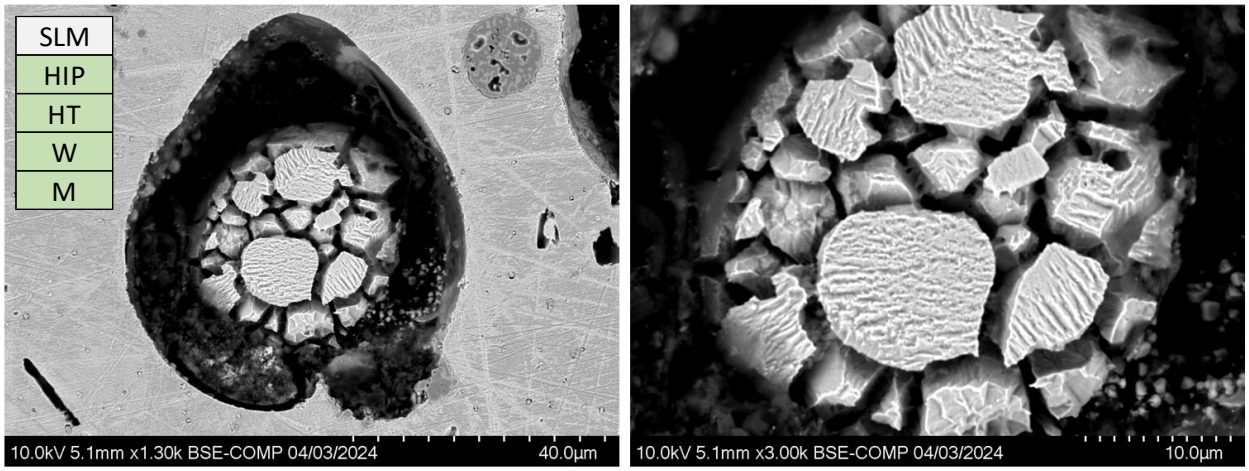

Sample 8531 Burn Tip Oxide 1300x | Sample 8531 Burn Tip Oxide 3000x

Fig. 136 – Polished Burn Tip Oxide SEM Micrographs of Sample 8531 (1300x and 3000x)

Along the outer perimeter of the burn tips, solidified melt pool surface oxides were also observed and imaged. The composition of these features follows what was seen for the spherical oxides seen in the burn tip - the lighter regions were rich in niobium and titanium while the darker areas had higher concentrations of aluminum and oxygen. The thickness of such oxide layers was generally shallow (approximately 25-30 µm), but they were non-homogenously distributed along the melt pool surface and could be thicker in some areas while completely absent in others.

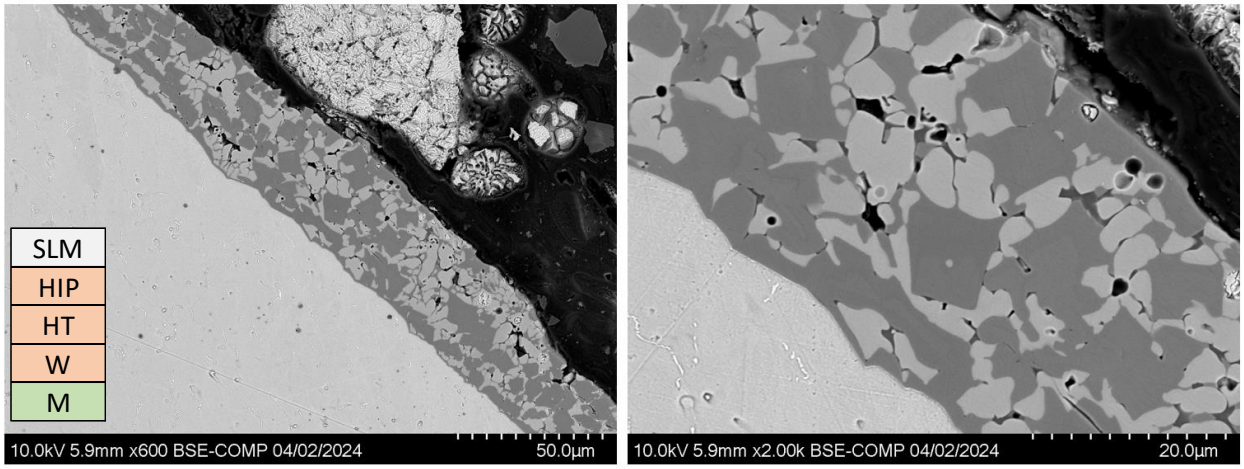

Sample 8065 Solidified Melt Pool Surface Oxide 600x | Sample 8065 Solidified Melt Pool Surface Oxide 2000x

Fig. 137 – Polished SMPS Oxide SEM Micrographs of Sample 8065 (600x and 2000x)

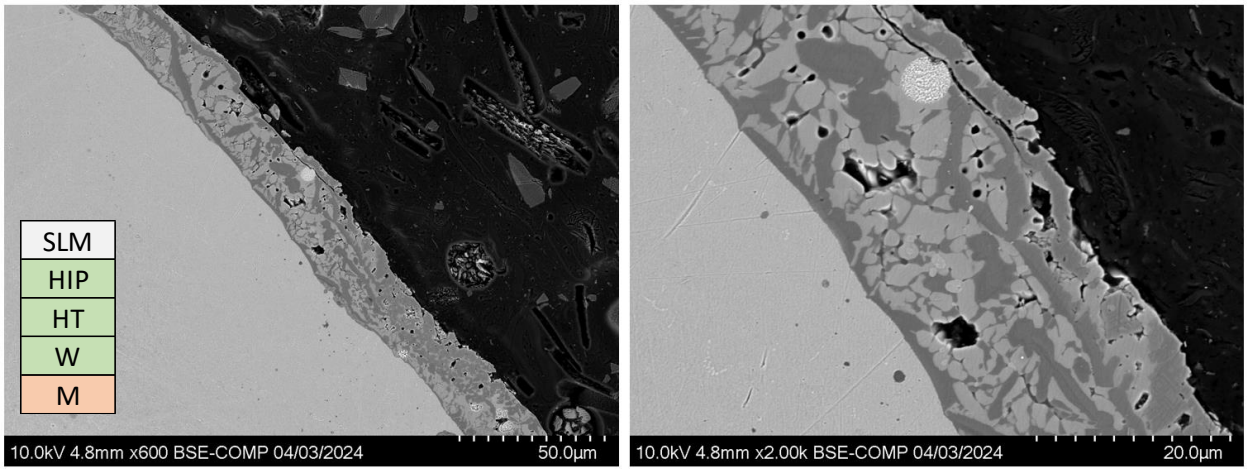

Sample 8082 Solidified Melt Pool Surface Oxide 600x | Sample 8082 Solidified Melt Pool Surface Oxide 2000x

Fig. 138 – Polished SMPS Oxide SEM Micrographs of Sample 8082 (600x and 2000x)

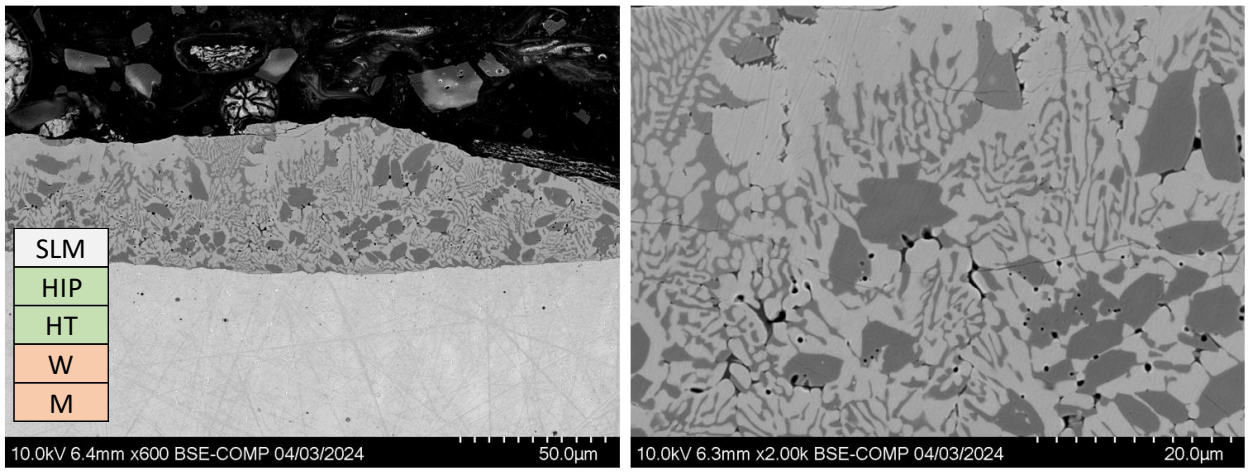

Sample 8488 Solidified Melt Pool Surface Oxide 600x | Sample 8488 Solidified Melt Pool Surface Oxide 2000x

Fig. 139 – Polished SMPS Oxide SEM Micrographs of Sample 8488 (600x and 2000x)

Dendritic crevices were seen in slightly more than half of the sample set 1 rods (9 had them and 7 did not). They appeared to follow the same ordering and pattern as the niobium structures seen throughout the burn tips, though themselves appeared to be concentrated to the center of the burn tips and adjacent to the burn interface. At higher magnifications it can be seen that the crevices seem to be areas of material pull-out, with clear indications of an attempt by the material to lower its surface energy as the residual holes left behind can be highly angular with sharp geometries.

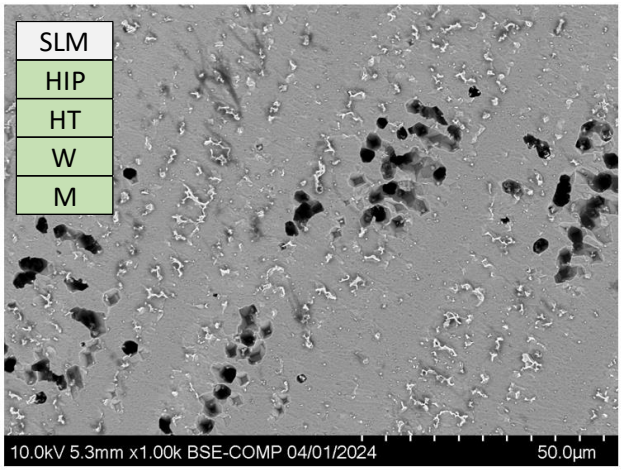

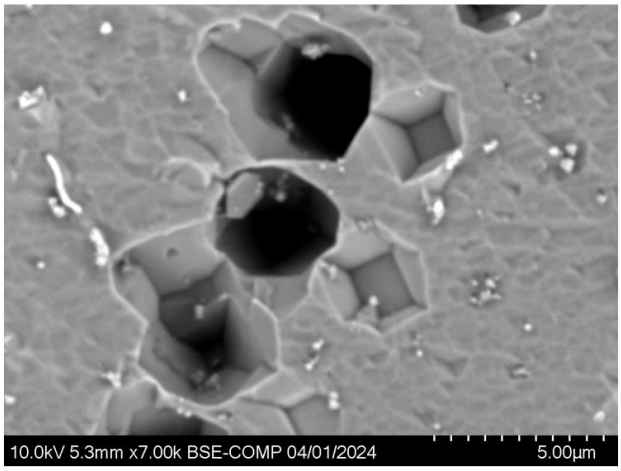

Sample 8544 Burn Tip Crevices 1000x

Sample 8544 Burn Tip Crevices 7000x

Fig. 140 – Polished Burn Tip Crevice SEM Micrographs of Sample 8544 (1000x and 7000x)

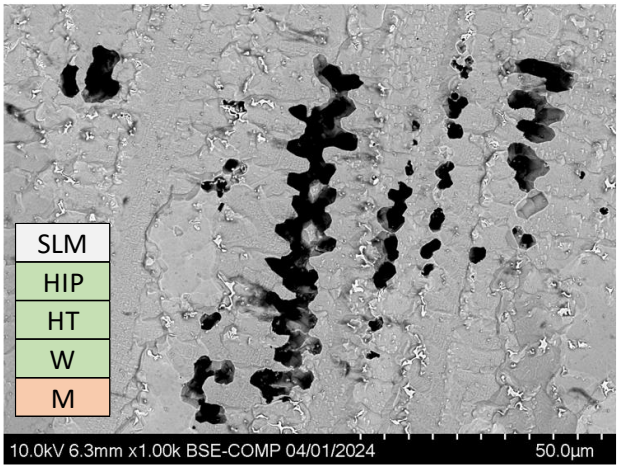

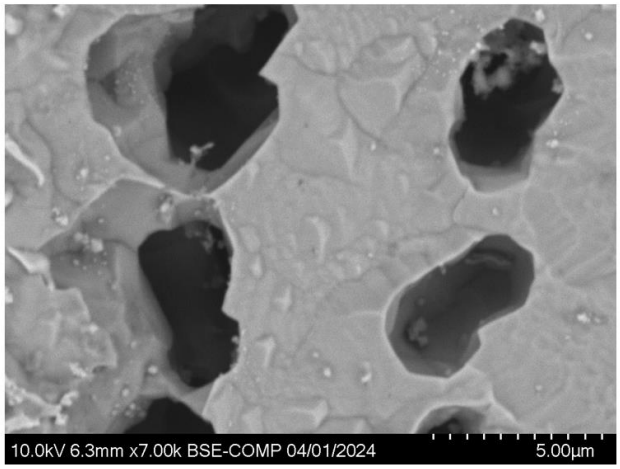

Sample 8522 Burn Tip Crevices 1000x

Sample 8522 Burn Tip Crevices 7000x

Fig. 141 – Polished Burn Tip Crevice SEM Micrographs of Sample 8522 (1000x and 7000x)

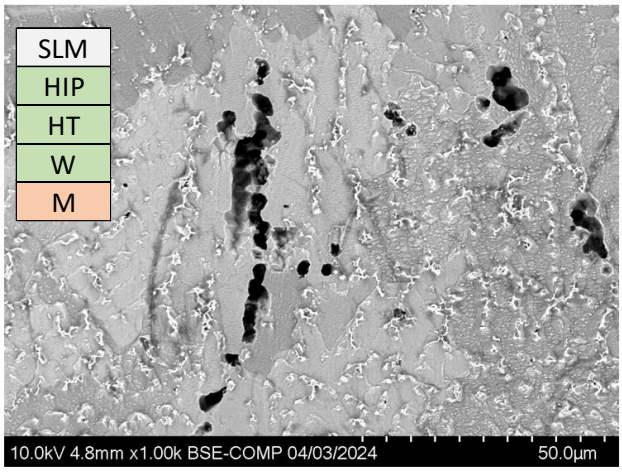

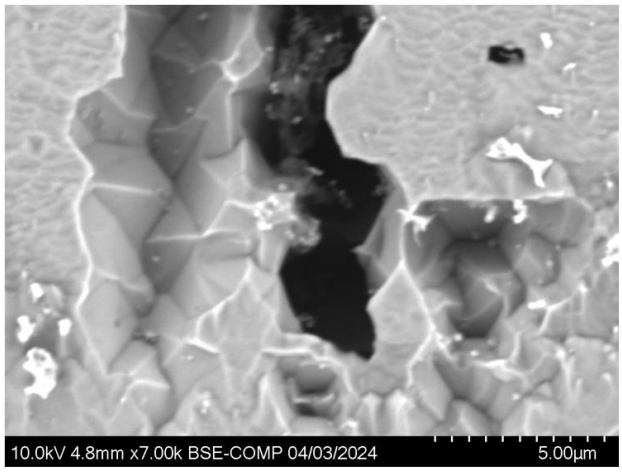

Sample 8082 Burn Tip Crevices 1000x

Sample 8082 Burn Tip Crevices 7000x

Fig. 142 – Polished Burn Tip Crevice SEM Micrographs of Sample 8082 (1000x and 7000x)

With regards to sample burn interfaces, three areas of interest were imaged as initial observations identified that the center of such interfaces and their respective melt tip and bulk adjoining sides are distinct from each other. Both the melt tip and bulk sides of the burn interface were imaged at 800x in order to demonstrate the shift in structure between the regions, whereas the center of the interface was imaged at 2000x to show similarities to the niobium structures seen throughout the burn tip.

Typically, the side of the interface which transitions to the bulk is coarse and rocky while the opposite end of the interface (melt tip side) sees a gradual decline in concentration of the niobium structures coupled with nodule-like holes which are finely dispersed. Examples representative of these observations can be seen below.

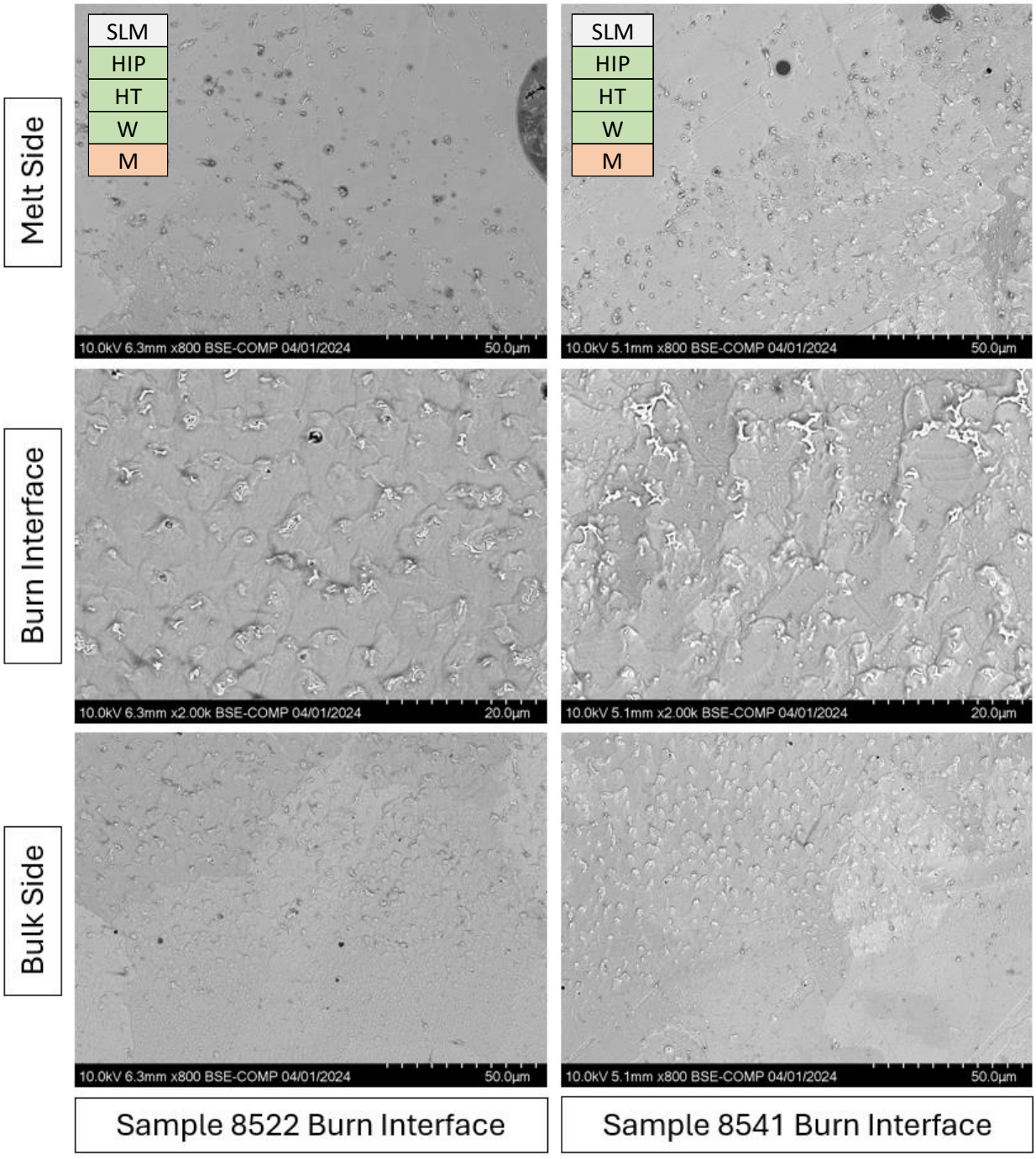

Fig. 143 – Polished Burn Interface SEM Micrographs for Samples 8522 and 8541 (800x for bulk and melt sides, 2000x for center)

Bulk microstructures were documented as being essentially what was seen with optical microscopy – binary phase austenitic matrices with annealing twins and acicular precipitates (a result of the stress-relieving heat treatment during processing) present throughout. The “green

state" samples (8065 and 8184) displayed as-printed characteristics such as rastered melt-pools and dendritic inter-scan boundary layers. At least one sample (7679) also exhibited strings of embedded niobium-molybdenum deposits.

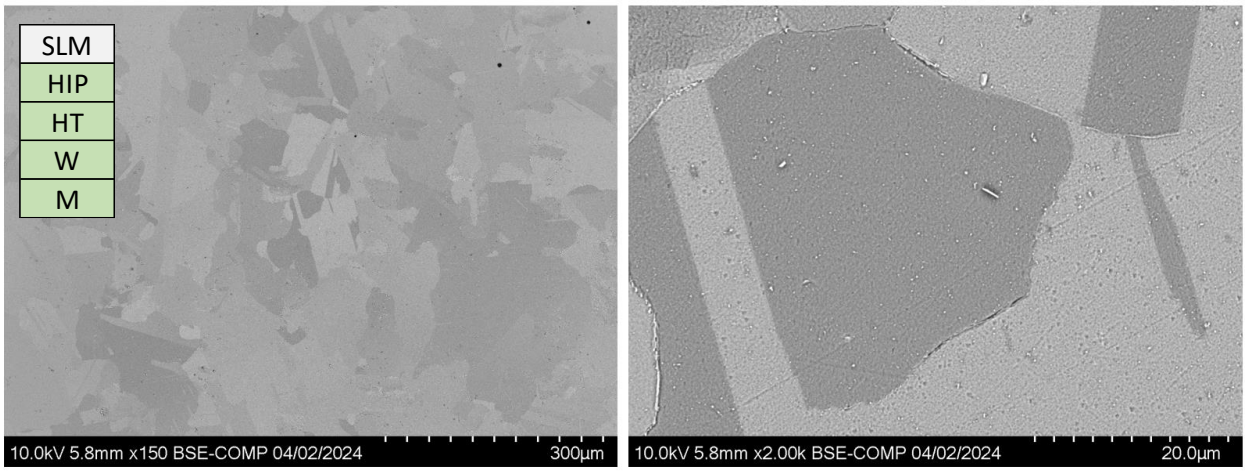

Sample 8158 Bulk 150x | Sample 8158 Bulk 2000x

Fig. 144 – Polished Bulk SEM Micrographs of Sample 8158 (150x and 2000x)

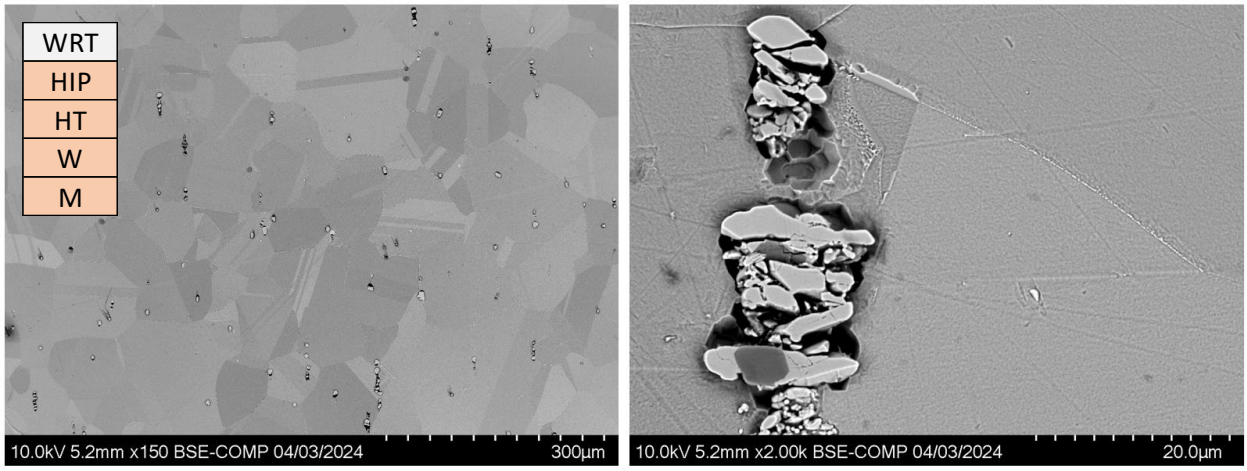

Sample 7679 Bulk 150x | Sample 7679 Bulk 2000x

Fig. 145 – Polished Bulk SEM Micrographs of Sample 7679 (150x and 2000x)

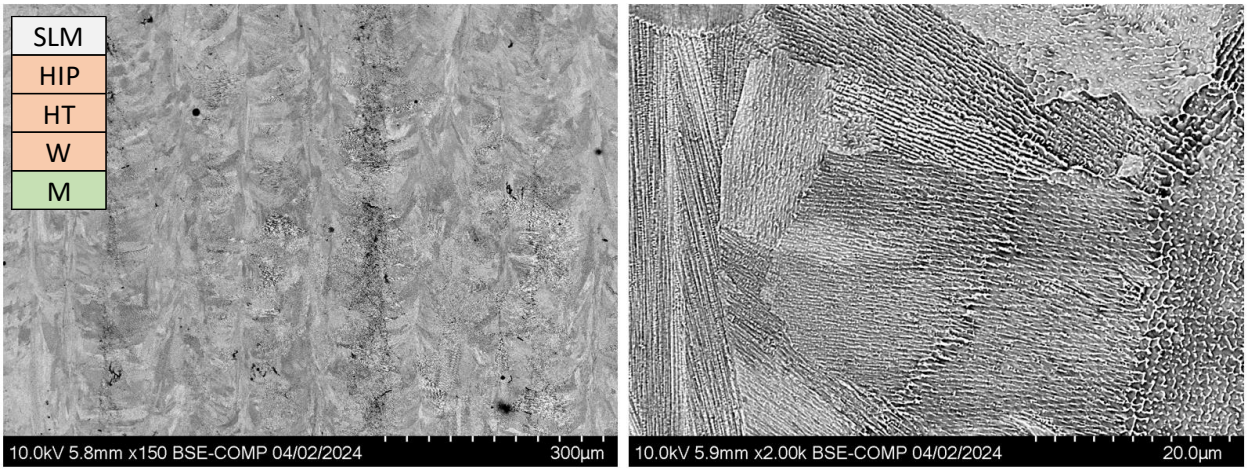

Fig. 146 – Polished Bulk Sem Micrographs of Sample 8065 (150x and 2000x)

The outer surface of the bulk regions tended to reflect what was seen at the interior of the bulk, with the only differences truly being observed with EDS in the following section with samples that had wrapping in conjunction with hot isostatic pressing.

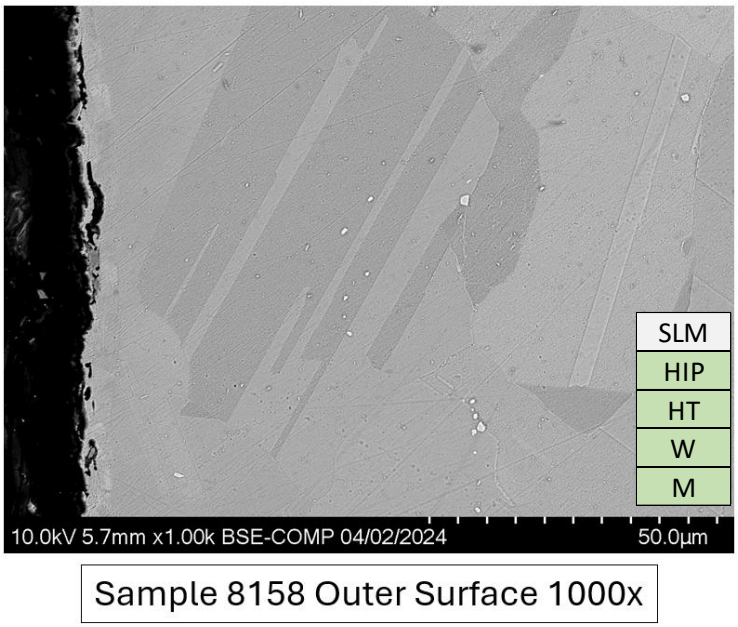

Fig. 147 – Polished Outer Surface SEM Micrograph of Sample 8158 (1000x)

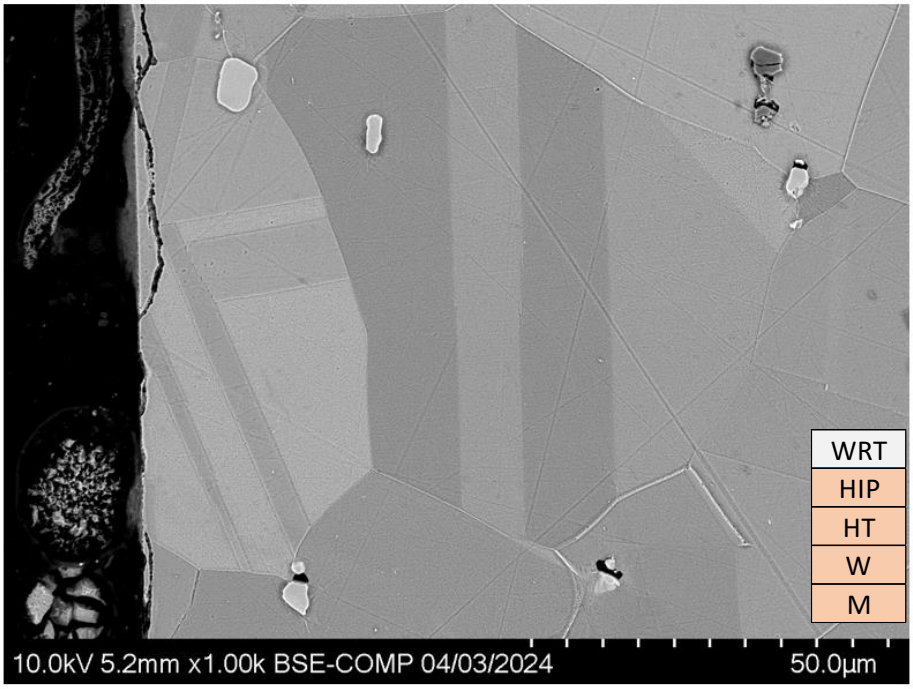

Sample 7679 Outer Surface 1000x

Fig. 148 – Polished Outer Surface SEM Micrograph of Sample 7679 (1000x)

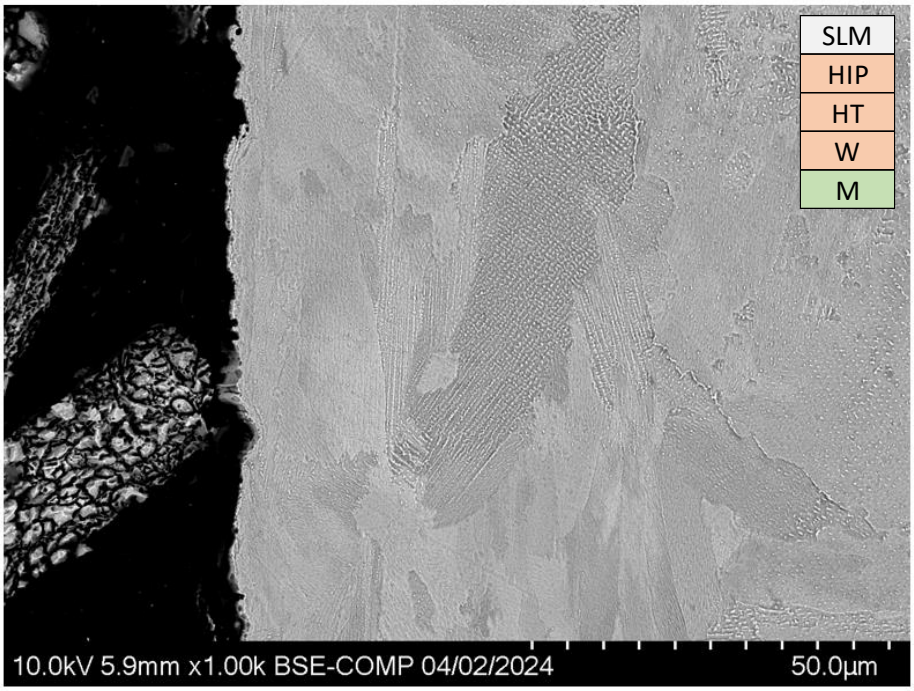

Sample 8065 Outer Surface 1000x

Fig. 149 – Polished Outer Surface SEM Micrograph of Sample 8065 (1000x)

Polished Energy Dispersive Spectroscopy

Upon completion of the polished rods SEM imaging, EDS was conducted as per the schedule described above in the procedure section. The burn tips were mapped and point scanned (to estimate quantitative differences from the bulk), the spherical oxides were mapped and point scanned (to confirm constituents of the light and dark phases contained within them), the burn interface was mapped and also line scanned (to track elemental trends through the interface, thus analogizing relative diffusion characteristics), and the outer surface of the rods was also mapped and point scanned to identify any deviations from the bulk material. Mapping was also conducted on the bulk of the rods, but yielded no discernible conclusions as the interior of the rods were found to be roughly homogenous throughout. The point scans in the bulk were useful however in corroborating the chemical analysis conducted within the x-ray fluorescence section above.

Sample burn tips maps were characterized by a depletion of chromium (coupled with the thin concentrated layer on the burn tip surface) and a concentration of nickel. Niobium contributed towards oxides, more heavily so those existing on the burn tip surface, and at times overlapped with molybdenum. Aluminum and titanium could also be seen overlapping with each other as they comprised a majority of the spherical oxides contained in the area. Spectra and tabularized data show that the burn tip region saw an estimated increase of nickel content from approximately 50% in the bulk to 65-70%. Iron content generally stayed consistent or decreased slightly, while chromium typically saw a decrease in concentration from approximately 18% to below 10%. As these trends were common across all samples, a few representatives are included below.

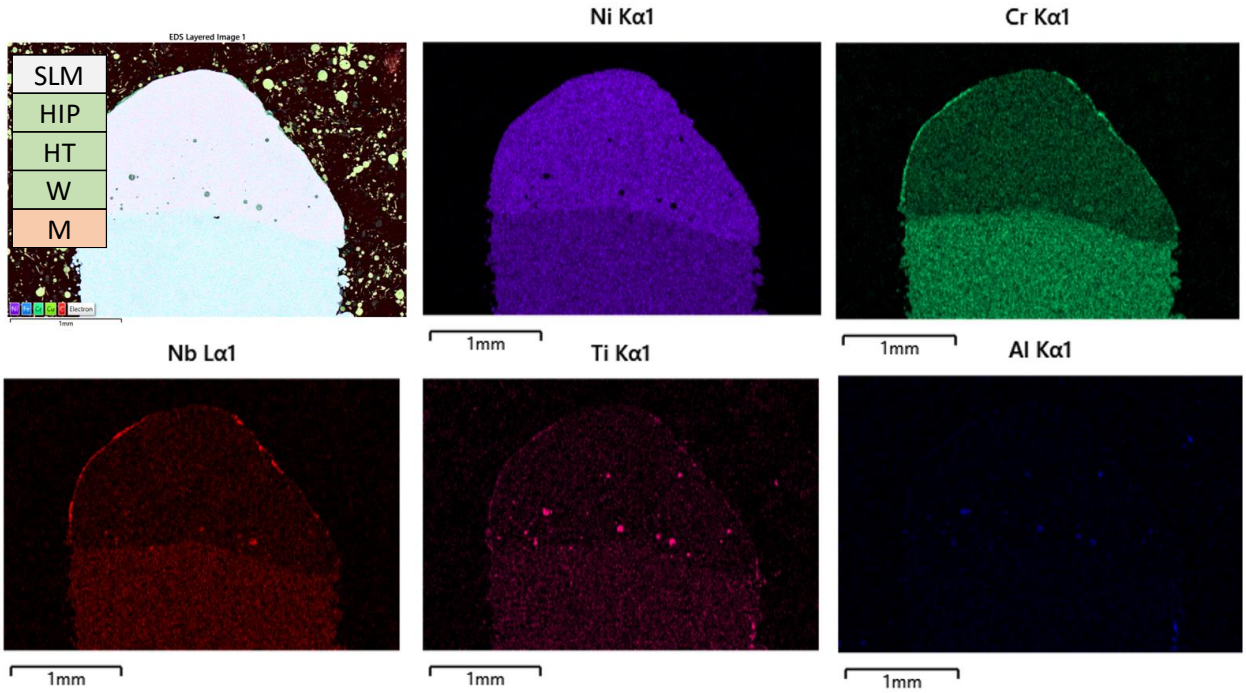

Fig. 150 – Polished Burn Tip EDS Maps of Sample 8044 (35x)

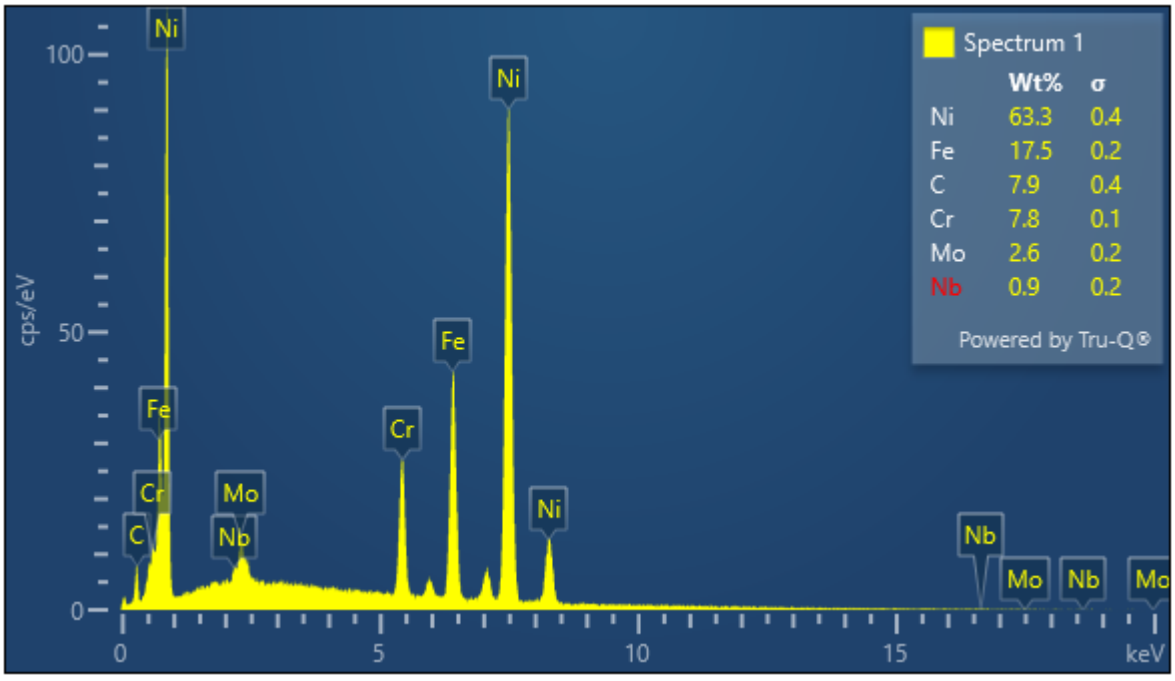

Fig. 151 – Polished Burn Tip EDS Spectra with Weight Percentages of Sample 8044

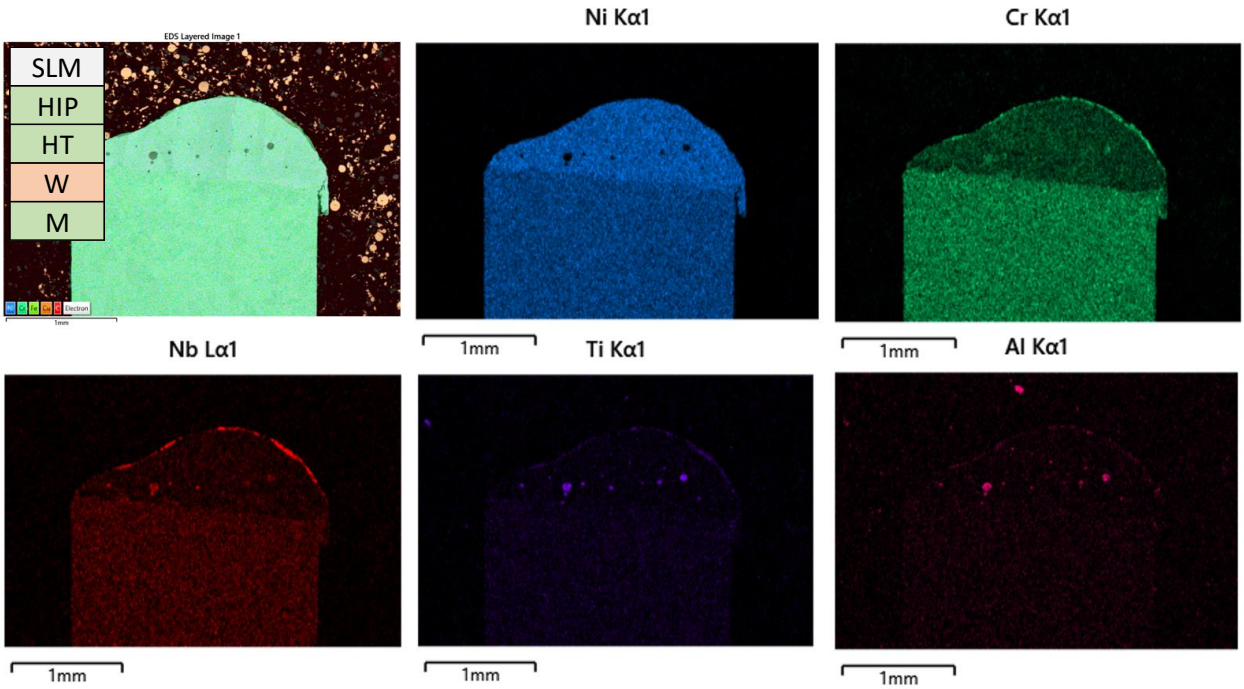

Fig. 152 – Polished Burn Tip EDS Maps of Sample 8174 (35x)

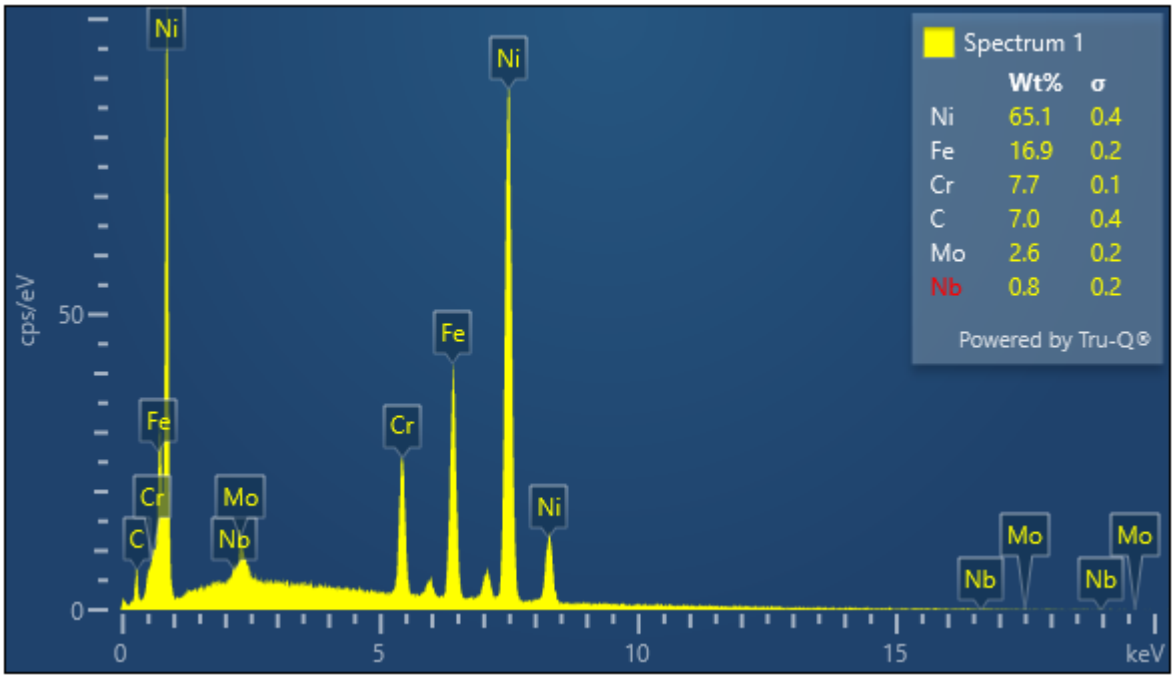

Fig. 153 – Polished Burn Tip EDS Spectra with Weight Percentages of Sample 8174

The spherical oxides in the sample burn tips are dual phase, with a lighter oxide constituent comprised of niobium and titanium and a darker oxide constituent comprised of aluminum and chromium. The oxygen present seems more highly concentrated in the Al-Cr phase, as evidenced by the EDS maps below. The spectra and weight percentages generated from these oxides corroborate these statements and are included with their respective oxide maps.

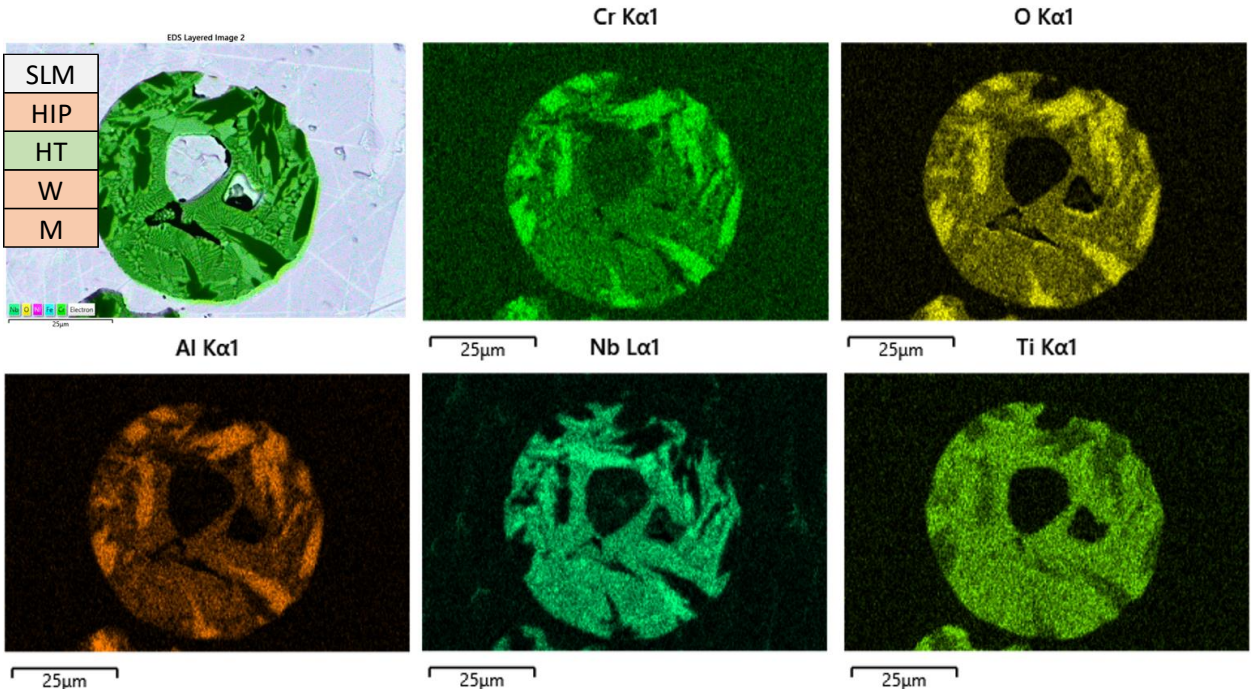

Fig. 154 – Polished Spherical Oxide EDS Maps of Sample 7670 (1300x)

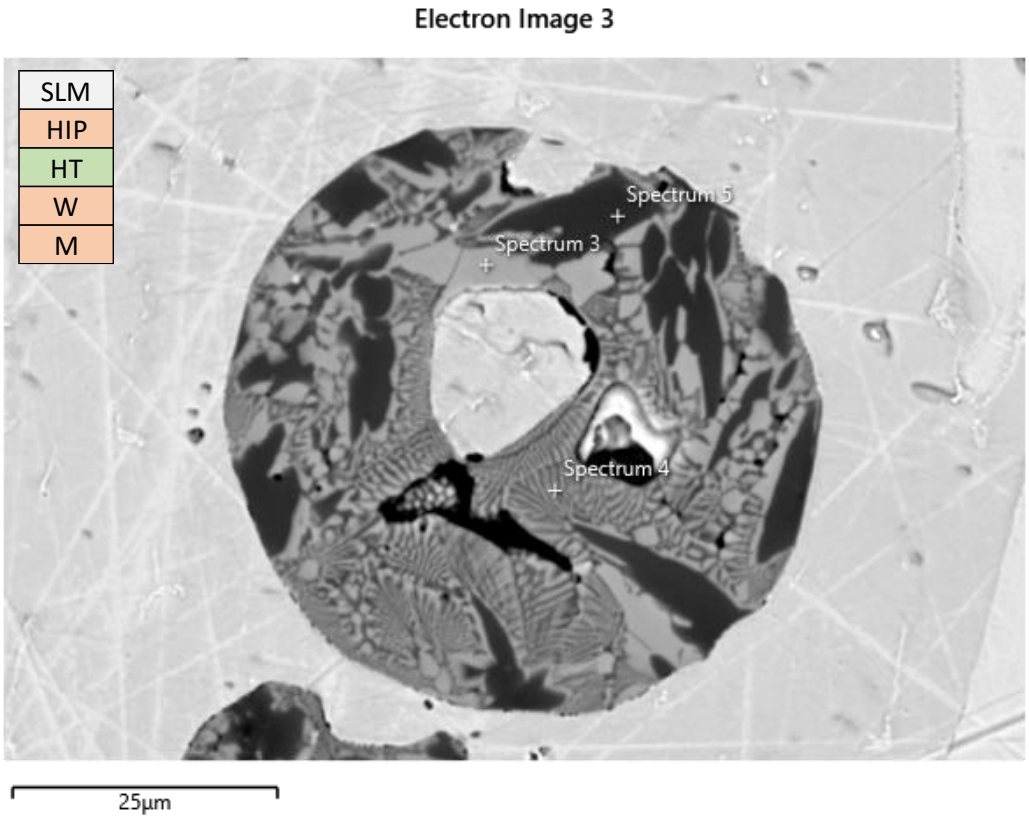

Fig. 155 – Polished Spherical Oxide EDS Point Scan Locations for Sample 7670 (1300x)

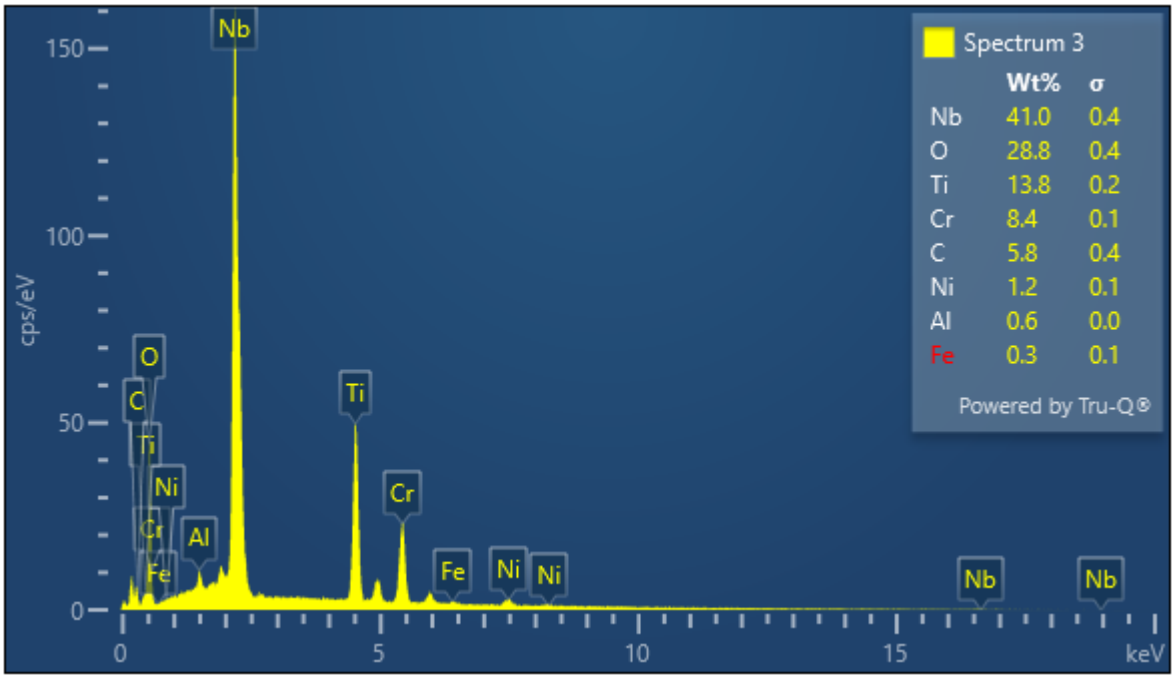

Fig. 156 – EDS Point Scan Spectra with Weighted Percentages for Light Phase Oxide, Sample 7670

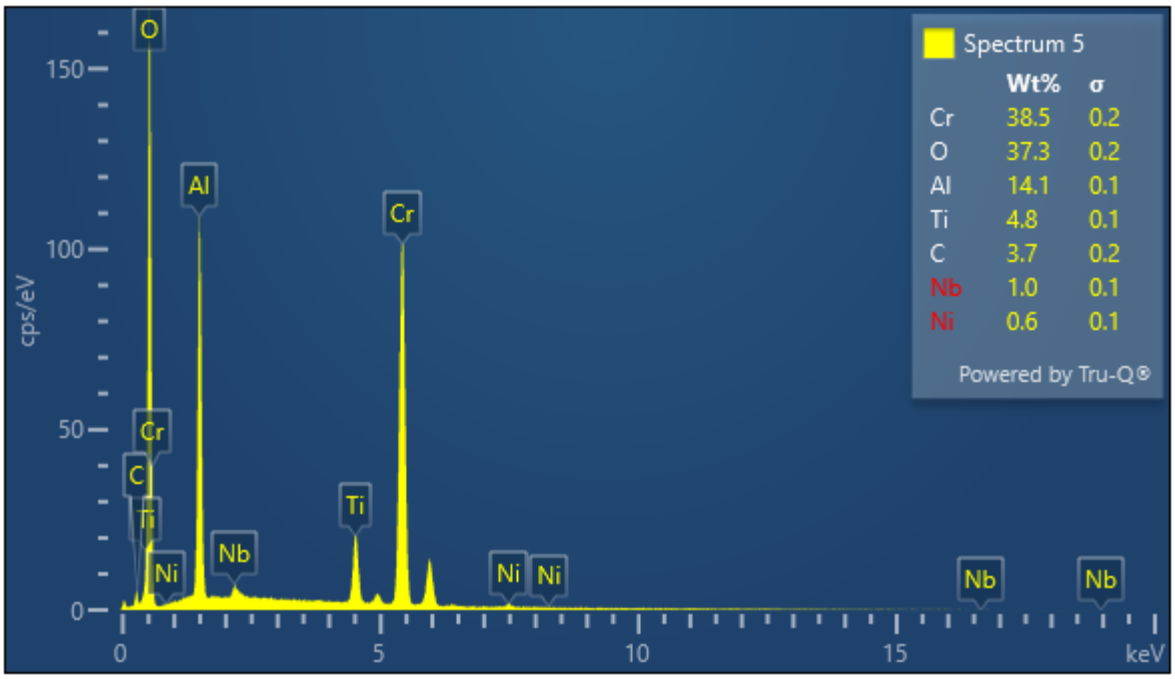

Fig. 157 – EDS Point Scan Spectra with Weight Percentages for Dark Phase Oxide, Sample 7670

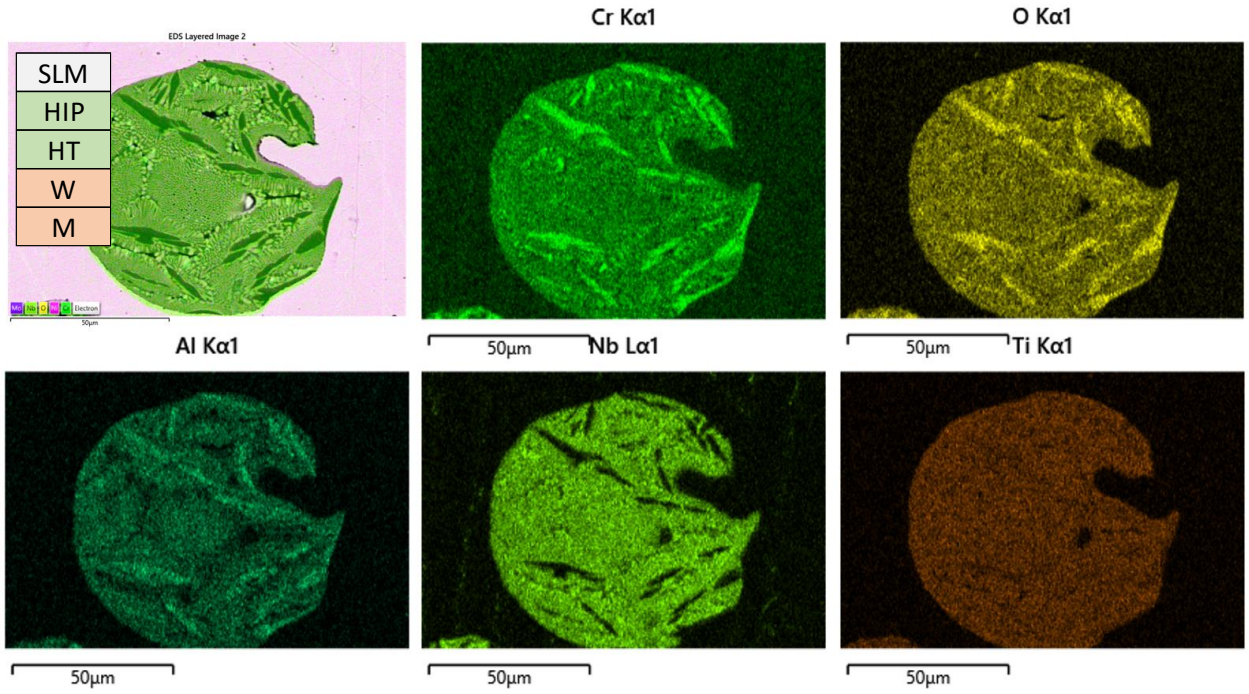

Fig. 158 – Polished Spherical Oxide EDS Maps of Sample 8488 (1000x)

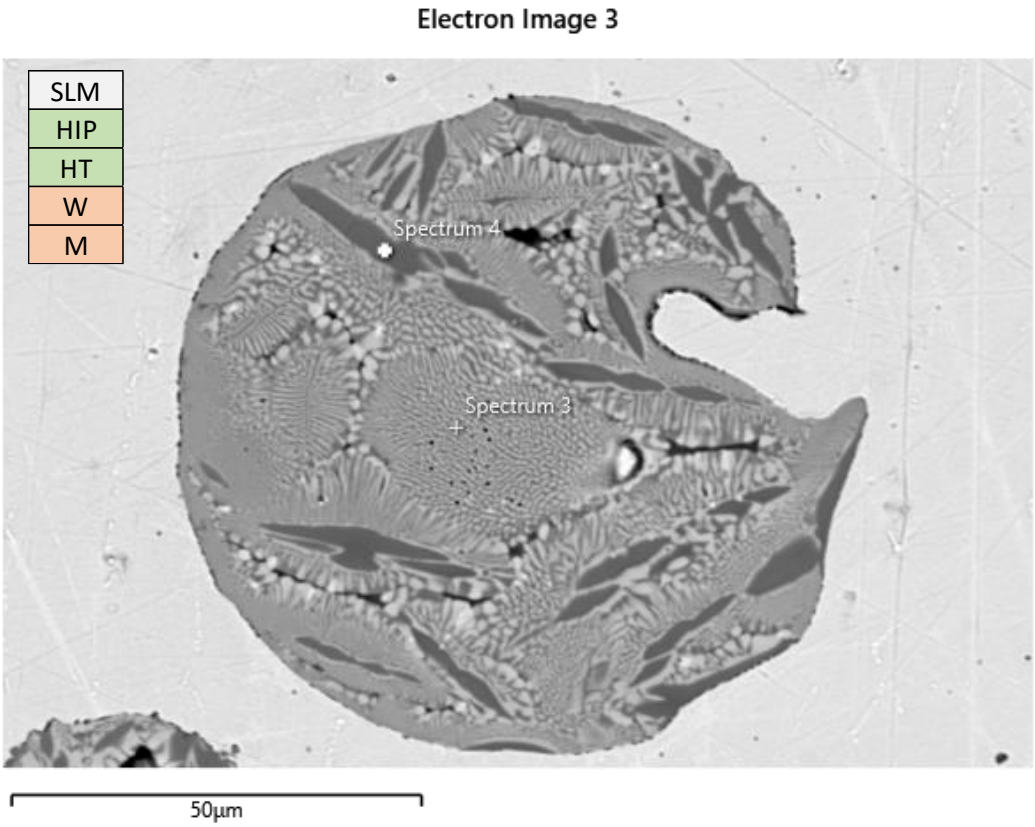

Fig. 159 – Polished Spherical Oxide EDS Point Scan Locations for Sample 8488 (1000x)

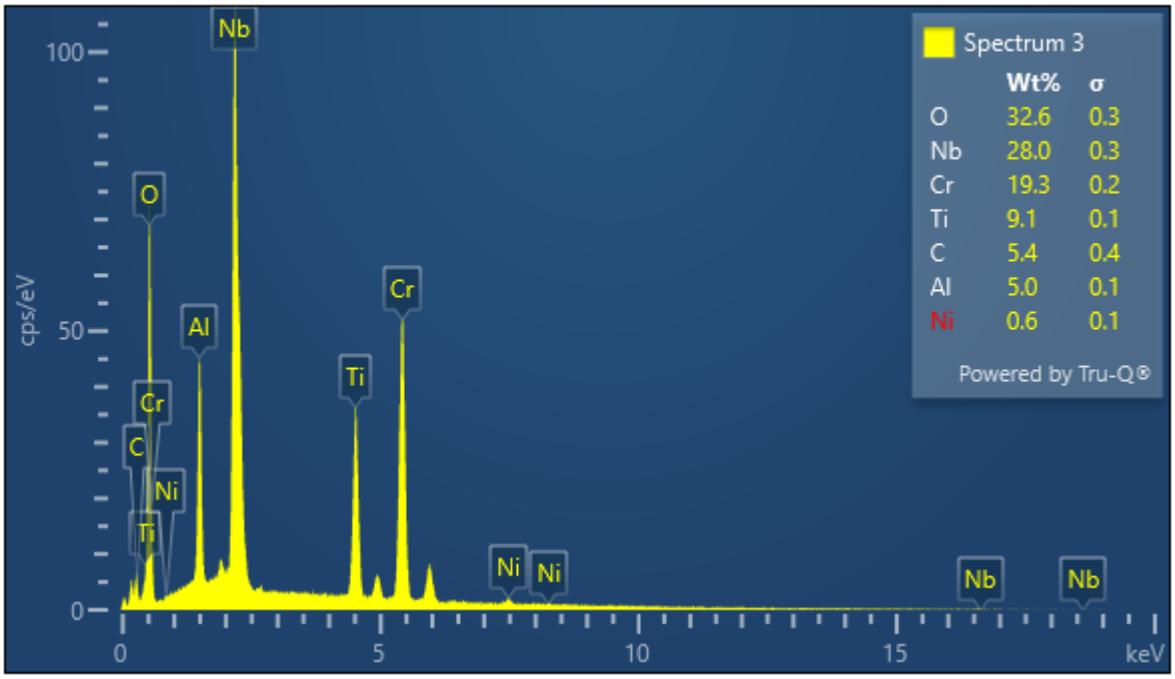

Fig. 160 – EDS Point Scan Spectra with Weight Percentages for Light Phase Oxide, Sample 8488

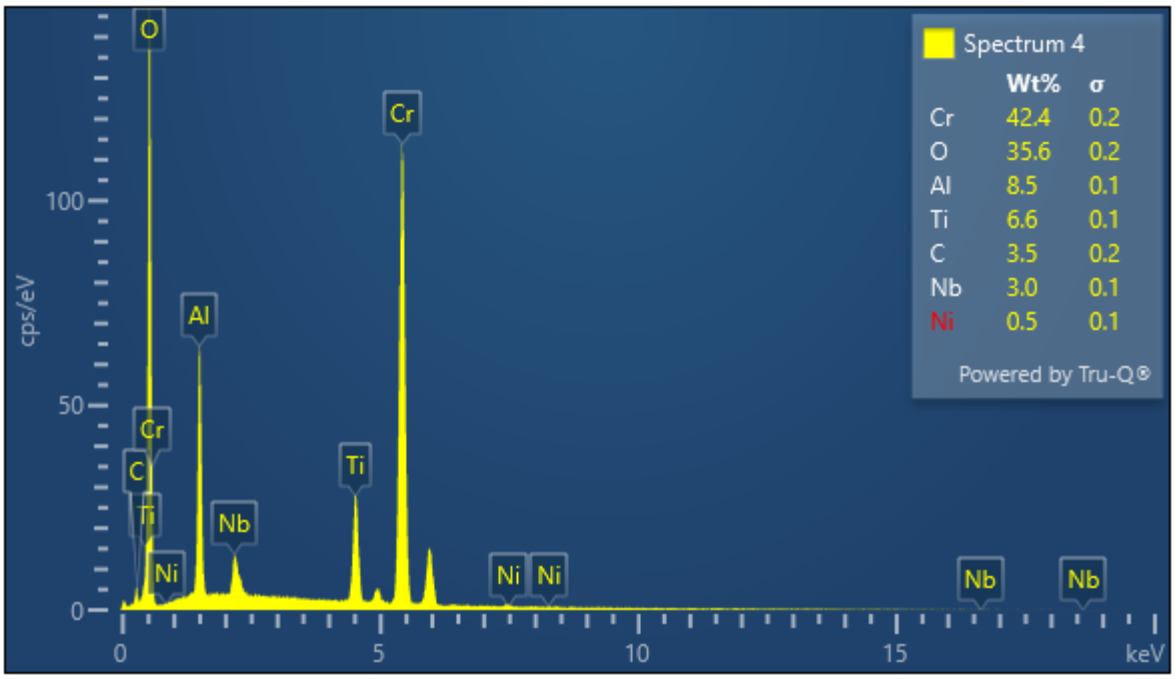

Fig. 161 – EDS Point Scan Spectra with Weight Percentages for Dark Phase Oxide, Sample 8488

EDS mapping and line-scans of sample burn interfaces reinforce what has been seen in previous analysis, namely that as one travels from the bulk to the burn tip there's a negative gradient of chromium and niobium and a positive gradient of nickel. The line-scan analysis in particular also shows that for many samples the detected molybdenum intensity flattens out once one reached the burn tip area.

The niobium dendrites that have been seen previously were line-scanned at high magnification for one sample (8522) which interestingly displayed that in terms of intensity the dendrites seemed to be almost the same amount molybdenum as niobium.

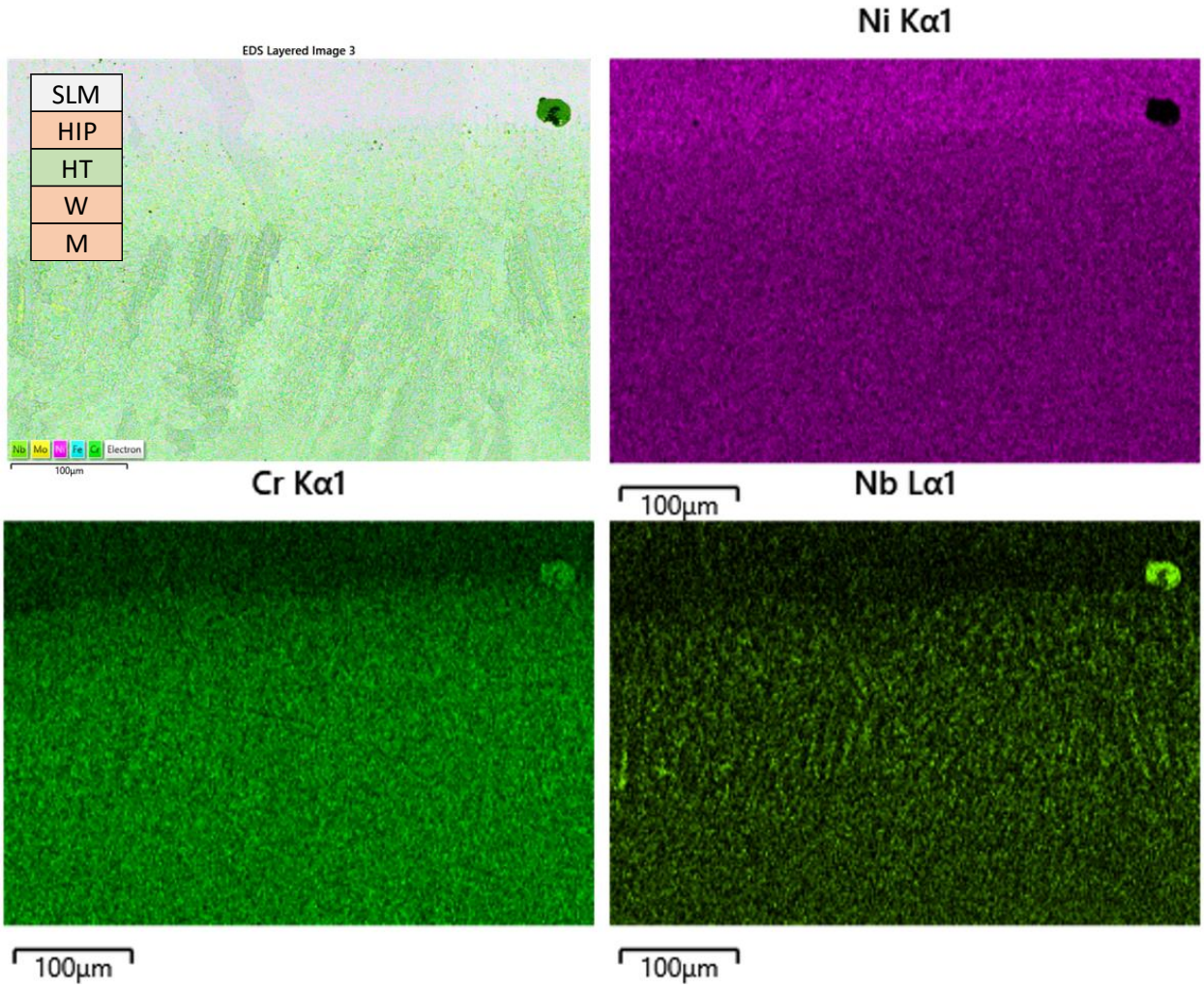

Fig. 162 – Polished Burn Interface EDS Maps of Sample 7670 (250x)

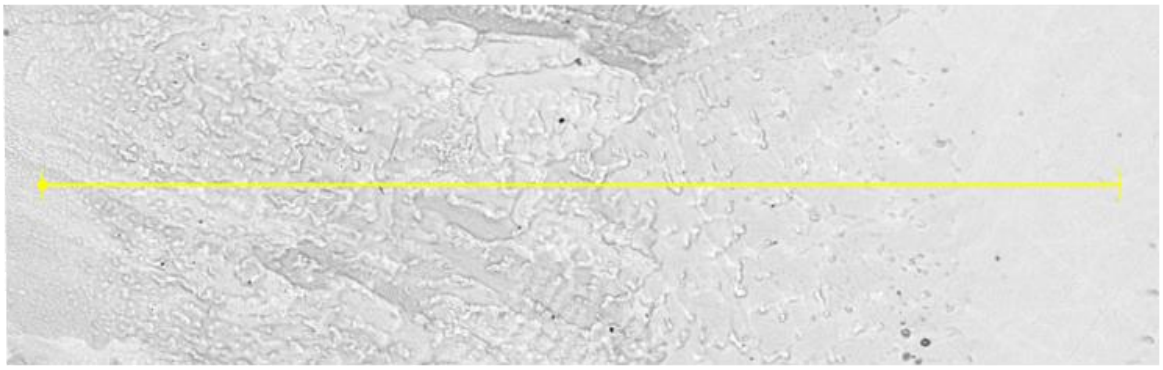

Fig. 163 – Burn Interface EDS Line Scan Reference Image for Sample 7670 (left bulk to right burn tip)

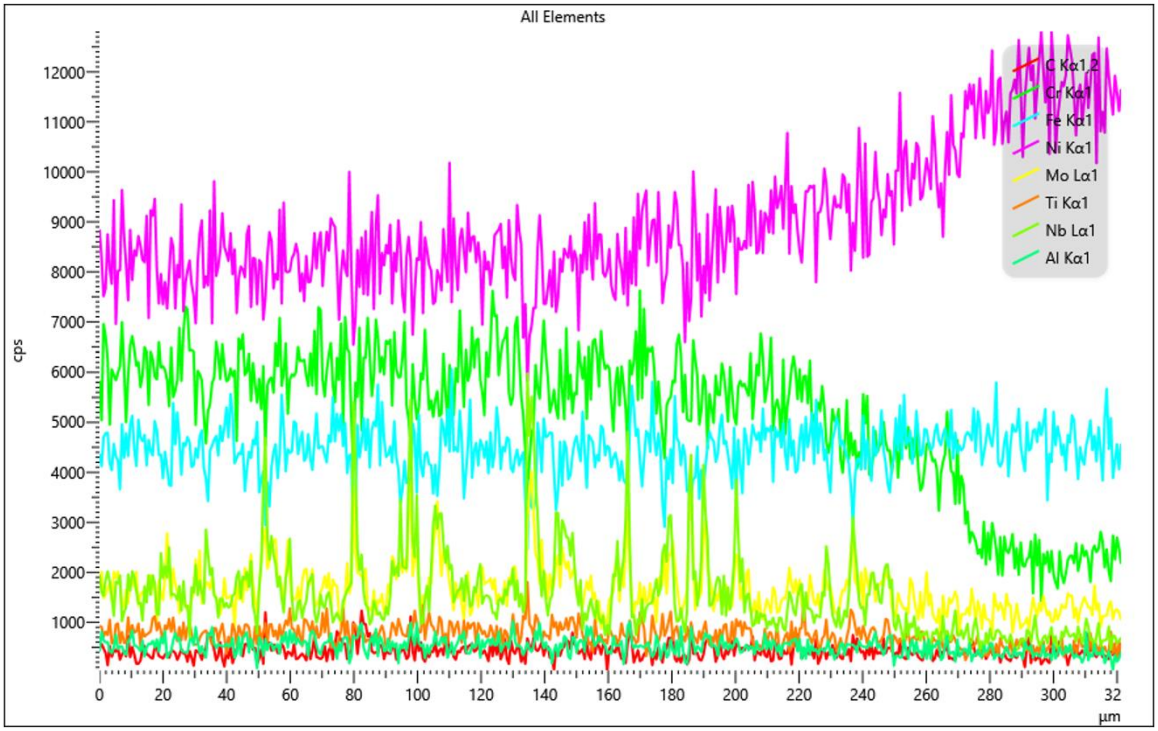

Fig. 164 – Burn Interface Stacked Line Scan EDS Spectra for Sample 7670

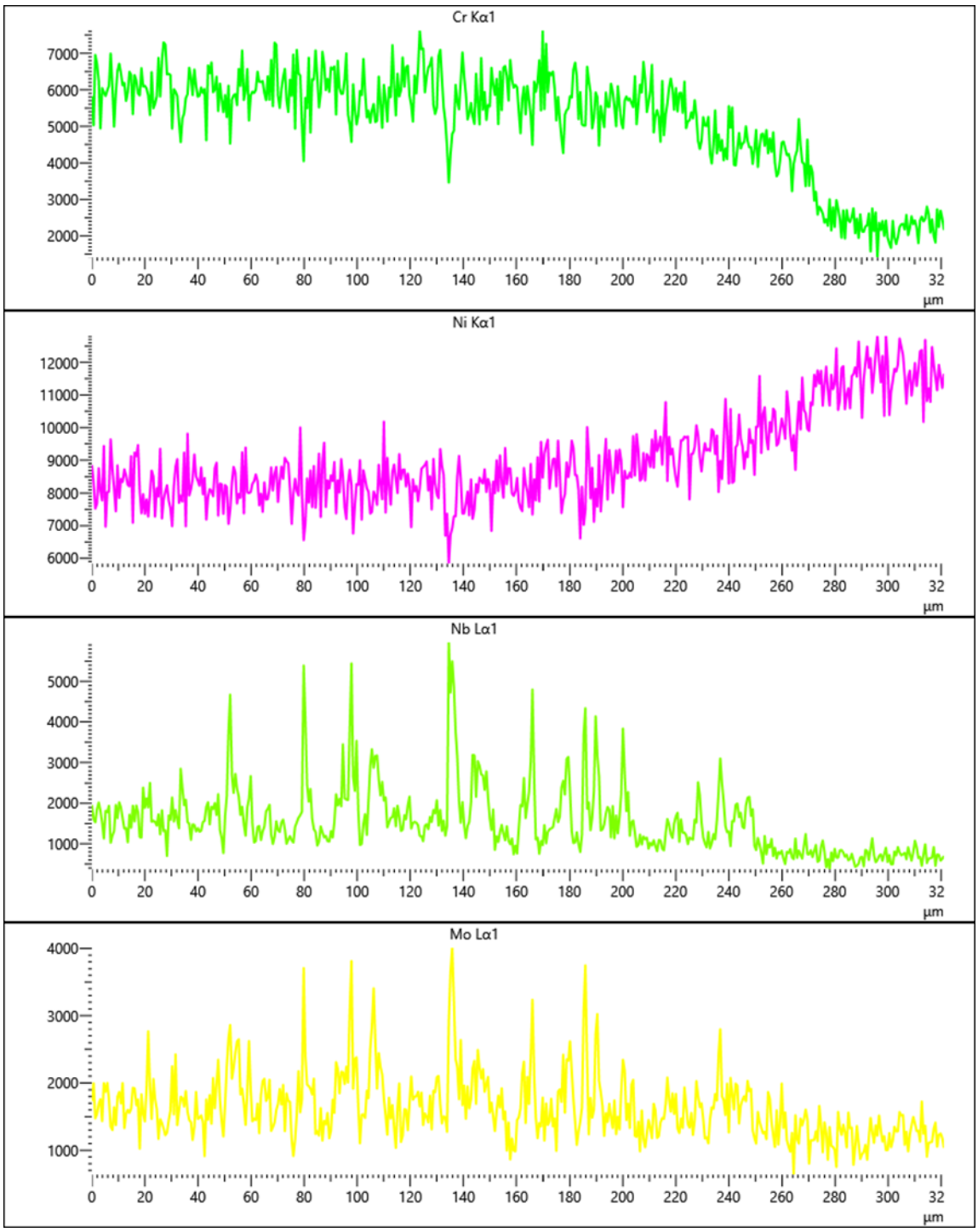

Fig. 165 – Burn Interface Tiled Line Scan EDS Spectra for Sample 7670

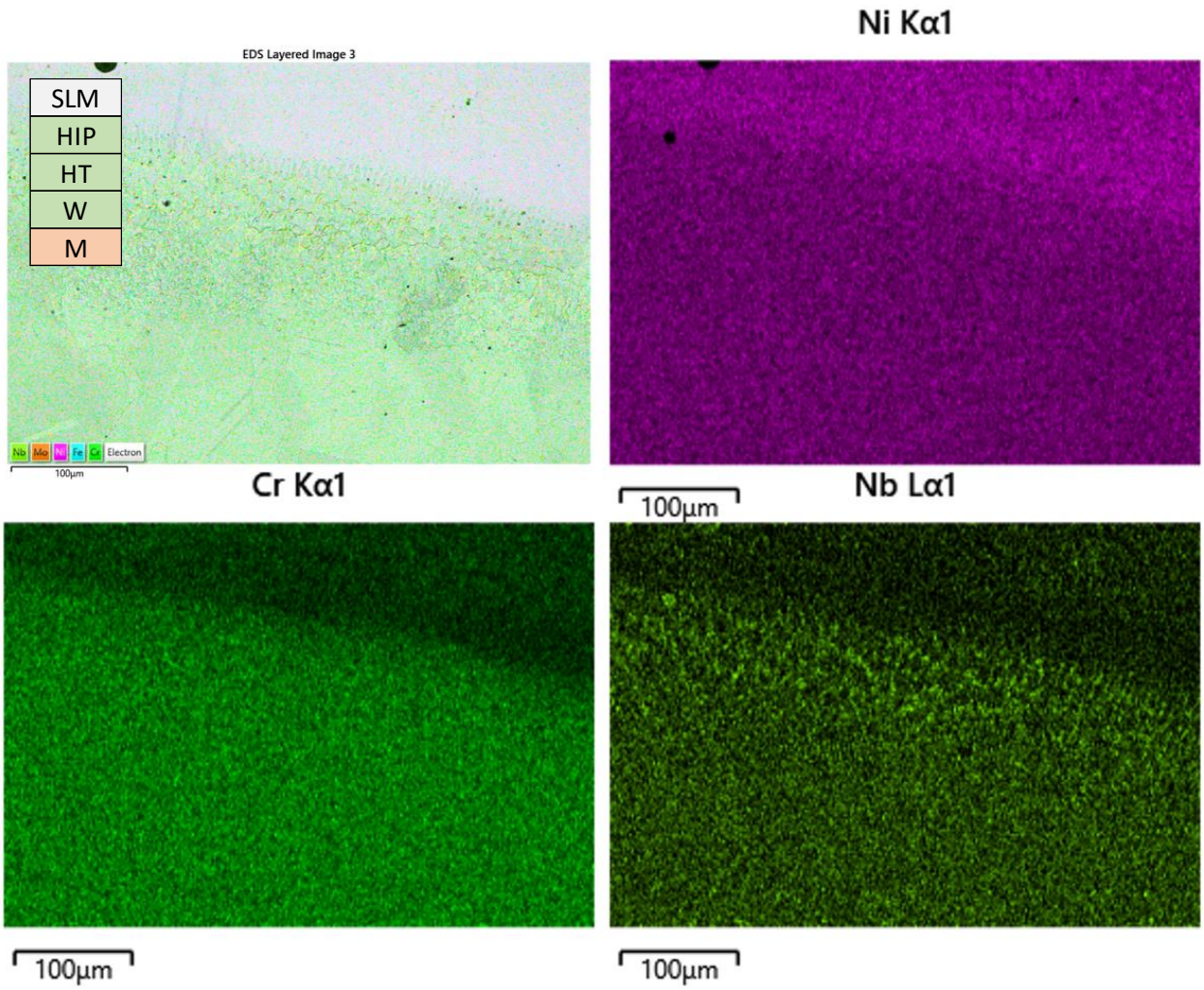

Fig. 166 – Polished Burn Interface EDS Maps of Sample 8522 (250x)

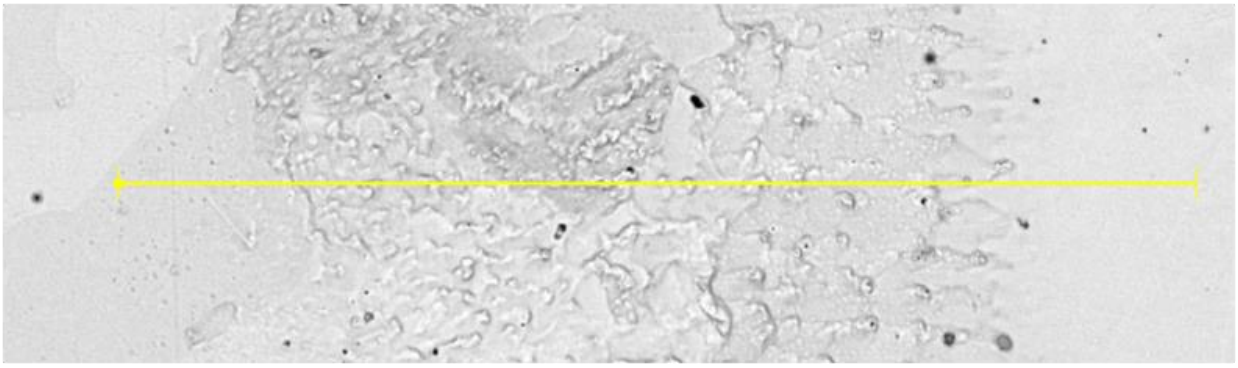

Fig. 167 – Burn Interface EDS Line Scan Reference Image for Sample 8522 (left bulk to right burn tip)

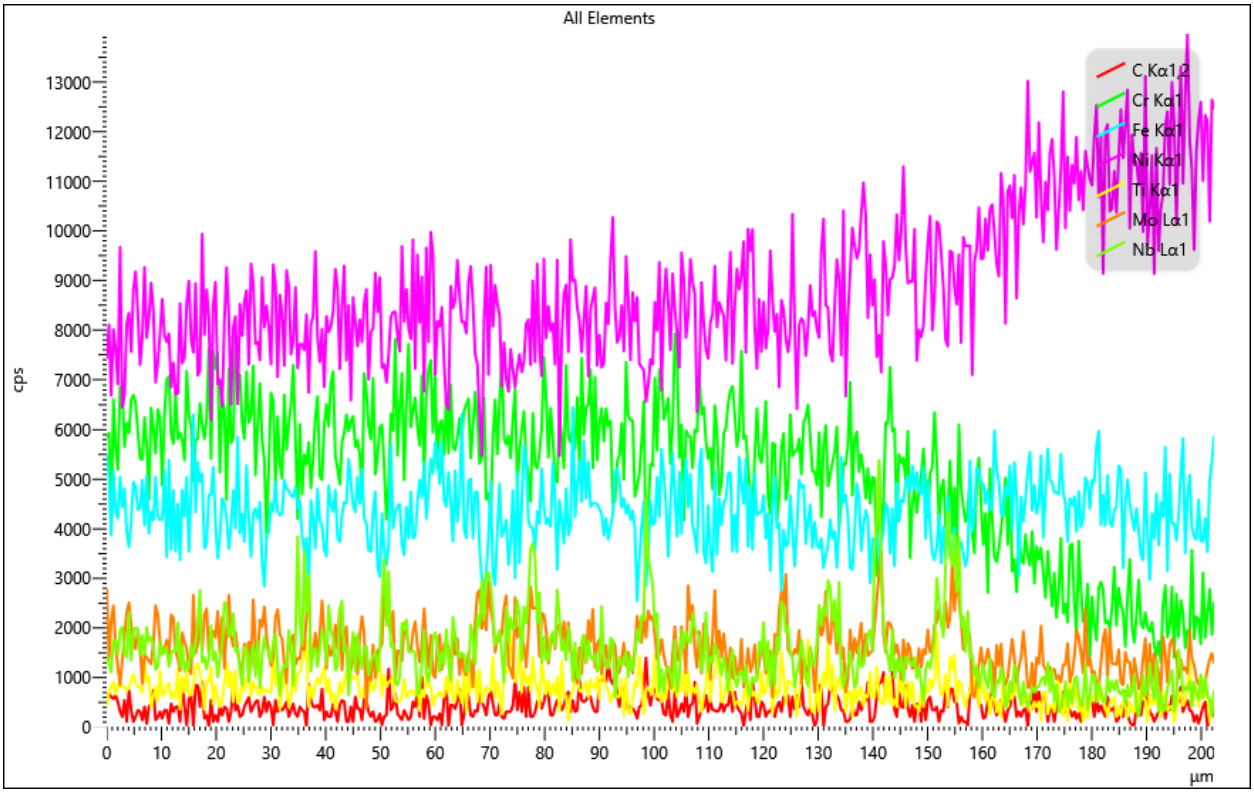

Fig. 168 – Burn Interface Stacked Line Scan EDS Spectra for Sample 8522

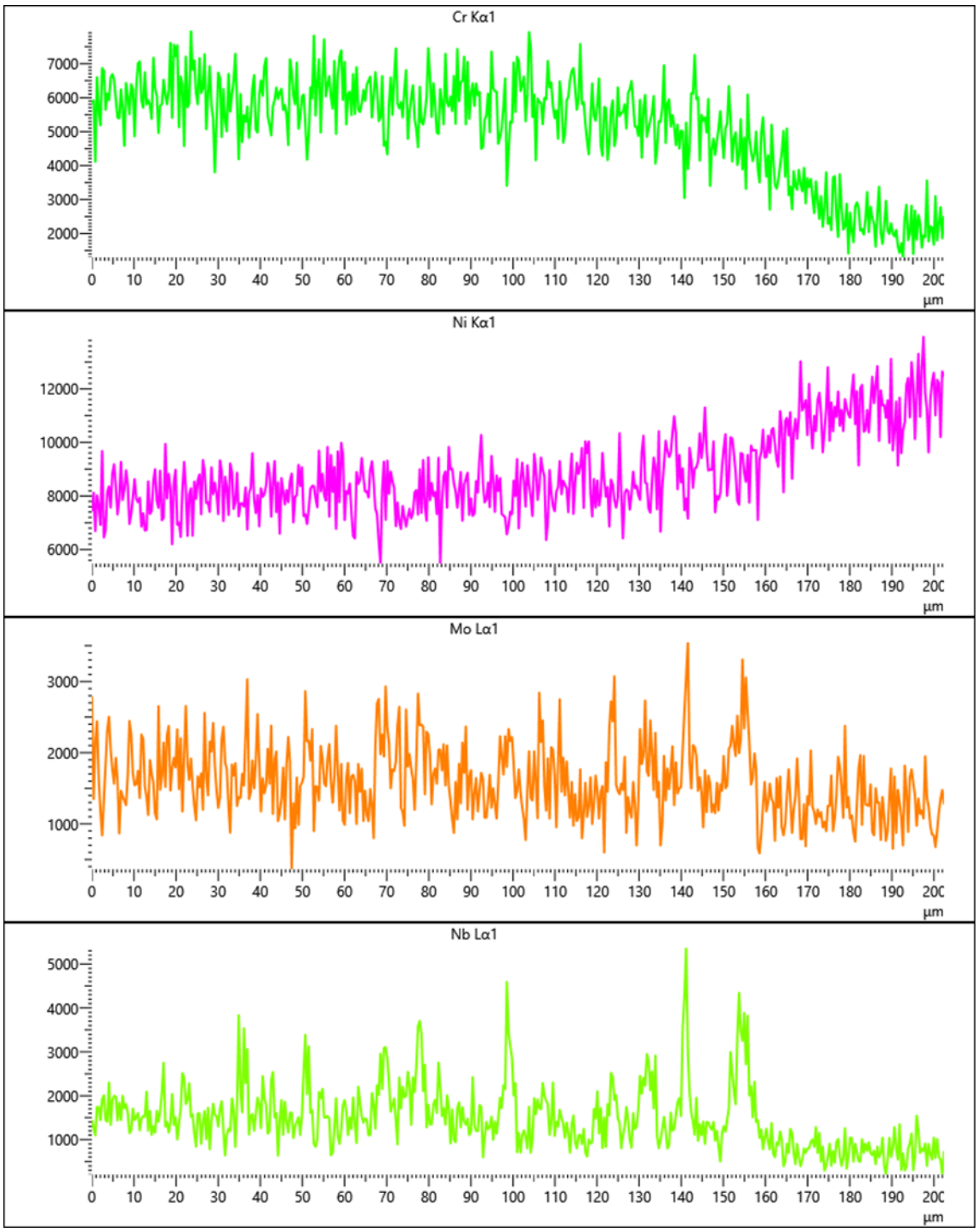

Fig. 169 – Burn Interface Tiled Line Scan EDS Spectra for Sample 8522

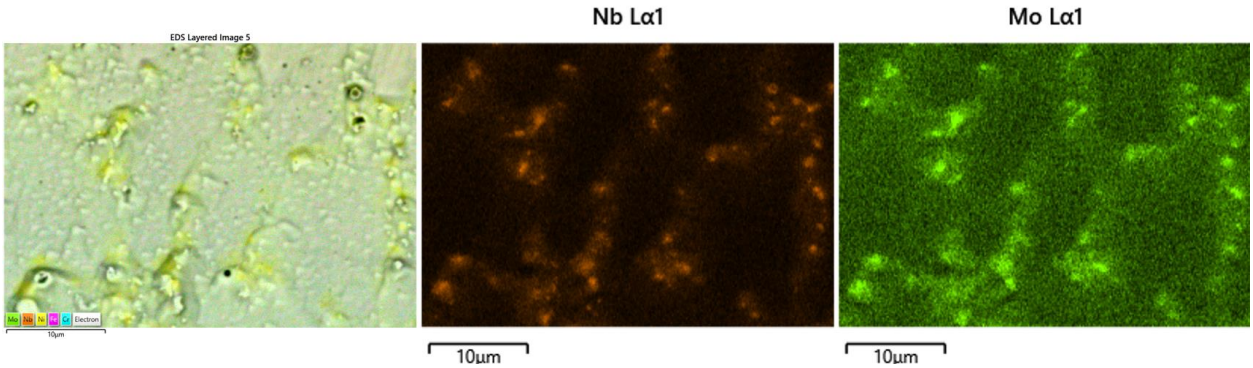

Fig. 170 – Burn Interface Dendritic Structure EDS Maps of Sample 8522

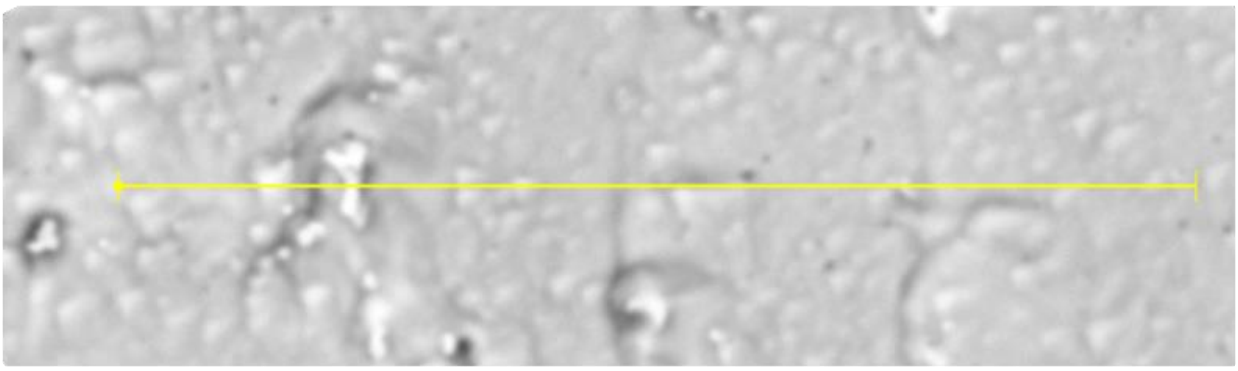
Fig. 171 – Burn Interface Dendritic Structure Line Scan EDS Reference Image for Sample 8522

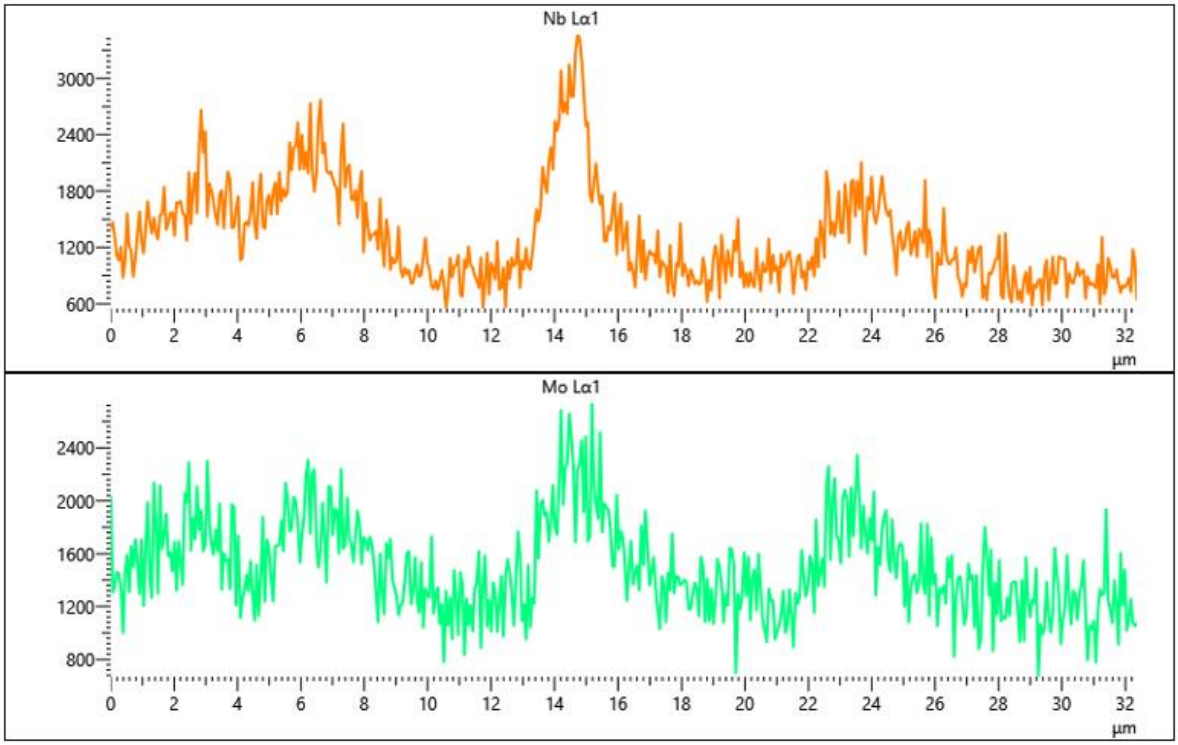

Fig. 172 – Burn Interface Dendritic Structure Tiled Line Scan EDS Spectra for Sample 8522

The outer surface EDS analysis showed general chemical homogeneity (corroborating what was seen in the bulk) but with slight differences at high magnification. Three samples are included below to represent rods which were not wrapped and not machined (8488), wrapped but not machined (8541), and not wrapped but machined (8525).

For sample 8488, what can be seen is that despite not receiving any wrapping during the hot-isostatic press, titanium and aluminum diffused to the surface to form thinly concentrated layers. Additionally, Nb-Mo deposits can be found which at times show a slight overlap with titanium. From a point scan perspective, the chemical composition of this region does not differ significantly from the bulk.

Sample 8541 (which was not machined following initial manufacture but was wrapped with titanium foil during the hot-isostatic process) still shows that thin layers of concentrated titanium and aluminum formed on the rod surface, though here the Nb-Mo structures are not present. Again, point scan analysis does not show an appreciable difference in composition when compared to the bulk however carbon content remains elevated (likely a result of nearby carbon signal supplied by the mount material).

Sample 8525 (which was machined following manufacture but did not receive titanium foil wrapping during the hot-isostatic pressing process) shows that neither phenomenon observed above occurred. Nb-Mo structures were not seen, and titanium did not accumulate on the rod surface (though aluminum could be seen as having diffused and also seemed to contribute towards internal oxides in the region). Once more, point scan analysis did not reveal any significant deviation from bulk chemistry.

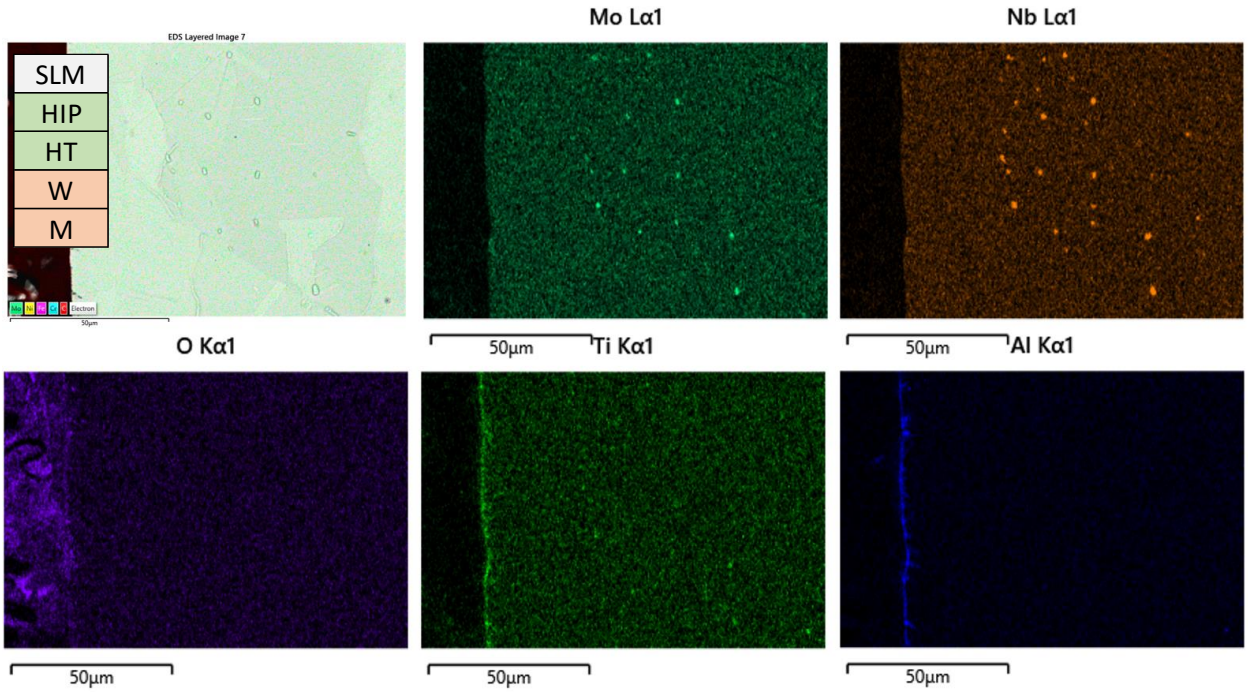

Fig. 173 – Polished Outer Surface EDS Maps of Sample 8488 (1000x)

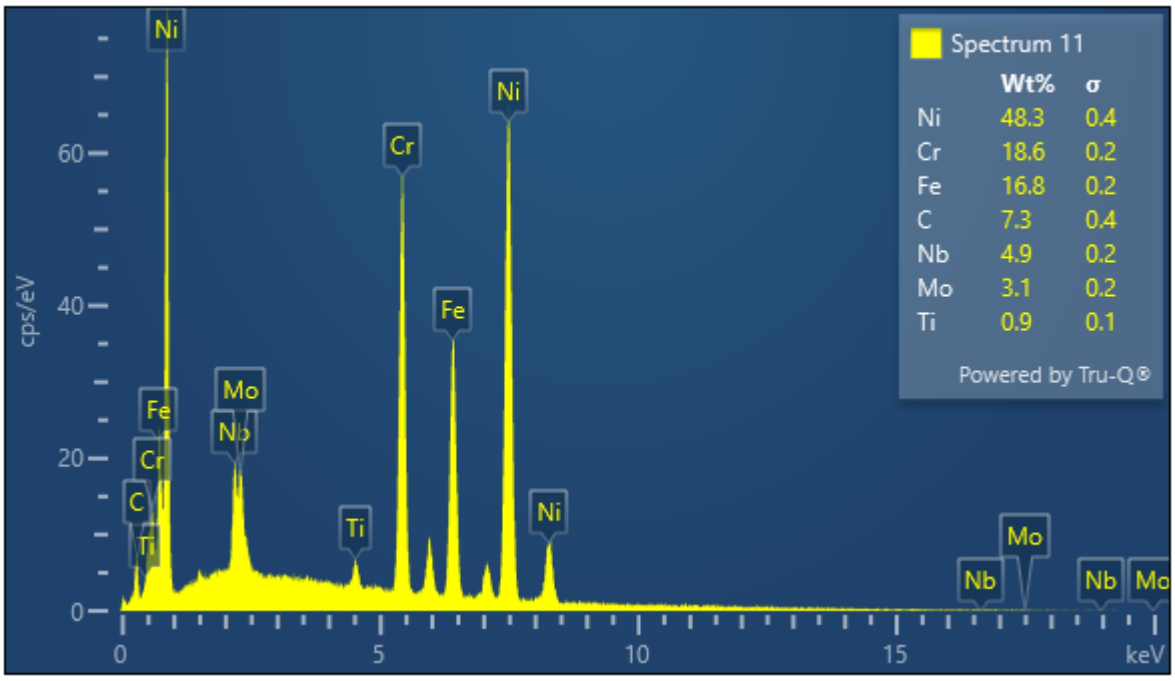

Fig. 174 – EDS Point Scan Spectra with Weight Percentages, Outer Surface Region of Sample 8488

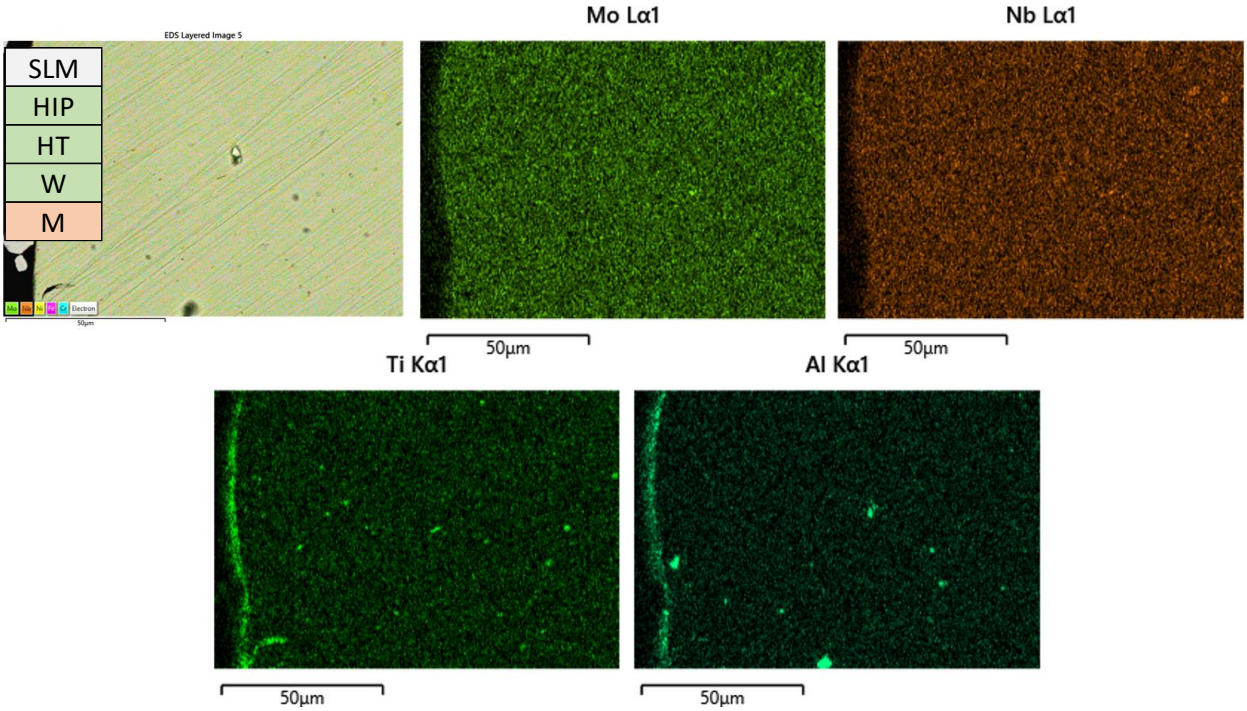

Fig. 175 – Polished Outer Surface EDS Maps of Sample 8541 (1000x)

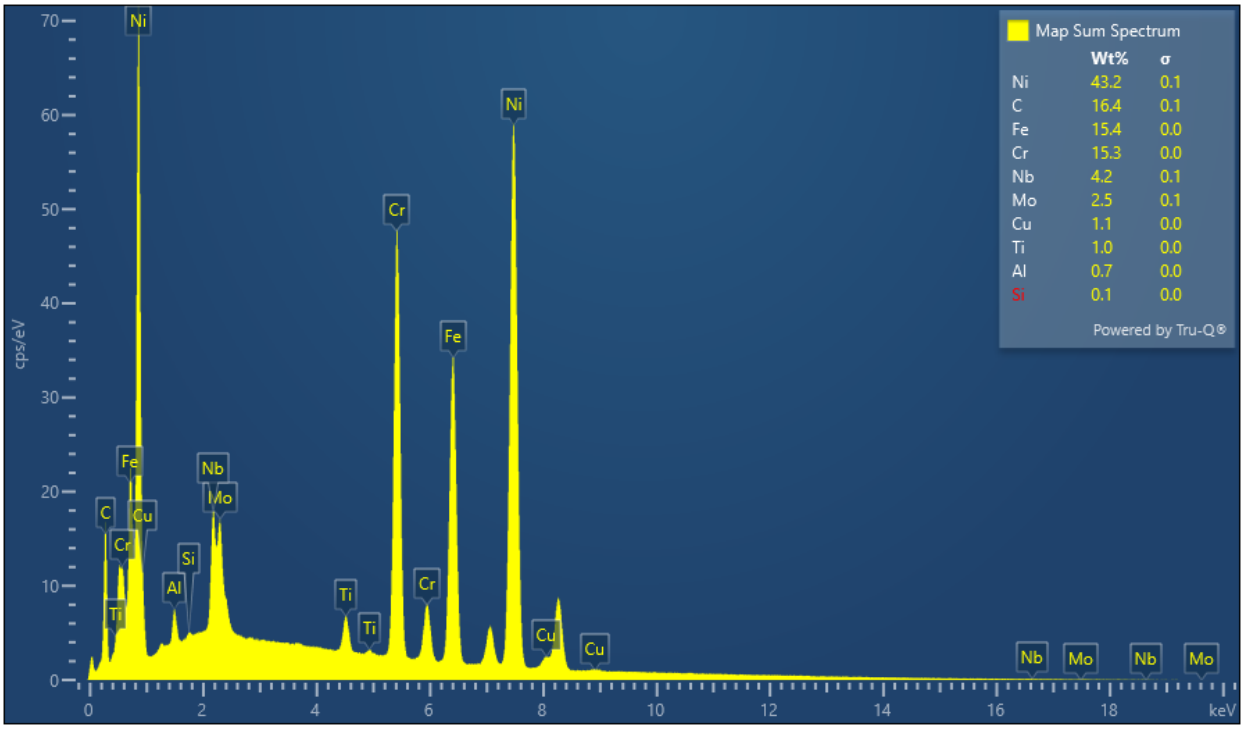

Fig. 176 – EDS Point Scan Spectra with Weighted Percentages, Outer Surface Region of Sample 8541

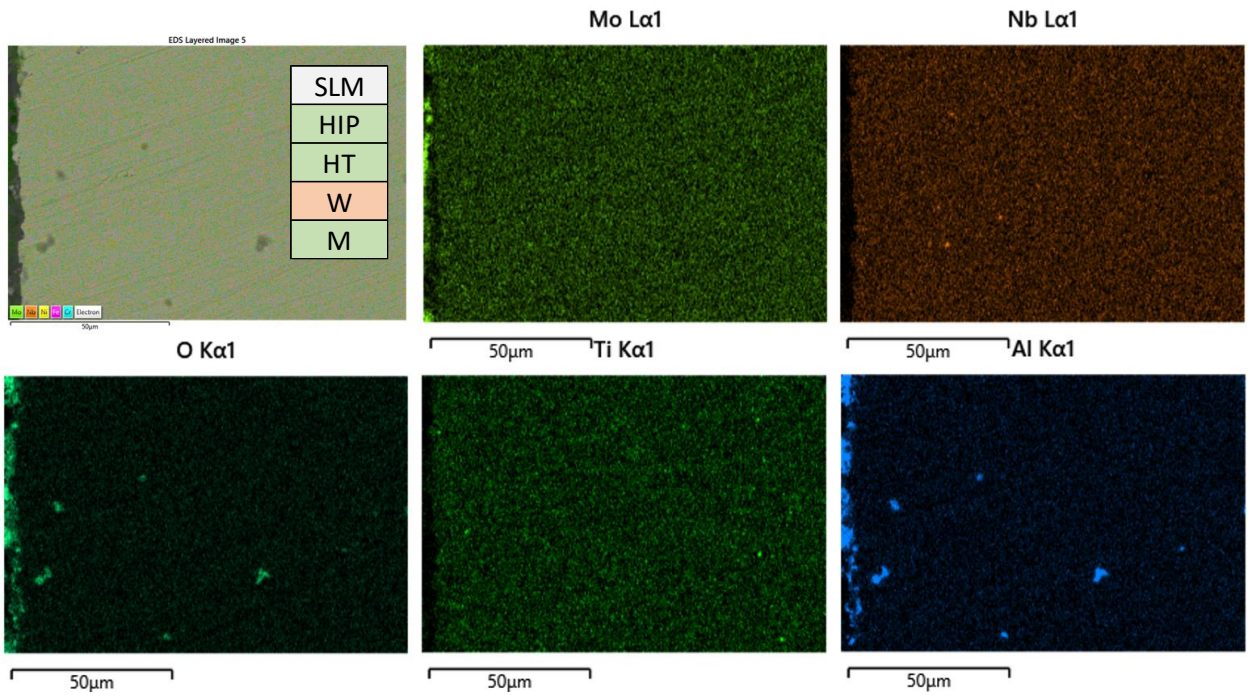

Fig. 177 – Polished Outer Surface EDS Maps of Sample 8525 (1000x)

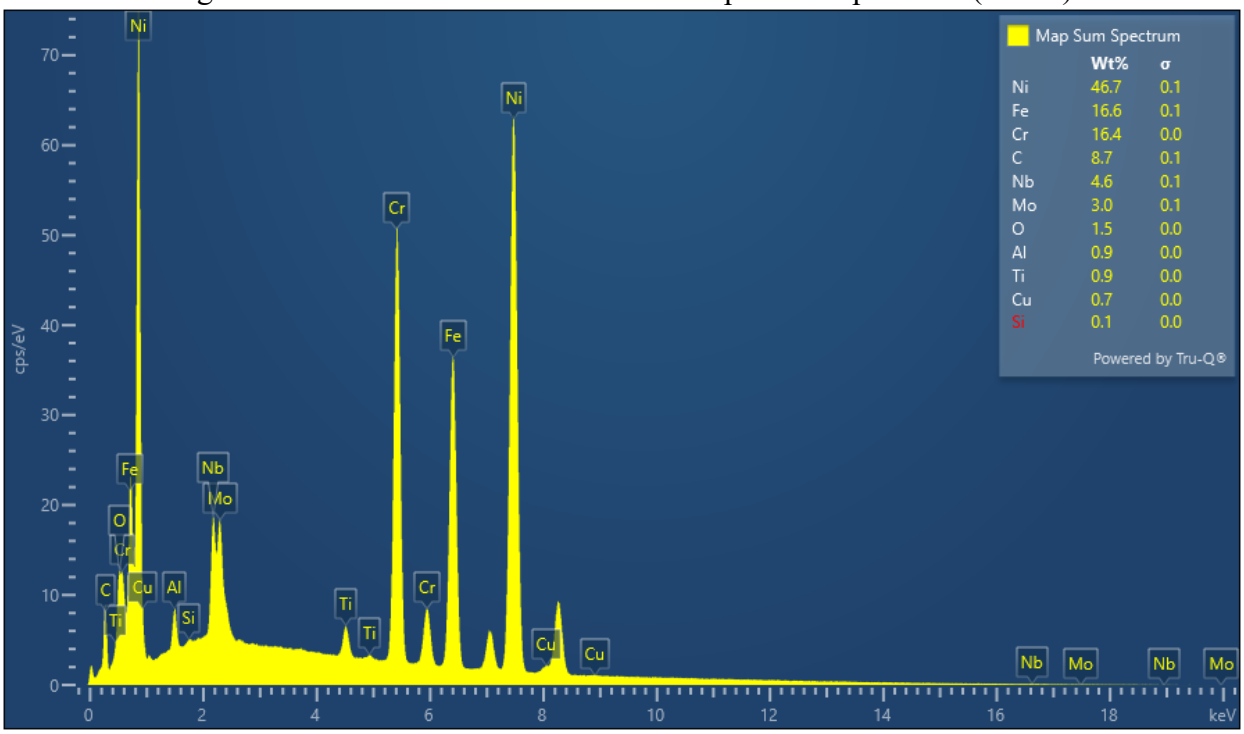

Fig. 178 – EDS Point Scan Spectra with Weight Percentages, Outer Surface Region of Sample 8525

X-Ray Diffraction

Upon completion of all microscopy and chemical analysis, x-ray diffraction was conducted on each sample in order to characterize what structures were present in the bulk and heat affected zone of each rod. Phases anticipated to exist within Inconel 718 were observed, with the primary γ-matrix of nickel-chromium solid solution documented alongside spectra peaks for simple nickel, δ-phase (Ni_3Nb), γ' precipitates (Ni_3Al), and γ" precipitates (Ni_3Nb).

For the vast majority of samples, bulk spectra generated via XRD displayed characteristic peaks for the Ni_3Al γ' precipitate phase at approximately 45˚ (2θ), the secondary Ni_3Nb γ" precipitate peak closer to 50˚ (2θ), the δ-phase Ni_3Nb at approximately 75˚ (2θ), and the simple nickel phase at around 90˚ (2θ). Deviation was typically introduced when the spectra for heat affected zones were overlayed on the bulk spectra, demonstrating that for many samples there was drastic variability in the intensity seen for several phases. As one example, the bulk spectra for sample 7679 showed an intensity for the Ni_3Al γ' precipitate phase at nearly 6000 cps (counts-per-second) while its' heat affected zone showed a significantly weaker intensity (approximately 400 cps) for the same phase. Notably, this trend was reversed in the case of the Ni_3Nb phase as it was much more intense in the heat affected zone than the bulk.

Other samples could at times demonstrate a change in the predominant peak, such as sample 8082. While the majority of samples have as their primary phase the Ni_3Al γ' precipitate seen at 45˚, this sample instead showed a higher intensity for the Ni_3Nb γ" precipitate. The measured intensity for the δ-phase Ni_3Nb was nearly identical in the bulk scan, though this tapered off significantly for the scan conducted on the heat affected zone.

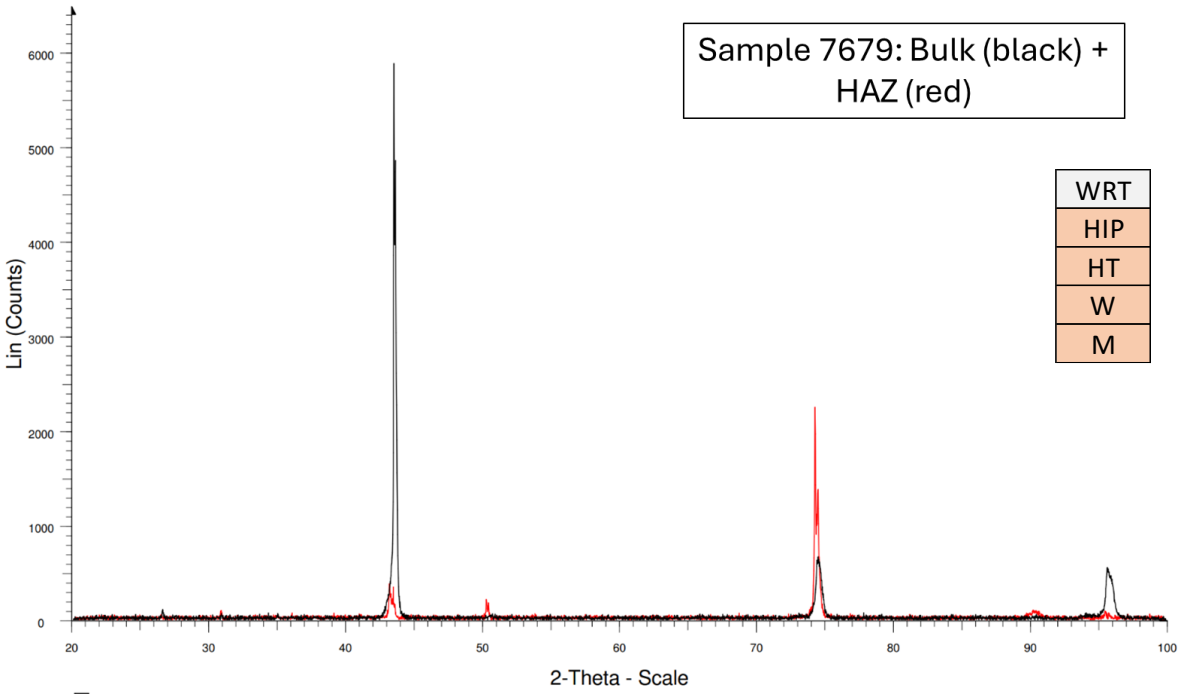

Fig. 179 – XRD Spectra Generated for Sample 7679

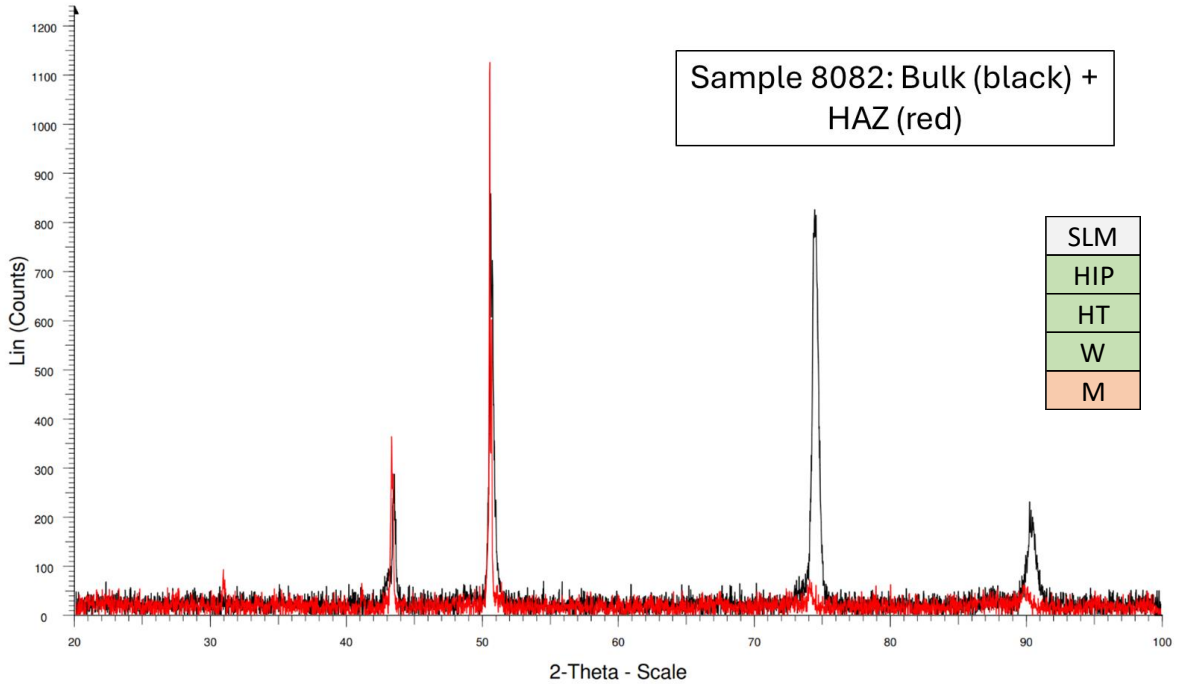

Fig. 180 – XRD Spectra Generated for Sample 8082

The XRD spectra for the two samples with the shortest burn lengths (8065 and 8544) are shown below. Though their bulk scans appear to be fairly similar, the heat affected zone spectra for sample 8544 does not identify any appreciable signal for the δ-phase Ni_3Nb or simple nickel phase but does show an elevated intensity for Ni_3Nb γ" precipitates.

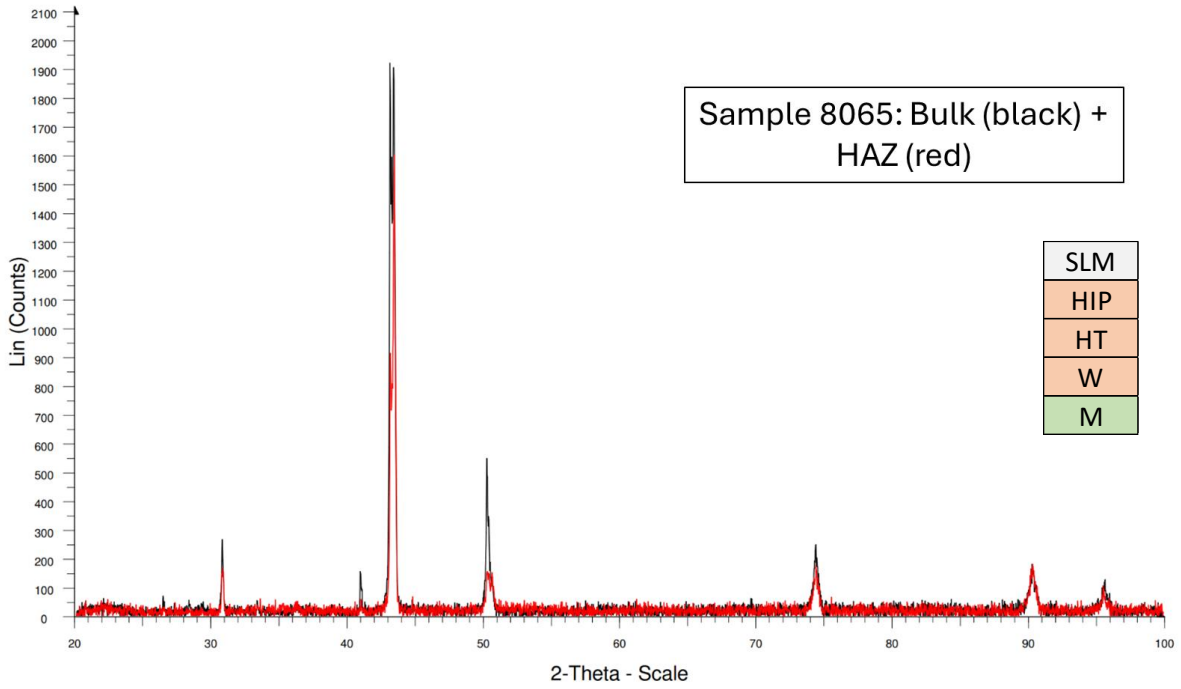

Fig. 181 – XRD Spectra Generated for Sample 8065

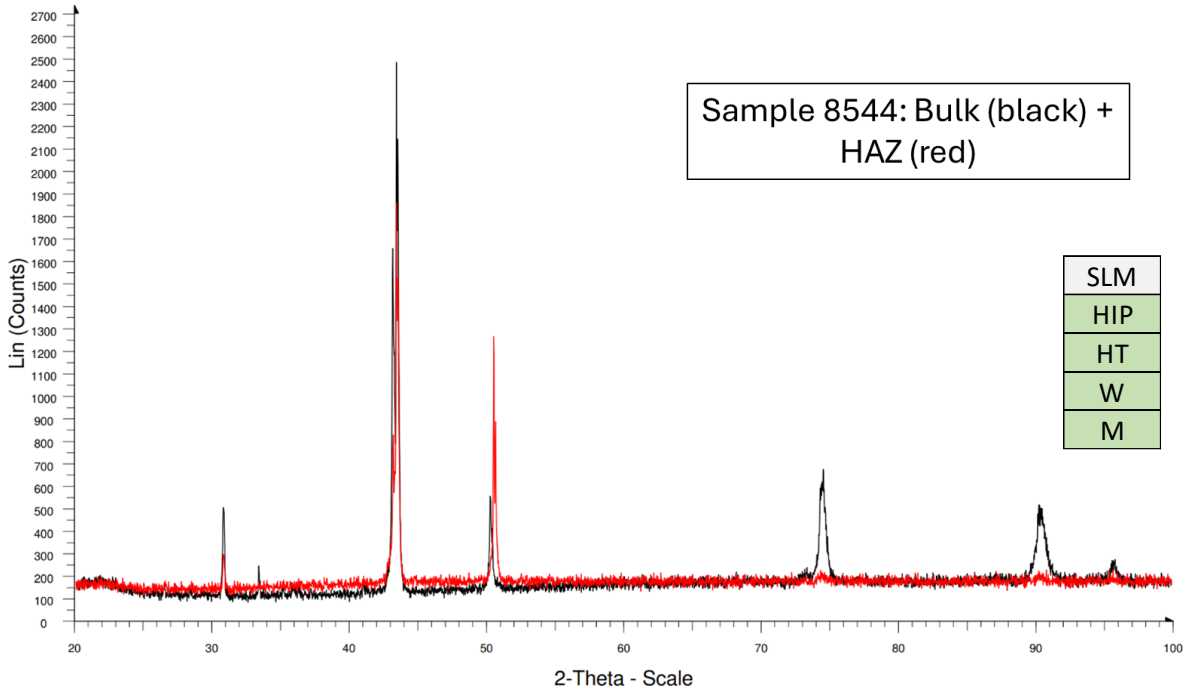

Fig. 182 – XRD Spectra Generated for Sample 8544

The sample with the largest burn length of the study was sample 8488, whose XRD spectra is included below. The most obvious detail to note from this figure is that the heat affected zone spectra shows a detected signal above 9500 cps for Ni_3Al γ' precipitates, not only substantially overtaking any other peak on the spectra for this sample but also being orders of magnitude greater than the same peak signal for other samples.

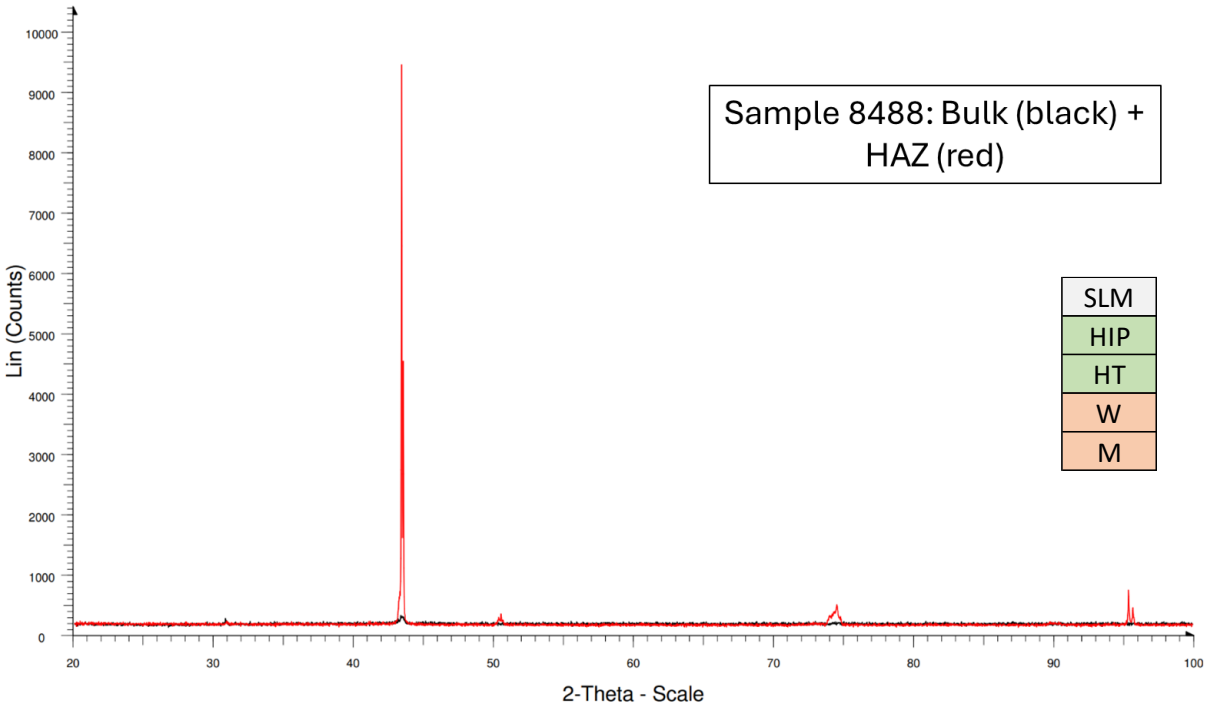

Fig. 183 – XRD Spectra Generated for Sample 8488

SAMPLE SET 2 RESULTS

Transmission Electron Microscopy Imaging

Sample 8046

The TEM micrographs below are of sample 8046 (HIP + Wrapped + Heat Treated + Not Machined). Less magnified views of the sample via the OneView camera show complex misorientations of crystallites along with thickness fringes.

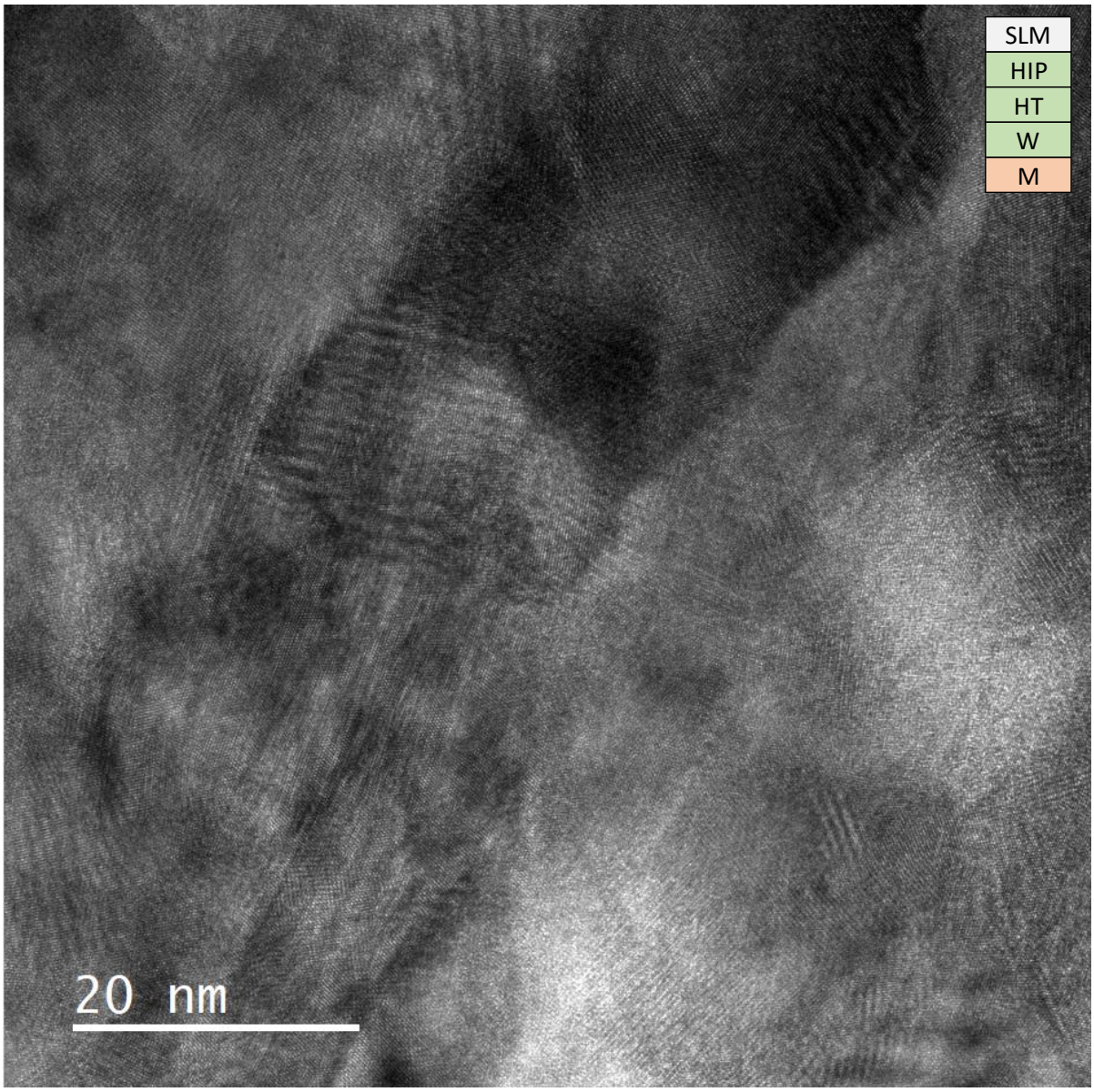

Fig. 184 – TEM Micrograph (OneView Cam) of Sample 8046 (600,000x)

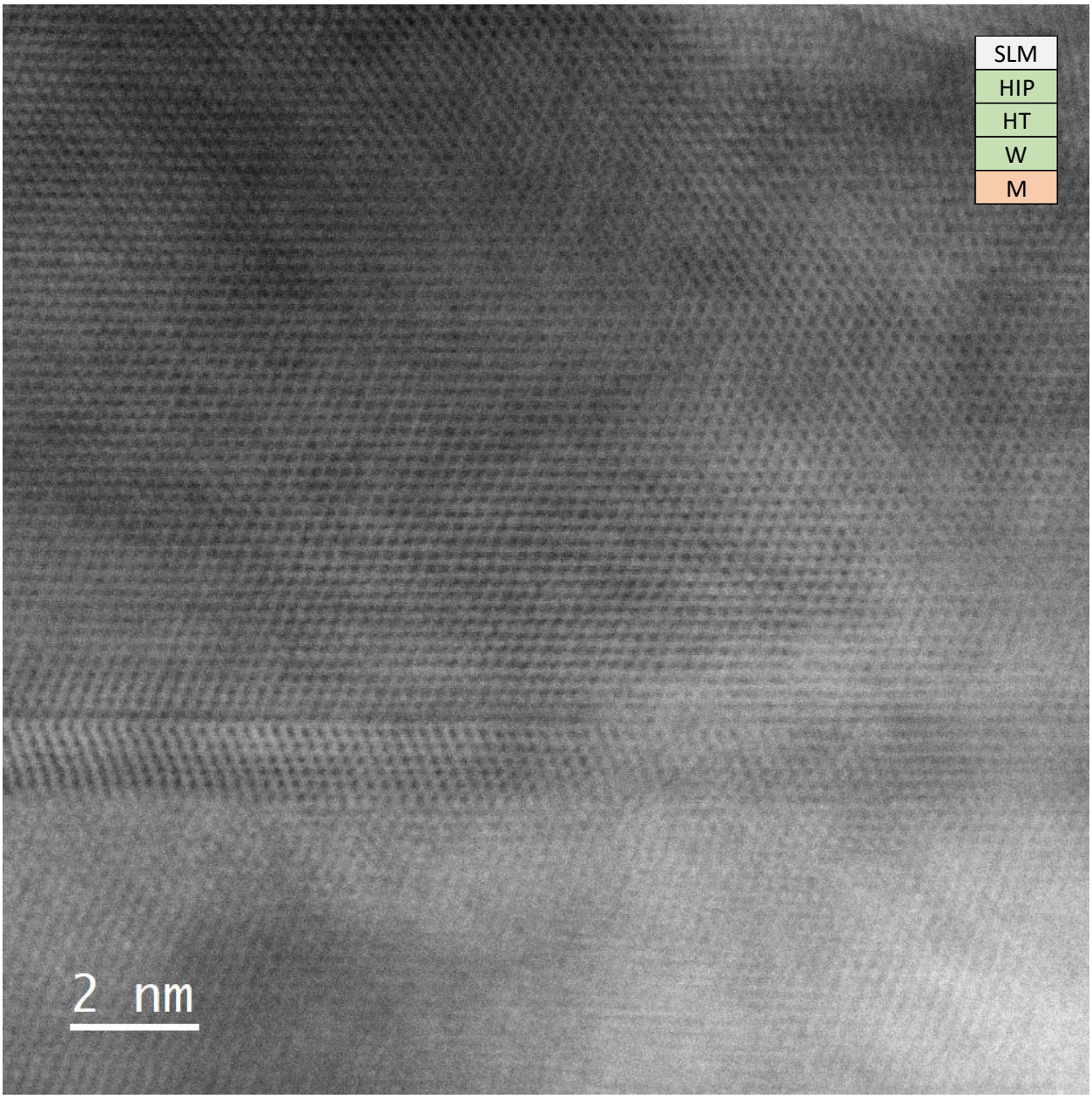

Fig. 185 – TEM Micrograph (Bright Field) of Sample 8046 Region 1 (12,000,000x)

The figures above and below show bright and annular dark field images of a twin grain boundary which has formed in the burn interface of sample 8046, likely as a result of rapid recrystallization during the solidification process.

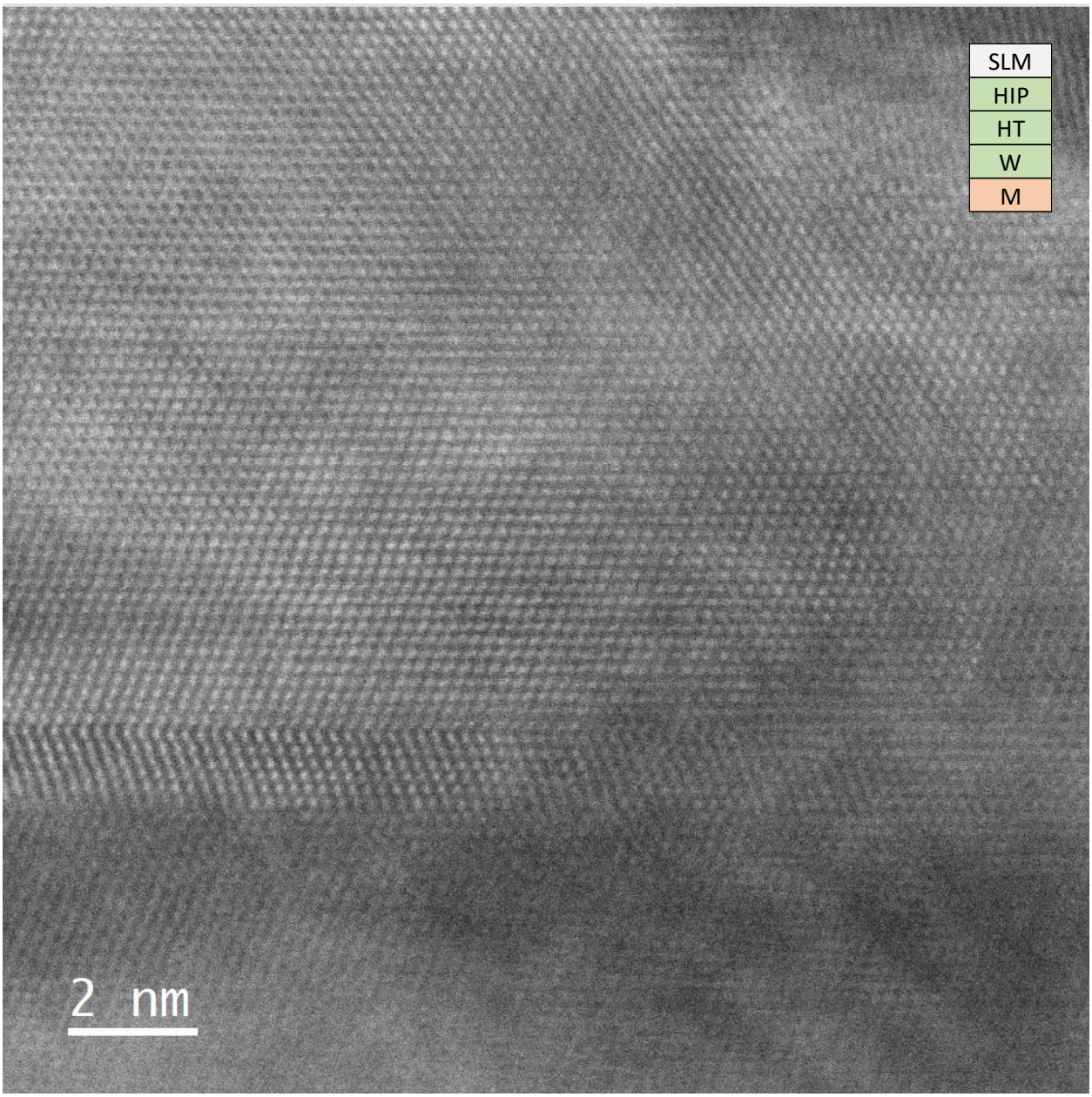

Fig. 186 – TEM Micrograph (Annular Dark Field) of Sample 8046 Region 1 (12,000,000x)

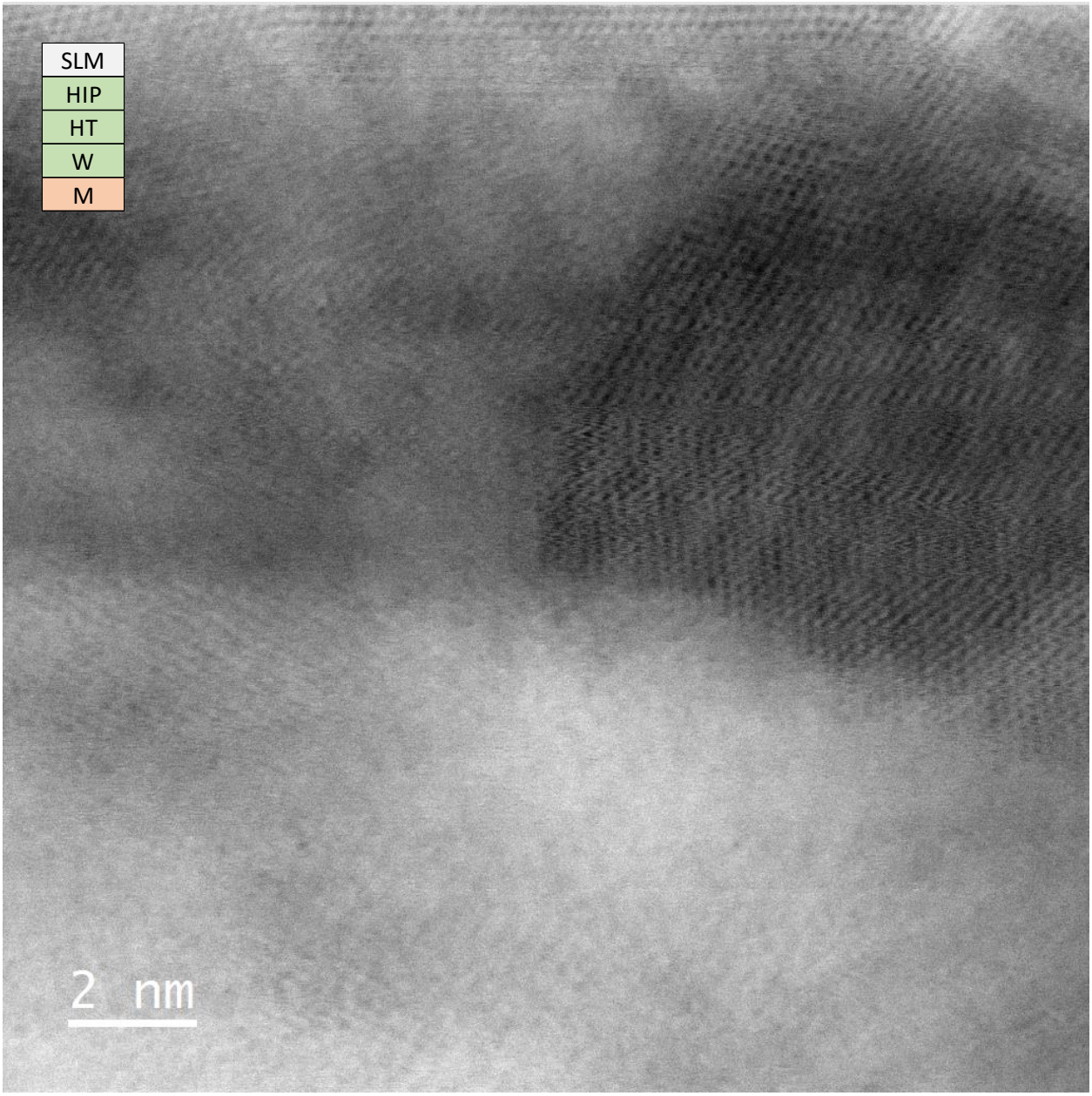

Fig. 187 – TEM Micrograph (Bright Field) of Sample 8046 Region 2 (12,000,000x)

The micrographs seen above and below here show a region of the lamella which was particularly thin and as such demonstrates the local atomic lattice.

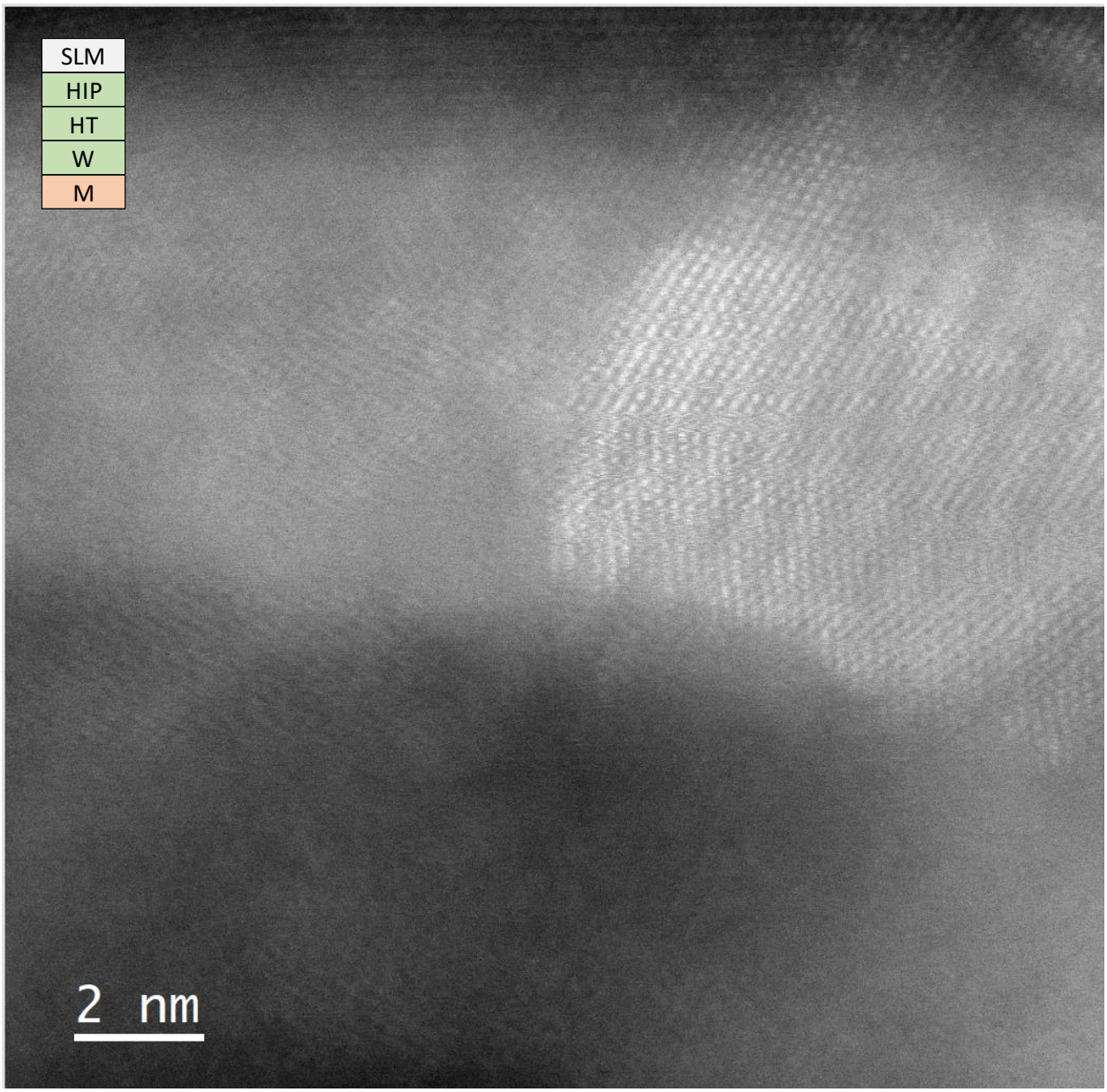

Fig. 188 – TEM Micrograph (Annular Dark Field) of Sample 8046 Region 2 (12,000,000x)

Sample 8064

The TEM micrographs below are of sample 8064 (HIP + Wrapped + Heat Treated + Not Machined). This is the same processing history as sample 8046 above, however this rod was from powder batch lot A2 and serves as a couple to sample 8159 which also had identical processing but a much longer burn length.

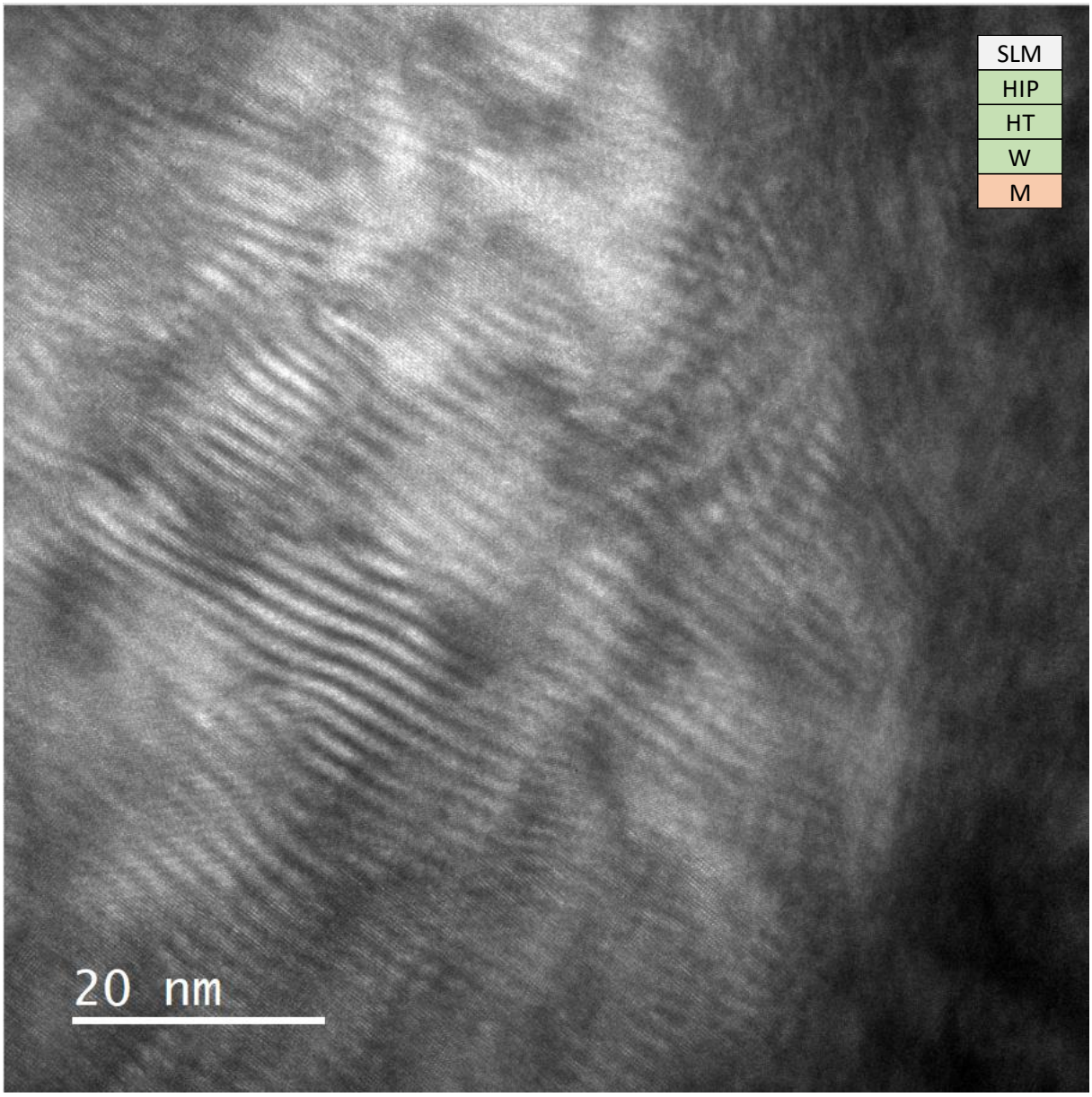

Fig. 189 – TEM Micrograph (OneView Cam) of Sample 8064 Region 1 (500,000x)

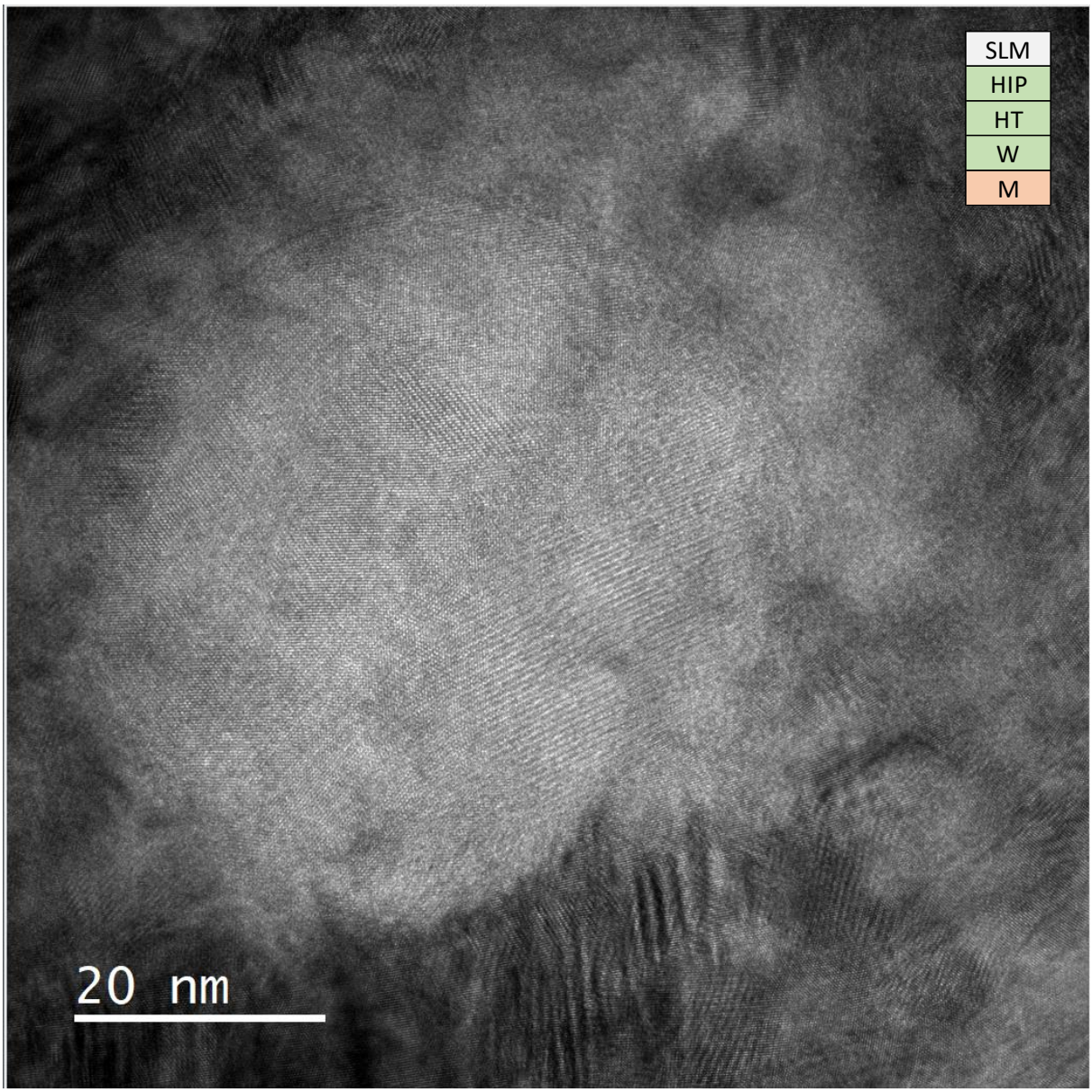

Fig. 190 – TEM Micrograph (OneView Cam) of Sample 8064 Region 2 (500,000x)

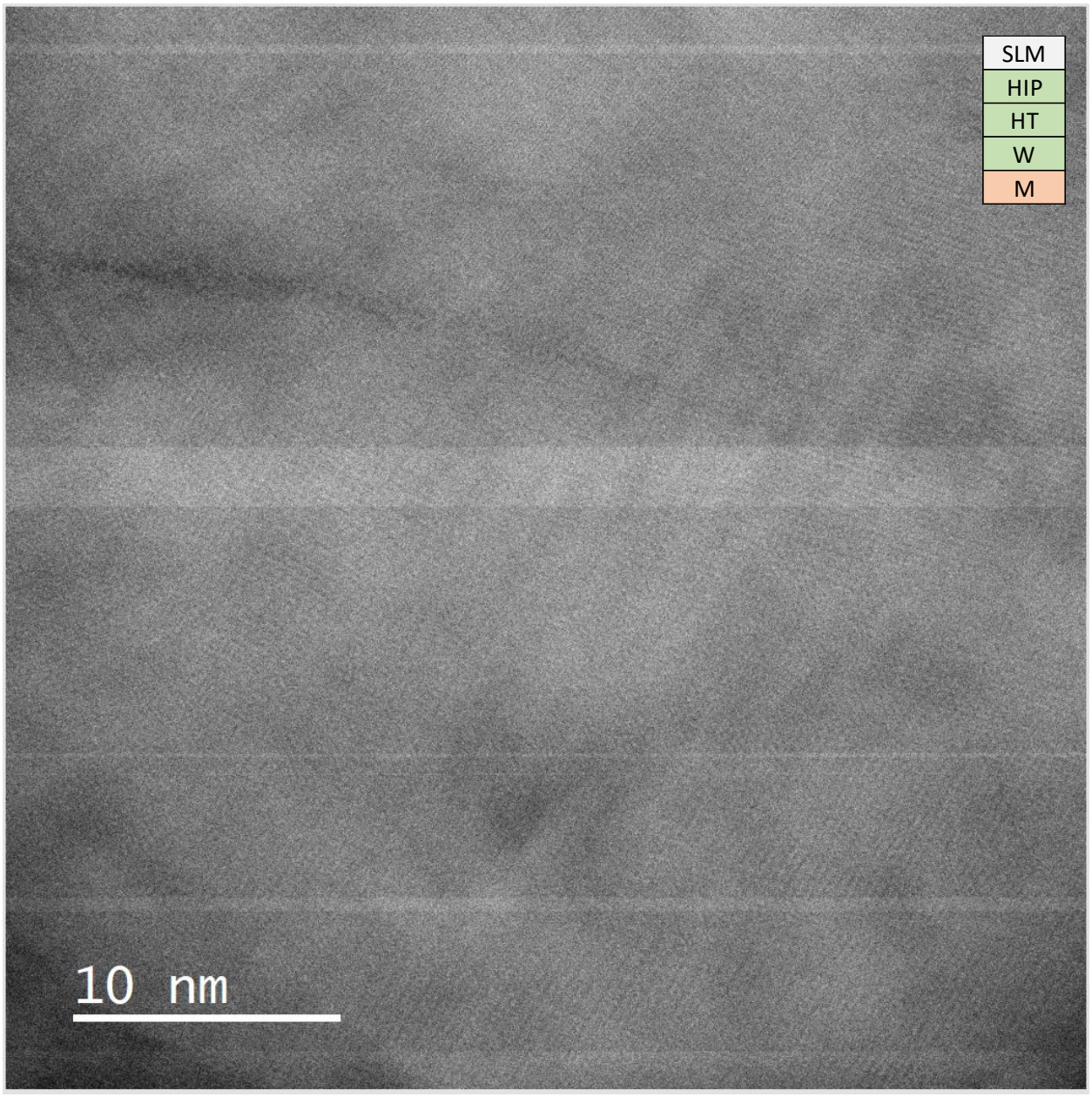

Fig. 191 – TEM Micrograph (Bright Field) of Sample 8064 Region 3 (5,000,000x)

This sample (8064) demonstrated abnormal difficulty when imaging, as artifacts (horizontal lines) were present when the camera settings (bright field and dark field) were in place. Though light thickness fringes could be observed, little else was documented while analyzing this lamella.

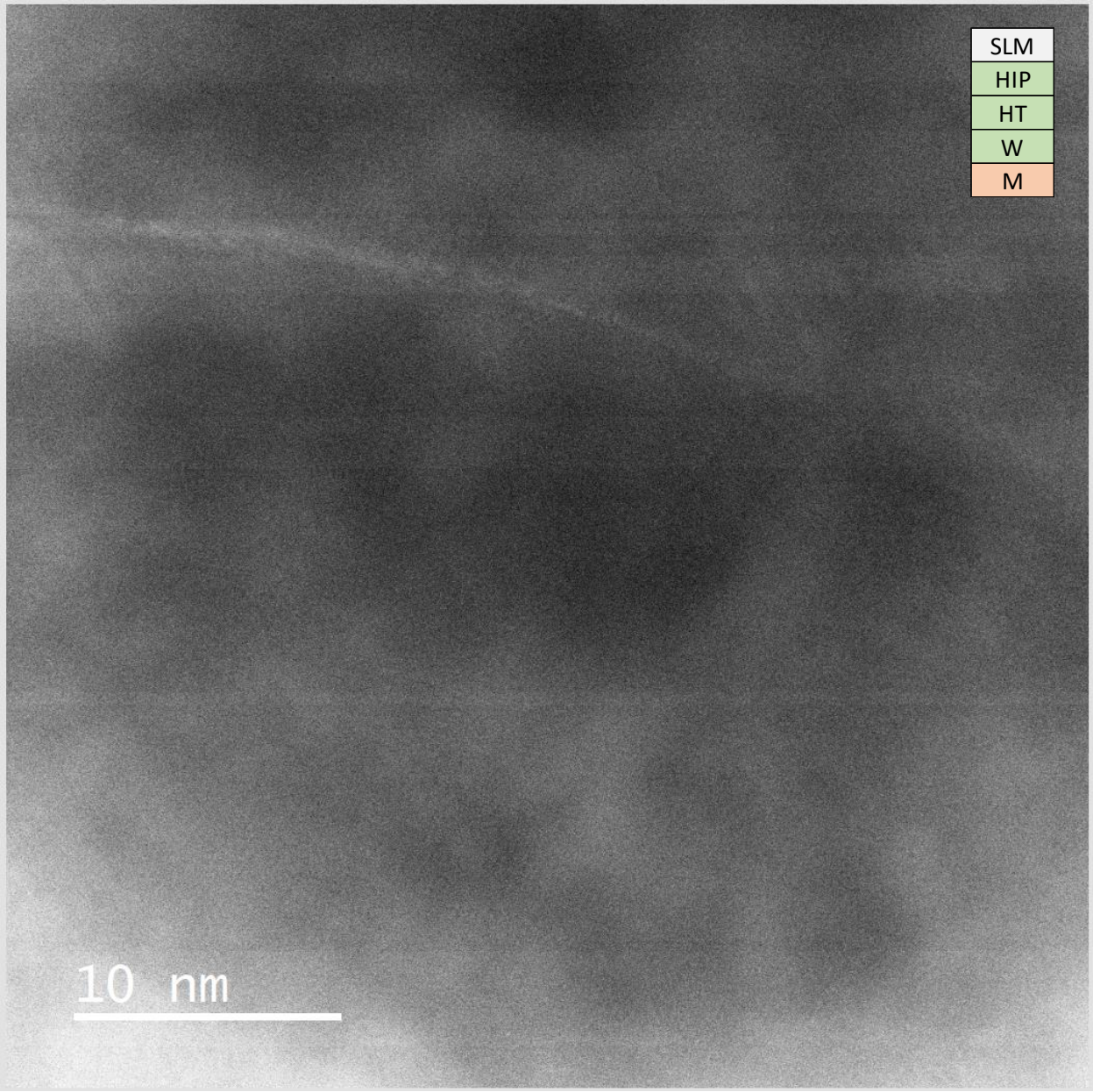

Fig. 192 – TEM Micrograph (Annular Dark Field) of Sample 8064 Region 4 (5,000,000x)

Sample 8068

The TEM micrographs below are of sample 8068 (HIP + Not Wrapped + Heat Treated + Not Machined).

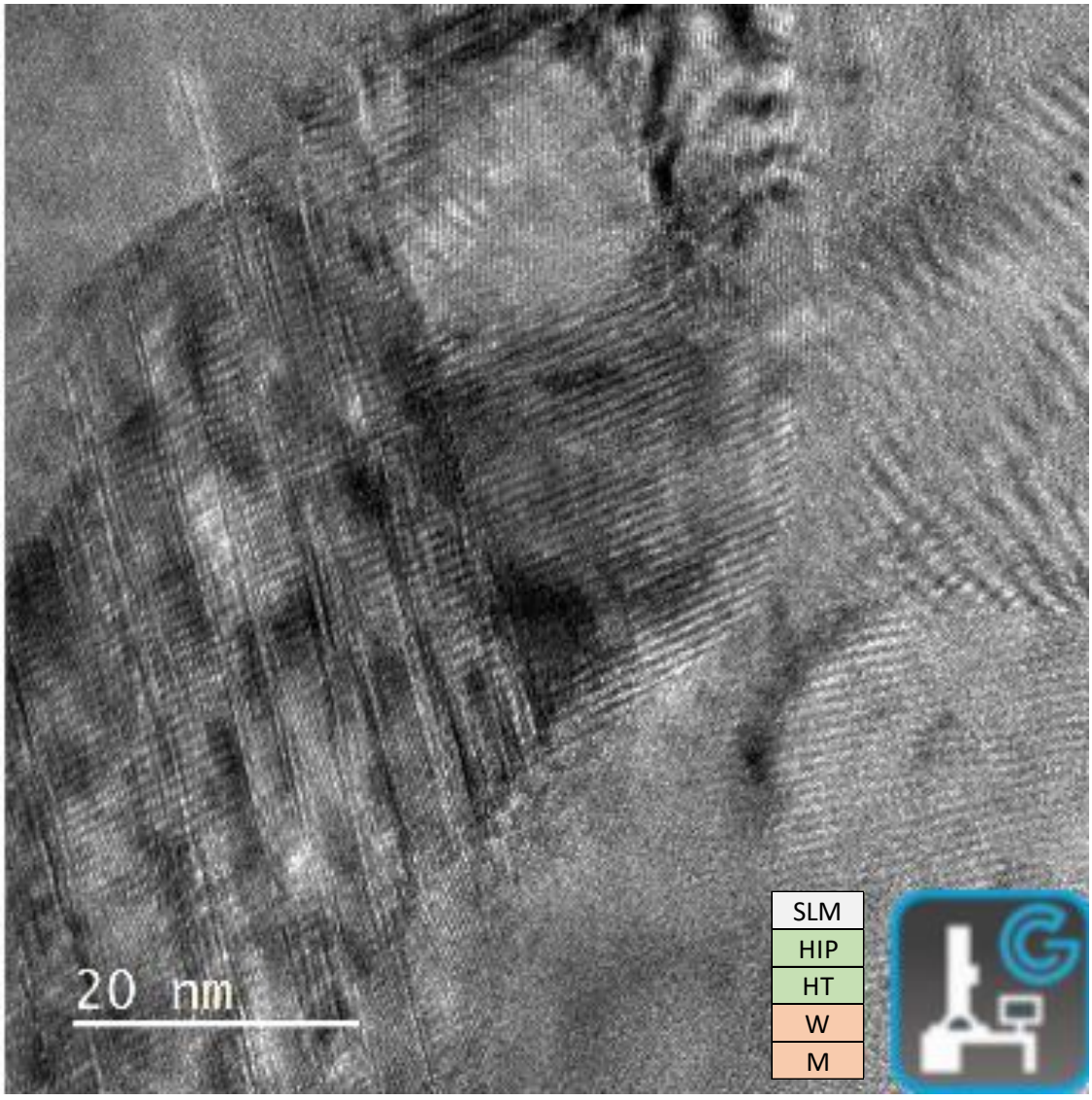

Fig. 193 – TEM Micrograph (OneView Cam) of Sample 8068 Region 1 (600,000x)

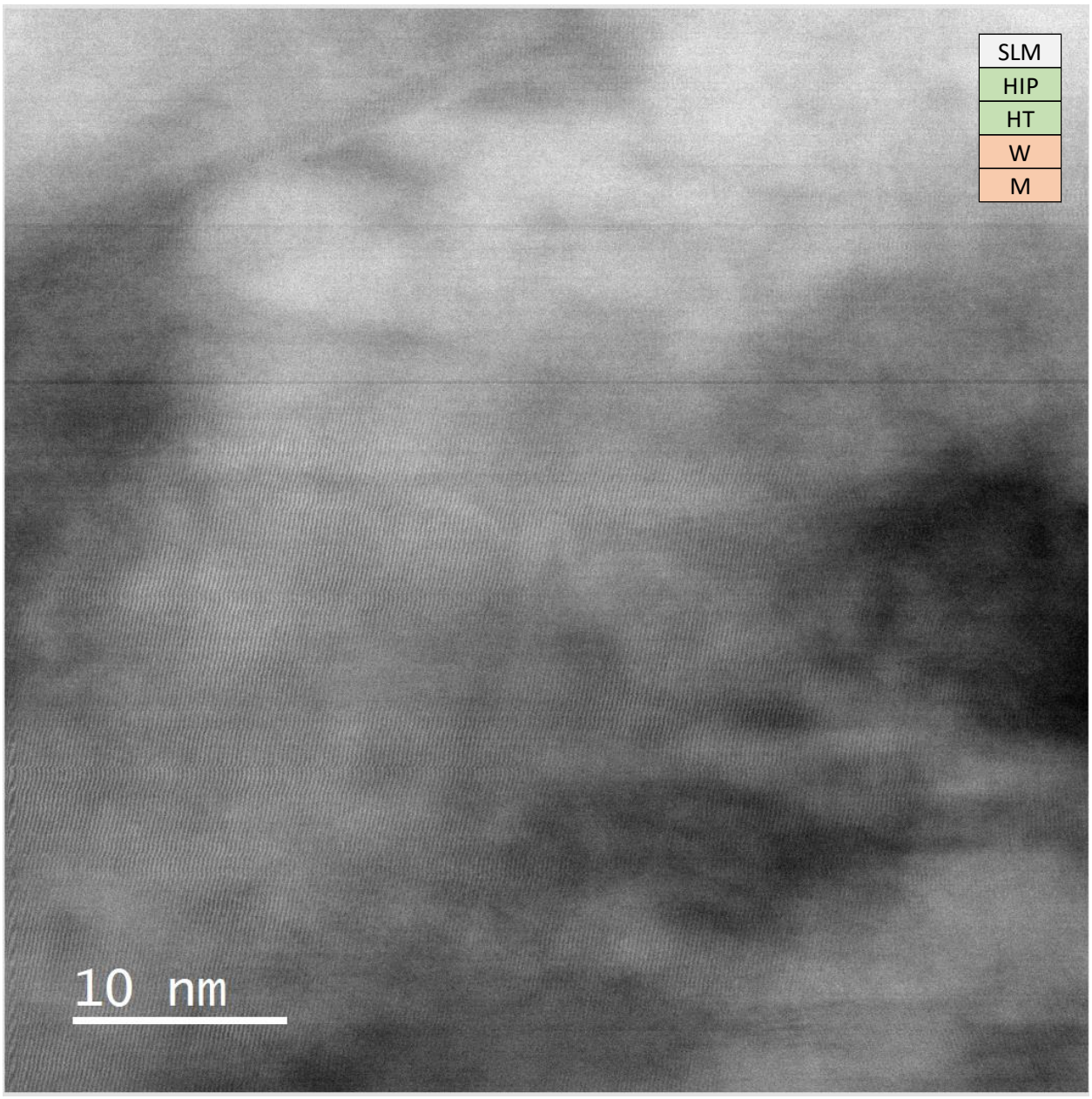

Fig. 194 – TEM Micrograph (Bright Field) of Sample 8068 Region 2 (4,000,000x)

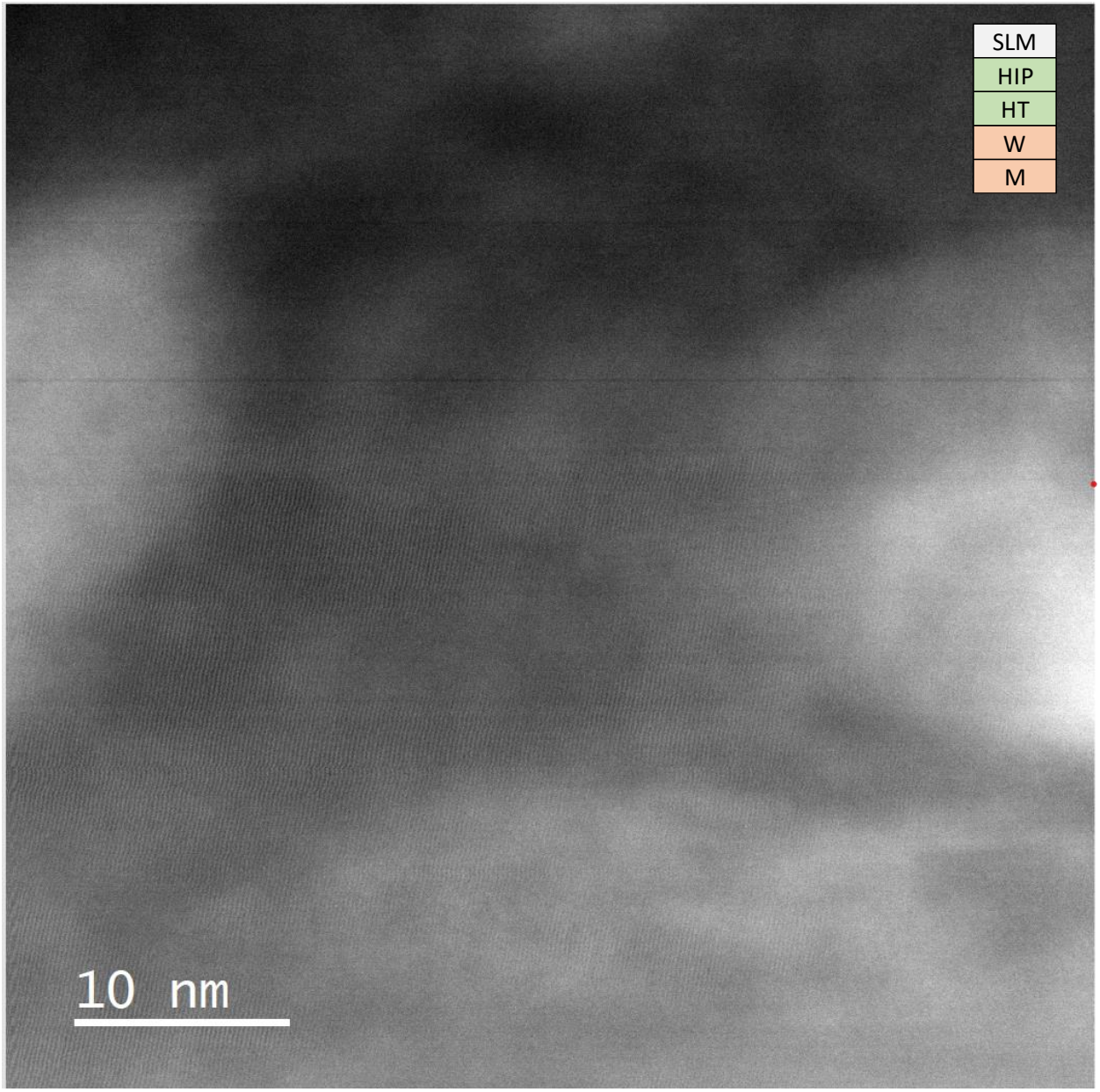

Fig. 195 – TEM Micrograph (Annular Dark Field) of Sample 8068 Region 2 (4,000,000x)

Sample 8152

The TEM micrographs below are of sample 8152 (HIP + Not Wrapped + Heat Treated + Machined). Bright field imaging was not particularly successful, and as such the images below will be from the OneView camera and annular dark field imaging settings.

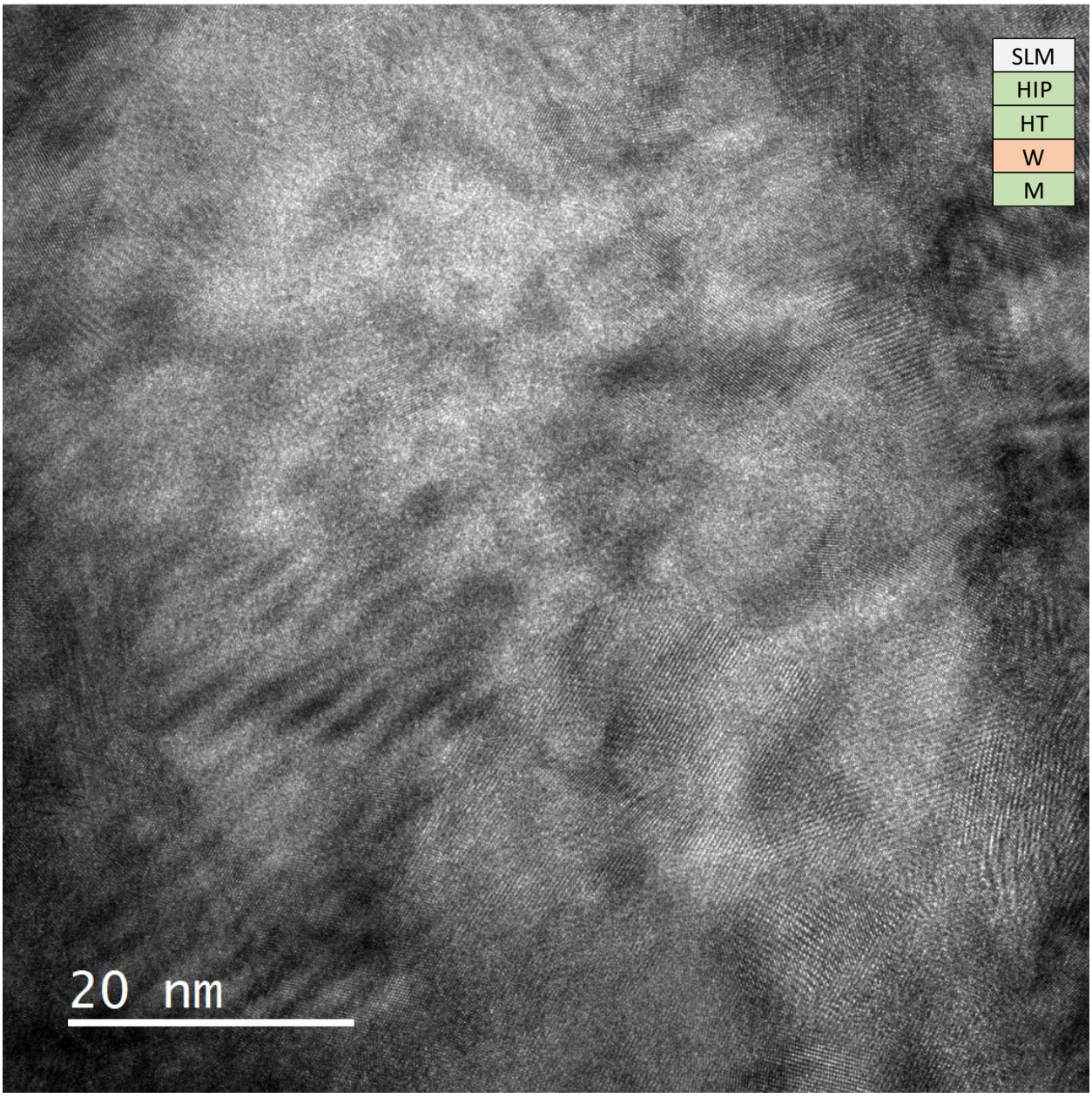

Fig. 196 – TEM Micrograph (OneView Cam) of Sample 8152 Region 1 (600,000x)

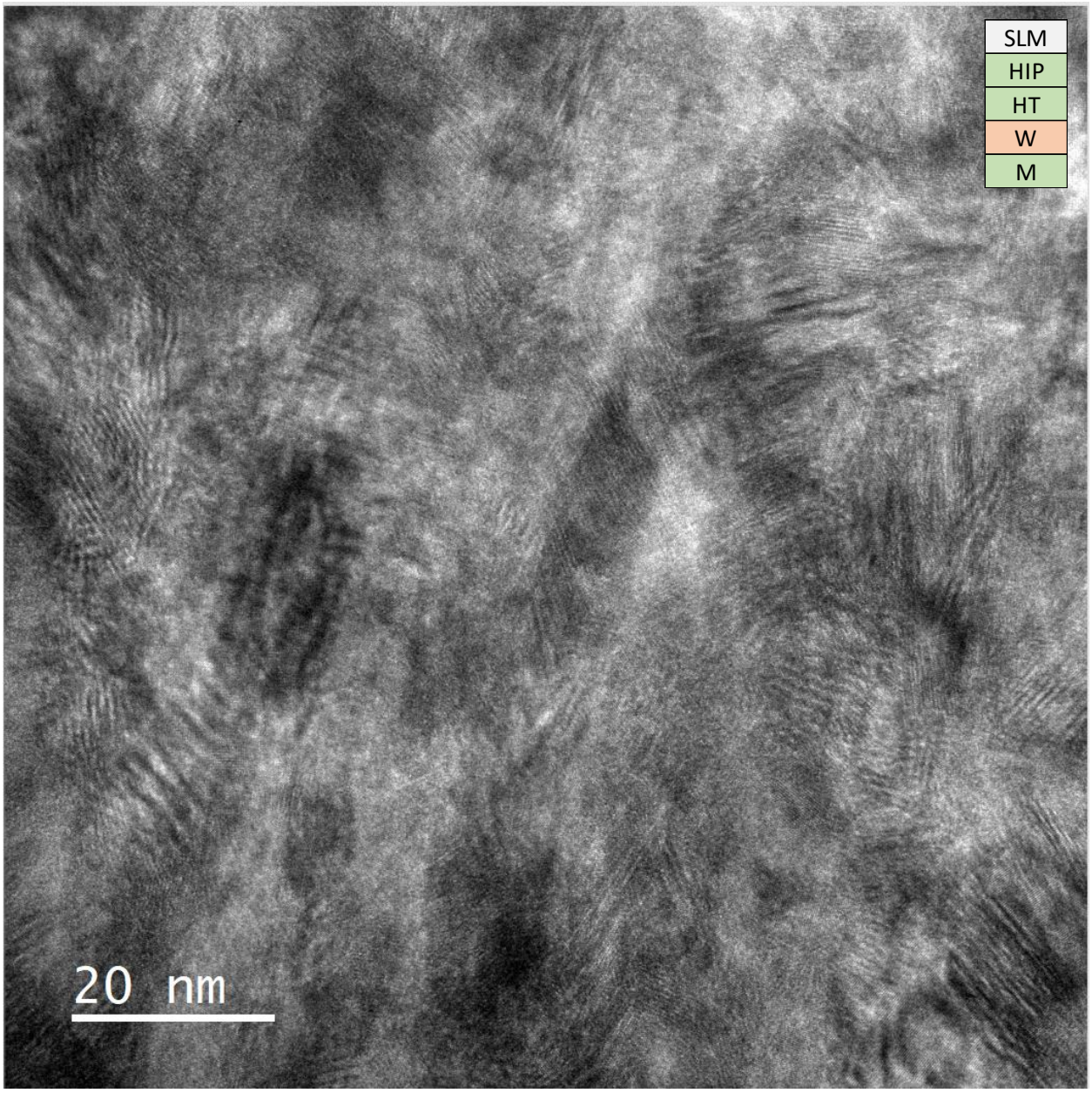

Fig. 197 – TEM Micrograph (OneView Cam) of Sample 8152 Region 2 (400,000x)

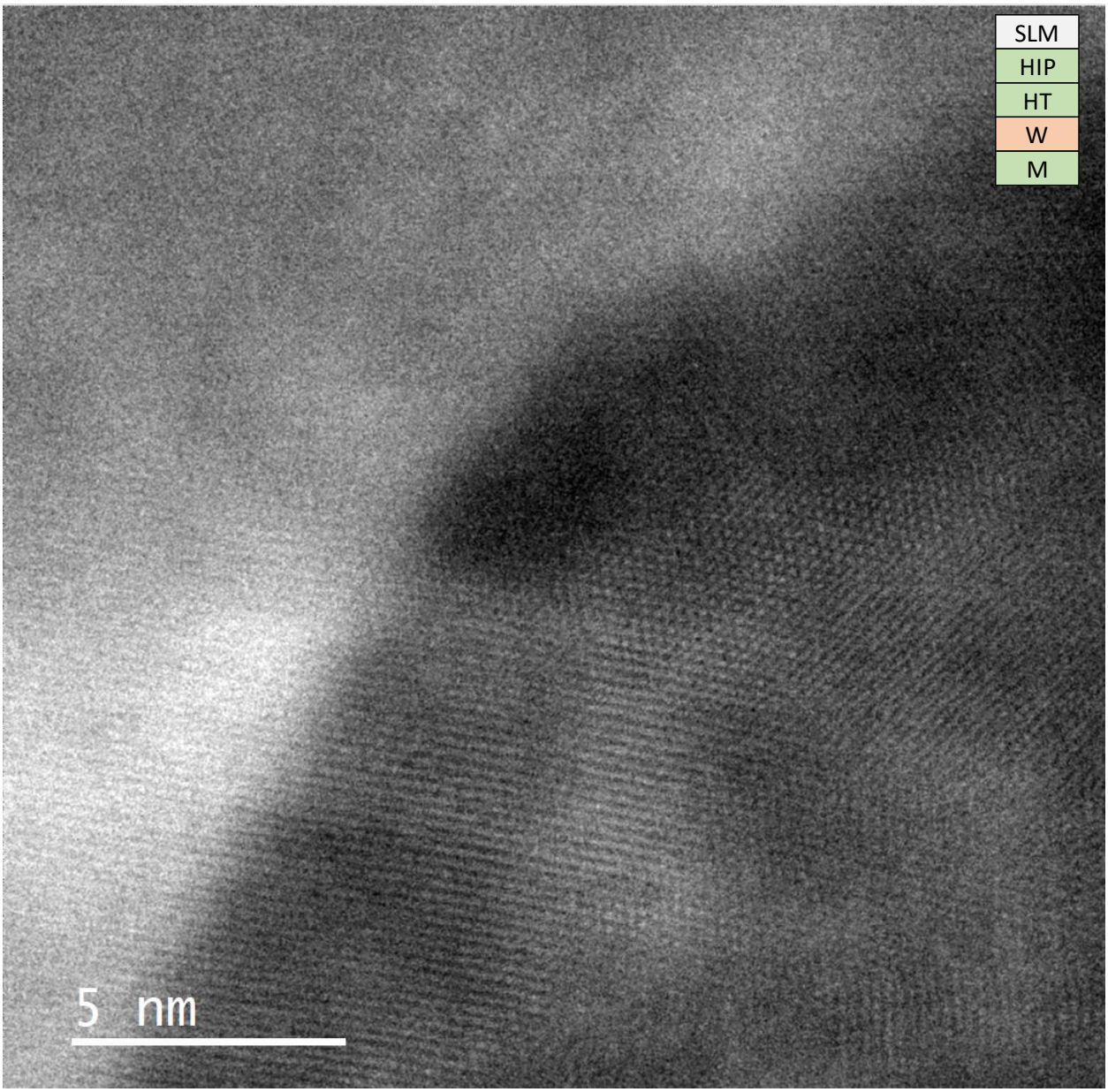

Fig. 198 – TEM Micrograph (Annular Dark Field) of Sample 8152 Region 3 (10,000,000x)

Sample 8159

The TEM micrographs below are of sample 8159 (HIP + Wrapped + Heat Treated + Not Machined). Unfortunately, the integrity of this lamella began to compromise during imaging preventing the ability for higher magnification pictures to be taken with the bright field and annular dark field settings – the micrographs included here are exclusively from the OneView camera.

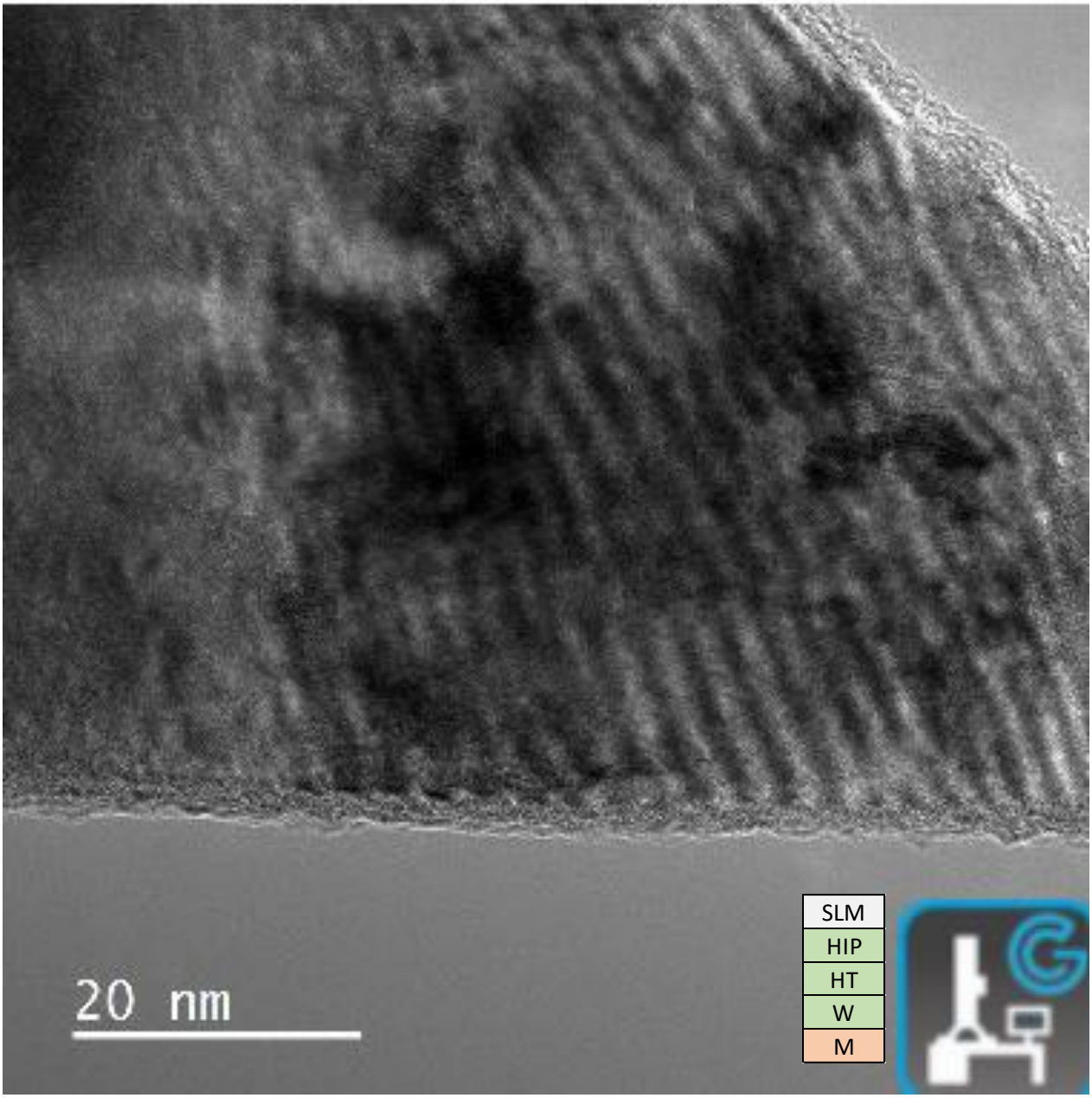

Fig. 199 – TEM Micrograph (OneView Cam) of Sample 8159 Region 1 (600,000x)

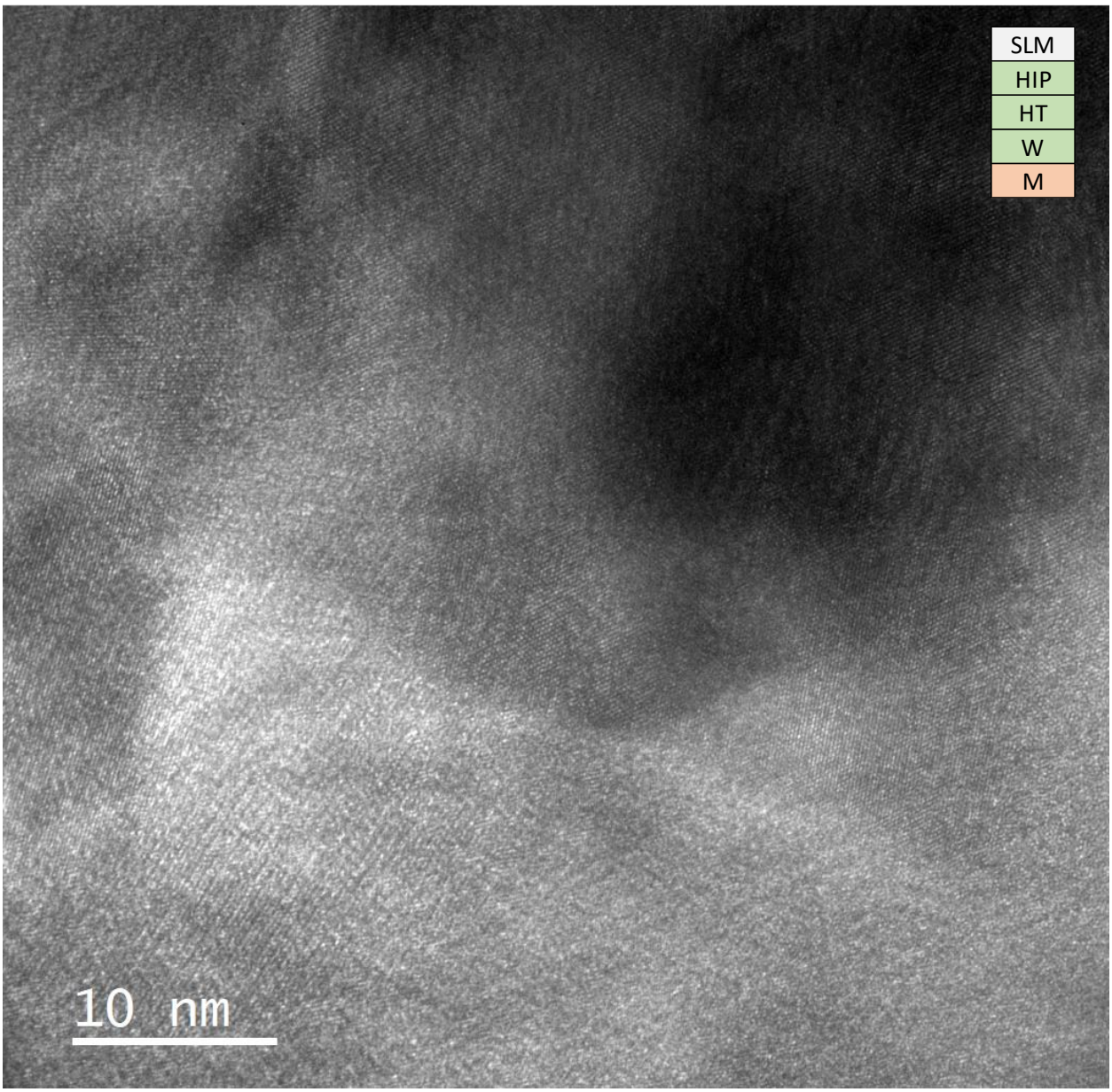

Fig. 200 – TEM Micrograph (OneView Cam) of Sample 8159 Region 2 (800,000x)

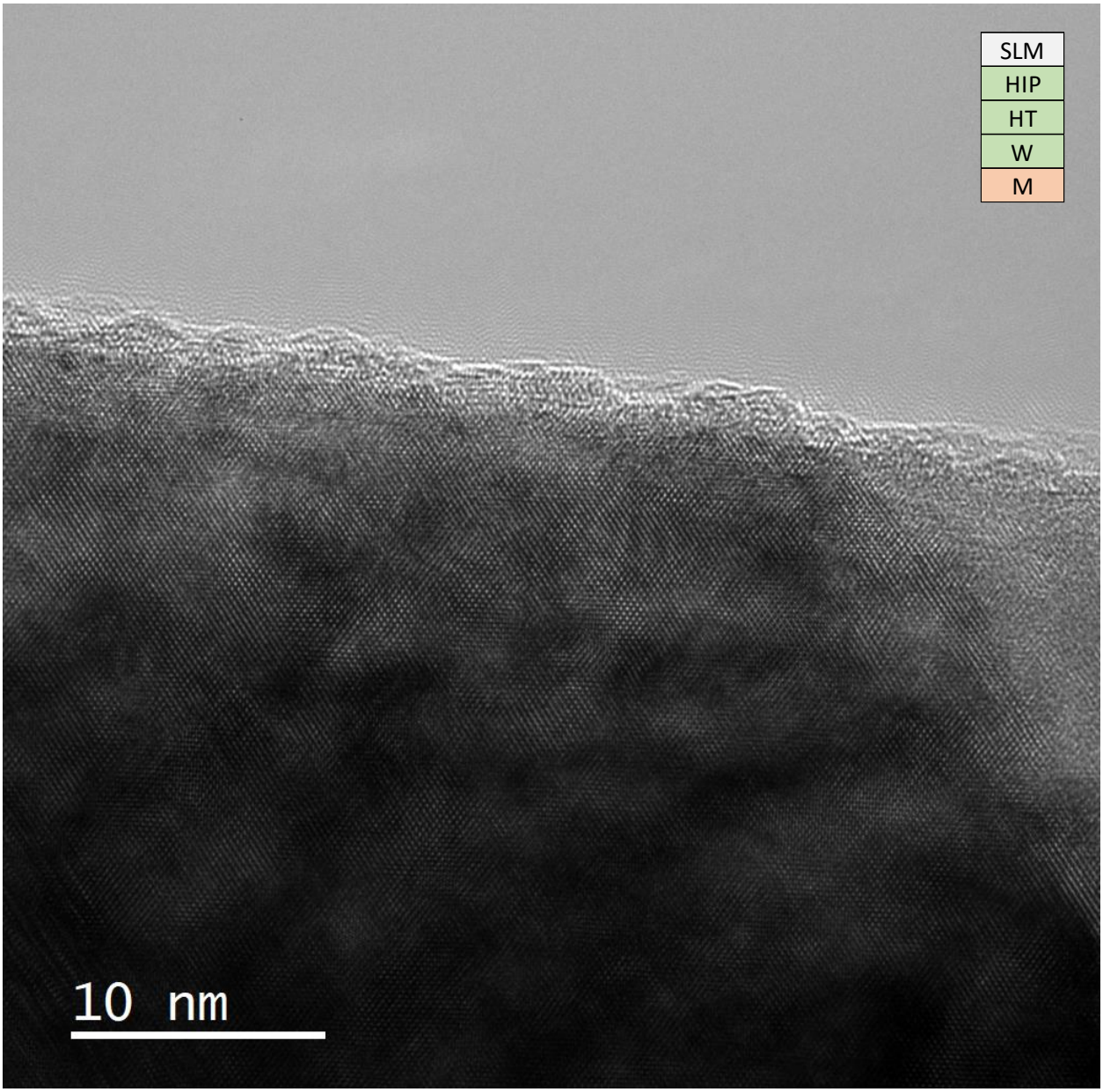

Fig. 201 – TEM Micrograph (OneView Cam) of Sample 8159 Region 3 (1,000,000x)

Sample 8473

The TEM micrographs below are of sample 8473 (HIP + Wrapped + Heat Treated + Machined).

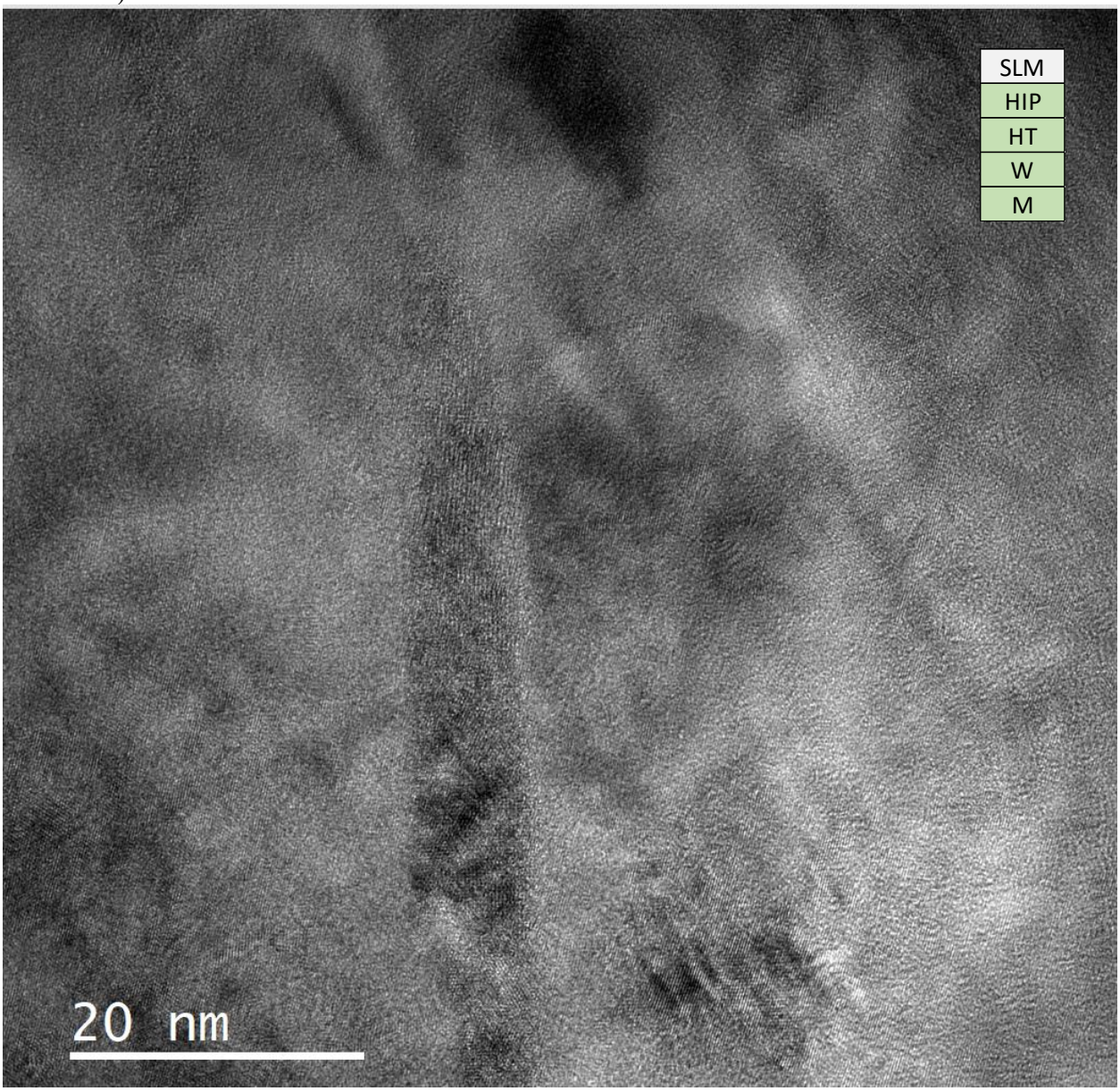

Fig. 202 – TEM Micrograph (OneView Cam) of Sample 8473 Region 1 (600,000x)

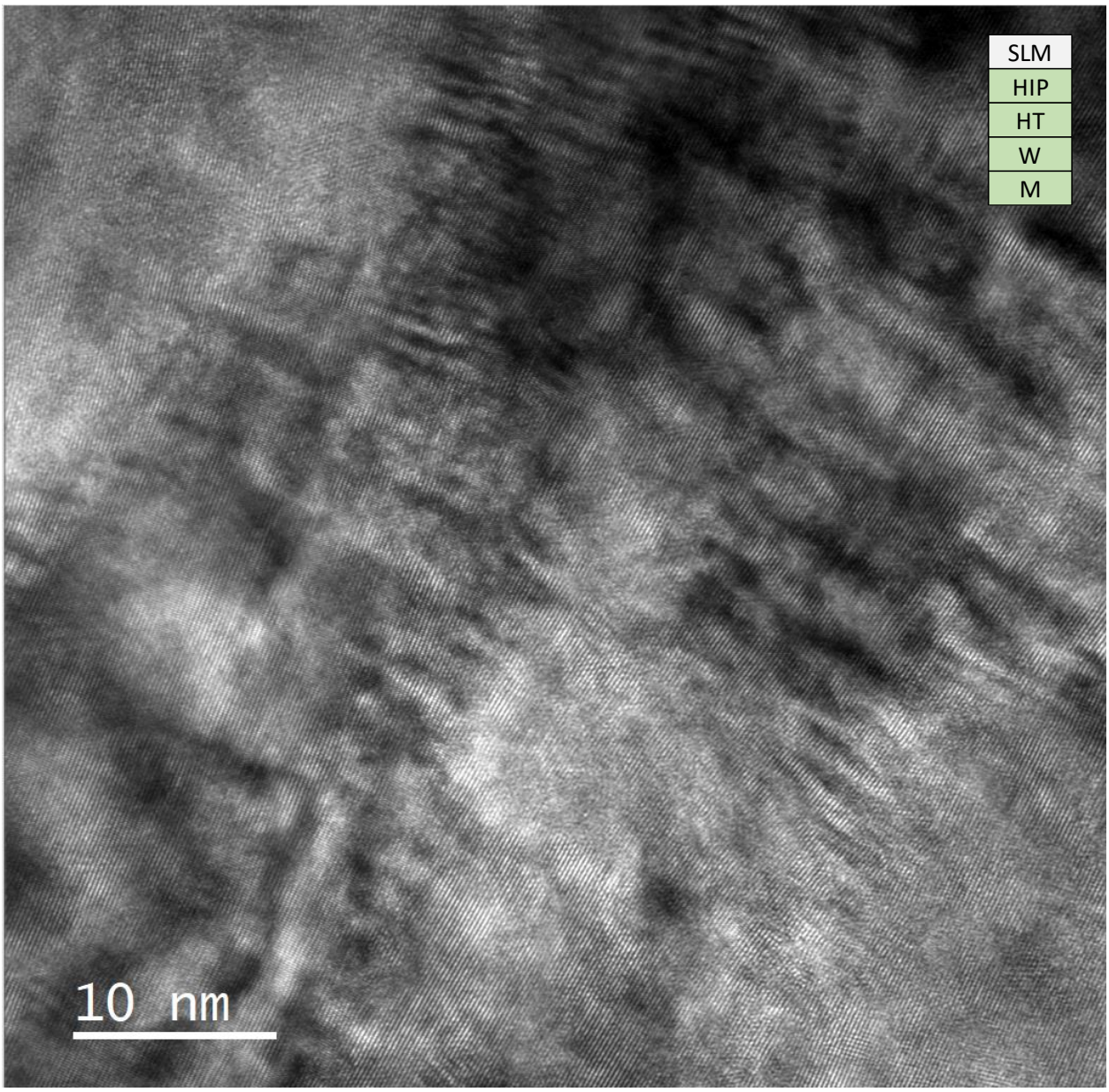

Fig. 203 – TEM Micrograph (OneView Cam) of Sample 8473 Region 2 (800,000x)

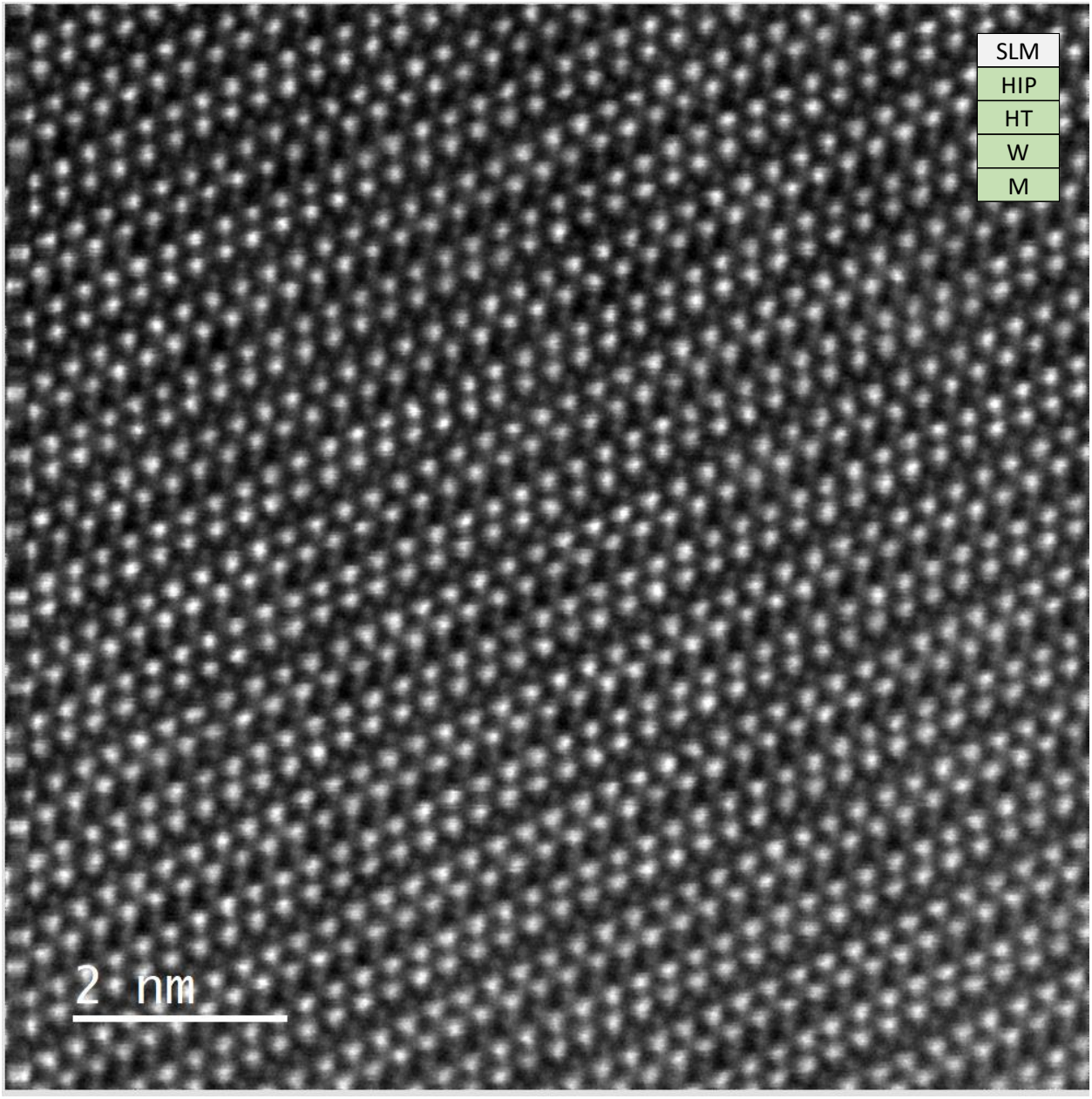

Fig. 204 – TEM Micrograph (Annular Dark Field) of Sample 8473 Region 3 (20,000,000x)

Transmission Electron Microscopy EDS

Sample 8046

The EDS analysis conducted on the TEM lamella from sample 8046 appears to show general homogeneity, with the exception of an aluminum oxide that also lightly overlaps with the detected signal for titanium. The spectra and tabularized data demonstrate that the region has been oxygenated heavily, with the next most abundant constituent being nickel followed by relatively equal concentrations of aluminum, chromium, and iron (atomic %).

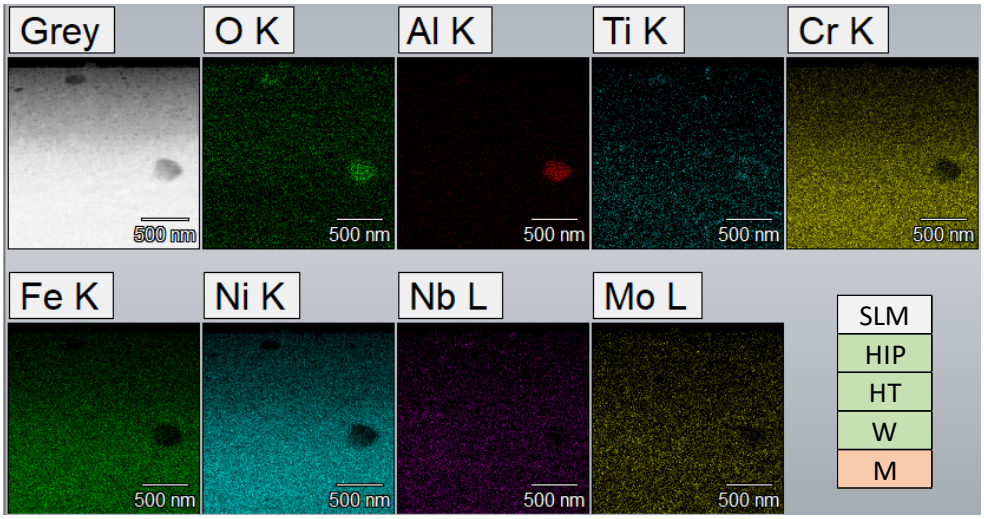

Fig. 205 – TEM EDS Maps of Sample 8046

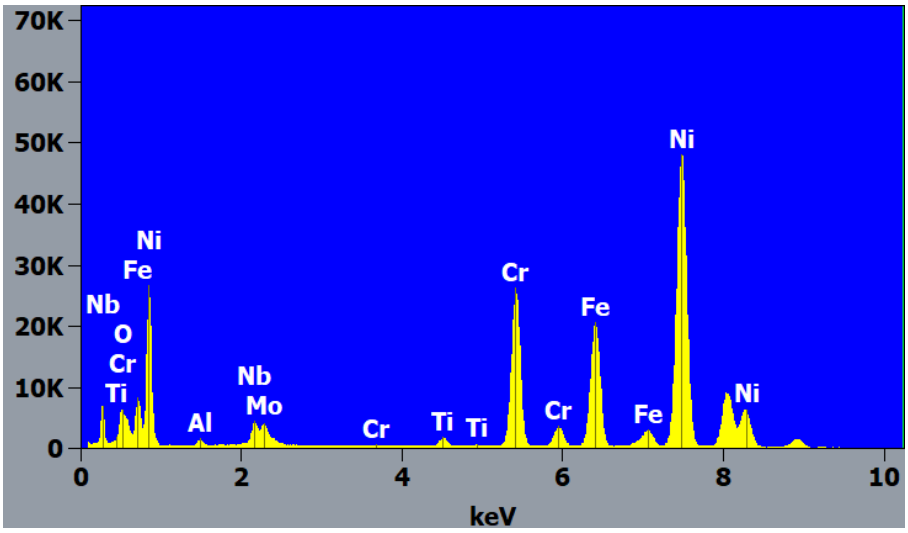

Fig. 206 – TEM EDS Spectra of Sample 8046

Table 17 – Tabularized EDS Data for Sample 8046

	Weight %	Atom %
O K	40.63	68.76
Ni K	31.82	14.67
Al K	5.51	5.52
Cr K	10.50	5.47
Fe K	10.31	5.00
Ti K	0.81	0.46
Nb K	0.30	0.09
Mo K	0.14	0.04

Sample 8064

The EDS analysis conducted on the TEM lamella for sample 8064 shows that an aluminum oxide is again present, which interestingly also includes a concentration of titanium surrounding instead of participating. Compositionally, it was surprising to see nitrogen detected in a significant amount. It's not believed that any source could have introduced nitrogen to the system, and as a result is thought to be a false signal overlapping with titanium.

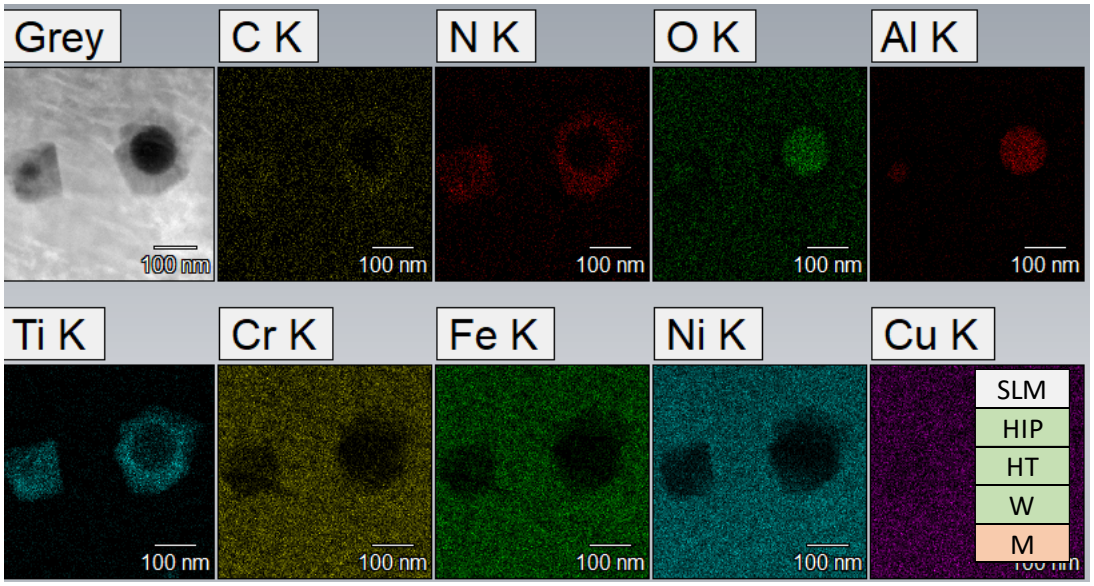

Fig. 207 – TEM EDS Maps of Sample 8064

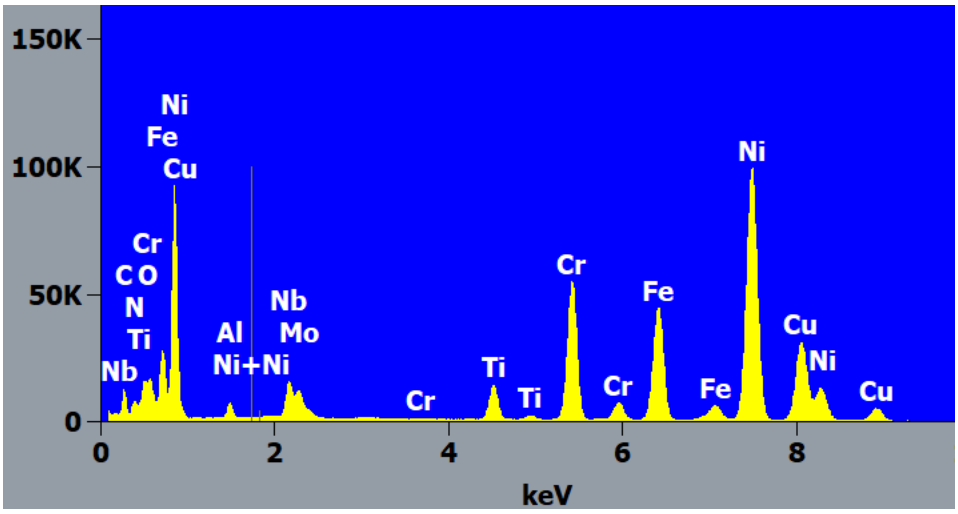

Fig. 208 – TEM EDS Spectra of Sample 8064

Table 18 – Tabularized EDS Data for Sample 8064

	Weight %	Atom %
O K	24.58	27.30
C K	22.48	33.26
N K	21.59	27.39
Ni K	10.72	3.25
Al K	6.43	4.23
Cr K	4.93	1.69
Fe K	4.23	1.34
Cu K	3.10	0.87
Ti K	1.70	0.63
Nb K	0.18	0.04
Mo K	0.07	0.01

Sample 8068

The EDS analysis conducted on the TEM lamella for sample 8068 shows homogenous maps with the exception of titanium structures (approximately 50-150 nm in diameter) that locally displace nickel. Notably, these deposits of titanium do not overlap with oxygen as is seen with the previous samples, and instead have a light correlation with niobium.

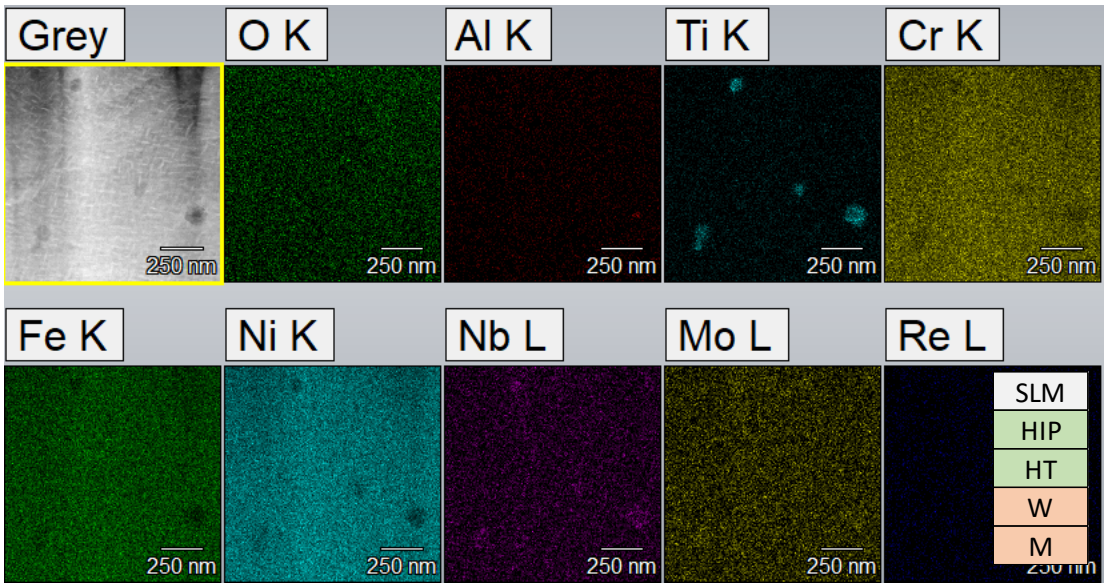

Fig. 209 – TEM EDS Maps of Sample 8068

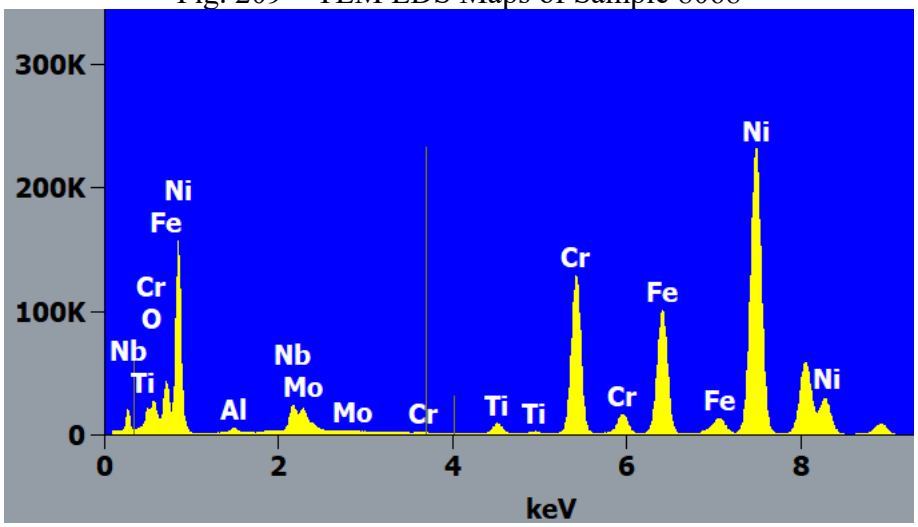

Fig. 210 – TEM EDS Spectra of Sample 8068

Table 19 – Tabularized EDS Data for Sample 8068

	Weight %	Atom %
Ni K	38.04	20.00
O K	30.85	59.53
Cr K	12.41	7.37
Fe K	12.34	6.82
Al K	4.68	5.36
Ti K	1.13	0.73
Nb K	0.37	0.12
Mo K	0.18	0.06

Sample 8152

The EDS analysis conducted on the TEM lamella for Sample 8152 showed very similar characteristics for what was seen with sample 8068, in that homogeneity was observed for most elemental maps besides titanium. The concentrations of Ti overlapped with aluminum and in one area niobium, though notably an oxygen signal was not detected in significant amounts. Overall constituency follows the standard for Inconel 718 with the exception of higher-than-normal amounts of aluminum (both in weight and atomic %).

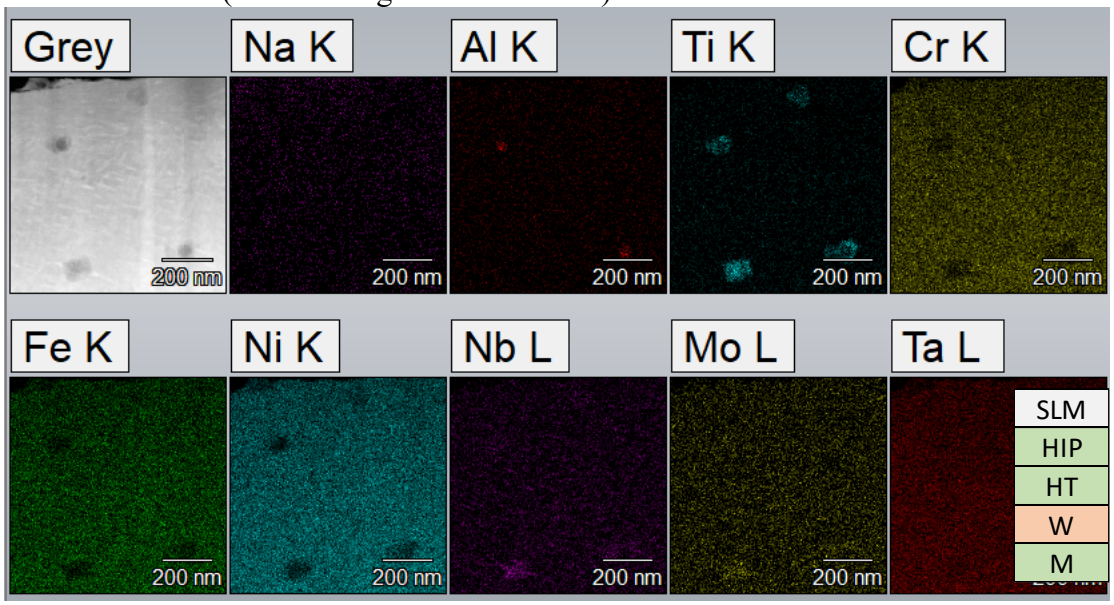

Fig. 211 – TEM EDS Maps of Sample 8152

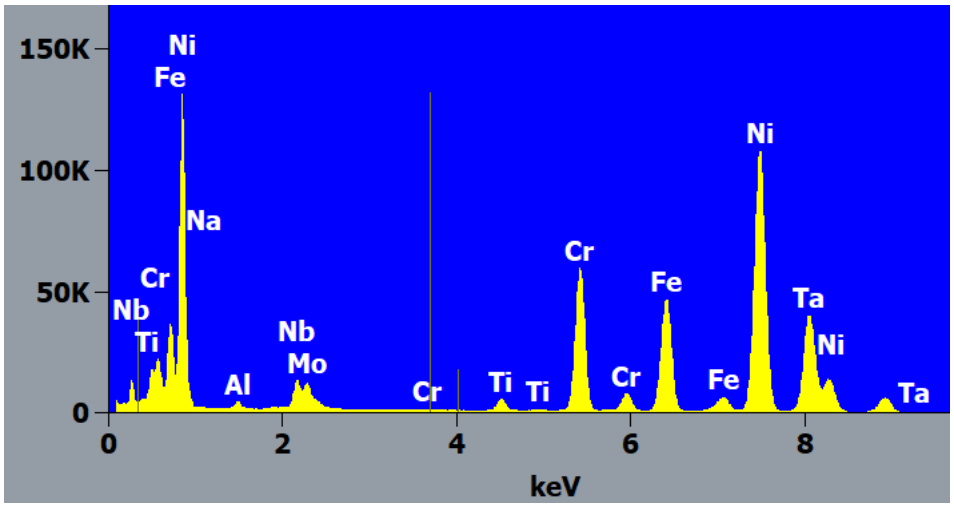

Fig. 212 – TEM EDS Spectra of Sample 8152

Table 20 – Tabularized EDS Data for Sample 8152

	Weight %	Atom %
Ni K	54.36	47.84
Fe K	17.19	15.90
Cr K	16.86	16.76
Al K	8.84	16.93
Ti K	2.00	2.16
Nb K	0.51	0.28
Mo K	0.23	0.13

Sample 8159

The EDS analysis conducted on the TEM lamella for sample 8159 displays a concentrated fringe of aluminum oxide adjacent to a thin line of titanium. From a perspective of elemental constituency, this sample shows a highly oxygenated plane also consisting of elevated carbon and aluminum.

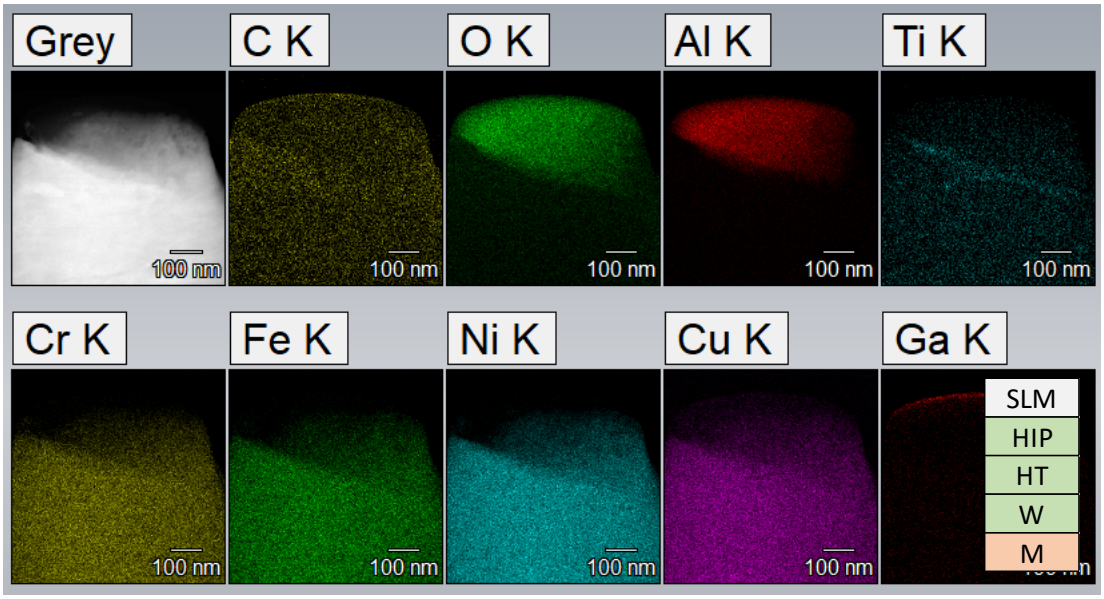

Fig. 213 – TEM EDS Maps of Sample 8159

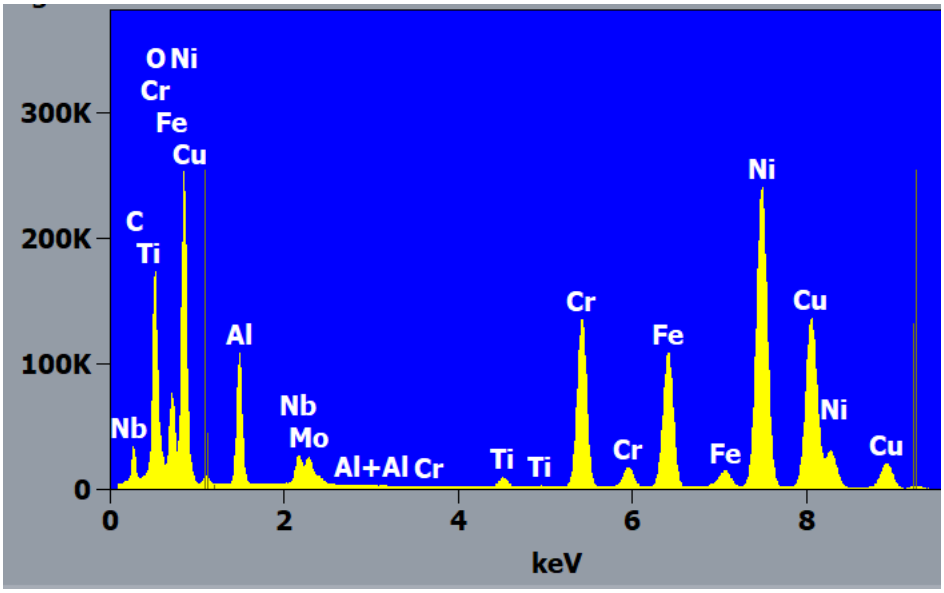

Fig. 214 – TEM EDS Spectra for Sample 8159

Table 21 – Tabularized EDS Data for Sample 8159

	Weight %	Atom %
O K	58.77	63.97
Al K	17.28	11.15
C K	15.34	22.25
Ni K	3.05	0.91
Cr K	2.15	0.72
Cu K	1.67	0.46
Fe K	1.47	0.46
Ti K	0.19	0.07
Nb K	0.04	0.01
Mo K	0.02	0.00

Sample 8473

The EDS analysis conducted on the TEM lamella for sample 8473 shows that (like with other samples) titanium concentrates in structures which generally overlap oxygen (though that map was not generated by the Pathfinder EDS software for the results below). Perhaps more notably, platelets of Nb-Mo could be seen which also overlapped with a detected signal for sulfur, which was unique to this lamella. A discrete observation for this sample as well was that carbon was the predominant constituent, followed by nickel and oxygen.

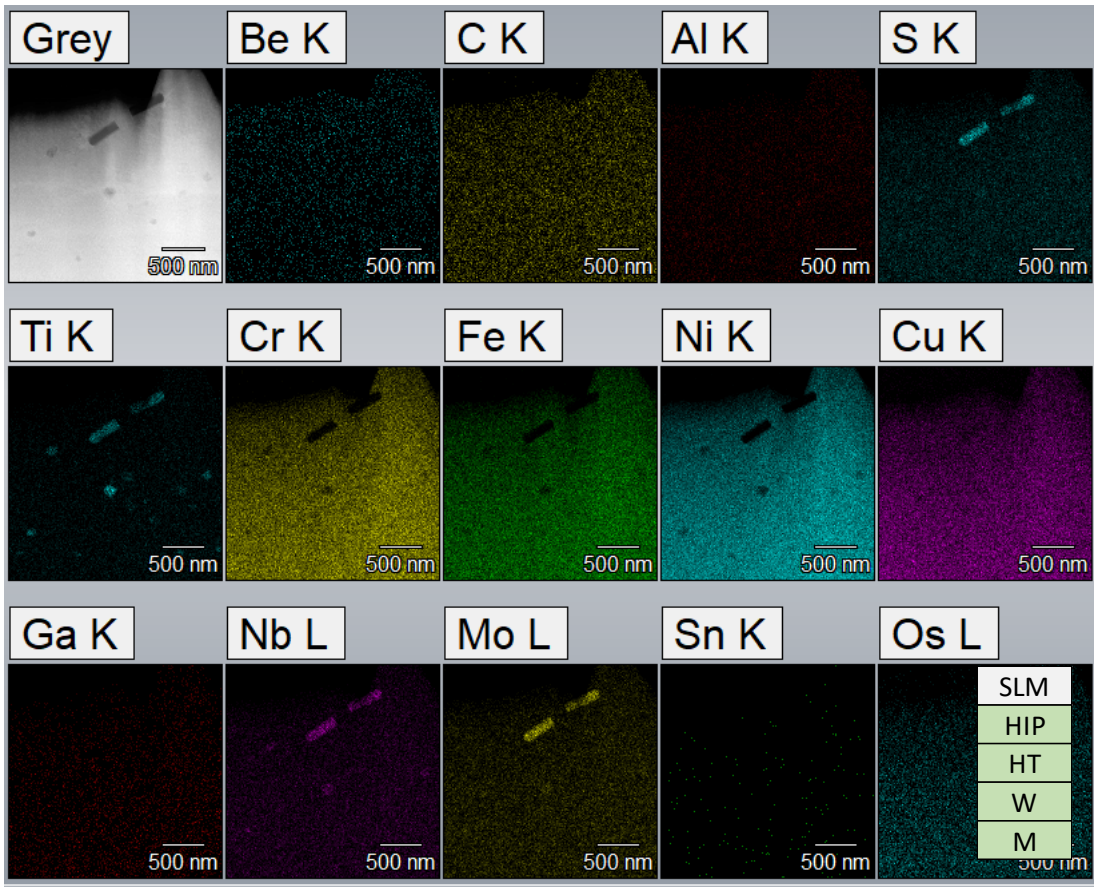

Fig. 215 – TEM EDS Maps of Sample 8473

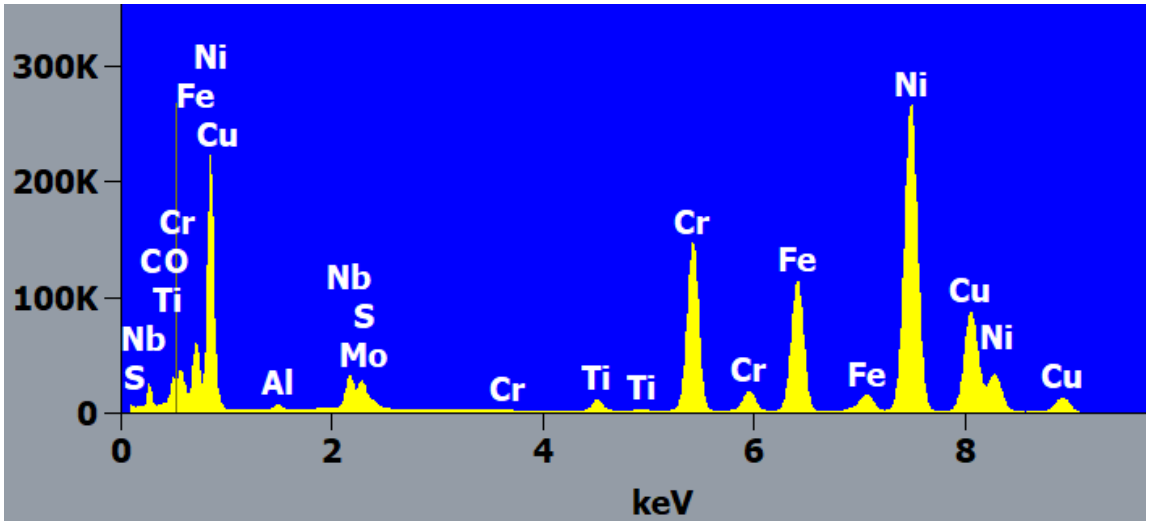

Fig. 216 – TEM EDS Spectra for Sample 8473

Table 22 – Tabularized EDS Data for Sample 8473

	Weight %	Atom %
C K	28.07	51.10
Ni K	22.49	8.37
O K	19.65	26.85
Cr K	8.46	3.56
Fe K	7.54	2.95
Cu K	6.77	2.33
Al K	3.28	2.66
S K	2.49	1.70
Ti K	0.85	0.39
Nb K	0.27	0.06
Mo K	0.12	0.03

Chapter 6: Discussion

The promoted combustion behavior of 16 rods manufactured of Inconel 718 has been described above from the standpoint of optical microscopy and microstructural characterization, elemental analysis via x-ray fluorescence and energy dispersive spectroscopy, scanning electron microscopy, and x-ray diffraction. Additionally, baseline characterizations of 6 additional additively manufactured rods were imaged within their burn interfaces via transmission electron microscopy and were also subsequently analyzed with energy dispersive spectroscopy.

SAMPLE SET 1

16 sample rods (14 manufactured through selective laser melting, 2 wrought) were analyzed as a group known as sample set 1. These rods represented a variety of different post-manufacturing histories which included hot-isostatic pressing, wrapping with oxygen-getting titanium foil during the hot-isostatic press, surface machining, and standardized heat treating. Specific details regarding these treatments can be found in the introduction section.

Upon sample reception, as-received photography and burn tip stereomicroscopy was completed both to document the initial conditions of the rods pre-analysis as well as to provide basic descriptions of the burned ends of each rod as they displayed a wide range of shapes and sizes. The burn lengths for sample set 1 rods ranged from 1.5 cm (shortest) to 13.4 cm (longest), and typically displayed surface finishes that corroborated post-processing (i.e. rough grainy surfaces for those without machining, smoother finishes for those with, etc.).

Stereomicroscopy was able to demonstrate that for virtually all of the rods the burn tip could be characterized as a slightly bulbous head of brittle metal with slight lips of overhanging material around their circumference which appeared cloud-like in texture and shape. Though burn tips were generally centered along the axis of the rods, some had noticeable leans or slants to them

where they extended further or shorter lengths over the bulk material. Some rods (such as sample 8082 – HIP, wrapped, heat treated, not machined) were essentially flat with almost no protruding burn tip, while others (like sample 8158 – HIP, wrapped, heat treated, machined) had significant masses of material attached to their ends.

Following initial documentation, sample rods were inserted into a scanning electron microscope for surface imaging and chemical analysis. This initial round of microscopy further confirmed the observations made regarding the burn tips and surrounding areas during stereomicroscopy, namely when samples received machining their surfaces tended to be significantly smoother than those without (which generally exhibited varying degrees of un-sintered particulate as a result of the SLM process). The more significant finding from this analysis step was that ten of the rods (7679, 8065, 8082, 8174, 8184, 8488, 8522, 8525, 8531, and 8541) showed a network of fine granular features upon the surface of their burn interfaces which were only visible upon higher magnification. These rocky agglomerations of material tended to exist in the range of 0.2 – 0.5 μm in diameter, and though were round in shape for most samples a few did appear sharper and more angular (like those seen on sample 7679). It has been hypothesized that this material, being on the interface between melted and bulk material, may have rapidly oxidized and then quenched at the conclusion of combustion testing. The author does not have at this time a firm rationale for why this only occurred in 10 of the samples and not the other 6, and this point should be considered for future analysis.

Energy dispersive spectroscopy during this stage of analysis yielded fairly standard results across all samples. The burn tips typically demonstrate a concentration of chromium, niobium, and oxygen – coupled with depletion of nickel and iron. Data from the polished EDS analysis displays that the interior of the burn tip sees the reverse of this trend with regards to metallics, showing that

the elements chromium and niobium “float” to the surface of the liquid melt pool as opposed to staying concentrated in the liquid like nickel and iron. These higher concentrations of chromium and niobium then appear to solidify after flame extinguishment as a thin layer around the volume of the burn tip, explaining their observed intensities for the samples shown below. Nickel and iron then solidify preferentially in the interior of the burn tip as opposed to on the outer surface, as demonstrated by their depletion relative to the surrounding rod material.

Mapping of the burn interfaces themselves show thin concentrated deposits of titanium along the lower ridge (bulk side) and iron along the upper ridge (initiation of the burn tip volume). Surface scans generally did not show anything of note, besides higher abundances of aluminum oxide on unsintered particulates on non-machined rods.

X-ray fluorescence was selected as a readily available and cost-efficient means of conducting baseline chemical analyses on the sample rods following initial SEM analysis. However, the author notes that there were difficulties with utilizing this method for analysis on these samples as their small size and diameter proved to be troublesome in scanning with the window of the instrument. For this reason, several rods (8082, 8184, and 8488) were unable to be analyzed. For the rods which could be tested, inflated values for aluminum, silicon and sulfur were often seen and as such artificially lowered the average nickel content. Samples were still correctly identified as Inconel, though the grade was undetermined via the instrument’s software. It’s believed that the samples’ inability to fully cover the window of the XRF gun prevented accurate readings, as surrounding material may have been able to skew the detected signal. For these reasons, the XRF data was still included in this report but with the understanding that it’s not precise and shouldn’t be considered representative of bulk chemistry.

Samples were then metallographically polished and etched, and optically imaged to characterize microstructure. One clear observation of burn tip micrographs was that they tended to exhibit discrete regions of highly directional acicular structures which exist in various orientations. This lack of homogeneity in directionality may suggest variable solidification conditions at flame extinguishment following combustion testing. Some samples are particularly notable for these features and even resemble Widmanstatten-like patterns (such as samples 7676, 7679, and 8522). Spherical oxides were also present, with thin layers of darker oxide observable non-homogenously along the outer rim of the burn tips.

With regards to burn interfaces, the microstructures are significantly darker (thus were preferentially affected by the chemical etching) and show dendritic features which are present throughout the region but tended to concentrate in the centers. Of note is the variability in burn interface geometry and size, for some samples the interface is relatively perpendicular to the rod (such as samples 8174 and 8525) whereas others see the line slanted and more wedge-shaped (samples 7676 and 7679). In terms of size, the interfaces could be quite short (approximately 100 μm for sample 8174) or much longer (over 350 μm for sample 8488). It would appear that for samples with greater burn lengths the burn interfaces were also larger, and vice versa. This observation should be noted for future analysis.

Additionally, a majority of the rods showed convex interfaces (where they form a “c-shape” with relation to the rod) but two did not and were instead concave relative to the rod. This would lead to the belief that in the case of those samples (8082 – SLM, HIP, Wrapped, Heat Treated, Not Machined; and 8531 – SLM, HIP, Wrapped, Heat Treated, Machined), material was consumed by combustion at a faster rate in the center of the rods than the material at the outer

surface. Interestingly, those two rods also had the second and third longest burn lengths (respectively) from the entire sample set.

Within these burn interfaces, some samples also displayed significant crevices which overlapped with the dendritic structures previously observed. Though the length and width of these features varied, the majority were fairly shallow. The exception to this rule would be those seen in sample 8488 which had enough depth to be completely out of focus with the plane at the polished surface of the rod.

In comparing the heat affected zone to the bulk of the rods, it's generally observed that grains have recrystallized and grown in contrast to the standard austenitic microstructure seen in the bulk. In the case of both regions, the microstructure can be characterized as a binary phase matrix comprised of equiaxed grains. Some samples display acicular precipitates (a residual from the post-processing heat treatment) as well as annealing twins. As grain recrystallization can promote the formation of these twins, their concentration is typically higher in the heat affected zone in comparison to the bulk.

Following optical microscopy, polished samples were again analyzed with SEM in order to image and conduct EDS on the newly exposed internal cross section of the rods. Similar to what was seen in optical microscopy, the sample burn tips tended to display regions of varying solidification directionality. With higher magnification it became clear that these regions also demonstrated differences in hardness, as the polishing process was not visible on darker areas but scratches could be seen in lighter ones. What was most clearly obvious after polished SEM imaging was that virtually all of the samples exhibit very fine stringed structures throughout the burn tip which were later confirmed through EDS to be primarily composed of niobium. This characteristic was not particular to any processing history combination.

Within the burn tip region, spherical oxides were present and subsequently imaged. These oxides did vary in size, but generally existed in the range of 40 – 100 μm in diameter. They typically contained a light and dark phase, and through EDS these phases were found to be higher in niobium and titanium (for lighter regions) and aluminum and oxygen (for darker regions). These oxides show large plates of the Al-O rich regions surrounded by a matrix of the lighter Nb-Ti oxide material, with what can be described as lamella of the Al-O rich oxide propagating within

Along the outer perimeter of the burn tips, solidified melt pool surface oxides were also observed and imaged. The composition of these features follows what was seen for the spherical oxides seen in the burn tip - the lighter regions were rich in niobium and titanium while the darker areas had higher concentrations of aluminum and oxygen. The thickness of such oxide layers was generally shallow (approximately 25-30 μm), but they were non-homogenously distributed along the melt pool surface and could be thicker in some areas while completely absent in others.

Dendritic crevices were seen in slightly more than half of the sample set 1 rods (9 had them and 7 did not). They appeared to follow the same ordering and pattern as the niobium structures seen throughout the burn tips, though themselves appeared to be concentrated to the center of the burn tips and adjacent to the burn interface. At higher magnifications it can be seen that the crevices seem to be areas of material pull-out, with clear indications of an attempt by the material to lower its surface energy as the residual holes left behind can be highly angular with sharp geometries.

With regards to sample burn interfaces, initial observations identified that the center of such interfaces and their respective melt tip and bulk adjoining sides are distinct from each other. Typically, the side of the interface which transitions to the bulk is coarse and rocky while the opposite end of the interface (melt tip side) sees a gradual decline in concentration of the niobium structures coupled with nodule-like holes which are finely dispersed.

Polished EDS mapping further illuminated some of the observations made above. Sample burn tips maps were characterized by a depletion of chromium (coupled with the thin concentrated layer on the burn tip surface) and a concentration of nickel. Niobium contributed towards oxides, more heavily so those existing on the burn tip surface, and at times overlapped with molybdenum.

Aluminum and titanium could also be seen overlapping with each other as they comprised a majority of the spherical oxides contained in the area. Spectra and tabularized data show that the burn tip region saw an estimated increase of nickel content from approximately 50% in the bulk to 65-70%. Iron content generally stayed consistent or decreased slightly, while chromium typically saw a decrease in concentration from approximately 18% to below 10%.

EDS mapping and line-scans of sample burn interfaces reinforce what has been seen in previous analysis, namely that as one travels from the bulk to the burn tip there's a negative gradient of chromium and niobium and a positive gradient of nickel. The line-scan analysis in particular also shows that for many samples the detected molybdenum intensity flattens out once one reached the burn tip area. The niobium dendrites that have been seen previously were line-scanned at high magnification for one sample (8522) which interestingly displayed that in terms of intensity the dendrites seemed to be almost the same amount molybdenum as niobium.

The outer surface EDS analysis showed general chemical homogeneity (corroborating what was seen in the bulk) but with slight differences at high magnification. For sample 8488, what can be seen is that despite not receiving any wrapping during the hot-isostatic press, titanium and aluminum diffused to the surface to form thinly concentrated layers. Additionally, Nb-Mo deposits can be found which at times show a slight overlap with titanium. From a point scan perspective, the chemical composition of this region does not differ significantly from the bulk.

Sample 8541 (which was not machined following initial manufacture but was wrapped with titanium foil during the hot-isostatic process) still shows that thin layers of concentrated titanium and aluminum formed on the rod surface, though here the Nb-Mo structures are not present. Again, point scan analysis does not show an appreciable difference in composition when compared to the bulk however carbon content remains elevated (likely a result of nearby carbon signal supplied by the mount material).

Sample 8525 (which was machined following manufacture but did not receive titanium foil wrapping during the hot-isostatic pressing process) shows that neither phenomenon observed above occurred. Nb-Mo structures were not seen, and titanium did not accumulate on the rod

surface (though aluminum could be seen as having diffused and also seemed to contribute towards internal oxides in the region). Once more, point scan analysis did not reveal any significant deviation from bulk chemistry.

With regards to XRD, the vast majority of sample spectra displayed characteristic peaks for the Ni_3Al γ' precipitate phase at approximately 45˚ (2θ), the secondary Ni_3Nb γ" precipitate peak closer to 50˚ (2θ), the δ-phase Ni_3Nb at approximately 75˚ (2θ), and the simple nickel phase at around 90˚ (2θ). Deviation was typically introduced when the spectra for heat affected zones were overlayed on the bulk spectra, demonstrating that for many samples there was drastic variability in the intensity seen for several phases. As one example, the bulk spectra for sample 7679 showed an intensity for the Ni_3Al γ' precipitate phase at nearly 6000 cps (counts-per-second) while its' heat affected zone showed a significantly weaker intensity (approximately 400 cps) for the same phase. Notably, this trend was reversed in the case of the Ni_3Nb phase as it was much more intense in the heat affected zone than the bulk.

Other samples could at times demonstrate a change in the predominant peak, such as sample 8082. While the majority of samples have as their primary phase the Ni_3Al γ' precipitate seen at 45˚, this sample instead showed a higher intensity for the Ni_3Nb γ" precipitate. The measured intensity for the δ-phase Ni_3Nb was nearly identical in the bulk scan, though this tapered off significantly for the scan conducted on the heat affected zone.

The sample with the largest burn length of the study was sample 8488 (SLM, HIP, Not Wrapped, Heat Treated, Not Machined). The most obvious detail to note from this sample's spectra is that the heat affected zone shows a detected signal above 9500 cps for Ni_3Al γ' precipitates, not only substantially overtaking any other peak on the spectra for this sample but also being orders of magnitude greater than the same peak signal for other samples.

SAMPLE SET 2

The samples from Sample Set 2 were selected on the basis of powder batch lot and burn length variability. Samples 8068, 8152, 8046 and 8473 are all from the G2 batch lot and also represent the 4 sequences (HIP + Not Wrapped + Not Machined, HIP + Not Wrapped + Machined, HIP + Wrapped + Not Machined, and HIP + Wrapped + Machined) of processing histories available for analysis as all were heat treated. Samples 8064 and 8159 were chosen because they are from the same batch lot and have identical processing history but have significantly different burn lengths.

Sample 8046 (HIP + Wrapped + Heat Treated + Not Machined) imaged via the OneView camera can be generally characterized as having complex misorientations of crystallites along with thickness fringes. Twin grain boundaries (resultant of the localized recrystallization) were visible and dispersed throughout. EDS analysis conducted on the TEM lamella from sample 8046 appears to show general homogeneity, with the exception of an aluminum oxide that also lightly overlaps with the detected signal for titanium. The spectra and tabularized data demonstrate that the region has been oxygenated heavily, with the next most abundant constituent being nickel followed by relatively equal concentrations of aluminum, chromium, and iron (atomic %).

Sample 8064 (HIP + Wrapped + Heat Treated + Not Machined) has the same processing history as sample 8046 above, however this rod was from powder batch lot A2 and serves as a couple to sample 8159 which also had identical processing but a much longer burn length. The viability of the lamella made imaging difficult, however wavy fringes could be observed across the sample along with relatively abundant cross lattices. EDS analysis conducted on the TEM lamella for sample 8064 shows that an aluminum oxide is again present, which interestingly also includes a concentration of titanium surrounding instead of participating. Compositionally, it was surprising to see nitrogen detected in a significant amount. It's not known what the source of the nitrogen may be (the HIP process conducted on this sample used argon gas), and its' Kα1 keV of

3.92 does not overlap with any other constituents. It appears to concentrate in the same area as titanium and carbon.

Sample 8068 (HIP + Not Wrapped + Heat Treated + Not Machined) showed distinctly high angle grain boundaries in comparison to other samples and was also significantly more brittle than others making uniformity in the lamella preparation difficult. EDS analysis conducted on the TEM lamella for sample 8068 shows homogenous maps with the exception of titanium structures (approximately 50-150 nm in diameter) that locally displace nickel. Notably, these deposits of titanium do not overlap with oxygen as is seen with the previous samples, and instead have a light correlation with niobium.

Sample 8152 (HIP + Not Wrapped + Heat Treated + Machined) was difficult to image via bright field, and as such all images collected were from the OneView camera and annular dark field imaging settings. Images appear to show generally lower angle boundaries in comparison to other samples, as well as the inclusion of platelets of what EDS later confirmed were titanium. EDS analysis overall showed very similar characteristics for what was seen with sample 8068, in that homogeneity was observed for most elemental maps besides titanium. The concentrations of Ti overlapped with aluminum and in one area niobium, though notably an oxygen signal was not detected in significant amounts. Overall constituency follows the standard for Inconel 718 with the exception of higher-than-normal amounts of aluminum (both in weight and atomic %).

Unfortunately, the lamella integrity of Sample 8159 (HIP + Wrapped + Heat Treated + Not Machined) began to compromise during imaging preventing the ability for higher magnification pictures to be taken with the bright field and annular dark field settings. As such the micrographs collected were exclusively from the OneView camera and appear to show higher amounts of deformation and lattice strain, though it would be difficult to say whether this was from temperature driven expansion/contraction during testing or an artifact of the TEM sample preparation. EDS analysis conducted on the TEM lamella for sample 8159 displays a concentrated fringe of aluminum oxide adjacent to a thin line of titanium. From a perspective of elemental

constituency, this sample shows a highly oxygenated plane also consisting of elevated carbon and aluminum.

Sample 8473 (HIP + Wrapped + Heat Treated + Machined) was perhaps the most successfully prepared lamella, as it allowed for the greatest high magnification resolution of the lattice (and included twin grain boundaries). EDS analysis conducted on the TEM lamella for sample 8473 shows that (like with other samples) titanium concentrates in structures which generally overlap oxygen (though that map was not generated by the Pathfinder EDS software). Perhaps more notably, platelets of Nb-Mo could be seen which also overlapped with a detected signal for sulfur, which was unique to this lamella. A discrete observation for this sample as well was that carbon was the predominant constituent, followed by nickel and oxygen.

IN REFERENCE TO PRECURSOR WORK

As mentioned in the background and introduction chapter of this document, previous work done by Jonathan Tylka showed distinct observations which appear to be significant:

a. When wrapped during HIP, machining did not seem to influence burn lengths for the samples significantly. When not wrapped during HIP however, machined samples appeared less flammable and non-machined samples seemed more flammable.
b. For a set of samples which were all HIP + wrapped + heat treated but not machined, three variables were found statistically to drive approximately 80% of the flammability response observed (titanium nitride volume fraction, carbon percentage, and molybdenum percentage).
c. The dendritic niobium features that could be seen in some sample burn interfaces appeared to coincide with carbon content, leading to a hypothesis that perhaps the structures were residual NbC carbides which were able to remain bonded together in the region.

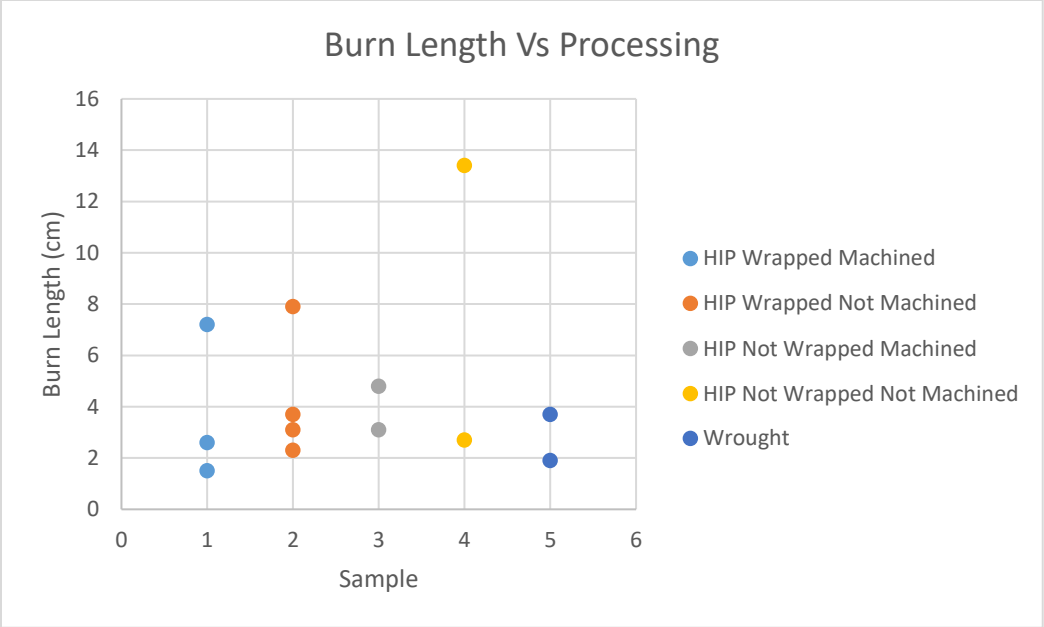

Fig. 217 – Scatter Plot of Burn Length vs Processing

Given the sample size of this study, it was not possible to statistically support or deny the notion that wrapping during HIP prevents variability for burn length in samples that were machined vs not, or that if there is no wrapping during HIP the samples are more or less likely to burn as a result of machining status. However, in the small set of samples analyzed here it can be seen that the processed SLM rods trend towards higher burn lengths than the two wrought rods included for comparison. It should be noted that this is not decisive on comparing the two manufacturing categories against each other per se, and just a simple observation of burn length plotting for the samples given. Interestingly, for these samples it would appear that machining does have a small observable trend of slightly lower burn lengths than their direct non-machined counterparts. This would lead once more to the idea that surface chemistry or configuration may have significance in burn responses, as the surface is what's most directly influenced by machining.

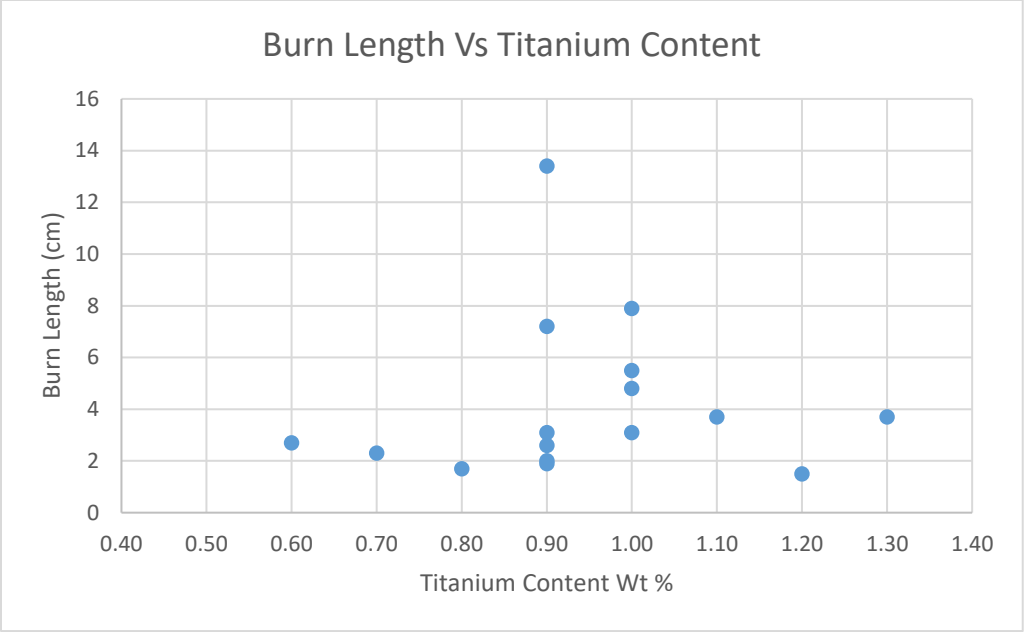

Fig. 218 – Scatter Plot of Burn Length vs Titanium Content

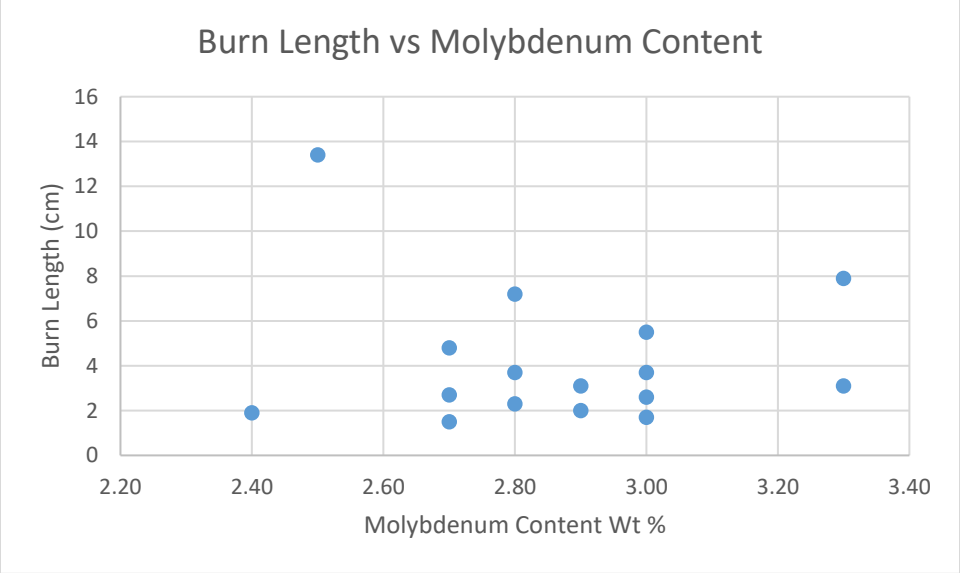

Fig. 219 – Scatter Plot of Burn Length vs Molybdenum Content

The above scatter plots display burn length as a function of either titanium or molybdenum content. This data should be considered to have a reasonable amount of error associated with it (as it was collected via EDS which is not a truly quantitative analysis method), however for what it can represent appears to show that a titanium content of 0.9 – 1.0% is where the most samples

were documented, and also saw the highest burn lengths included in its range. Samples with higher or lower titanium content appeared to show comparable burn length (2-4 cm). Again, it should be noted this is only within the context of this sample set. Molybdenum was more random, with the highest and lowest burn lengths only being 0.1% different with regards to chemical content.

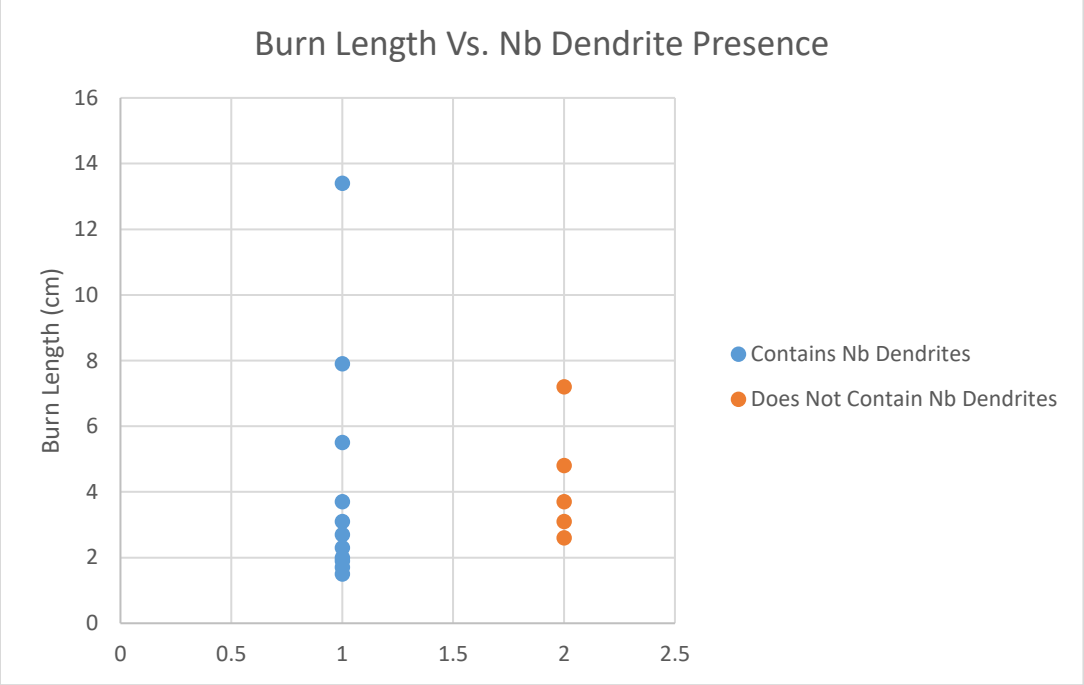

Fig. 220 – Scatter Plot of Burn Length vs Niobium Dendrite Presence

The niobium dendrites often mentioned throughout this document were tracked and plotted against burn length, and appear to show that for samples where they were present there was a wider range of flammability responses than for samples where they were not. It should be noted that EDS mapping also did not appear to show significant overlap with carbon in these regions, however they did display common overlap with molybdenum (both elements of which form carbides in this alloy system).

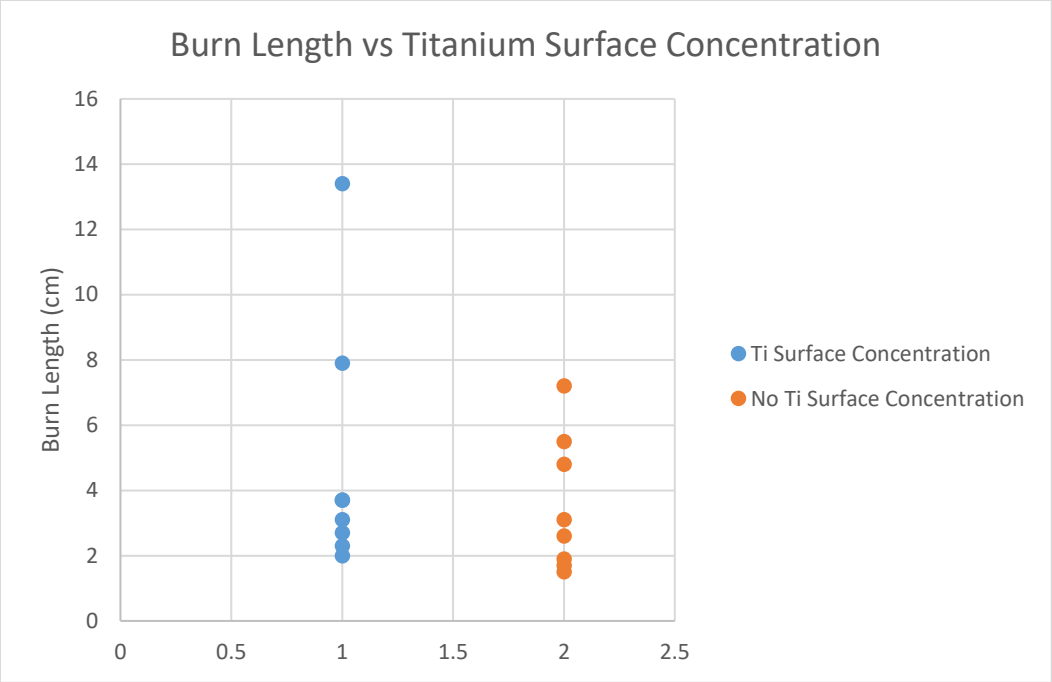

Fig. 221 – Scatter Plot of Burn Length vs Titanium Surface Concentration

The figure above shows a plot of burn length as a function of whether or not a sample displays a concentrated layer of titanium on its outer surface (as confirmed by EDS mapping). What can be seen is that for samples with no such concentration, burn lengths trend slightly lower than those which have a surface concentration of titanium. Hard conclusions would require a significantly larger sample size, but these rods would seem to support the idea that by not having a layer of titanium on the surface (either by removing it via machining or by not introducing additional titanium through wrapping for HIP), one might be able to improve a flammability response.

Chapter 7: Conclusions

Promoted combustion of additively manufactured Inconel 718 is a volatile process which does not immediately follow trends seen for cast or wrought Inconel 718. Combinations of post processing methods such as hot isostatic pressing and surface machining introduce variability (albeit, within a small sample size for this study) in flammability that the author hypothesizes is influenced by resultant structures being able to supply more or less efficiently the necessary constituents up to and across the burn interface.

In a slight majority of rods seen in sample set 1 (10 of 16), fine networks of agglomerated material were present on the surface of the burn interfaces and is likely the result of rapid oxidation and quenching at the completion of combustion testing. Energy dispersive spectroscopy shows that burn tips have non-uniform composition – a surface layer rich in chromium, niobium, and oxygen (and depleted of nickel and iron), while the internal volume is rich in nickel and depleted of chromium.

Bulk chemical analysis was inconclusive for this work, as x-ray fluorescence was not the most accurate method of analysis for samples of this size (besides also being a surface analysis technique which would not have been representative of the interior bulk in any case). EDS point scans of the bulk were more consistent but still don't have the precision necessary to confidently track minute differences in chemistry between powder batch lots.

Microstructurally, burn tips display variable solidification patterns that can at times resemble Widmanstatten. Burn interfaces are not homogenous in size or volume across samples, and though gleaning from a small sample size it would appear that rods which have concave interfaces relative to their axis may be more flammable. If true, a possible mechanism for this may

be that material in the center of those rods has higher flammability than the outer surface allowing the molten interface to be pulled further along the sample.

Dendritic crevices can form in burn interfaces, typically in areas of high niobium structure concentration. Though shallow in most cases, they can have significant depth in others demonstrating that not only are they not consistent across sample types but also don't proliferate at the same rate once present.

Post processing methods can heavily influence the surface chemistry of the rods, and partial aluminum and titanium oxidation has been observed on several samples. X-ray diffraction shows that for most samples there is a sizable difference in spectral peak intensity when comparing the bulk to the heat affected zone, and for the most flammable sample analyzed there was an inordinately strong detection of Ni_3Al γ' near the burn interface.

Transmission electron microscopy analysis and interpretation was less robust than other methods in this work but should provide baseline images and chemistries for future analysis which will attempt to more strongly correlate lattice strain, twin boundaries, and high vs low angle boundaries to flammability.

Chapter 8: Future Work

First and foremost, future work should include a true quantitative chemical analysis of the sample bulk regions – ideally inductively coupled plasma optical emission spectroscopy – so that very fine differences in chemical constituency can be tracked between powder batch lots.

The outer surface of the rods should be more closely examined from the perspective of titanium and aluminum oxidation occurring (regardless of whether a sample was wrapped during hot isostatic pressing or not, or whether it received surface machining following printing). Particular attention should be paid to whether this oxidation layer assists or inhibits the mobility of the burn interface, or if it influences the convexity or concavity of said interface.

Additional x-ray diffraction should be conducted on polished rods to identify if an abundance of Ni_3Al γ' at the burn interface has an influence on flammability, and if so how recrystallization in the heat affected zone promotes or suppresses that structure.

Additional transmission electron microscopy would also be useful for samples representing variable burn lengths (short, medium, long) to establish characteristic lattices in both the transverse and axial orientations and to collect diffraction patterns so crystallographic interpretation can be included.

References

[1] ASTM G124. Standard Test Method for Determining the Combustion Behavior of Metallic Materials in Oxygen-Enriched Atmospheres, *ASTM Standards Related to Flammability and Sensitivity) of Materials in Oxygen-Enriched Atmospheres,* ASTM International, West Conshohocken, PA, 1995.

[2] Tylka, J. (2016). *Evaluation of additively manufactured metals for use on oxygen systems* (No. JSC-CN-37294).

[3] Shao, L., Xie, G., Zhang, C., Liu, X., Lu, W., He, G., & Huang, J. (2020). Combustion of metals in oxygen-enriched atmospheres. *Metals*, *10*(1), 128.

[4] Sparks, K., Stoltzfus, J., Steinberg, T., & Lynn, D. (2009). Determination of burn criterion for promoted combustion testing. *Journal of the American Society for Testing and Materials (ASTM) International*, *6*(10), 1-11.

[5] Campbell, F. C. (Ed.). (2008). *Elements of metallurgy and engineering alloys*. ASM international.

[6] Lewis, M., Jeffers, N., & Stoltzfus, J. (2010). *Promoted Combustion Test Data Re-Examined* (No. JSC-CN-20776).

[7] "INCONEL Alloy 718." *Special Metals*, www.specialmetals.com/assets/smc/documents/inconel_alloy_718.pdf.

[8] Murr, L. E., Martinez, E., Amato, K. N., Gaytan, S. M., Hernandez, J., Ramirez, D. A., ... & Wicker, R. B. (2012). Fabrication of metal and alloy components by additive manufacturing: examples of 3D materials science. *Journal of Materials Research and technology*, *1*(1), 42-54.

[9] Amato, K. N., Gaytan, S. M., Murr, L. E., Martinez, E., Shindo, P. W., Hernandez, J., ... & Medina, F. J. A. M. (2012). Microstructures and mechanical behavior of Inconel 718 fabricated by selective laser melting. *Acta Materialia*, *60*(5), 2229-2239.

[10] Frick, V., Hunt, V., Inouye, F. T., & Janser, G. R. (1967). *Application of Alloy 718 in M-1 engine components* (No. NASA-CR-788).

[11] Zhang, D., Niu, W., Cao, X., & Liu, Z. (2015). Effect of standard heat treatment on the microstructure and mechanical properties of selective laser melting manufactured Inconel 718 superalloy. *Materials Science and Engineering: A*, *644*, 32-40.

[12] Tucho, W. M., Cuvillier, P., Sjolyst-Kverneland, A., & Hansen, V. (2017). Microstructure and hardness studies of Inconel 718 manufactured by selective laser melting before and after solution heat treatment. *Materials Science and Engineering: A*, *689*, 220-232.

[13] Jiang, R., Mostafaei, A., Wu, Z., Choi, A., Guan, P. W., Chmielus, M., & Rollett, A. D. (2020). Effect of heat treatment on microstructural evolution and hardness homogeneity in laser powder bed fusion of alloy 718, Addit. Manuf. 35 (2020) 101282.

[14] Nunes, R. M., Pereira, D., Clarke, T., & Hirsch, T. K. (2015). Delta phase characterization in Inconel 718 alloys through X-ray diffraction. *ISIJ International*, *55*(11), 2450-2454.

[15] Chlebus, E., Gruber, K., Kuźnicka, B., Kurzac, J., & Kurzynowski, T. (2015). Effect of heat treatment on the microstructure and mechanical properties of Inconel 718 processed by selective laser melting. *Materials Science and Engineering: A*, *639*, 647-655.

[16] Tylka, Jon, et al. "AMSII Updates : Flammability Study." *PowerPoint slides.*

[17] Ochoa, Ngozi. "Post-test Analysis of Flammability-Tested Additively Manufactured Inconel 718."
https://www.mdpi.com/2075-4701/10/1/128

[18] Tylka, J. (2019, April). Update: Evaluation of Additively Manufactured Metals for Use in Oxygen Systems. In *ASTM (American Society for Testing and Materials) Committee G04 Meeting on Compatibility and Sensitivity of Materials in Oxygen Enriched Atmospheres* (No. JSC-E-DAA-TN66801).

Glossary

ABF – Annular Bright Field

ADF – Annular Dark Field

AM – Additively Manufactured

AMS – Aerospace Material Specification

ASTM – American Society for Testing and Materials

EBSD – Electron Backscatter Diffraction

EDS – Energy Dispersive Spectroscopy

FIB SEM – Focused Ion Beam Scanning Electron Microscope

GB – Grain Boundary

HAZ – Heat Affected Zone

HIP – Hot Isostatic Pressed

ICP OES – Inductively Coupled Plasma Optical Emission Spectroscopy

ISLO – In Situ Lift Out

JSC – Johnson Space Center

MC – Metal Carbide

OCA – Oxygen Compatibility Assessment

OES – Optical Emission Spectroscopy

PC – Promoted Combustion

PH – Precipitation Hardenable

SEM – Scanning Electron Microscopy

SLM – Selective Laser Melted

SMPS – Solidified Melt Pool Surface

TEM – Transmission Electron Microscopy

WSTF – White Sands Test Facility

XRD – X Ray Diffraction

XRF – X Ray Fluorescence

Vita

Dominic George Dieguez is a materials engineer born and raised in El Paso, Texas. He received his Bachelor of Science in Metallurgical, Material and Biomedical Engineering (MME) from the University of Texas at El Paso in December of 2019, and will be receiving his Doctor of Philosophy in Material Science and Engineering (MASE) from the same university in May of 2024.

During his time at the University of Texas at El Paso he served as an undergraduate research assistant at the Center for the Advancement of Space Safety and Mission Assurance (CASSMAR) conducting failure analysis on components retrieved from the space shuttle Columbia disaster. Once he returned for graduate school he was hired as a teaching assistant with duties including lecturing, grading, tutoring, and leading lab activities for a variety of courses such as Failure Analysis, Materials Characterization, and Electron Microscopy Applications. Additionally, he was a senior operator of his departments scanning electron microscopes assisting several research groups across the college with obtaining images and chemical analyses for their publications and theses.

While in graduate school, he completed 8 internships for NASA (6 at White Sands Test Facility, 2 at Johnson Space Center). This was his inspiration to join civil service, and as such he will be joining NASA Johnson Space Center's Materials and Processes (ES4) branch within their Structural Engineering division upon graduation.

Contact Information: ddieguez97@live.com